

**Functionalized calcium carbonate based peptide formulation:  
Aspects of the development for oral delivery to the buccal  
and intestinal mucosa**

**Inauguraldissertation**

zur

Erlangung der Würde eines Doktors der Philosophie

vorgelegt der

Philosophisch-Naturwissenschaftlichen Fakultät

der Universität Basel

von

**Roger Roth**

aus Zell (LU)

Basel, 2019

Genehmigt von der Philosophisch-Naturwissenschaftlichen Fakultät  
auf Antrag von

**Prof. Dr. Jörg Huwiler**

**Prof. Dr. Georgios Imanidis**

Basel, den 19. Februar 2019

---

**Prof. Dr. Martin Spiess** (Dekan)

## Acknowledgement

I want to thank Prof. Dr. Jörg Huwyler for giving me the opportunity to realize my PhD project in the laboratories of the pharmaceutical technology group. He always provided a pleasant atmosphere in the group and gave valuable inputs that led to the success of this project.

I especially appreciate the collaboration with my direct supervisor Dr. Maxim Puchkov. He was a great inspiration regarding this work, as well as to my mindset in general. It was exciting and a great pleasure to discuss theories and hypotheses in the office or proactively in the lab.

I wish to thank Omya international AG for the financial support of this thesis. Especially, Joachim Schoelkopf, Laura de Miguel, and Carolina Diaz Quijano Reichert for the interesting discussions during meetings and the confidence in my work.

One of the most important factors for this fruitful working environment were my coworkers and team members. I would like to express my gratitude to the team of drug delivery, especially my lab partners Maryam Farzan, Viktoria Schreiner, Marine Camblin, Veronika Eberle, Tanja Stirnimann, Leonie Wagner-Hattler, Andreas Schittny, and Darryl Borland, members from the targeting division; Susanne Schenk, Gabriela Québatte, Anna Pratsinis, Sandro Sieber, Jonas Buck, Stefan Siegrist, Emre Cörek, Dominik Witzigmann, Tomaz Einfalt, Pascal Detampel, and Patrick Hauswirth as well as external colleagues; Ariane Schmidt, Tim Dreckmann, Joachim Schuster for providing an excellent and unforgettable time. Special thanks goes to Gabriela Québatte and Darryl Borland for proofreading this manuscript.

Highly appreciated is also the contribution of Giuseppina Cammarata during her master thesis.

I thank Denise Ruoff for her excellent planning and organization of administrative challenges.

Credited are also Evi Bieler, Daniel Mathys, and Markus Dürrenberger from the Nano Imaging Lab for an excellent job at the scanning electron microscope.

Indirectly responsible for the success of this work was my girlfriend Valérie Gasparini. She was the greatest mental support for the period of this thesis, and went through hours of discussions about particulate delivery systems, drug loading strategies, and other “crazy scientist” topics. Must have been terrible: Thank you so much.

Special thanks go to Dr. Daniel Preisig who carefully introduced me into the topic and offered me the possibility to initiate this work as a master student a long time ago.

A great thank you goes to my parents Renate and Roland, who gave me the freedom to go my way and never judged me based on success. My grandparents Hildegard and Heinrich as well as Maria and Eugen, who taught me some important details of life. My sister Chantal and her family for their confidence as well as my aunt Susi and her husband Kurt for helping spontaneously in many situations. Finally, a great thank you goes to all my friends for sharing good and bad times with me.

## Table of Contents

<b>Acknowledgement.....</b>	<b>I</b>
<b>Summary .....</b>	<b>V</b>
<b>1. Introduction.....</b>	<b>1</b>
1.1 Non parenteral delivery of peptide drugs.....	1
1.2 The gastro intestinal tract (GIT) .....	4
1.2.1 Function and anatomy of the oral cavity.....	4
1.2.2 Function and anatomy of the small intestine .....	6
1.2.3 Function and anatomy of the large intestine.....	7
1.3 Penetration of drugs through the mucosa .....	8
1.4 Mucoadhesion .....	11
1.4.1 Testing mucoadhesion .....	13
1.5 Physicochemical properties of proteins, enzymes, and peptides .....	15
1.5.1 Proteins on solid surfaces .....	17
1.5.2 Enzyme Activity.....	19
1.6 Functionalized Calcium Carbonate .....	21
1.6.1 Omyapharm OG-500 .....	21
1.7 Electrospinning and Electrospraying .....	23
<b>2. Aims.....</b>	<b>25</b>
<b>3. Publications in peer-reviewed journals .....</b>	<b>27</b>
3.1 Functionalized calcium carbonate microparticles for the delivery of proteins .....	27
3.2 Mucoadhesive microparticles for local treatment of gastrointestinal diseases .....	37



3.3 Loading of porous functionalized calcium carbonate microparticles: Distribution analysis with focused ion beam electron microscopy and mercury porosimetry .....	49
3.4 Coating of PLA-nanoparticles with cyclic, arginine-rich cell penetrating peptides enables oral delivery of liraglutide .....	65
<b>4. Discussion.....</b>	<b>89</b>
4.1 FCC for the delivery of peptide drugs – Validity of the model system. ....	89
4.2 Incomplete release of BSA.....	90
4.3 Modified release .....	91
4.4 Penetration of liquids into pores.....	92
4.5 Strategies to maximize drug load .....	94
4.6 Mucoadhesion .....	98
4.7 Colloidal electrospray for drug loading and coating of microparticles.....	101
<b>5. Conclusion and Outlook.....</b>	<b>107</b>
<b>6. References.....</b>	<b>109</b>
<b>7. Curriculum Vitae.....</b>	<b>121</b>

## Summary

Diseases and malfunctions of the gastro intestinal tract belong to the most common illnesses in humans. This includes infections, caused by bacteria and fungi as well as food intolerances against a variety of dietary products. The prevalence of such diseases is increasing due to either bacterial resistances or changes in alimentary behavior.

Peptide drugs are a promising class of active pharmaceutical ingredients that have the potential to overcome the drawbacks of conventional small molecules such as increasing bacterial resistances. Since peptides regulate a variety of functions in the human body, they offer attractive therapeutic strategies such as enzyme replacement therapy or hormone substitution. However, oral delivery of peptide drugs is challenging mainly due to their low physical and chemical stability and poor bioavailability. Therefore, formulation of such compounds is challenging and only a few products exist on the market.

Functionalized Calcium Carbonate (FCC) was recently introduced as a new pharmaceutical excipient. FCC is a microparticulate material composed of calcium carbonate and hydroxyapatite with a high porosity of up to 60%, and an average particle size of approx. 10  $\mu\text{m}$ . It shows excellent compaction behavior due to a nano-structured surface and it combines properties of nanoparticles such as high surface area with the processibility of larger particles.

The aim of this thesis was to explore the possibilities of using FCC for the delivery of sensitive biomolecules such as enzymes, proteins, and peptides via the oral cavity respecting the requirements of a multiparticulate mucoadhesive system. Further, the goal was to improve analytical methods to study material distribution within the porous particles in order to finally improve loading and coating processes.

Therefore, FCC was loaded with the two model substances lysozyme and bovine serum albumin. Release was measured in a customized flow cell, showing that lysozyme was released after 100 minutes, while considerable amounts of BSA remained adsorbed to the particles surface. Structural integrity and enzymatic activity of the released model substances were compared to unloaded material and were shown to be unchanged.

A two-step fluidized bed process, which allows drug loading and mucoadhesive coating of FCC was developed and mucoadhesion was assessed in a flow cell on porcine mucosa from the colon. The process is suitable for scale up and the produced particles showed good mucoadhesion *in vitro*. Release rate was found to be lower compared to uncoated particles, this was mainly attributed to a reduced surface area of the agglomerated particles.

Loaded particles were imaged by focused ion beam scanning electron microscopy to reveal the internal structure as well as intraparticulate material distribution. The findings were compared to results from mercury intrusion porosimetry in order to point out limitations of each method. It was concluded, that material distribution is dependent on a materials physical properties, and that a combination of the two methods is required for the correct interpretation of material distribution within porous microparticles.

Colloidal electrospray was investigated in a pilot study for its potential to load and coat individual particles. Preliminary trials showed promising results in terms of producibility, particle morphology, and size.

Generally, FCC is a suitable carrier for the models BSA and lysozyme and potentially other peptide drugs. However, poor release of BSA suggests further investigation on adsorption phenomena and how to avoid these. Mucoadhesion of the particles was good *in vitro*, although its performance *in vivo* still needs to be evaluated. With the gained knowledge on material distribution and the internal structure of FCC, new loading methods to promote material deposition in deeper regions of the particle should be considered. This might include further investigation of the colloidal electrospray process.



# 1. Introduction

## 1.1 Non parenteral delivery of peptide drugs

Peptide based drugs (PD) including short peptides, proteins, and enzymes, which all count as members of this category are regulating a variety of biological functions in the human body. It is obvious, that they present an attractive class of active pharmaceutical ingredients (API) to treat several diseases or malfunctions. The medicinal application of peptide therapeutics started in the beginning of the 20<sup>th</sup> century with the use of insulin, originating from animal (bovine and porcine) sources, for the regulation of blood glucose levels. Other peptide hormones like the follicle stimulating hormone or luteinizing hormone releasing hormone which are both involved in pubertal maturation and reproductive mechanisms as well as erythropoietin to stimulate the production of red blood cells (erythropoiesis) are used frequently [1]. PD also include enzyme inhibitors, immunomodulators, and antimicrobial agents like penicillins or so called cationic peptides, a class of small positively charged peptides which are also acting as a part of the innate immune system [2].

In 2005 it was reported, that a total of 324 PD are either in human clinical trial or under revision of the regulatory authorities [3]. The rate of approvals for PD rose from 1.3 per year in the 2000s up to 3 per year for the years 2010 to 2013 [4]. Probably this trend will continue and PD might become important APIs in the future. A primary reason for the increasing interest in PD is that they bind with outstanding specificity to a target which is the reason for their high potency, resulting in less adverse effects when compared to conventional small molecules. Additionally, recombinant protein expression, advanced molecular biology tools, purification, and analytics of such PD has led to intensified research in the field [5].

However, PD show in general extremely poor bioavailability when administered via the gastrointestinal tract (GIT). Besides their susceptibility to degradation by proteases and the harsh conditions in the GIT (mainly the low pH in the stomach), PD show poor membrane permeability due to their hydrophilicity and their large molecular weight. This is the reason, why the majority of the existing formulations are intended to be used as an injectable. Examples of frequently used PD are insulin, gonadotropin, and glucagon.

Only a few formulations exist, which take advantage of alternative delivery pathways such as via mucosal tissues. Mucosal tissues are present in many compartments of the body like the GIT, nasal, pulmonary, vaginal, and rectal cavities. They present a promising route for PD delivery since it would circumvent the hepatic first pass effect and presystemic metabolism in the GIT. So far, several formulations for the nasal route are marketed successfully: In Switzerland, the short peptide desmopressin (1183 Da) is sold under

the tradename Minirin® nasal spray to treat mainly polyuria, oxytocin (1007 Da) is traded under the name Syntocinon® to facilitate breastfeeding and to prevent mastitis, synthetic salmon calcitonin (3432 Da) is available as Miacalcic® nasal spray as preventive treatment against osteoporosis, and nafarelin (1321 Da) is commercially available under the brand name Synrelina® nasal spray to treat endometriosis. However, next to its high permeability, the nasal mucosa has disadvantages regarding accurate dosing caused by a rapid clearance with a high inter and intra individual variability, which makes formulation development challenging. In addition, long term medication via the nasal mucosa is associated with irritation and toxicity to ciliary cells, thus excluding long term treatments such as insulin therapy. The lungs provide an extremely large surface area of up to 140 m<sup>2</sup> and a highly permeable membrane with intensive vascularization, which makes it the ideal site for drugs which benefit from a fast onset of action. Pulmonary delivery of insulin has been realized with the product Exubera® until it was discontinued due to poor sales volume and the occurrence of side effects like, cough, and increased risk of respiratory infections. Studies also demonstrated a negative effect on the pulmonary function when compared to placebo [6]. Other PD show promising results especially when they are supposed to act locally like in the treatment of cystic fibrosis, chronic obstructive pulmonary disease, and asthma [7]. The vaginal and rectal route both are technically attractive sites for drug delivery due to rich vascularization and large surface area for absorption, but they suffer from poor patient acceptance and compliance [8].

In general, PD are promising candidates to improve the efficiency of a therapy, but they are not able to reach the systemic circulation after oral administration. However, in some cases, systemic uptake is not necessary or disadvantageous, and high local drug concentrations are desirable. Therefore, local delivery to the GIT presents a promising strategy for the treatment of gastro intestinal diseases. The following section outlines three cases, which could profit from a local treatment of PD as antibiotics.

It has been shown *in vitro*, that diseases of the oral cavity (including the esophagus), such as oral mucositis, dental and periodontal disorders, candidiasis and other infections as well as aphthous ulcerations could profit from a local treatment with PD therapy [9–11]. Studies could demonstrate activity of the peptide cathelicidin (LL-37) against clarithromycin resistant *Helicobacter Pylori*, as well as disruption and inhibition of the biofilm formation in rats [12]. The resistance of *H. Pylori* against commonly used antibiotics raises concerns especially in developing countries. For example, in China the resistance of *H. Pylori* against the standard antibiotics clarithromycin, metronidazole, and levofloxacin are 21.5, 95.4, and 20.6 %, respectively [13,14]. The mentioned standard antibiotics are also frequently used in the treatment of small intestinal bacterial overgrowth (SIBO). SIBO is defined as a situation when bacteria concentration in the small

intestine exceeds the number of  $10^5$ - $10^6$  organisms per ml of intestinal fluid [15,16]. The symptoms associated with SIBO are diverse and depend on the amount and the type of colonizing microorganism. Typical symptoms are abdominal pain and discomfort, bloating, diarrhea, and in severe cases weight loss and other symptoms related to malabsorption [17]

Besides antimicrobial treatment, PD can be used locally to replace insufficient amounts of active enzymes in the GIT. Celiac disease is a good example to explain the concept of oral enzyme replacement therapy.

Celiac disease (CD) is an immunologically mediated disorder, mainly affecting the mucosa of the small intestine due to an intolerance towards gluten. Irritation of the microvilli structure leads to the main symptoms such as malabsorption and diarrhea, which can cause a disturbance of growth in children. So far a lifelong gluten free diet is the only treatment for the disease that affects approx. 1% of the human population [18]. Even though a variety of therapeutic strategies, including genetically modified wheat, antibodies to neutralize gluten, oral enzyme therapy, inhibition of gluten absorption or the immune response are considered, only a small number of formulations are in clinical trials. A number of studies have demonstrated, that glutamine and proline-specific endopeptidases contribute to the enzymatic breakdown of dietary gluten *in vitro* and *in vivo* [19]. Especially prolyl endopeptidases show a high affinity towards proline rich residues which are relatively prominent (15 %) in gluten [20]. Promising attempts to use prolyl endopeptidases in combination with other glutamine specific endoproteases have initiated clinical trials due to their ability of detoxifying relevant amounts of gluten under gastric conditions [20,21]. The authors pointed out, that the acidic pH of the stomach decreases the activity of potential enzymes favoring a release of the active enzymes after the passage through the stomach. Ideally, gluten is already processed in the stomach to prevent contact of toxic peptides with the small intestine. However, if this is not applicable due to low activity of enzymes under acidic conditions, instant distribution in the duodenum and prolonged residence time is essential for rapid and efficient breakdown of immunologically critical peptides. Therefore, advanced drug delivery strategies have to be considered.

Even though, diseases related to the GIT account for the most common illnesses in human, there is still a lack of appropriate formulations available, which satisfy the demanding requirements for drug delivery to the gastro intestinal mucosa. This includes the ability to carry cargo safely to the site of application, to control the release and local distribution of the API, as well as the potential to prolong its residence time at the site of action. Further, it should support the ease of administration to improve patient compliance and eventually a therapeutic success. The list below points out some relevant qualities, a porous drug carrier should meet from a patient as well as from an industrial point of view.

- **High compressibility**
- **Mechanical strength**
- **Flowability**
- **Size**
- **High drug loading capacity**
- **Compatibility with API and other excipients**
- **Price/Cost**
- **Availability**
- **Low batch to batch variability**
- **Well characterized**
- **Pharmacologically inactive**
- **Comfort of administration**
- **Modified release**
- **Residence time**
- **Site specific delivery**

## **1.2 The gastro intestinal tract (GIT)**

For local delivery of PD within the GIT, understanding and knowledge about anatomical as well as physiological aspects of the GIT is essential. Therefore, the following chapter gives an overview on some relevant aspects of the GIT.

### **1.2.1 Function and anatomy of the oral cavity**

The mouth or oral cavity represents the first part of the gastro intestinal tract of the human body. It serves as the entry for food and initiates the digestion process, by physically breaking down aliments into small fractions. Complex interplay between tongue, teeth and cheeks, ensures, that the surface of the food is enlarged for efficient digestion. Insalivation of the ground food produces a smooth chyme ready for the passage through the pharynx into the stomach where further processing takes place. Not only physical but also chemical breakdown of food compartments takes place: Mainly salivary amylase starts breaking down long carbohydrates while lingual lipase hydrolyzes triglycerides into diglyceride and fatty acids [22]. The anatomy of the oral cavity is depicted in figure 1. The oral cavity is confined by the hard and soft palate on the upper side and the sublingual region on the floor of the mouth. Laterally, it is the buccal area that form the inner wall of the cavity. Teeth are embedded in the upper (maxilla) and lower (mandible) jawbone and



are sealed by the upper and lower gingivae, which is connected firmly to the supporting bone. Behind the tongue and the uvula, the pharynx creates the connection between the oral cavity and the esophagus.

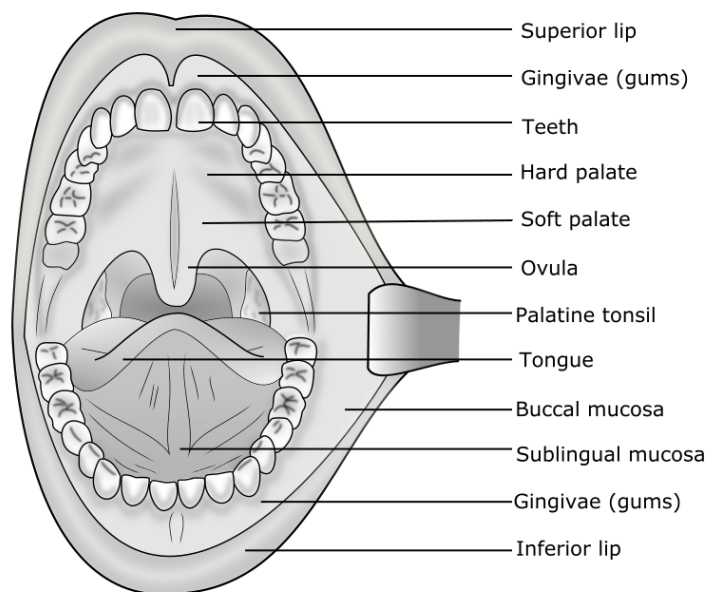


*Figure 1: Anatomy of the oral cavity.*

The entire surface of the oral cavity is lined by the oral mucosa. The oral mucosa, can be anatomically classified into four sites, which are the palatal, gingival, sublingual, and buccal mucosa. The buccal mucosa refers to the mucosa of the cheeks including the inside region of the upper and lower lips. Histologically, the mucosae can be divided into two types with different properties of the epithelium. The palatal and gingival mucosa have a keratinized epithelium that contains a larger fraction of high molecular weight keratins than the non-keratinized epithelium that can be found in the sublingual and buccal mucosa [23]. Due to their relatively high permeability and low enzymatic activity, mainly the sublingual and buccal areas are investigated for the delivery of drugs. Even though, the buccal mucosa is less permeable than the sublingual area, it presents an attractive site for drug absorption due to its high surface area and reduced exposure to salivary flow, which can lead to altered drug absorption [24]. Saliva is excreted mainly by the parotid, submandibular, and sublingual glands at a unstimulated flow rate of about 0.3 ml/min which can increase up to 7 ml/min when stimulated [25]. The total amount of saliva, which is secreted into the oral cavity is approximately 1.5 l/d [26]. Saliva is viscous, transparent and has a slightly acidic pH of 6.2-7.4.

Saliva is composed of mainly water, but also contains mucus, electrolytes, proteins and the above mentioned digestive enzymes. Mucus is an aqueous secret, which is produced by all mucosa membranes. It consists of water and mainly mucins which will be described in the chapter on mucoadhesion. Compared to the small intestine and colon, the oral cavity presents an attractive site for systemic delivery of PD for two distinct reasons. First, the enzymatic activity in the oral cavity is lower. Second, the oral cavity is well accessible, what allows for accurate positioning of a formulation, e.g. mucoadhesive tablets, patches, and ointments.

### **1.2.2 Function and anatomy of the small intestine**

The main task of the small intestine is the digestion of alimentary components and their absorption into systemic circulation. Besides nutrients, the small intestine is responsible for the resorption of water (approx. 6 l/d) [26]. The small intestine has a total length of approx. 5-7 m and is divided into three segments which are the duodenum, jejunum, and the final section ileum. The duodenum is C-shaped and is the shortest section of the small intestine (20-30 cm). In the duodenum, enzymatic processing of food is initiated. When gastric chyme enters the duodenum via the sphincter pylori, bile salts and pancreatic juices enter the descending duodenum via sphincter of oddi. Pancreatic enzymes break down proteins, while bile emulsifies fats. So called Brunner's glands (located in the submucosa) can be found above the sphincter of oddi. These cells secrete an alkaline mucus, which neutralizes the acidic chyme from the stomach in order to protect the duodenal mucosa and provide a more alkaline environment for pancreatic enzymes. The pH gradient in the first 10 cm of the duodenum ranges from 1.7 to 5, which present a critical environment for the delivery of pH sensitive drugs, e.g. PD [27]. The jejunum accounts for approx. 40% of the total length of the small intestine. Its main task is the resorption of nutrients and xenobiotics from the chyme. The inner surface of the jejunum is equipped with finger like projections called villi. Cells on the surface of the villi are decorated with microvilli to maximize the surface area that is in contact with the chyme and hence to increase the resorption of nutrients. The jejunum is surrounded with circular and longitudinal muscles, which are responsible for peristalsis. Therefore, the smooth muscle tissue contract in sequence in order to mix, shear, and transport the bolus towards the colon. The pH in the jejunum ranges from 7-9. The last section of the small intestine is the ileum which is mainly responsible for the resorption of bile salts, vitamin B-12 and all products which have not been resorbed by the jejunum thus far. The diameter of the lumen is smaller than in the jejunum and the circular folds are decreasing and finally disappearing when reaching the colon. The pH in the ileum is between 7 and 8.

### 1.2.3 Function and anatomy of the large intestine

Main function of the large intestine is the resorption of the remaining water (approx. 2L/d)[26] and residual nutrients such as vitamins, as well as transport and storage of feces before they are removed by defecation. The large intestine measures approx. 160 cm [28]. Digested food enters the large intestine via the ileocecal valve into the caecum, which represents the first section. Attached to the lower end of the caecum lies the appendix, which is not directly involved in the process of digestion, but contains microflora, similar to the one found in the colon. The caecum is followed by the ascending, transverse, and descending colon, where further dehydration of the feces and resorption of salts takes place. Finally, the sigmoidal colon pushes the stool into the rectum from where it is eliminated. The inner wall of the large intestine differs from the small intestine. Circular folds (plicae circulares) which can be found in the small intestine as well as villi structures are not present in the large intestine. The inner surface of the large intestine consists of crypts instead of villi and it appears smooth. Compared to the small intestine, peristalsis is less intense and mainly for transport instead of mixing for digestive purposes.

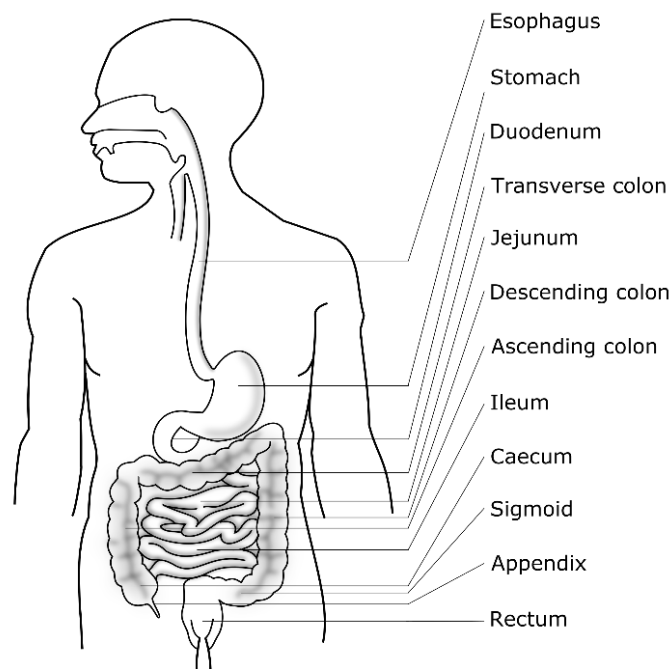


Figure 2: Gastro intestinal tract.

### 1.3 Penetration of drugs through the mucosa

Although, in this work, the use of PD for local applications is emphasized, the potential of PD for systemic applications cannot be ignored. Therefore, some general aspects of transmucosal absorption are presented in the following section.

Once a drug gets released from its dosage form, it dissolves into the saliva and penetrates into the mucus. Subsequently, it diffuses through the epithelium of the mucosa into the connective tissues, where it goes into systemic circulation. There are two modes of transport through the mucosa: Figure 3 shows the general structure of the oral mucosa and the different pathways that a drug can take to reach the underlying blood vessels.

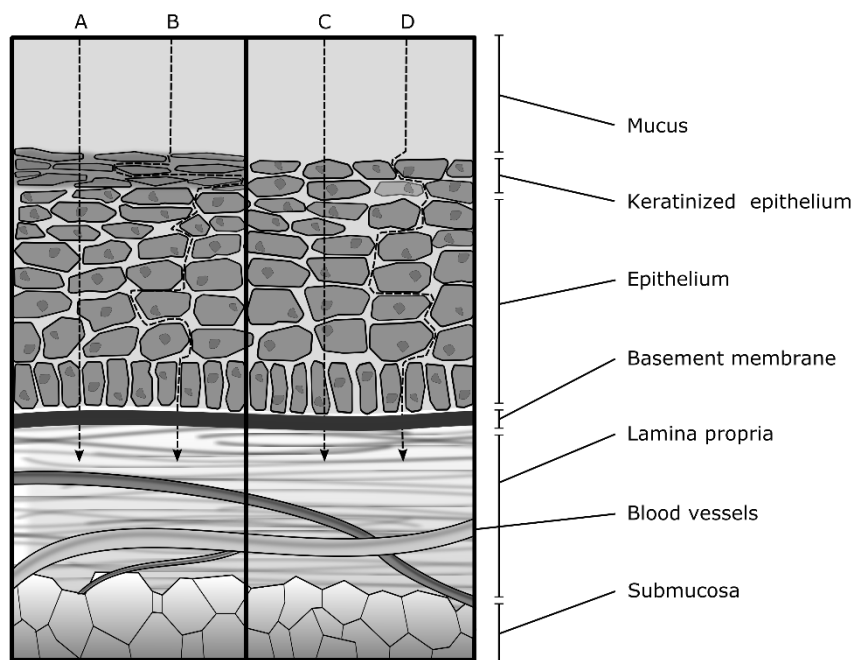


Figure 3: Transport of drugs through the mucosa. A) Transcellular pathway in keratinized epithelium. B) Paracellular pathway in keratinized epithelium. C) Transcellular pathway in non-keratinized epithelium. D) Paracellular pathway in non-keratinized epithelium.

Predominantly lipophilic and small hydrophobic drugs undergo the transcellular pathway, which includes the passage across the apical cell membrane, the intercellular space, and the basolateral cell membrane. Since the cell membrane has lipophilic character, hydrophilic drugs have difficulties permeating into the

cell membrane due to low partition coefficients. Therefore, hydrophilic drugs diffuse through the epithelium via the paracellular also referred as the intercellular pathway. The paracellular pathway is the preferred route for PD, due to their hydrophilic nature.

Even though, the enzymatic activity across the oral mucosa can be considered as moderate, it still presents a barrier function. In addition, the half-life of peptides in the systemic circulation is short. Therefore, intensive effort is spent on identifying molecular cleavage sites, thus limiting the enzymatic degradation of the peptides through structural substitution [29]. More relevant with respect to formulation development is the passive diffusion barrier created by the epithelium, which was identified by Squier et al.

Experiments with horse radish peroxidase (40 kDa) have demonstrated, that the enzyme does not penetrate more than 25% of either non-keratinized or keratinized epithelium [30–32]. The differences in permeability within the different regions of the oral mucosa were studied with tritiated water and was shown to be higher for the non-keratinized epithelia of the buccal and sublingual area than for the keratinized areas of the gingivae and palate [32]. Furthermore, it was shown, that the permeability in the sublingual area is higher than in the buccal area due to a considerable difference in their thickness. Table 1 summarizes the main barrier relevant characteristics of mucosae along the GIT and in other locations of the human body.

*Table 1: Characteristics of different mucosa.*

Location	Thickness [ $\mu\text{m}$ ]	Keratinization	Mucus layer [ $\mu\text{m}$ ]
<b>Buccal</b>	500-600	No	70-100 [33]
<b>Sublingual</b>	100-200	No	70-100 [33]
<b>Gingival</b>	200	Yes	70-100 [33]
<b>Palatal</b>	250	Yes	70-100 [33]
<b>Esophagus</b>	-	No [34]	-
<b>Stomach</b>	1000-1600 [35]	-	190-275 [36]
<b>Small intestine</b>	-	-	170-480 [36]
<b>Colon</b>	-	-	830 [36]
<b>Nasal</b>	300-500 [37]	-	-
<b>Rectum</b>	600-1100 [35]	-	-

The relatively high permeability of the sublingual mucosa is favorable for the administration of drugs that profit from a fast onset of action. One of the most prominent example is the treatment of acute pain associated with angina pectoris with nitroglycerin. However, for the delivery of peptides and proteins, which fall into a less permeable class of drugs, a slow release system is beneficial. Unfortunately, the sublingual area, besides being highly permeable comes with two major drawbacks, which are increased salivary flow and intensive movement of the tongue. A more attractive site for the use of slow release dosage forms is the buccal area, since it offers a larger surface area, is less exposed to salivary washout, and less affected by the movement of the tongue [8]. Over the last decades, a variety of pharmaceutical formulations for oral delivery of PD have been developed, this includes tablets, capsules, micro and nanoparticles, hydrogels, as well as oral and intestinal patches. However, even for smaller peptides such as insulin (5.8 kDa), the epithelium presents a serious obstacle, hence the oral bioavailability is low [38–40]. On one hand, this represents a major problem with respect to systemic delivery, on the other hand, this offers an attractive occasion for local applications, since local drug concentration is not reduced by absorption processes.

## 1.4 Mucoadhesion

A key point of local drug delivery is the prolonged residence time of the delivery device at the site of application. Floating, swelling, and magnetic systems are described in the literature to control the residence time [41–43]. However, a very promising strategy to achieve prolonged residence time is the concept of mucoadhesion, which will be described in the following chapter.

Mucoadhesion is a special case of bioadhesion, in which one of the two materials which are held together is a mucus covered membrane (mucosa) and the other usually a polymer either from synthetic or biological offspring. Mucins, which represent a fraction of 1-5 % w/v of the mucus are a group of glycoproteins which consist of a central cysteine rich protein strand that is decorated with branched and linear polysaccharides which account for 50-80% w/w and give the molecule a negative charge [36].

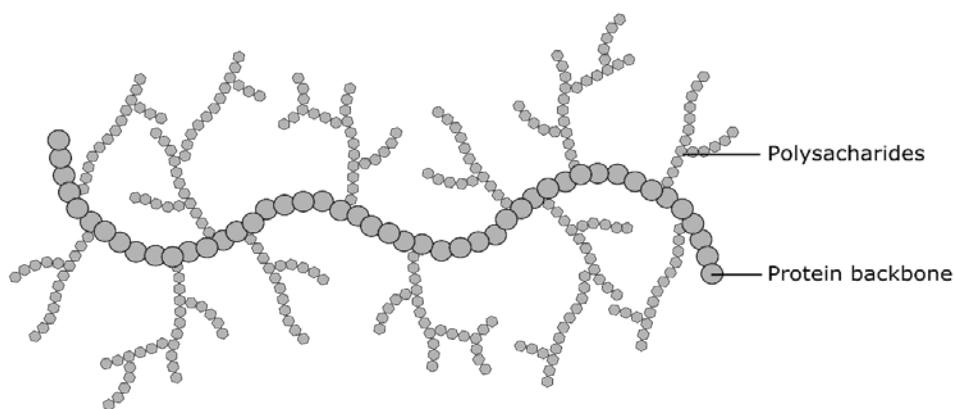


Figure 4: Schematic representation of a mucin molecule. The protein backbone is decorated with branched and linear polysaccharides, which give the molecule its characteristic negative charge.

There are multiple theories behind the phenomena of mucoadhesion, which are schematically shown in figure 5. The wetting theory takes into account the different surface and interfacial energies and applies mostly for system with one component being a liquid that spreads over a solid surface. The ability of a liquid to spread over a surface is a requirement to initiate the contact between the two surfaces and can be expressed as described in equation 1:

$$S_{SL} = \gamma_S - \gamma_L - \gamma_{SL}, \quad (1)$$

where  $S_{SL}$  is the spreading coefficient,  $\gamma_L$  is the surface energy of the liquid,  $\gamma_s$  is the surface energy of the solid, and  $\gamma_{SL}$  is the interfacial energy between the solid and liquid. The liquid will spread spontaneously over the solid, when  $S_{SL}$  is positive. The energy, which is necessary to separate the two phases represent the work of adhesion ( $W_A$ ) and can be described by equation 2:

$$W_A = \gamma_s + \gamma_L - \gamma_{SL}, \quad (2)$$

The electronic theory attributes the adhesion to the formation of an electrical double layer at the interface between the negatively charged mucin and positively charged mucoadhesive materials, e.g. polymers like chitosan. The diffusion theory assumes the two different polymer chains to interpenetrate into each other along the adhesive interface driven by concentration gradients. The penetration is dependent on the mobility of the polymers and the length of their chains. The depth of penetration and therefore also the strength of the adhesion is dependent on the diffusion coefficient and the time in which the surfaces are in contact. The mechanical theory describes the phenomena as an interlocking of an adhesive liquid into crevices of a rough surface [44,45]. The adsorption theory links the attractive forces to the formation of hydrogen bonding and van der Waals interaction. It is well accepted, that these forces are the main contributors to the resulting mucoadhesion.

Even though several types of interaction are necessary to form a mucoadhesive bond between the mucosa and the adhesive material, the process can be separated into two phases. Initially, the adhesive material gets hydrated and swells to make contact with the mucus. At this point, the adhesion is formed by the mechanism of wetting and the formation of an electrical double layer, followed by the interpenetration of the polymer chains. In a second phase, the mucoadhesion is further consolidated by forces described by the mechanical and adsorption theory, e.g. hydrogen bonding and van der Waals [46].



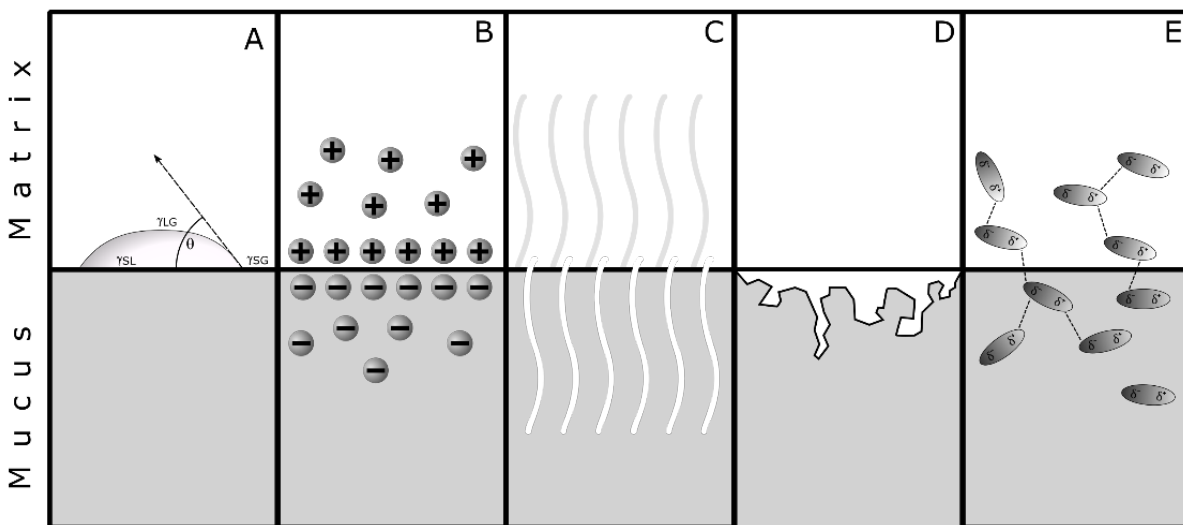


Figure 5: Theories of mucoadhesion between the mucus layer and the matrix of a mucoadhesive device. A) Surface energy. B) Electronic theory. C) Interdiffusion of polymer chains. D) Mechanical theory. E) Disperse interactions.

#### 1.4.1 Testing mucoadhesion

The European pharmacopoeia defines mucoadhesive preparations as dosage forms that contain one or more API (s) intended for systemic absorption through the buccal mucosa over a prolonged period of time, including tablets, films, liquid, and semi-solid preparations. The only test required by the European pharmacopoeia is to demonstrate the appropriate release of the API(s) [47]. There is a variety of methods and procedures to assess mucoadhesion. The following section presents an overview on systems that are used in research.

Ideally, a standardized test method that covers a wide range of possible dosage forms should be used in order to compare results. It should simulate the conditions at the site of application, this includes body temperature, the use of an appropriate medium like artificial saliva or gastric fluid, and the application of realistic forces acting on the system. Since there is still no defined procedure for testing mucoadhesive properties of a formulation, several methods have been suggested over the last decades, based on mechanical, physicochemical and optical methods. The following section provides an overview on test systems and materials that are frequently used in research.

The substrate for mucoadhesive testing often originates from animal sources. This includes dermis from rat, rabbit, pig and human but also lyophilized porcine dermis and tanned leather were used as models in the past [48,49]. Newer approaches include the use of cell culture methods. Keely et al. used a monolayer of mucus secreting goblet cells, to test polymer solutions and could demonstrate a similar rank order in mucoadhesivity when compared to rat intestinal sac [50]. Rather than using animal or human derived mucosa samples, artificial substrates should be considered, since it eliminates variabilities and provides defined composition, permeability, and surface topography. Several artificial

systems have been proposed. Hall et al. developed a library of synthetic mucosa-mimetics, based on hydrogels [51]. A promising candidate, containing the two monomers N-acryloyl glucosamine and 2-hydroxyethyl methacrylate showed mucoadhesive properties, comparable to those of porcine buccal mucosa. It was also shown, that the hydrogel showed similar deformation behavior to buccal mucosa during tablet removal. The same monomers were also covalently bound to glass for the characterization of liquid and semi-solid mucoadhesive formulation [52,53]. Agar was used to study the mucoadhesion of inhalable polymer particles and for the assessment of a mucoadhesive nasal formulation [54]. The mucoadhesion of tablets on PVC (polyvinylchloride) and Plexiglas (polymethylmetacrylate) was compared to rat intestinal mucosa and bovine buccal mucosa, respectively [55,56]. As aforementioned, the physiological characteristic of the mucosa can vary a lot including pH, viscosity, and thickness of the mucus layer (table 1). Therefore, a single mucosa-model to study and compare mucoadhesion is not feasible.

Besides a variety of mucosa mimetic materials there is a variety of test procedures described in the literature, which can be categorized into direct and indirect methods. Direct methods evaluate the force or time that is required to remove a dosage from a mucosa substrate, while indirect methods aim to characterize the physical interactions between a mucoadhesive material and the mucin glycoproteins [57]. Direct methods include the use of a material or tensile test apparatus or simply a modified balance. The procedures aim to measure the forces involved in the detachment process by either pulling (tensile force), dragging (shear force) or peeling a formulation of a mucosa [58,59]. Schnürch et al. used intestinal porcine mucosa that was spanned on a rotating cylinder to measure the time for detachment [60]. The same principle of applied shear force is also commonly used for the assessment of particulate, semisolid and liquid formulations in continuous flow assays. The formulation of interest is distributed on a mucosa or mucosa mimetic, which is mounted in a flow cell or channel, and is subjected to a continuous flow of a washing media (usually saline or digestive fluids). The results are represented as detached or remaining particles against time. Several geometries have been described in literature, e.g. flat and round bottom as well as open- or closed-cell systems, using flat or tubular sections of mucosa [61–63]. A selection of direct methods to measure mucoadhesion is presented in figure 6.

A method, that can be placed in between direct and indirect measurements is the use of an AFM to measure the forces between mucin and a potentially mucoadhesive polymer on a nearly molecular level [64–66]. In rare cases, mucoadhesion is directly evaluated *in vivo*. Henriksen et al. studied the bioadhesion of radioactive labeled chitosan coated liposomes on the cornea of wistar rats by measuring the remaining radioactivity after certain time intervals [67]. Albrecht et al. investigated the mucoadhesion of particulate formulations in rats by oral administration and subsequent magnetic resonance imaging (MRI)[68].

Compared to the above mentioned direct methods for the assessment of mucoadhesion, indirect methods focus on the characterization of physicochemical interactions between mucin and potential mucoadhesive polymers. Rheology can be used to measure the change in viscosity of mucins when interacting with mucoadhesive polymers [69]. This method has been used extensively thanks to its simplicity, but Hägerström et al. concluded, that the method should not be used as a stand-alone due to high variation (different rank order of mucoadhesion) at different test conditions [70]. Fourier

transform infrared spectroscopy (FTIR) has been used to show the interpenetration of polymers and mucin and contact angle measurements were indicative for the contribution of interfacial energies to mucoadhesion [71,72]. Different approaches of using the ability of mucin covered surfaces to adsorb mucoadhesive polymers have been implemented by several research groups. The change in surface properties of mucin particles due to adsorption of mucoadhesive polymers can be quantified by measurement of the zeta potential, while the BIACORE method uses surface plasmon resonance (SPR) to detect changes in solute concentration on a chips surface [73,74]. In general, indirect methods focus on isolated events of the mucoadhesion process and are well suited to characterize individual contributions to the entire effect and can help to estimate the mucoadhesive potential of a substance. However, since indirect techniques are very isolated systems, they cannot give valuable information about the efficiency of a mucoadhesive dosage form.

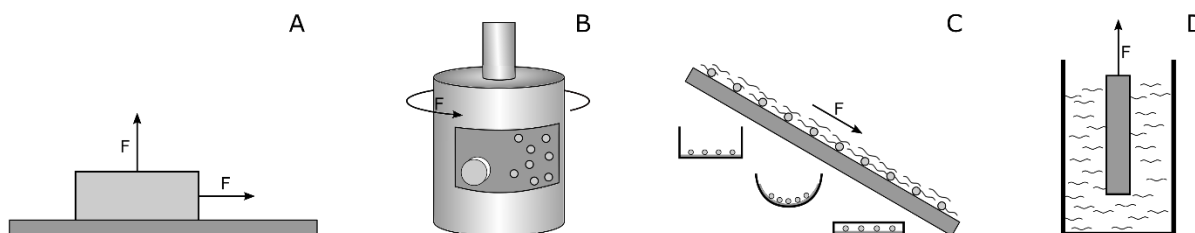


Figure 6: Direct test methods to measure mucoadhesion. A) Force tester or tensiometer applies force (pull or drag). B) Rotating cylinder method with particles and tablet. C) Flow cells with different cross sectional geometries. D) Mucoadhesive device embedded in artificial mucus. The arrow represents the direction of force applied to the mucoadhesive device.

## 1.5 Physicochemical properties of proteins, enzymes, and peptides

PD differ from small molecules. The following section provides an overview on relevant characteristics of peptide based materials. Proteins, enzymes and peptides consist of at least one chain of amino acids that are chemically linked via peptide bonds. The length of that chain varies from a few to several thousand units (amino acids), although, short chains (<100 amino acids) are not considered to be proteins, but often referred as peptides or oligopeptides. One special group of proteins is called enzymes. Enzymes are proteins which act as biological catalysts.

The structure of peptide based substances can be divided into four regimes reaching from primary to quaternary structure. The primary structure describes the sequence of the linked amino acids starting at the amino terminus (N-terminus) and ending at the carboxyl-terminus (C-terminus). The secondary structure determines the 3-dimensional form of local segments in the protein that is stabilized by hydrogen bonds. Most often occurring elements are  $\alpha$ -helices and  $\beta$ -sheet. The tertiary structure of the polypeptide

is defined by the arrangement of the secondary structure elements, often stabilized by the formation of hydrophobic regions, to form the protein unit or monomer. In some cases, a protein consists of more than one equal or different monomers. Therefore, the quaternary structure describes the assembly of multiple monomers in one protein. Figure 7 shows the 4 different classes of protein structure.

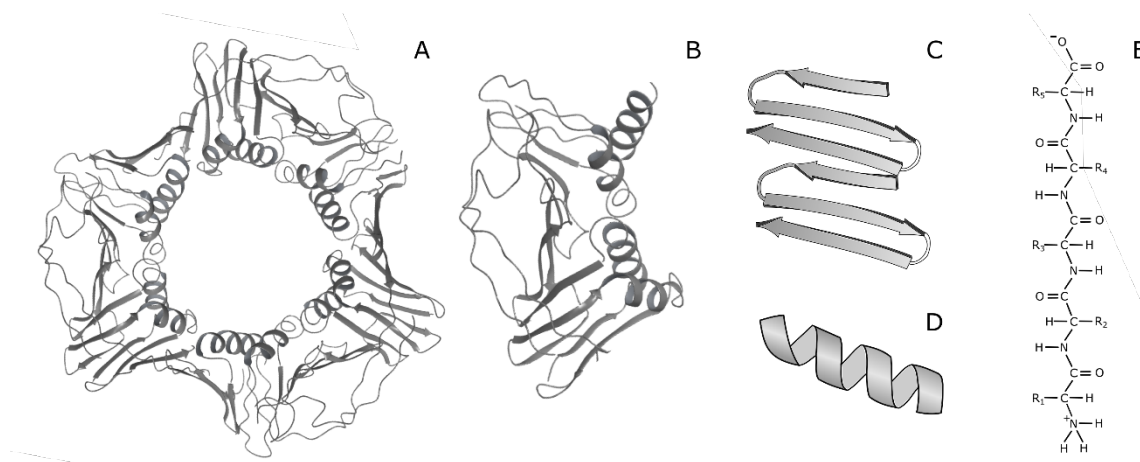


Figure 7: Protein structure. A) Quaternary structure composed of three monomers. B) Tertiary structure assembled from secondary structure elements. C) Secondary structure:  $\alpha$ -helices. D) Secondary structure:  $\beta$ -sheet. E) Primary structure with C-terminus (top), and N-terminus (bottom).

Unfortunately, the forces, which are stabilizing the peptides 3-dimensional conformation are relatively weak (hydrophobic interactions, hydrogen bonds) and can be disrupted by many factors, e.g. organic solvents are known to disrupt the peptides conformation by interacting with the inner hydrophobic part [75]. The pH controls the charge of a peptide and this will affect its solubility and its conformation [76]. Ionic strength, temperature [77], freeze thaw cycles [78], interaction with solid (mostly hydrophobic) surfaces, and other interfaces like the common air-water interface [79] or intensive shear forces during spray drying are further examples that have been shown to interrupt a peptides structure. In general, the stability of peptides in solution is lower, compared to a dry state, therefore a solid formulation is usually preferable. However, forces during the production of tablets have been reported to influence the structure and activity of proteins as well [80–83]. Therefore, loading sensitive substances into a rigid inert carrier can help to overcome issues associated with a production process.

### 1.5.1 Proteins on solid surfaces

In this thesis, the excipient FCC was investigated for its potential to be used for the delivery of PD. Therefore, one of the fundamental question was, whether peptides will maintain their activity and conformation, once they become released from the surface of FCC. The interaction of peptide molecules with solid surfaces is in general a very complex phenomenon, which includes adsorption, conformational changes, and desorption processes [84]. The next section intends to give a brief overview on the topic by highlighting the most important properties of the surrounding media, the protein and the solid surface, which control the interactions.

There are several external factor that are related to the surrounding medium, e.g. temperature, pH, and ionic strength. As the temperature of the system increases, the rate of adsorption increases due to higher mobility of the peptides, but also the equilibrium state shifts towards higher amounts [85–87]. The pH has a strong effect on the charge of peptides. Each peptide has a so called isoelectric point (PI) at which its net charge is zero. At pH values below this PI, the peptide has a positive net charge, while pH values above the PI lead to a negative net charge. The rate of adsorption reaches a maximum, when the charge of the surface and the peptide are opposite, due to electrostatic attraction, but reaches the highest packing density at the PI, since repulsive forces between the peptides are at a minimum [88,89]. By increasing the ionic strength, which represents the concentration of all ions in the medium, electrostatic interactions between peptide molecules, but also between peptide molecules and the solid surface are dampened. On one hand this can lead to enhanced surface adsorption, due to reduced repulsive forces between equally charged surface and peptide as well as less repulsion between peptides themselves leading to higher packing densities. On the other hand high salt concentrations can reduce the adsorption of oppositely charged surface and peptide due to a dampening effect on the electrostatic attraction. The so called salting out effect is used to precipitate peptides from an aqueous solution by increasing the solutions ionic strength, in order to weaken the electrostatic repulsion between the molecules leading to aggregation [90].

Peptides are complex molecules. Therefore, assessment of the performance when they contact solid surfaces based on their three dimensional structure is difficult. Nevertheless, there is the concept of hard and soft proteins, which categorizes peptides into two classes, hard and soft proteins [91]. Hard proteins are small, have a rigid structure, and are often spherical, e.g. lysozyme or  $\alpha$ -chymotrypsin. Hard proteins mostly show weaker affinity toward surfaces and since they are more rigid, do not undergo conformational changes upon contact with solid surfaces. Soft proteins on the other side are large, have a more flexible structure and a more complex shape like, e.g. BSA and immunoglobulins. They tend to adsorb stronger

due to their ability of conformational changes and enlargement of the contact surface. To estimate the potential of a peptide to interact with a solid surface, the structure can be simplified into lipophilic or hydrophilic, polar or non-polar, and charged or uncharged regions. In general, small peptides adsorb faster than large ones, but bind less strong. This leads to a phenomenon called the Vroman effect, which describes the kinetics of adsorption from protein mixtures and shows that small peptides adsorb first, but get replaced by larger ones at a later stage.

Last element in the complex interplay is the solid surface. The main driving forces for peptide adsorption are related to surface energy, polarity, charge, and to a smaller extent the morphology of the surface. Generally, peptides tend to adsorb more intensively to high surface energy than low surface energy, to non-polar than to polar, and to charged than to uncharged substrates. This explains the common experimental finding that proteins tend to adsorb to hydrophobic surfaces more readily than hydrophilic. There are exceptions, e.g. glycoproteins, where glycosylation leads to a shielding of the hydrophobic core and makes the protein more susceptible to adsorption to hydrophilic surfaces [92]. A similar approach can be used to passivate surfaces in order to make them less susceptible for protein adsorption, e.g. poly ethylene oxide coatings. These coatings are very effective, and can help to overcome several hurdles, which arise with the development of, e.g. blood contacting implants, but could also help to change surface properties of delivery devices in order to tailor their release kinetics or to improve drug loading.

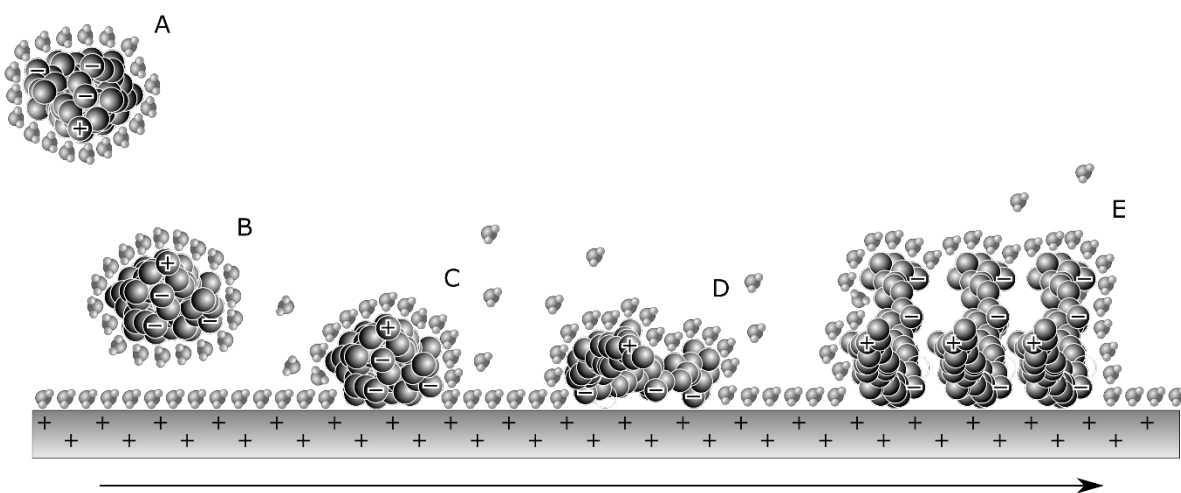


Figure 8: Protein adsorption to solid surface. A) Molecule approaches a solid surface. B) Molecule orients to match opposite charge of the solid surface. C) Contact and dissociation of water, that was associated to the solid surface and the molecule (hydrophobic effect). D) Structural deformation of the molecule. E) Reorientation of the molecule.

### 1.5.2 Enzyme Activity

In this work, the compatibility of FCC with the model enzyme lysozyme was investigated. Therefore, the activity of released lysozyme was measured and compared to unprocessed lysozyme via Michaelis-Menten experiments. This section provides a short overview on enzymatic reaction kinetics.

Enzymes are proteins that are able to specifically catalyze chemical reactions. They increase the rate of a reaction by reducing its activation energy by stabilizing a transition state of a molecule. The number of known enzymes is enormous. It is estimated, that approx. 75000 enzymes are present in the human body, controlling large parts of homeostasis and metabolic events. They can be classified into different groups according to the type of reaction that they are catalyzing, e.g. transferring functional groups from one to another molecule (transferases), cleaving molecules (hydrolases), or joining two molecules to create a new chemical bond (ligases). Therefore enzymes have extreme potential in many fields of the industry, e.g. food or petroleum industry, wastewater treatment, as well as for pharmaceutical application[93–96]. The principle of an enzymatic reaction is shown in equation 3:



where E is the enzyme, S is the substrate, ES is the enzyme-substrate complex, EP is the enzyme-product complex, and P is the product that is formed.

The rate at which enzymatic reactions take place is dependent on environmental conditions, including pH, temperature, ionic strength, the presence of co-factors, and inhibitors. As aforementioned, proteins (in this case enzymes) can undergo conformational changes, which usually affects the performance and therefore the kinetic of a reaction. In 1913, Leonor Michaelis and Maud Menten proposed a mathematical model for the characterization of enzymatic reactions, the Michaelis-Menten equation (equation 4):

$$V = \frac{V_{Max} * [S]}{K_M + [S]}, \quad (4)$$

where  $V$  is the rate of the enzymatic reaction,  $V_{Max}$  is the maximal rate of enzymatic reaction,  $S$  is the substrate concentration, and  $K_m$  is the Michaelis-Menten constant. Figure 9 shows an ideal representation of the Michaelis-Menten equation, where the rate of enzymatic reaction is plotted against the substrate concentration. The black line shows the function of a fully functional and active enzyme. The function starts almost linear showing first order like reaction kinetic and approaches a maximum rate ( $V_{Max}$ ) at a certain substrate concentration where  $V$  is not increasing proportional with the substrate concentration anymore

(zero-order kinetic). The  $K_M$  describes the substrate concentration at half of the maximum rate ( $V_{Max}/2$ ) and defines the substrate concentration at which half of the active sites are occupied. When the activity of an enzyme is impaired, there are two possible mechanisms: Competitive and non-competitive inhibition. A competitive inhibitor reduces the activity by competing with the substrate for the active site of the enzyme. In the graph it can be seen, that  $V_{Max}$  is the same as for a normal enzyme, but requires higher substrate concentration. Therefore, the  $K_M$  is shifted towards higher concentrations. This indicates, that the affinity to the substrate is not reduced, but higher concentrations are required to saturate the reaction, since the enzyme cannot convert the substrate when the active site is temporarily occupied by the inhibitor. Competitive inhibition influences the reaction by lowering the number of enzymes, which are available for binding the substrate. Noncompetitive inhibition occurs, when the inhibitor and the substrate are not competing for the same binding site. By binding the inhibitor, the conformation of the enzyme changes and the enzyme is no longer able to bind the substrate. Therefore the number of functional enzymes that are available for the reaction is reduced. The reaction of non-competitive inhibition will therefore never reach the same  $V_{Max}$  as a normal enzyme even though substrate concentration is increased, just because the number of functional enzymes is reduced. In contrast to competitive inhibition the  $K_M$  value is not changed. The unchanged  $K_M$ , but reduced  $V_{Max}$  reflects the fact, that the rate of substrate binding is not affected by the inhibitor, but the number of functional enzymes is reduced, since inhibitor binding leads to inactivation of the enzyme.

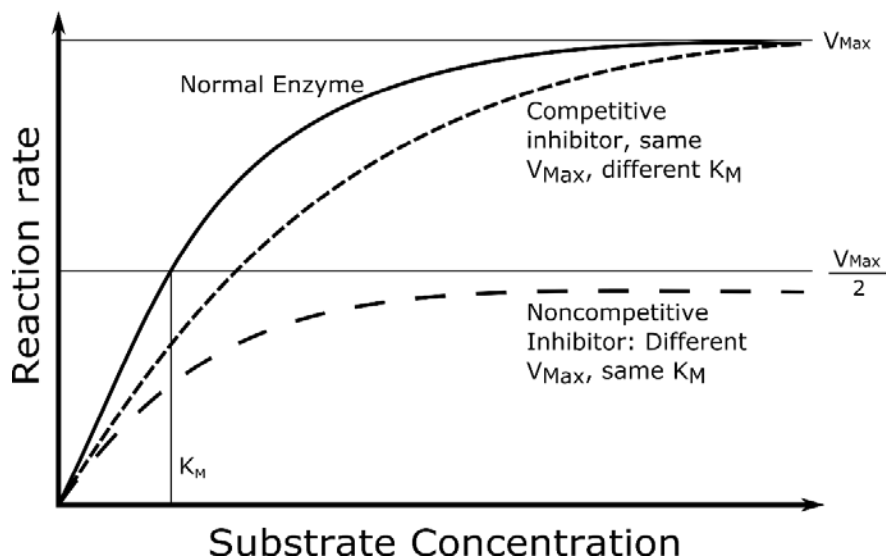


Figure 9: Michaelis-Menten enzyme kinetics. Changes in  $V_{Max}$  and  $K_M$  can be used to determine the mechanism of enzymatic inhibition. Competitive inhibition is characterized by the same  $V_{Max}$  but changed  $K_M$ . Non-competitive inhibition is characterized by reduced  $V_{Max}$  but unchanged  $K_M$ .



## 1.6 Functionalized Calcium Carbonate

Functionalized Calcium Carbonate (FCC) is produced by the company Omya International AG, which is located in Oftringen, Switzerland. Omya International AG is specialized in the production of particulate calcium carbonate products, which are used in many fields such as construction area, agricultural and forestry, water and air treatment, polymer applications, packaging, paint and paper, animal and human nutrition, cosmetics and recently also pharmaceutical excipients. FCC is a composite material consisting of calcium carbonate ( $\text{CaCO}_3$ ) and hydroxyapatite ( $\text{Ca}_5[\text{OH}(\text{PO}_4)_3]$ ). It is manufactured by precipitation from aqueous solutions, using the calcium carbonate as a starter core followed by functionalization with a porous structure of hydroxyapatite. There is a variety of grades available, chemically only varying in the ratio of the two components ranging from 13 to 85 % w/w hydroxyapatite content [97]. The difference in the composition, leads to a variety of particles with distinct properties with respect to surface topography, particle size distribution, specific surface area, porosity, and pore size distribution. Table 2 gives an overview on the available types of FCC and their specific properties.

Table 2: Examples of different types of FCC that have been produced by Omya International AG. OG-500 is registered as pharmaceutical excipient and was earlier denoted as FCC-S01 or FCC-TP. Table adopted from [98].

Type	Particle size (d50) [ $\mu\text{m}$ ]	Surface Area [ $\text{m}^2/\text{g}$ ]	Porosity [%]	Hydroxyapatite content [% w/w]
FCC 02	4.9	54.1	61.16	43
FCC 03	3.1	33.5	49.33	14
FCC 06	5.5	141.5	67.3	85
FCC 07	6.3	48.5	57.84	13
FCC 12	10	81	70.08	50
FCC 12	23.5	66	53.36	50
OG-500	7	55.4	61.55	51

### 1.6.1 Omyapharm OG-500

FCC type OG-500 was recently introduced as a pharmaceutical excipient. Similar types (S01, S02, S03) were investigated for the use as excipients in different solid dosage forms. Stirnimann et al. could show, that

FCC has excellent properties with respect to compactability. With FCC it is possible to produce hard tablets at low compaction pressure, which makes it an ideal material for the production of orally disintegrating tablets or granules. Low compaction pressures lead to reduced ejection forces during the tableting process, which is beneficial for the quality of the final product, and less generation of heat, which is important with respect to thermolabile compounds such as PD [99,100]. Eberle et al. developed gastro retentive floating mini tablets based on a surface modified (lipophilic) FCC [41,101], and Preisig et al. investigated the particles potential to be loaded with different drugs to enhance their solubility. In addition it was demonstrated that FCC can be coated with the mucoadhesive polymer chitosan using a precipitation method in order to prolong the residence time of the particles *in vitro* [63,102].

Besides the high porosity, which enables the particle to be loaded with high amounts of drug, the lamellar structure that covers the particle represents a key feature of the particle. It was demonstrated, that the lamellae are responsible for the high mechanical stability of FCC compacts, by a mechanical interlocking mechanism [100]. The lamellae measure approx. 1  $\mu\text{m}$  in Feret diameter and have a thickness of approx. 30 nm. The inner structure of the particle can be visualized by using a focused ion beam (FIB), which enables milling operation in the sub-micrometer range [103], resulting in detailed cross sectional images of individual particles. The particle can be divided into subunits that show comparable internal organization: Non-porous, solid cores of calcium carbonate, which are surrounded by a dense, porous meshwork of calcium phosphate. The pores of the dense meshwork measure up to approx. 100 nm in diameter. This dense meshwork is again surrounded by the above mentioned lamellar structure, which creates large cavities up to approx. 1  $\mu\text{m}$ . It can be assumed, that during the synthesis of FCC, multiple subunits agglomerate to form the final particle. Figure 10 shows a schematic representation of the internal structure of a typical OG-500 Particle.

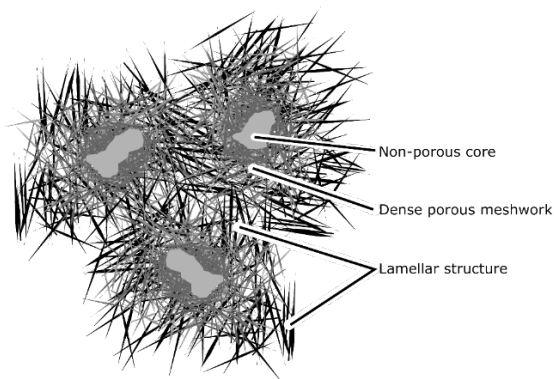


Figure 10: Schematic representation of the internal structure of FCC. Subunits construct the final particles. The subunits are composed of a non-porous core that is surrounded by a dense meshwork and the lamellar structure.

## 1.7 Electrospinning and Electrospraying

Coating and loading of substances into porous microparticles is challenging and alternative technologies to conventional methods such as soaking or solvent evaporation have to be established. We are convinced, that the incorporation of electrospinning principles has the potential to improve the quality of coatings and increase the loading efficiency.

Electrospinning is a process, which enables the production of fibers with diameters in the micro to nanometer range by applying a strong electric field to polymer solutions or melts. It has been used for the production of specialized non-woven fabrics and energy related applications such as fuel cells or lithium ion batteries [104], filter materials [105–107], biosensors [108], and performance enhancement of protective textiles [109]. Also in the medical field, electrospinning has gained interest during the last 20 years: Wound dressings could profit from the porous nature of fibrous mats which allow wound drainage while enabling atmospheric oxygen to permeate to the wound [110]. Electrospun nanofibers have shown their potential for drug delivery as well as for tissue engineering [111,112].

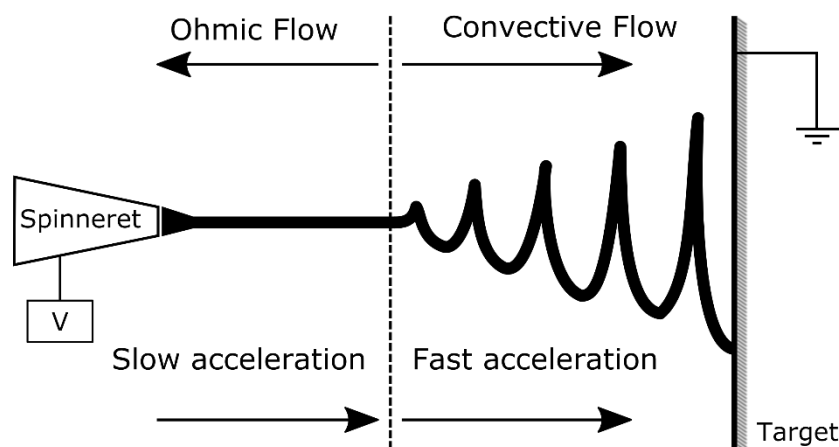


Figure 11: Basic setup for electrospinning. A syringe contains the polymer solution or melt, a high voltage supply is connected to the polymer solution. The collector plate is grounded to earth. Initially, polymer solution is accelerated by ohmic flow, and by convective flow in a second phase.

The principle of electrospinning is based on the electric field induced acceleration of a liquid jet from bulk material. The basic setup for electrospinning consist of three main components, which are a high voltage power supply, a so called spinneret (e.g. a needle connected to a syringe pump) and a collector. Figure 11

shows a basic setup for electrospinning. When a strong electric field is applied to a small volume of electrically conductive liquid, e.g. a droplet that sits on the tip of a syringe, the shape which is defined by the liquids surface tension changes. When forces, arising from the electrical field converge the magnitude of forces induced by the liquids surface tension, the spherical droplet deforms into a cone. When the angle of the cone reaches a value of  $98.6^\circ$ , it is called Taylor cone. By further increasing the applied voltage, eventually exceeding the cohesive forces of the surface tension, a jet of liquid (cone jet) is ejected from the tip of the cone. First, the liquid jet is accelerated by electrostatic forces (ohmic flow) and later by convection towards the collector. The convection is created by the electrostatic acceleration of ionized air. The electrostatic acceleration of the liquid allows to perform the process under reduced pressure conditions [113]. Depending on the polymer solution and the experimental setup, fibers with different diameters ranging from several nanometers to a few micrometer can be produced.

Even though electrospinning is a very old process, intensive research has again focused on the technique, especially on the modification of the equipment. Modifications mainly on the spinnerets as well as on collector plates have led to a variety of new fiber morphologies such as, e.g. core shell structure by coaxial electrospinning and aligned polymer fibers by using a rotating cylinder collector [114].

Depending on the setup and chosen parameters, one can also achieve so called electrospraying. When a cone jet gets elongated while subjected to an electric field, the jet might get deformed and eventually disrupted into small droplets, which can have diameters, smaller than droplets obtained by conventional spray nozzles. Additionally to their small size, the size distribution is narrow and the charged droplets are self-dispersing due to repulsive electrostatic forces [115]. This is fundamental to avoid agglomeration of the sprayed particles. Colloid electrospinning is another variation of the electrospinning process that uses polymer solutions containing dispersed particles. It has been used for the production of composite materials, e.g. nanoparticles immobilized in an non-woven mesh, but also to obtain separated nanoparticles for analytical purposes [116–118]. Obviously for the latter case, the formation of fibers is not desired and the process falls into the category of electrospraying. With respect to porous microparticles, colloid electrospraying offers a unique possibility for processes such as loading and coating.

## 2. Aims

The aim of this thesis was to explore the possibilities of using FCC for the delivery of sensitive biomolecules such as enzymes, proteins, and peptides (PD) via the oral cavity respecting the requirements of a multiparticulate mucoadhesive system. This includes a proof of concept study, using the two model substances BSA and lysozyme in order to demonstrate compatibility with FCC as well as the ability to be loaded into, and released from the carrier, the development of a scalable mucoadhesive formulation, and evaluation of the mucoadhesive potential of the produced particles. Further the goal was to identify techniques to reveal the inner structure of FCC as well as the analysis of material distribution within the porous structure of the microparticles after loading and to explore new loading methods for improved material deposition and coating quality.

Therefore, three projects were realized, which resulted in peer reviewed publications (I-III).

Additional experiments (IV) were carried out to evaluate the mucoadhesion of a nanoparticulate system and to further explore the scope of application for the flow cell, which was developed by D. Preisig et al.

Finally, it was the goal to initiate the development of alternative techniques for drug loading and coating of FCC. Preliminary results of the study are shown and discussed in the discussion section (V).

### **I) Functionalized Calcium Carbonate for the delivery of Proteins**

Assessment of FCC as a delivery platform of PD. The aim was to prove the applicability of a simple loading method, investigation of the release, and confirmation of conserved enzymatic activity and structural integrity of the model substances lysozyme and BSA.

### **II) Mucoadhesive microparticles for local treatment of gastro intestinal diseases**

The development of a scalable method to coat FCC with a mucoadhesive polymer. Investigation of the particles mucoadhesive properties using a flow cell in order to optimize future formulations.

### **III) Loading of Porous Functionalized Calcium Carbonate Microparticles: Distribution Analysis with Focused Ion Beam Electron Microscopy and Mercury Porosimetry**

Comparison of two analytical techniques for the analysis of material distribution within porous microparticles and identification of their limitations. Imaging of the internal structure of FCC and analysis of the intra particulate distribution of BSA and DPPC after loading by solvent evaporation.

**IV) Coating of PLA-nanoparticles with cyclic, arginine-rich cell penetrating peptides enables oral delivery of liraglutide**

Assessment of the mucoadhesive potential of PLA-nanoparticles, using the flow cell developed by Preisig et al. to identify possible limitations of the experimental setup (manuscript under revision).

**V) Electrospray for coating and loading of individual particles.**

Preliminary study, to explore the potential of a colloidal electrospray technique in order to improve drug loading and coating of individual FCC particles.

### **3. Publications in peer-reviewed journals**

#### **3.1 Functionalized calcium carbonate microparticles for the delivery of proteins**

Roger Roth <sup>1</sup>, Joachim Schoelkopf <sup>2</sup>, Maxim Puchkov <sup>1</sup>, Jörg Huwyler <sup>1</sup>

<sup>1</sup> Departement of Pharmaceutical Sciences, University of Basel, Switzerland

<sup>2</sup> Omya international AG, R&D Mineral and Surface Chemistry, Oftringen, Switzerland

**European Journal of Pharmaceutics and Biopharmaceutics 122(2018)266-275**

#### **Personal contribution**

My contribution to this research article includes the design of the study and the experimental setup. I planned and carried out all experiments, and evaluated the results. I wrote the manuscript with the help of Maxim Puchkov and Joachim Schoelkopf and prepared all figures.







## Research paper

## Functionalized calcium carbonate microparticles for the delivery of proteins

R. Roth<sup>a</sup>, J. Schoelkopf<sup>ab</sup>, J. Huwyler<sup>a</sup>, M. Puchkov<sup>a,\*</sup><sup>a</sup> Pharmaceutical Technology, University of Basel, Klingelbergstrasse, 50, 4056 Basel, Switzerland<sup>b</sup> Fundamental Research, Omya International AG, 4665 Oftringen, Switzerland

## ARTICLE INFO

## Keywords:

Oral drug delivery  
Functionalized calcium carbonate (FCC)  
Protein loading  
Microparticle  
Protein release  
Lysozyme  
Enzyme kinetics

## ABSTRACT

The recently introduced functionalized calcium carbonate (FCC), a porous microparticle with a nano-structured, lamellar surface, shows promising properties in the field of oral drug delivery. In this work, FCC was loaded with biomolecules e.g. lysozyme (Lys) and bovine serum albumin (BSA) in order to investigate its suitability to deliver protein based drugs. Loading efficiency for our model proteins was >90% and enzyme activity was preserved as demonstrated by Michaelis-Menten enzyme kinetic experiments. Circular dichroism analysis confirmed, that neither the structure of both model substances, nor the activity of Lys was affected by the loading process or the interaction with the surface of FCC. Electron microscopy (SEM) and mercury porosimetry were indicative of protein deposition on the particle surface as well as within the particle pores. Release properties were investigated in a customized flow cell, which simulates the conditions in the oral cavity. Depending on the isoelectric point of the investigated proteins, complete release was obtained within 1.5 h. This work shows, that FCC is a suitable pharmaceutical excipient for delivery of proteins.

## 1. Introduction

Delivery of biologics, such as therapeutic proteins, critically depends on the availability of formulation strategies, which can be used to deliver such macromolecules to a target tissue. Thereby, structural and functional integrity of the biologics have to be preserved during manufacturing and storage. In particular, particulate drug carriers (i.e. nanoparticles or microparticles) have gained increasing attention during the last years due to their high specific surface area, porosity and loading capacity [1]. For example porous materials like calcium silicate [2,3], zirconium dioxide [4], magnesium aluminometasilicate [5], and silicon dioxide were used as delivery devices for small and large molecules.

Oral administration of drugs is a widely spread drug delivery route since dosing and handling is convenient and well-established. On one hand, active pharmaceutical ingredients (API) can be absorbed into systemic circulation via the gastro intestinal tract or the oral mucosa, on the other hand there are a few locally acting formulations to treat mucosal diseases in the oral cavity [6], esophagus, and intestines [6,7]. The oral cavity is easily accessible and it has multiple features [8,9] for the delivery of macromolecules such as enzymes and protein based drugs or molecules with a low oral bioavailability. The oral mucosa is relatively permeable, depending on the degree of keratinization [9], especially the buccal and sublingual areas are well suited for systemic drug delivery. Intensive blood supply allows for efficient absorption

into systemic circulation by circumventing the hepatic first pass metabolism. The enzymatic activity in the oral cavity has also been shown to be moderate [10] and the recovery time of the mucosa is short [11–13]. Delivery of drugs close to the site of absorption can lead to enhanced bioavailability [14,15].

During the last few years, our group has focused on the characterization and development of delivery systems, based on the novel micro particulate excipient “functionalized calcium carbonate (FCC)”. FCC is characterized by a high porosity of 60% (v/v), which allows for intensive drug loading [16]. The surface of FCC shows lamellar structures, which leads to a high specific surface area in the range of 70 m<sup>2</sup> per gram and represents the functional part of the particles. During synthesis, FCC is produced by re-precipitation of inorganic mixed salts, which leads to the formation of the mentioned lamellar structure (see Fig. 2,i). The FCC particles are isolated from each other with sizes of approx. 10 µm and spherical geometry. The outer surface of these particles are exposing the debris of the developed lamellae, whereas deeper levels consist of smaller interconnected pores with an average diameter of approx. 100 nm. The inner porous structure shows high mechanical stability even at intense compression pressures up to 200 MPa [17]. Drug loading into FCC particles would allow facilitated handling and processibility of compounds, like proteins, which are susceptible to mechanical stress-induced conformational changes [18]. Based on FCC, we have designed fast disintegrating tablets [19], floating [20], and mucoadhesive drug delivery systems [6]. These

\* Corresponding author.

E-mail address: [maxim.puchkov@unibas.ch](mailto:maxim.puchkov@unibas.ch) (M. Puchkov).<http://dx.doi.org/10.1016/j.ejpb.2017.10.012>

Received 21 June 2017; Received in revised form 13 October 2017; Accepted 14 October 2017

Available online 17 October 2017

0939-6411/ © 2017 Elsevier B.V. All rights reserved.

studies have shown, that FCC is a versatile carrier for small molecule drugs and it shows unique properties regarding its processibility.

For the present work, the enzyme lysozyme (Lys) and bovine serum albumin (BSA) were chosen as two representative model substances, since both are well characterized and they represent a positively (cationic) and negatively (anionic) charged species under physiological conditions, respectively. Furthermore, Lys is a member of a promising new class of therapeutic macromolecules. They are components of the innate immune system and show strong antibacterial, antifungal, antiviral and antiendotoxic activity. In contrast to traditional antibiotics, their mode of action is based on physical or enzymatic disruption of the bacterial cell wall. This process is fast and may also be less susceptible to development of resistance against treatment [21,22]. Lys can be found in saliva and is considered as a well-tolerated and safe representative of this class of compounds. It is contained in marketed oral health care products such as lozenges and chewing gum [23] to treat local infections of the oral cavity and upper respiratory tract. In combination with other substances, such as hydrogen peroxide, ascorbic acid [24], and chitosan the antimicrobial spectrum can be enhanced [25] or can have synergistic effects e.g., in combination with  $\beta$ -defensins [26]. In addition, mucoadhesive polymers like chitosan or long chain poly ethylene oxides prolong the residence time of a therapeutic substance [27] and can therefore improve their therapeutic efficacy [28].

Besides a prolonged residence time, the therapeutic activity of enzymes is heavily dependent on the enzymes conformation, and this conformation can be affected by the interaction at the solid liquid interface of a particle and the surrounding medium [29–31]. One of the main concerns for any formulation development is the compatibility of an active pharmaceutical ingredient (API) with the excipients [32]. For therapeutic enzymes, enzyme integrity in terms of functional activity can be determined by Michaelis-Menten type kinetic experiments [33]. By this procedure, the rate of catalysis ( $V$ ) of an enzyme is determined at increasing substrate concentrations to obtain information about the maximal achievable rate of catalysis ( $V_{\max}$ ) as well as indications about the affinity of the enzyme to its substrate ( $K_M$ ). A prerequisite for this type of investigations is the availability of reliable and sensitive enzyme assays. For Lys, a turbidimetric assay, based on the lysis of bacterial cell compartments, is widely used to estimate the activity of Lys in pharmaceutical and biological preparations [34,35]. However, this method is reported to be not sensitive enough at low enzyme concentrations. In addition it does not truly reflect the enzymatic reaction, because of the complex mechanism of the lysis process [36]. For this reason the enzymatic substrate 4-Methylumbelliferyl-N,N',N''-triacyetyl- $\beta$ -chitotriose is advantageous over conventional methods due to its solubility in water and the fluorescent properties of the enzymatic product. These properties increase the sensitivity of the assay [37].

Since there is no standard procedure to evaluate a drug release within the oral cavity, a variety of different test systems have been suggested [38–40]. Influence of parameters such as small volumes of dissolution medium as well as reduced volumetric flow to closer mimic the conditions during drug release in the oral cavity have been discussed in the review by Patel et al. [41]. In this project, a closed cell design with low volumetric flow (to reduce the analytical challenge of low protein concentration) was used. This closed cell design helps to hold the particles in place without additional retention aids. Additionally the closed cell design allows for a more defined flow, when compared to an open cell design [6], that was used.

It was the aim of this work to assess FCC as a delivery platform for proteins and enzymes with a focus on loading, stability, and release kinetics. Porosimetry and scanning electron microscopy (SEM) were used to visualize the deposition of the proteins within the nanostructures of FCC. Lys was a model enzyme to study the impact of binding and desorption on enzymatic activity. Michaelis-Menten type kinetic experiments were used for qualitative assessment of enzymatic activity, while circular dichroism measurements were used to

investigate possible changes in the secondary structure of Lys.

## 2. Materials and methods

### 2.1. Materials

FCC (Type S01) was kindly provided by Omya AG (Oftringen, Switzerland). Dialyzed, lyophilized powder of lysozyme from chicken egg white (Lys), heat shock fractionated bovine serum albumin (BSA), 4-Methylumbelliferyl-N,N',N''-triacyetyl- $\beta$ -chitotriose, 4-Methylumbelliferone, sodium phosphate monobasic dihydrate, Tween 20, dimethylformamid, and glycine were purchased from Sigma Aldrich (St. Louis, MA). HEPES-buffer (bioscience-grade) was obtained from Carl Roth GmbH (Karlsruhe, Germany). Pierce™ BCA protein assay kit was purchased from Thermo Fischer Scientific (Massachusetts, MA). Sodium hydroxide solution was obtained from Riedel de Haen (Seelze, Germany). Ultrapure water (<18.2 M $\Omega$  cm resistivity) was obtained using a Milli-Q filtration station (Millipore, Billerica, MA).

### 2.2. Protein loading

To load the FCC particles with the model proteins, 2 g of FCC were mixed with 3 ml of aqueous Lys or BSA solution (13.34, 23.34, and 66.67 mg/ml in water) for 2 min using a beaker (10 ml) and a spatula in order to get a paste like consistency. The theoretical drug load ( $DL_{Th}$ ) was calculated using Eq. (1):

$$DL_{Th} = \frac{m_{Lys}}{m_{Lys} + m_{FCC}}, \quad (1)$$

where  $DL$  is drug load (%),  $m_{Lys}$  is the mass of Lys (mg), and  $m_{FCC}$  is the mass of FCC (mg).

Subsequently, the resulting paste was dried for 24 h at room temperature under reduced pressure. The dry powder was finally pulverized using a melamine pestle and mortar. Formulations containing 1.96% (w/w), 4.76% (w/w), and 9.09% (w/w) protein load ( $DL_{Th}$ ) were prepared.

### 2.3. Determination of protein load

To determine protein load, 50 mg of Lys or BSA loaded FCC was dissolved in 10 ml of 0.1 M HCl to ensure complete release of the protein. The solution was diluted with 0.1 M HCl (containing 5 mg/ml of dissolved FCC), and the protein concentration was measured with a BCA-assay, using a linear calibration curve (coefficient of correlation:  $R^2 > 0.995$  and  $> 0.980$  for Lys and BSA, respectively). The calibration curve was measured in 0.1 M HCl containing 5 mg/ml of dissolved FCC. Experimental drug load ( $DL_{Exp}$ ) was calculated using Eq. (2):

$$DL_{Exp} = \frac{C_P \cdot V_D}{m_F}, \quad (2)$$

where  $C_P$  is the measured protein concentration,  $V_D$  is the volume used to dissolve the sample, and  $m_F$  is the mass of the formulation used.

The efficiency of the drug-load ( $DL_{Eff}$ ) was calculated as a ratio between experimental and theoretical drug load using Eq. (3):

$$DL_{Eff} = \frac{DL_{Exp}}{DL_{Th}}, \quad (3)$$

where  $DL_{Exp}$  and  $DL_{Th}$  is the experimentally measured and theoretically calculated drug loads respectively.

### 2.4. Scanning electron microscopy (SEM)

BSA and Lys loaded particles were analyzed with a Nova NanoSEM 230 (FEI Company, Hillsboro, OR). The samples were sputtered with a 20 nm gold layer using a high vacuum sputter coater (EM ACE600, Leica, Germany). Magnification was 12,000 $\times$  and 4000 $\times$ . Images were

inspected for agglomerates, external protein crystals, and particle surface properties e.g. extent of deposits and preservation of lamellar structures.

## 2.5. Mercury porosimetry

Pore size distribution was measured using an autopore IV 9500 (Micromeritics Instrument, Norcross, GA.). A 5 cm<sup>3</sup> penetrometer for powder with a stem volume of 0.392 ml and an intrusion volume of 0.366 ml was used. Pressure for mercury intrusion ranged from 3.59 kPa to 206.64 kPa, and from 206.64 kPa to 206.78 MPa for the low-pressure and the high-pressure intrusion, respectively. Equilibration time was set to 10 s for both intrusions. Results were plotted as log of differential intrusion volume (ml/g) vs. pore size (nm) as described [19], using a moving average function with a window of 4.

## 2.6. Solubility and sink conditions

To ensure sink conditions, 150 mg of each model protein was dissolved in 1 ml of PBS at pH 7.4 in a 5 ml beaker and stirred at 4 °C over night. These solutions were then centrifuged at 14,000 rpm in a Centrifuge 4515 C (Eppendorf AG, Hamburg, Germany) for 60 min. The supernatant was then diluted and the optical density was measured at 278 nm in a UV-spectrometer, (Spectramax M2, Molecular devices, Sunnyvale, CA) using a quartz cuvette with 10 mm path length. Samples were measured in triplicates. The resulting equilibrium concentration of the protein was used to calculate the validity of sink conditions during the dissolution studies.

## 2.7. Dissolution using a closed flow cell

To simulate the conditions on the buccal mucosa, a custom made, flow cell with closed channel geometry was used. The flow cell was adapted from Preisig et al. [6]. The cell was operated in a horizontal position. The inner dimensions of the cell were 15 mm in width, 95 mm in length, and 1 mm in height resulting in an inner volume of 1.4 ml. A 0.45 µm Titan series syringe filter (Thermo Scientific, Waltham, MA) was attached to the outlet, to prevent particles from being flushed out of the cell. An amount of 150 mg of Lys or BSA loaded FCC was distributed evenly on the bottom of the cell. The volume of the dissolution medium in the reservoir was 50, 125, and 250 ml for low, medium, and high protein loadings, respectively, to exclude influences from variable equilibrium concentrations. In contrast to the setup from Preisig et al. [6], where fresh dissolution medium was used, in this experiment the dissolution medium was re-circulated through the flow cell for 160 min. Phosphate buffered saline at pH 7.4 was used as dissolution medium and the flowrate was set to 1 ml/min. Dissolution was carried out at 37 °C. Samples of approximately 100 µl were collected at defined time intervals using a custom-built autosampler (University of Basel). Total volume of dissolution medium removed from the closed system due to sampling was <3% (v/v) of the total volume. Protein concentration of the samples was determined with the BCA-assay (see below).

## 2.8. BCA protein assay

To determine the concentration of Lys and BSA in release samples, the standard BCA-assay was used (Thermo Scientific, Waltham, MA). A microplate procedure with a sample to working reagent ratio of 1:8 (v/v) was used according to manufacturer's instructions. Clear, flat bottom, polystyrene, 96-well plates were used in all experiments. They were sealed with an adhesive cover and incubated for 30 min at 60 °C in a heating oven (Heraeus, Hanau, Germany). Subsequent, the plates were cooled for 5 min prior to optical density measurements using a microplate reader (Spectramax M2, Molecular devices, Sunnyvale, CA) at 562 nm. Relative standard deviation of the assay was ±9.9%.

## 2.9. Michaelis-Menten kinetics

Michaelis-Menten kinetics of released Lys was compared to the native enzyme by measuring the concentration dependent rate of hydrolysis from the fluorogenic substrate, 4-Methylumbelliferyl β-D-N,N',N''-triacylchitotrioside into the fluorescent compound 4-Methylbelliferone. Fluorescence was measured using a microplate reader (Spectramax M2, Molecular Devices) and clear 96-well plates with a flat bottom and a fill volume of 200 µl. The samples were exited at 365 nm and emission was registered at 445 nm.

60 mg of Lys-loaded FCC with a DL<sub>Th</sub> of 9.09% (w/w) was dispersed in 10 ml of milli-Q water for 30 min under stirring at room temperature and subsequently filtered through 0.45 µm hydrophilic syringe filter (KX, Kinesis, Cambridgeshire, UK). The enzyme solution was diluted 10:1 with 500 mM citrate buffer and pH was adjusted to 5.6. Control and blanks were directly prepared in 50 mM citrate buffer and adjusted to pH 5.6. Enzyme concentration was measured and diluted to 20 µM stock solution. Substrate concentrations were 5, 10, 20, 30, 40, 60, and 100 µM. Samples were incubated for 2 h at 37 °C in a thermocycler (Biometra, Jena, Germany). Reaction was stopped by adding 100 µl of 300 mM glycine buffer at pH 11. Concentrations were then calculated using a linear calibration curve prepared in an identical buffer system, but containing only the product 4-Methylbelliferone. The Michaelis-Menten parameters  $K_M$  and  $V_{max}$  were determined by fitting the Michaelis-Menten equation (Eq. (4)) to the experimental data using origin pro 9.1 software.

$$V = \frac{V_{max} * S}{K_M + S}, \quad (4)$$

where  $V$  is the experimentally determined rate of the reaction at given substrate concentration (M/s/unit),  $V_{max}$  is the maximum rate that the system achieved at saturating substrate concentration (M/s/unit),  $S$  is the substrate concentration (µM) and  $K_M$  is the Michaelis-Menten constant (µM) (OriginLab, Northampton, MA).

## 2.10. Circular dichroism

Circular dichroism (CD) spectra of released Lys and BSA were obtained in order to detect rearrangements in the secondary structure of the molecules due to surface interactions with FCC. Measurements were carried out on a Chirascan CD spectrometer (Applied Photophysics Ltd., Letherhead, UK). Lys or BSA loaded FCC was suspended in 20 mM, phosphate buffer, pH 7.4, stirred for 60 min at room temperature, filtered, and diluted to a final concentration of 7 µM. Reference sample was native Lys or BSA, which were dissolved in the same buffer. Blanks were measured in 20 mM phosphate buffer at pH 7.4. Scans from 190 to 240 nm were carried out. Scanning time per wavelength interval of 1 nm was 5.4 s. A cuvette with a path length of 0.1 mm was used. To avoid different ionic strength in all solutions, FCC saturated water was used as a base for all preparations. FCC saturated water was prepared by suspending 10 mg of FCC per ml of ultrapure water for 1 h and subsequent filtration. Protein concentration of all solutions was finally measured by BCA-assay, and the data was normalized to the mean residual ellipticity,  $\theta$  (Eq. (5)):

$$\theta = \frac{CD_{Lys} - CD_{blank}}{C * L * N} * 10^6, \quad (5)$$

where  $\theta$  is the residual ellipticity (deg cm<sup>2</sup> dmol<sup>-1</sup>),  $CD$  is the signal intensity of Lys or blank reference,  $C$  is the molar concentration (µM) of Lys,  $L$  is the path length of the cuvette (mm), and  $N$  is the number of amino acids in Lys.

Fractional helicity ( $\theta_F$ ) was calculated using Eq. (6):

$$\theta_F = \frac{\theta_E - \theta_0}{\theta_{100} - \theta_0}, \quad (6)$$

where  $\theta_E$  is the experimental mean residual ellipticity (222 nm),  $\theta_0$  is

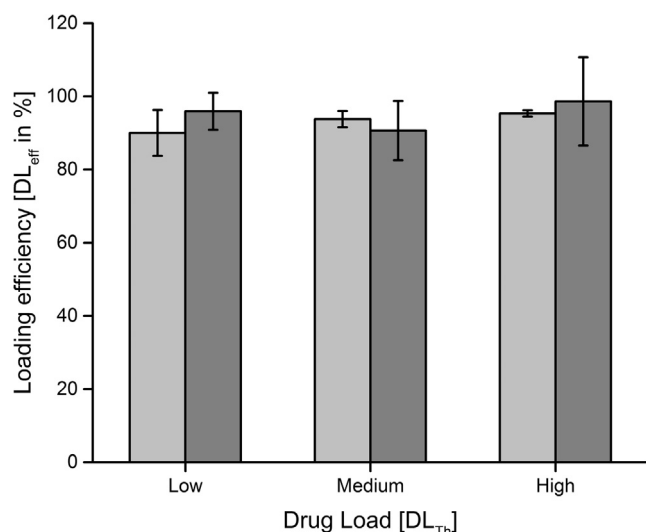


Fig. 1. Loading efficiency ( $DL_{eff}$ ) for Lys (light grey) and BSA (dark grey). FCC particles were prepared with the aim to obtain theoretical drug loads ( $DL_{Th}$ ) of low (1.96% (w/w)), medium (4.76% (w/w)), and high (9.09% (w/w)) protein. Values are means  $\pm$  SD,  $n = 3$ .

the calculated mean residual ellipticity (222 nm) of a protein containing 0%  $\alpha$ -helix, and  $\theta_{100}$  is the calculated mean residual ellipticity (222 nm) of a protein containing 100%  $\alpha$ -helix structure [42].

### 3. Results

#### 3.1. Drug loading

Final drug loads were measured and compared to theoretical values to calculate loading efficiency. Fig. 1 shows loading efficiency of BSA and Lys for high, medium, and low loadings. There was no significant difference between the two model proteins BSA and Lys, as well as in between the high and low drug loads. Theoretical drug loads ( $DL_{Th}$ ) with both, BSA and Lys, were designed to be 1.96, 4.76, and 9.09% (w/w). The  $DL_{Th}$  were compared to the experimental values ( $DL_{Exp}$ ) to determine loading efficiency ( $DL_{eff}$ ). Fig. 1 shows loading efficiencies ( $DL_{eff}$ ) of the different formulations.

#### 3.2. Scanning electron microscopy

In general, SEM analysis of all samples showed homogeneously loaded, individual, and intact particles. Fig. 2 shows SEM images of FCC with low ( $DL_{Th} = 1.96\%$  (w/w)), medium ( $DL_{Th} = 4.76\%$  (w/w)), and high ( $DL_{Th} = 9.09\%$  (w/w)), loadings of BSA (Fig. 2a–c, g) and Lys (Fig. 2d–f, h), as well as a pure FCC reference particle (Fig. 2i). Although it cannot be completely excluded, there were no signs for major extraparticle agglomeration of proteins observed. Small fragments located between the FCC particles are due to attrition during the loading process, as lamellar structure of FCC could still be visually identified on those fragments. Differences in surface deposition of proteins on the surface of the particle could only be seen for the highest protein load. Less material was deposited on the surface of Lys loaded particles (Fig. 2f), than on BSA loaded particles (Fig. 2c). Secondary agglomeration has not been detected even at the highest protein load.

#### 3.3. Mercury porosimetry

Pore size distribution of pure FCC and drug loaded FCC (Fig. 3) was determined at different protein loads covering a range of 1.96–9.09% ( $DL_{Th}$ ). A local minimum in the vicinity of 500 nm separates intraparticle and inter-particle pores, respectively [19]. For both model substances, the accessible pore volume in the particle decreased

with increasing protein load. At the highest protein load, Lys loaded FCC shows a more pronounced decrease in intraparticle pore volume than that in BSA loaded FCC. For Lys, the intraparticle pore volume decreased down to 67%, while the intraparticle pore volume of BSA loaded FCC decreased only down to 89% compared to unloaded reference FCC (100%) suggesting deposition in deeper regions of the particle.

#### 3.4. Solubility and sink conditions

After stirring a highly concentrated solution of Lys and BSA at 4 °C over night and centrifugation for 60 min at 14,000 RPM, the final concentrations of the solutions were  $90.7 \pm 0.9$  and  $152.3 \pm 3.5$  mg/ml for Lys and BSA, respectively. The highest expected concentration of proteins during dissolution experiments was 55  $\mu$ g/ml. Therefore, the requirements for sink conditions were fulfilled.

To investigate whether proteins degrade or agglomerate during loading and release, the micro-flow imaging experiments and SDS gel-electrophoresis were used to detect protein agglomerates at the concentration ranges twice exceeding the highest expected concentrations during release experiments. No covalently linked dimers nor apparent degradation products of lysozyme and BSA were formed during these experiments (data not shown). In addition, no further agglomeration could be detected by micro-flow imaging (data not shown).

#### 3.5. Dissolution

Release profiles of Lys and BSA were determined at different protein loads (Fig. 4). The profiles were normalized to the measured  $DL_{Exp}$ . After 100 min, Lys has been completely released and the concentration in the dissolution medium has reached a steady state. The release kinetics of BSA are characterized by an initially high release rate period (15–20 min) followed by slow release rate period. During the first period, the release rate is directly proportional to drug loads. After 160 min the dissolution experiments were stopped. At this point, the low, medium, and high loadings released  $26.9 \pm 9.7$ ,  $47.1 \pm 5.9$ , and  $55.6 \pm 1.1\%$  of protein, respectively.

#### 3.6. Michaelis-Menten

Fig. 5 shows the results obtained from enzymatic rate measurements of released and native Lys. Data were fitted according to Michaelis-Menten kinetics and showed good correlation to the model. Table 1 shows the experimentally determined Michaelis-Menten parameters  $K_M$  and  $V_{max}$ . Both parameters did not change significantly: They were  $12.03 \pm 1.3$  and  $4.4 \cdot 10^{-6} \pm 5.2 \cdot 10^{-8}$  for native Lys and  $14.24 \pm 0.95$  and  $4.8 \cdot 10^{-6} \pm 9.4 \cdot 10^{-8}$  for the released Lys. Variation within the two parameters  $K_M$  and  $V_{max}$  give information about the type of potential inhibition of an enzyme. A shift in  $K_M$  value indicate competitive inhibition, when a decrease in  $V_{max}$  depicts a non-competitive inhibition mechanism [43]. The data shown, indicate that the loading of Lys into FCC did not impair the activity of Lys, since  $K_M$  and  $V_{max}$  did not change.

#### 3.7. Circular dichroism

The CD spectra of native and released Lys and BSA are closely correlated (Pearson correlation coefficient  $>0.99$ ). The calculated fractional helicity ( $\theta_F$ ) was 22.6% and 23.0%, and 68.4% and 69.9% for released and native Lys and BSA respectively (Fig. 6).

### 4. Discussion

#### 4.1. Drug loading and preservation of activity

It was the aim of the current project to use functionalized calcium



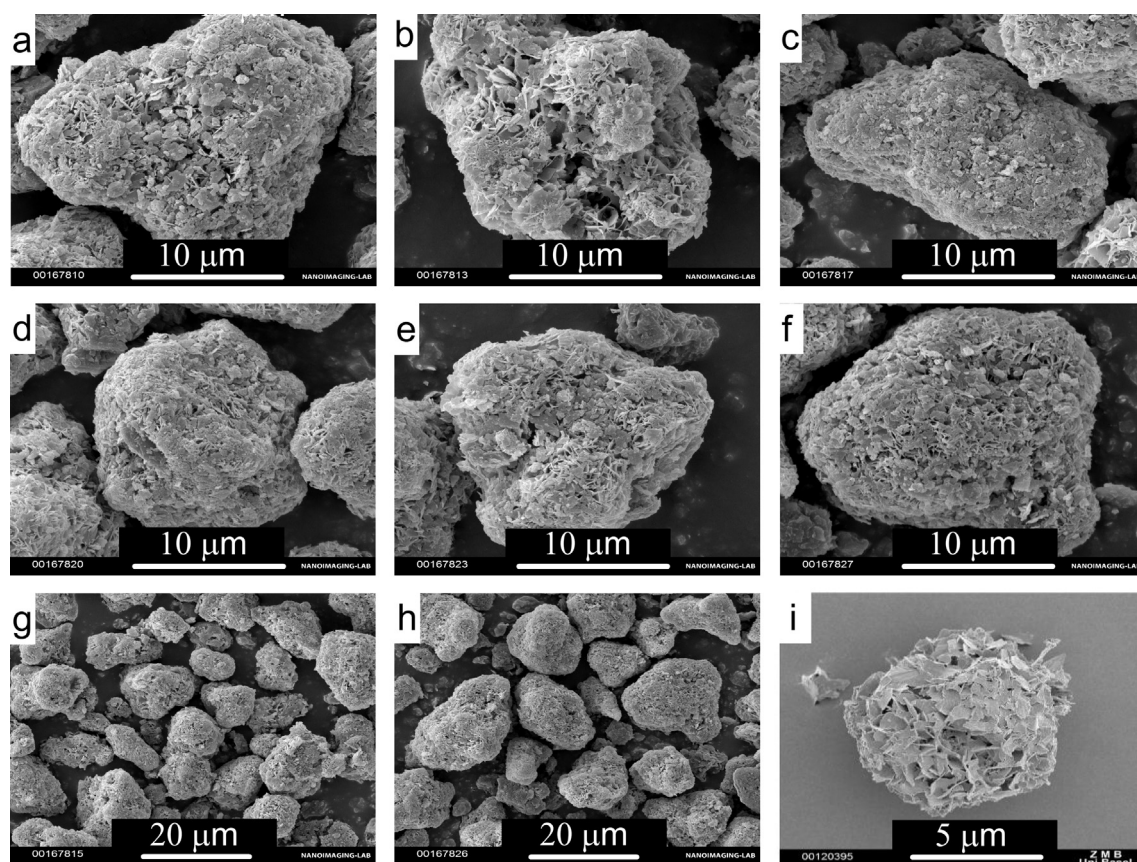


Fig. 2. SEM images of protein loaded FCC. Particles loaded with BSA at low ( $DL_{Exp} = 1.87\%$  (w/w)) (a), medium ( $DL_{Exp} = 4.31\%$  (w/w)) (b), and high ( $DL_{Exp} = 8.97\%$  (w/w)) (c) drug loads, and Lys at low ( $DL_{Exp} = 1.76\%$  (w/w)) (d), medium ( $DL_{Exp} = 4.46\%$  (w/w)) (e), and high ( $DL_{Exp} = 8.66\%$  (w/w)) (f) drug loads. Overview of the highest drug loads of BSA (g) and Lys (h). Unloaded FCC reference particle (i).

carbonate microparticles (FCC) as a carrier for proteins. Efficient loading was possible by simple soaking of FCC particles in an aqueous solution of the model proteins lysozyme (Lys) and bovine serum albumin (BSA). Up to 10% protein load is easily achievable with FCC. Up to these protein loads, FCC particles showed no agglomeration. Extra-particulate crystallization could not be detected at these loading by SEM. In contrast to pure FCC, the particle surface showed reduced porosity and roughness. Drug loading was efficient in that at least 90% of the targeted protein load could be achieved. However, since the loading method is a single pot procedure, there are no losses expected throughout the experiments. Given that batch sizes were small, the

observed protein loss of up to 10% (w/w) can partially be explained by protein deposition on the vessel and tubing wall during experiments [44], as well as BCA assay relative standard error as described in the methods section. The question arises, whether proteins are deposited on the particle surface only or if they can as well penetrate the porous inner structure of the particles. Previous studies have shown [19], that intra-particulate voids account for 60% of the particle volume. The mean inner diameter of these pores covers a range between 20 nm and 500 nm. Previous experiments with small drug molecules (MW < 500 Da) could achieve a drug load of 30% (w/w) using a solvent evaporation protocol [16]. In this study, results of mercury porosimetry show a

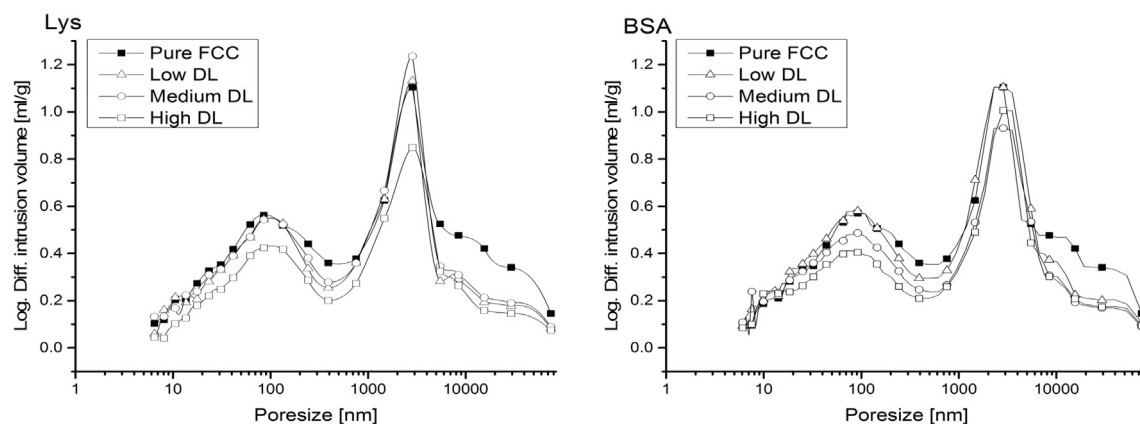


Fig. 3. Mercury porosimetry plot for Lys and BSA loaded FCC. Pore size distribution of pure FCC (■) and particles with low ( $DL_{Th} = 1.96\%$  (w/w)) (Δ), medium ( $DL_{Th} = 4.76\%$  (w/w)) (○), and high ( $DL_{Th} = 9.09\%$  (w/w)) (□) protein loads is shown. Pore size is plotted against the logarithm of the differential intrusion volume. Data points were smoothed using a moving median function with a window of 4.

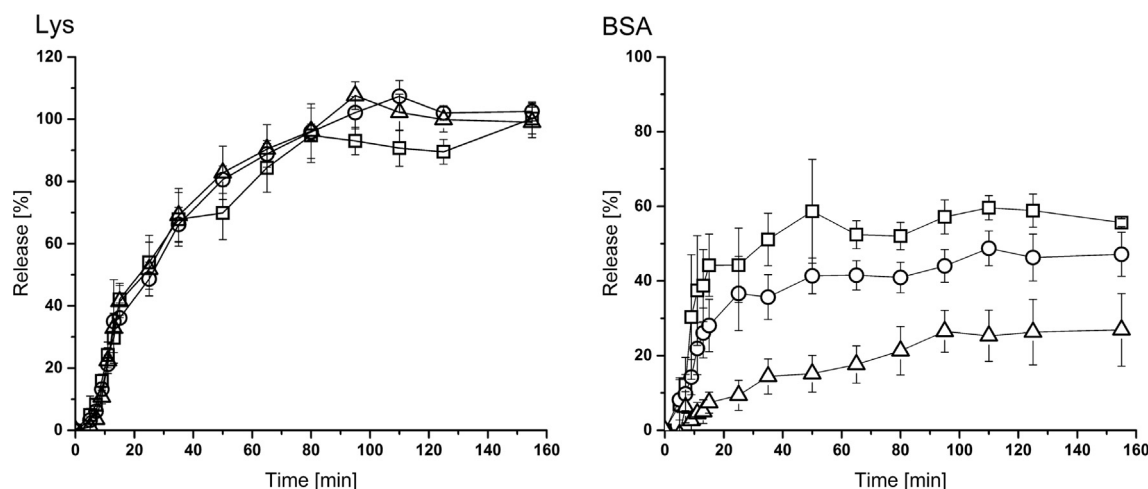


Fig. 4. Dissolution profiles of Lys and BSA. Protein release from FCC was measured in a customized flow cell at low ( $\Delta$ ), medium ( $\circ$ ), and high ( $\square$ ) protein load (see Fig. 1). 100% release corresponds to complete liberation of loaded drug ( $DL_{Exp}$ ). Values are means  $\pm$  SD,  $n = 3$ .

decrease in pore volume with increasing protein load. This suggests at least partial pore filling and deposition of proteins within the inner structures of FCC particles despite the high molecular weight (14.3 kDa for Lys and 66.5 kDa for BSA) and the corresponding larger size (BSA [32]: 14 nm  $\times$  4 nm  $\times$  4 nm) of these biomolecules. Drug loading efficiency is not influenced by the type of model substance (i.e. Lys or BSA). This behavior is very similar to the one of small molecules [16]. However, a precise estimation of the deposited quantity of these proteins within the pores or the particle surface is not possible since the mechanisms of pore filling as opposed to pore blocking cannot be distinguished by mercury intrusion porosimetry [46].

Dissolution experiments show that complete release for Lys and partial release for BSA can be achieved. For Lys, the release rate is independent of protein load. Complete release could be achieved within 100 min. In contrast, BSA is partially released only within 160 min. In addition, the release rate was significantly reduced at low BSA concentrations. At high protein loads, an initial burst release was followed by a much slower release over an extended period. It is tempting to speculate that BSA which is in direct contact with the surface of FCC is tightly bound to it. Therefore, is bi-phasic release pattern for BSA. Indeed, the isoelectric point of hydroxyapatite and calcite is reported to be above 7.4, which leads to a positive net charge of the surface [47,48]. BSA has an isoelectric point of 4.7, leading to a negative net charge under physiological conditions [49]. The resulting ionic interactions could be the reason for a strong surface attachment that slows down the release of BSA from the particle surface. This hypothesis is

Table 1

Michaelis-Menten parameters for native and released Lys. Kinetic parameters were calculated from data, shown in Fig. 5. Values are means  $\pm$  SD,  $n = 3$ .

	Native Lys	Released Lys
$K_M$ ( $\mu$ M)	$12.03 \pm 1.30$	$14.24 \pm 0.95$
$V_{max}$ (M/s/unit)	$4.4 \cdot 10^{-6} \pm 5.2 \cdot 10^{-8}$	$4.8 \cdot 10^{-6} \pm 9.4 \cdot 10^{-8}$
Model fit (adjusted $R^2$ )	0.994	0.996

also supported by the release profile of Lys, which carries a net positive charge at pH 7.4 and could be released completely and relatively fast compared to BSA. In addition, the higher molecular weight of BSA, as compared to Lys, might slow down diffusion through the porous meshwork of the FCC particles [45,50]. We conclude from these experiments, that there is a risk for anionic proteins to bind irreversibly to FCC, whereas cationic proteins show a weaker interaction and a facilitated release under physiological conditions like those in the oral cavity. At gastric pH, however, the situation might be different since FCC will dissolve under acidic conditions.

Binding of proteins to surfaces may induce conformational changes and thereby impact structural integrity and enzymatic activity [51]. In the present study, kinetic experiments were performed with Lys before and after FCC loading and subsequent release. There were no statistically significant differences with respect to the Michaelis-Menten parameters  $K_M$  and  $V_{max}$ . Values for  $K_M$  were comparable to reported values [52]. These findings are a clear indication, that the catalytic

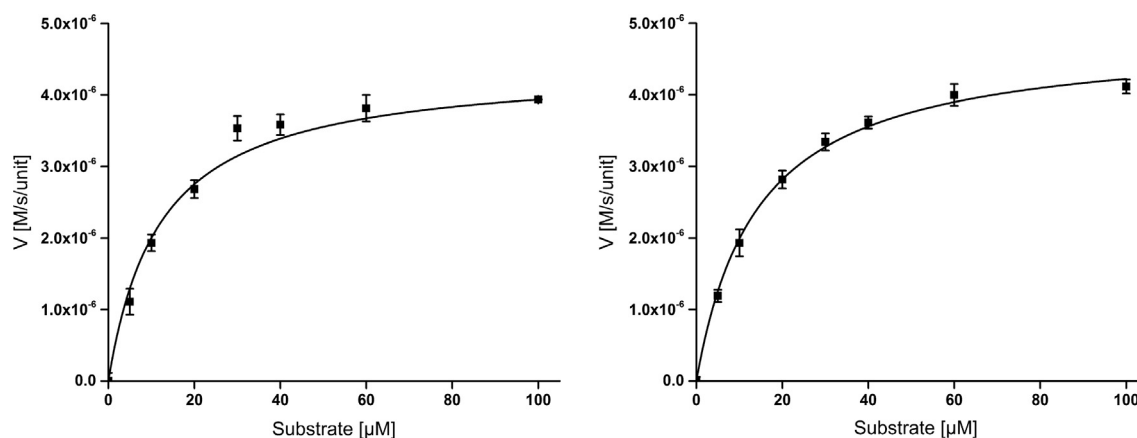


Fig. 5. Michaelis-Menten enzyme kinetics of native Lys (left) and Lys that was loaded and subsequently released from FCC (right). The rate of enzymatic product formation is plotted against the substrate concentration. Experimental data (symbols) as well as the fitted model (curves) are shown. Values are means  $\pm$  SD,  $n = 3$ .

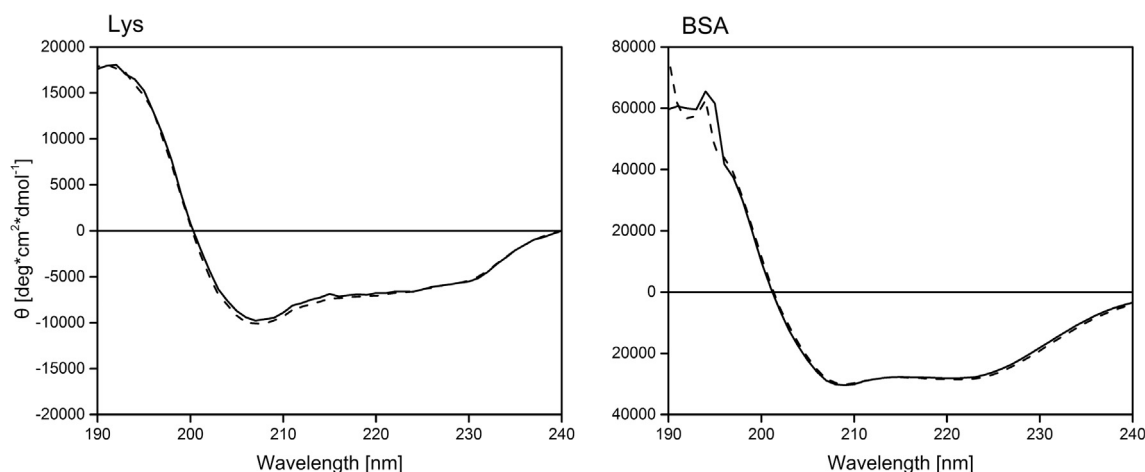


Fig. 6. Circular Dichroism (CD) spectroscopy. Mean residual ellipticity of native (dashed line) and released (solid line) Lys (left) and BSA (right), respectively. Structural integrity of Lys and BSA before and after binding to FCC was studied by circular dichroism (CD) spectroscopy.

activity of the enzyme was not impaired and that no irreversible changes were introduced. These results were confirmed by CD spectroscopy, which did not show any changes in secondary structure of the protein after being released from FCC.

Protein loaded FCC microparticles can be used to implement drug delivery strategies in different therapeutic areas such as oral formulations for topical or systemic delivery of biomolecules. The interaction of such particles with biological systems will thereby depend on the nature of the loaded substance and environmental conditions (e.g. pH). To enhance the therapeutic efficacy of an FCC based delivery system, mucoadhesive properties might be beneficial. The presented delivery system offers the possibility to combine it with an additional mucoadhesive coating [6]. However, since this project is focused on the study of basic interactions between the model substances and the surface of the FCC particles, a mucoadhesive coating using e.g. chitosan or long-chain variants of poly ethylene oxide [6,27] was not applied, as it can change the release kinetics [53]. Future applications might well include parenteral applications such as implants. Peptide based hormones, such as growth factors, can be adsorbed irreversibly on the surface of FCC and can then be released by destruction or biodegradation of the particles. This might be promising for the design of long term drug delivery devices such as bone substitutes. With this respect, hydroxyapatite (a constituent of FCC) has been shown to promote bone regeneration [54,55].

## 5. Conclusion

Our results indicate, that FCC is a suitable excipient for the loading of the two investigated model proteins, (Lys and BSA) ensuring structural stability. With respect to topical applications in the oral cavity, Lys is already used for marketed products (in Switzerland the product is marked under the brand name Lysopaine). An immobilization of Lys on microparticles offers the advantage of drug retention for prolonged periods of time on the mucosa, which could lead to increased efficacy of the already marketed formulations. Substantial amount of model proteins could be detected on the particles surface. Future investigations intend to characterize and understand crucial factors affecting the penetration of the proteins into deeper regions of the particles.

## Acknowledgements

RR is supported by a PhD. student grant from Omya international AG. We thank Markus Dürrenberger and Eva Bieler from the Nano Imaging Lab of the Swiss Nano Science Institute (SNI) for the SEM images, Dr. Timothy Sharpe and Xiaochun Li Blatter for help with CD,

and Darryl Borland for editorial assistance and technical support.

## References

- [1] J. Tu, A.L. Boyle, H. Friedrich, P.H.H. Bomans, J. Bussmann, N.A.J.M. Sommerdijk, W. Jiskoot, A. Kros, Mesoporous silica nanoparticles with large pores for the encapsulation and release of proteins, *ACS Appl. Mater. Interfaces* (2016) 32211–32219.
- [2] H. Yuasa, D. Asahi, Y. Takashima, Application of calcium silicate for medicinal preparation. I. Solid preparation adsorbing an oily medicine to calcium silicate, *Expert Opin. Drug Deliv.* (1994) 2327–2331.
- [3] Z. Ying-Ji, G. Xiao-Xu, S. Tsun-Kong, Calcium silicate-based drug delivery systems, *Expert Opin. Drug Deliv.* (2017) 215–228.
- [4] S. Tang, X. Huang, X. Chen, Hollow mesoporous zirconia nanocapsules for drug delivery, *Adv. Funct. Mater.* (2010) 2442–2447.
- [5] C. Sander, P. Holm, Porous Magnesium Aluminometasilicate Tablets as Carrier of a Cyclosporine Self-Emulsifying Formulation | SpringerLink 10 (2009) 1388.
- [6] D. Preisig, R. Roth, S. Tognola, F. Varum, R. Bravo, Y. Cetinkaya, J. Huwyler, M. Puchkov, Mucoadhesive microparticles for local treatment of gastrointestinal diseases. - PubMed - NCBI, *Eur. J. Pharm. Sci.* (2016) 156–165.
- [7] S. Amidon, J.E. Brown, V.S. Dave, Colon-targeted drug delivery system: design trends and approaches, *AAPS PharmSciTech.* (2015) 731–741.
- [8] V. Hearnden, V. Sankar, K. Hull, D. Vidovic Juras, M. Greenberg, R.A. Kerr, P.B. Lockhart, L.L. Patton, S. Porter, M.H. Thornhill, New developments and opportunities in oral mucosal drug delivery for local and systemic disease - ScienceDirect, *Adv. Drug Deliv. Rev.* (2012) 16–28.
- [9] C.A. Squier, The permeability of oral mucosa, *Crit. Rev. Oral Biol. Med.* (1991) 13–32.
- [10] G.F. Walker, N. Langoth, A. Bernkop-Schnürch, Peptidase activity on the surface of the porcine buccal mucosa, *Int. J. Pharm.* 233 (2002) 141–147.
- [11] A. Shojaei, Buccal mucosa as a route for systemic drug delivery, *J. Pharm. Pharm. Sci.* (1998) 15–30.
- [12] Y. Sudhakar, K. Kuotso, A.K. Bandyopadhyay, Buccal bioadhesive drug delivery—a promising option for orally less efficient drugs, *J. Controlled Release.* (2006) 15–40.
- [13] J.E. Glim, M. Van Egmond, F.B. Niessen, V. Everts, R.H. Beelen, Detrimental dermal wound healing: What can we learn from the oral mucosa? *Wound Repair Regen.* (2013) 648–660.
- [14] Y. Lu, Y. Sun, B. Gu, Development of mucoadhesive microspheres of acyclovir with enhanced bioavailability, *Int. J. Pharm.* (2009) 30–36.
- [15] N.M. Zaki, G.A. Awad, N.D. Mortada, S. Abd ElHady, Enhanced bioavailability of metoclopramide HCl by intranasal administration of a mucoadhesive in situ gel with modulated rheological and mucociliary transport properties, *Eur. J. Pharm. Sci.* (2007) 296–307.
- [16] D. Preisig, D. Haid, F.J.O. Varum, R. Bravo, R. Alles, J. Huwyler, M. Puchkov, Drug loading into porous calcium carbonate microparticles by solvent evaporation, *Eur. J. Pharm. Biopharm.* (2014) 548–558.
- [17] T. Stirnimann, S. Atria, J. Schoelkopf, P.A.C. Gane, R. Alles, J. Huwyler, M. Puchkov, Compaction of functionalized calcium carbonate, a porous and crystalline microparticulate material with a lamellar surface, *Int. J. Pharm.* (2014) 266–275.
- [18] E. Di Stasio, R. De Cristofaro, The effect of shear stress on protein conformation: physical forces operating on biochemical systems: the case of von Willebrand factor, *Biophys. Chem.* (2010) 1–8.
- [19] T. Stirnimann, N.D. Maiuta, D.E. Gerard, R. Alles, J. Huwyler, M. Puchkov, Functionalized calcium carbonate as a novel pharmaceutical excipient for the preparation of orally dispersible tablets, *Pharm. Res.* (2013) 1915–1925.
- [20] V.A. Eberle, J. Schoelkopf, P.A.C. Gane, R. Alles, J. Huwyler, M. Puchkov, Floating gastroretentive drug delivery systems: comparison of experimental and simulated



- dissolution profiles and floatation behavior, *Eur. J. Pharm. Sci.* (2014) 34–43.
- [21] R.E.W. Hancock, R. Lehrer, Cationic peptides: a new source of antibiotics, *Trends Biotechnol.* (1998) 82–88.
  - [22] A. Cherkasov, K. Hilpert, H. Jenssen, C.D. Fjell, M. Waldbrook, S.C. Mullaly, R. Volkmer, R.E.W. Hancock, Use of artificial intelligence in the design of small peptide antibiotics effective against a broad spectrum of highly antibiotic-resistant superbugs, *ASC Chem. Biol.* (2009) 65–74.
  - [23] K. Tonguc-Altin, N. Sandalli, G. Duman, S. Selvi-Kuvvetli, N. Topcuoglu, G. Kulekci, Development of novel formulations containing Lysozyme and Lactoferrin and evaluation of antibacterial effects on Mutans Streptococci and Lactobacilli, *Arch. Oral Biol.* 60 (2015) 706–714.
  - [24] T.E. Miller, Killing and Lysis of gram-negative bacteria through the synergistic effect of hydrogen peroxide, ascorbic acid, and lysozyme, *J. Bacteriol.* (1969) 949–955.
  - [25] S.I. Park, M.A. Daeschel, Y. Zhao, Functional properties of antimicrobial lysozyme-chitosan composite films, *J. Food Sci.* (2004) 215–221.
  - [26] X. Chen, F. Niyonsaba, H. Ushio, D. Okuda, I. Nagaoka, S. Ikeda, K. Okumura, H. Ogawa, Synergistic effect of antibacterial agents human  $\beta$ -defensins, cathelicidin LL-37 and lysozyme against *Staphylococcus aureus* and *Escherichia coli*, *J. Dermatol. Sci.* (2005) 123–132.
  - [27] Y.Y. Wang, S.K. Lai, J.S. Suk, A. Pace, R. Cone, J. Hanes, Addressing the PEG mucadhesivity paradox to engineer nanoparticles that “slip” through the human mucus barrier, *Angew. Chem. Int. Ed. Engl.* (2008) 9726–9729.
  - [28] E. Baloglu, Z.A. Senyigit, S.Y. Caravan, A. Bernkop-Schnürch, (1) Strategies to prolong the intravaginal residence time of drug delivery systems, *J. Pharm. Sci.* (2009) 312–336.
  - [29] M. Araki, Y. Okuno, Y. Hara, Y. Sugiura, Allosteric regulation of a ribozyme activity through ligand-induced conformational change, *Nucl. Acids Res.* (1998) 3379–3384.
  - [30] A.A. Vertegel, R.W. Siegel, J.S. Dordick, Silica nanoparticle size influences the structure and enzymatic activity of adsorbed lysozyme, *Langmuir* (2004) 6800–6807.
  - [31] S. Sieber, S. Siegrist, S. Schwarz, F. Porta, S.H. Schenk, J. Huwiler, Immobilization of enzymes on PLGA sub-micrometer particles by crosslinked layer-by-layer deposition, *Macromol. Biosci.* (2017) 1–10.
  - [32] H. Leuenberger, *Martin Physikalische Pharmazie*, Wissenschaftliche Verlagsgesellschaft mbH, Stuttgart, 2006.
  - [33] Gerd Wedler, *Lehrbuch der Physikalischen Chemie*, 5th ed., WILEY-VCH verlag GmbH & Co KGaA, 2014.
  - [34] M.T. Houser, Improved turbidimetric assay for lysozyme in urine, *Clin. Chem.* (1983) 1488–1493.
  - [35] P. Mörsky, Turbidimetric determination of lysozyme with *Micrococcus lysodeikticus* cells: Reexamination of reaction conditions, *Anal. Biochem.* (1983) 77–85.
  - [36] N. Yamasaki, T. Tsujit, M. Takakuwa, A simple colorimetric method for the determination of lysozyme activity, *Agric. Biol. Chem.* (1973) 1507–1508.
  - [37] Y. Yang, K. Hamaguchi, Hydrolysis of 4 Methylumbelliferyl N-Acetyl-Chitotriose catalyzed by hen and turkey lysozymes, *J. Biochem.* (1980) 1003–1014.
  - [38] W. Roa, R. Löbenberg, Current perspectives in dissolution testing of conventional and novel dosage forms, *Int. J. Pharm.* (2007) 12–21.
  - [39] J.L. Fabregas, N. Garcia, “In Vitro” studies on buccoadhesive tablet formulations of hydrocortisone hemisuccinate, *Drug Dev. Ind. Pharm.* (2008) 1689–1696.
  - [40] J. Akbari, A. Nokhodchi, D. Farid, M. Adrangui, M.R. Siahi-Shadbad, M. Saeedi, Development and evaluation of buccoadhesive propranolol hydrochloride tablet formulations: effect of fillers, *II Farm.* (2004) 155–161.
  - [41] Viralkumar F. Patel, Fang Liu, Marc B. Brown, Modeling the oral cavity: In vitro and in vivo evaluations of buccal drug delivery systems, *J. Controlled Release.* (2012) 746–756.
  - [42] Y. Wei, A.A. Thyparambil, R.A. Latour, Protein helical structure determination using CD spectroscopy for solutions with strong background absorbance from 190–230 nm, *Biochim Biophys Acta.* (2014) 2331–2337.
  - [43] I. Tinoco, K. Sauer, J.C. Wang, J.D. Puglisi, G. Harbison, D. Rovnyak, *Physical Chemistry: Principles and Applications in Biological Sciences*, 5th ed., Pearson, 2014.
  - [44] M. Goebel-Stengel, A. Stengel, Y. Taché, J.R. Reeve Jr., The importance of using the optimal plastic and glassware in studies involving peptides, *Anal Biochem.* (2011) 38–46.
  - [45] P.G. Squire, P. Moser, C.T. O’Konski, Hydrodynamic properties of bovine serum albumin monomer and dimer, *Biochemistry* (1968) 4261–4272.
  - [46] Herbert Giesche, Mercury Porosimetry, A general (Practical) overview, Part. Part. Syst. Charact. (2006) 9–19.
  - [47] L.C. Bell, A.M. Posner, J.P. Quirk, The point of zero charge of hydroxyapatite and fluorapatite in aqueous solutions, *Elsevier J. Colloid Interface Sci.* (1973) 250–261.
  - [48] P. Somasundaran, G.E. Agar, The zero point of charge of calcite, *J. Colloid Interface Sci.* (1967) 433–440.
  - [49] S. Ge, K. Kojio, A. Takahara, T. Kajiyama, Bovine serum albumin adsorption onto immobilized organotrichlorosilane surface: influence of the phase separation on protein adsorption patterns, *J. Biomater. Sci. Polym. Ed.* (1998) 131–151.
  - [50] A. Einstein, Über die molekularkinetischen Theorie der Wärme geforderte Bewegung von in ruhenden Flüssigkeiten suspendierten Teilchen, *Ann. Phys.* (1905) 549–560.
  - [51] T. Zounggrana, G.H. Findenegg, W. Norde, Structure, stability, and activity of adsorbed enzymes, *J. Colloid Interface Sci.* (1997) 437–448.
  - [52] C. Calderon, E. Abuin, E. Lissi, R. Montecinos, Effect of human serum albumin on the kinetics of 4-Methylumbelliferyl- $\beta$ -D-N-N-O-N-O0 Triacetylchitotriose Hydrolysis Catalyzed by Hen Egg White Lysozyme, *Protein J.* (2011) 367–373.
  - [53] K. Oungbho, B.W. Müller, Chitosan sponges as sustained release drug carriers, *Int. J. Pharm.* (1997) 229–237.
  - [54] P. Frayssinet, D. Mathon, A. Lerch, A. Autefage, P. Collard, N. Rouquet, Osseointegration of composite calcium phosphate bioceramics, *J. Biomed. Mater. Res.* (2000) 125–130.
  - [55] S. Langstaff, M. Sayer, T.J. Smith, S.M. Pugh, S.A. Hesp, W.T. Thompson, Resorbable bioceramics based on stabilized calcium phosphates. Part I: rational design, sample preparation and material characterization, *Biomaterials* (1999) 1727–1741.



### **3.2 Mucoadhesive microparticles for local treatment of gastrointestinal diseases**

Daniel Preisig <sup>1</sup>, Roger Roth <sup>1</sup>, Sandy Tognola <sup>1</sup>, Felipe Varum <sup>2</sup>, Roberto Bravo <sup>2</sup>, Y. Cetinkaya <sup>2</sup>, Jörg Huwyler <sup>1</sup>, Maxim Puchkov <sup>1</sup>

<sup>1</sup> Departement of Pharmaceutical Sciences, University of Basel, Switzerland

<sup>2</sup> Tillots Pharma AG, Rheinfelden, Switzerland

**European Journal of Pharmaceutics and Biopharmaceutics** 105(2016)156-165

#### **Personal contribution**

My contribution to this research article includes the development of the fluidized bed process and the production of the chitosan coated formulation. Additionally, I carried out the particle retention assays of the mucoadhesive formulations without dispersant, and assembled figure 1A.





## Research paper

## Mucoadhesive microparticles for local treatment of gastrointestinal diseases



Daniel Preisig<sup>a</sup>, Roger Roth<sup>a</sup>, Sandy Tognola<sup>a</sup>, Felipe J.O. Varum<sup>b</sup>, Roberto Bravo<sup>b</sup>, Yalcin Cetinkaya<sup>b</sup>, Jörg Huwyler<sup>a,\*</sup>, Maxim Puchkov<sup>a</sup>

<sup>a</sup> Department of Pharmaceutical Sciences, University of Basel, Klingelbergstrasse 50, 4056 Basel, Switzerland

<sup>b</sup> Tillotts Pharma AG, Baslerstrasse 15, 4310 Rheinfelden, Switzerland

## ARTICLE INFO

## Article history:

Received 14 December 2015

Revised 31 May 2016

Accepted in revised form 9 June 2016

Available online 11 June 2016

## Keywords:

Mucoadhesion

Bioadhesion

Microparticles

Fluidized-bed

Drug loading

Porous carriers

Chitosan

Dispersibility enhancement

Colon drug delivery

## ABSTRACT

Mucoadhesive microparticles formulated in a capsule and delivered to the gastrointestinal tract might be useful for local drug delivery. However, swelling and agglomeration of hydrophilic polymers in the gastrointestinal milieu can have a negative influence on particle retention of mucoadhesive microparticles. In this work, we investigated the impact of dry-coating with nano-sized hydrophilic fumed silica on dispersibility and particle retention of mucoadhesive microparticles. As a model for local treatment of gastrointestinal diseases, antibiotic therapy of *Clostridium difficile* infections with metronidazole was selected. For particle preparation, we used a two-step fluidized-bed method based on drug loading of porous microcarriers and subsequent outer coating with the mucoadhesive polymer chitosan. The prepared microparticles were analysed for drug content, and further characterized by thermal analysis, X-ray diffraction, and scanning electron microscopy. The optimal molecular weight and content of chitosan were selected by measuring particle retention on porcine colonic mucosa under dynamic flow conditions. Mucoadhesive microparticles coated with 5% (weight of chitosan coating/total weight of particles) of low molecular weight chitosan showed good *in vitro* particle retention, and were used for the investigation of dispersibility enhancement. By increasing the amount of silica, the dissolution rate measured in the USP IV apparatus was increased, which was an indirect indication for improved dispersibility due to increased surface area. Importantly, mucoadhesion was not impaired up to a silica concentration of 5% (w/w). In summary, mucoadhesive microparticles with sustained-release characteristics over several hours were manufactured at pilot scale, and dry-coating with silica nanoparticles has shown to improve the dispersibility, which is essential for better particle distribution along the intestinal mucosa in humans. Therefore, this advanced drug delivery concept bears great potential, in particular for local treatment of gastrointestinal diseases.

© 2016 Elsevier B.V. All rights reserved.

## 1. Introduction

Mucoadhesive drug delivery systems can be beneficial for local treatment of diseases related to mucosal membranes, such as fungal or bacterial infections [1,2]. Since the dosage form can be brought in close contact with the diseased tissue for an extended period of time, the therapeutic efficacy can be increased and lower

drug doses may be required, eventually reducing systemic adverse drug effects [3].

Colonic drug delivery is paramount for local treatment of diseases such as ulcerative colitis, Crohn's disease, or pseudomembranous colitis [4,5]. However, these diseases are often characterized by severe diarrhoea episodes [6], making it difficult to reach sufficiently high local drug concentrations for a long enough period of time, particularly in the ascending colon where the volume of fluids is higher [7]. The mucoadhesion approach can be an effective strategy to resist the wash-out of the drug. However, delivery and adhesion to the colonic mucosa still presents a great challenge [8].

In case of hard-gelatine capsules for delivery of a mucoadhesive formulation, there is a lack of strategies to prevent agglomeration after hydration. McGirr et al. [9] have observed an incomplete

Abbreviations: AUC, area under the curve; D50, median particle size; DSC, differential scanning calorimetry; FCC, functionalized calcium carbonate; LMW, low molecular weight; MBZ, metronidazole benzoate; MMW, medium molecular weight; SD, standard deviation; XRPD, X-ray powder diffraction.

\* Corresponding author.

E-mail address: [joerg.huwyler@unibas.ch](mailto:joerg.huwyler@unibas.ch) (J. Huwyler).

release of mucoadhesive polymers (carbomers) from IntelliSite® plastic capsules administered to beagle dogs and opened in the colon by remote control. This was explained by hydration and swelling of the polymer inside the capsule before the polymer could be released.

The gastrointestinal transit of multiparticulate formulations is less variable than single-units, and transit through the colon is slower than monolithic dosage forms due to a sieving effect of multiparticulates [10,11]. Therefore, a drug delivery platform combining mucoadhesive features in multiparticulates can contribute to an overall increased gastrointestinal residence time. Procedures describing the preparation of mucoadhesive multiparticulates, nanoparticles [12–14], microparticles [15–18], and pellets in the millimetre range [19,20] have been reported.

The particle size of mucoadhesive drug carriers plays an important role in terms of mucoadhesion and manufacturability. Schmidt et al. have carried out a first *in vivo* study investigating the size-dependency of carrier uptake to inflamed rectal mucosa [21]. The most striking finding was the significantly enhanced accumulation of microparticles (3 µm) in ulcerous lesions. The authors concluded that size-tuning of drug carriers in the micrometre range offers a possibility for passive targeting of the inflamed regions in the gastrointestinal tract. Moreover, the results of *ex vivo* transport experiments let suggest that nanoparticles are not suitable for local treatment of inflammatory bowel diseases, since translocation towards the serosal compartment could enhance systemic drug absorption leading to higher risk of adverse drug effects [21].

In general, manufacturability of microcarriers is easier compared to nanocarriers due to the improved flowability of larger particles and the possibility of using standardized processes suitable for scale-up. Mucoadhesive microparticles were prepared by spray drying [22], dry powder coating [20], suspension polymerization [15], ionic gelation [23], emulsion-solvent evaporation [24], and supercritical fluid technique [25]. Our group has developed a precipitation method to coat drug-loaded microparticles with the mucoadhesive polymer chitosan [26]. These model particles showed significant retention on porcine colonic mucosa, and they have been used for the implementation and validation of a new particle-retention assay based on marker-ion analysis. However, manufacture of mucoadhesive microparticles by chitosan precipitation was done at small scale, and therefore, a method suitable for large scale is essential.

The fluidized-bed technology is an efficient and established pharmaceutical process often used for drug layering of non-porous pellets, particularly for low drug dosages, with several products in the pharmaceutical market [27,28]. The suitability for drug loading of porous microcarriers has also been demonstrated [29]. Additionally, this technology can be used to stabilize the drug as a solid dispersion leading to increased dissolution rate and bioavailability of poorly water-soluble drugs [30–32]. Scarce literature is available on the preparation of mucoadhesive microparticles using a fluidized-bed process, being a publication from Möschwitzer and Müller [17] one of the few examples. However, no mucoadhesion studies with these chitosan-layered pellets have been carried out.

In the present work, we describe a two-step fluidized-bed method for preparation of mucoadhesive microparticles with optimized drug-loading and chitosan-coating process to address local drug delivery to the colon. Metronidazole benzoate (MBZ, prodrug of metronidazole) was used as a model drug for poor aqueous solubility and local treatment of gastrointestinal diseases (*Clostridium difficile* infections). Further objectives of this work were to evaluate the feasibility of hydrophilic fumed silica to improve the dispersibility of the mucoadhesive microparticles, and to investigate its impact on the mucoadhesivity.

## 2. Materials and methods

### 2.1. Materials

Functionalized calcium carbonate (FCC, Omyapharm 500-OG) was kindly provided by Omya, Switzerland. Metronidazole benzoate (MBZ) was purchased from Farchemia, Italy. Ammonium formate, formic acid (98%), HCl, methanol (all HPLC-grade), and chitosan with low and medium molecular weight (LMW and MMW, respectively) and 75–85% of deacetylation were purchased from Sigma-Aldrich, Switzerland. Ethocel® Std. 10 cp was received from Colorcon, UK. Aerosil 300 was obtained from Evonik Industries AG, Germany. Acetone, acetic acid (99%), sodium dihydrogen phosphate dihydrate (NaH<sub>2</sub>PO<sub>4</sub>·2H<sub>2</sub>O), and NaOH pellets were purchased from Häseler AG, Switzerland.

### 2.2. Particle preparation

For preparation of mucoadhesive microparticles, we used a laboratory-scale fluidized-bed equipment (Strea-1, Aeromatic Fielder, Switzerland) with top-spray configuration. A spray nozzle with an orifice diameter of either 0.5 or 0.8 mm was used (Schlick, Germany). The spray rate was controlled using a peristaltic pump and a balance. The mucoadhesive microparticles were prepared in two steps: (1) drug loading of the porous microcarrier FCC with the model drug MBZ dissolved in a mixture of ethanol and acetone co-loaded with a binder polymer, and (2) spray coating of the drug-loaded carrier particles with a chitosan solution.

After preliminary experiments, three different mucoadhesive formulations, and one non-mucoadhesive control formulation were prepared in this study. MMW-5 and MMW-10 particles containing 5% and 10% (w/w) MMW chitosan, respectively, were prepared to evaluate the optimal chitosan content in terms of mucoadhesivity. LMW-5 particles containing 5% (w/w) LMW chitosan were the optimized formulation in terms of higher drug load and easier manufacturability. The viscosity of the spray solution is lower for LMW chitosan than for MMW chitosan (20–300 cps vs. 200–800 cps, 1% (w/w) in 1% acetic acid [33,34]), which should result in decreased droplet size and reduced risk of nozzle blocking, leading to an overall improved coating quality. The fluidized-bed process parameters of the drug-loading and chitosan-coating batches are summarized in Tables 1 and 2, respectively.

#### 2.2.1. Drug loading

After a preliminary screening, two drug-loading batches were prepared according to Table 1. For preparation of PEG-MBZ-FCC particles, PEG 3000, MBZ, and FCC were used at a ratio of 28.6:28.6:42.8 (w/w). PVP-MBZ-FCC particles were prepared at a higher drug load using PVP K-25, MBZ, and FCC at a ratio of 37.5:37.5:25 (w/w). The drug solution consisted of 10% MBZ (w/w), and 10% polymer (w/w) dissolved in a mixture of acetone

**Table 1**

Fluidized-bed process parameters used for the two drug loading batches PEG-MBZ-FCC and PVP-MBZ-FCC.

	PEG-MBZ-FCC	PVP-MBZ-FCC
FCC (g)	180	96
MBZ (g)	120	144
Polymer (g)	120	144
Co-loaded polymer	PEG 3000	PVP K-25
Theoretical drug load (% w/w)	28.6	37.5
Inlet temperature (°C)	50	50
Air volume (level)	2–3	2–3
Atomization pressure (bar)	0.8	0.8
Spray rate (g/min)	5	5
Spray nozzle orifice diameter (mm)	0.8	0.8
Process time (h)	4	5

**Table 2**

Fluidized-bed process parameters for mucoadhesive coating with MMW and LMW chitosan on drug-loaded PEG-MBZ-FCC and PVP-MBZ-FCC particles, respectively.

	MMW-5	MMW10	LMW-5	EC-5
Drug-loading batch	PEG-MBZ-FCC	PEG-MBZ-FCC	PVP-MBZ-FCC	PVP-MBZ-FCC
MBZ-loaded FCC (g)	70	70	120	152
Chitosan coating (% w/w)	5	10	5	–
Theoretical drug load (% w/w)	27.14	25.71	35.63	32.39
Inlet temperature (°C)	50	50	50	40
Air volume (level)	2–4	2–4	2–4	2–4
Atomization pressure (bar)	0.8	0.8	0.8	0.8
Spray rate (g/min)	1–1.5	1–1.5	5	2.5
Spray nozzle orifice diameter (mm)	0.5	0.5	0.8	0.8
Process time (h)	4	8	2	1

and ethanol (60:40, v/v). The drug solutions were sprayed completely to reach the desired drug loads. The dimensions of the stainless steel chamber were as follows: cone height 330 mm, bottom diameter 100 mm, and top diameter 250 mm. The product was dried by fluidizing for 30 min at 40 °C, and by storing overnight in a vacuum oven set to 40 °C. The dried product was kept in closed jars and stored at room temperature.

### 2.2.2. Chitosan coating

Mucoadhesive coatings using MMW chitosan were applied on drug-loaded PEG-MBZ-FCC particles to a final chitosan content of 5% and 10% (w/w, MMW-5 and MMW-10, respectively). The coating solution was prepared by suspending 1.5% chitosan (w/v) in purified water and adding 1.5% acetic acid (w/v). After stirring for 12 h, the pH was adjusted to pH 5.8 using NaOH 1 M, and then the solution was passed through a metal sieve with a mesh size of 90 µm (Retsch, Switzerland). To reach the desired chitosan contents of 5% and 10% (w/w), the chitosan solutions (250 ml and 500 ml, respectively) were sprayed with a spray rate set to 1–1.5 g/min. The bottom diameter of the fluidizing chamber was slightly reduced to 55 mm to process smaller quantities of particles.

The optimized LMW-5 particles containing 5% (w/w) LMW chitosan were prepared using drug-loaded PVP-MBZ-FCC particles. A stainless steel chamber with 100 mm bottom diameter was used. An aqueous solution of LMW chitosan (1%, w/v) was prepared in 620 ml diluted acetic acid (10%, w/v) by stirring for 12 h and filtering through a metal sieve with a mesh size of 90 µm.

### 2.2.3. Granulation with ethyl cellulose

For preparation of the non-mucoadhesive control particles containing 5% (w/w) of ethyl cellulose (EC-5), 152 g of PVP-MBZ-FCC was granulated with 8 g of ethyl cellulose in a fluidized-bed process. The spray solution consisted of 16 g PVP dissolved in 124 ml of purified water, and was sprayed at a flow rate of 5 g/min. The process parameters for the EC-5 particles are summarized in Table 2.

### 2.2.4. Dry-coating with silica

Dry-coating of LMW-5 particles with hydrophilic fumed silica (Aerosil 300) was carried out by a simple blending procedure. The exact amounts of LMW-5 and silica particles were weighed to obtain silica concentrations of 2%, 5%, and 10% (w/w). The blends were sieved three times using a metal sieve with a mesh size of 500 µm (Retsch, Switzerland). Subsequently, the blends were processed in a laboratory-scale Turbula® mixer for 10 min, and sieved again (500 µm) three times.

## 2.3. Particle characterization

### 2.3.1. Particle-retention assay

Mucoadhesivity of chitosan-coated particles was characterized by measuring the relative particle retention on mucosal tissue in

a custom-built flow channel. Porcine colonic mucosal tissue was used as substrate to mimic the anatomy and mucus thickness of the human large intestine [8], which is the target tissue for local treatment of *Clostridium difficile* infections.

Segments of pig proximal colon obtained from a local slaughterhouse were kept on ice and processed the same day. The colonic tract was opened longitudinally and washed with tap water. After removing the outer muscle layers, the mucosal tissue was sectioned into smaller pieces and rinsed with isotonic saline (0.9% NaCl). The mucosal sections were wrapped in aluminium foil, flash-frozen with liquid nitrogen, and stored at –20 °C. Before use, the tissue was allowed to thaw in a refrigerator and equilibrate at room temperature [35].

Fig. 1A shows a diagram of the flow-channel assembly. The colonic mucosal tissue was spread on the mucosa holder of the support plate and immobilized with the fixation plate. The flow medium (37 °C) was transported with a peristaltic pump and distributed on the mucosa via three nozzles. The flow rate was set to 20 ml/min, and the mucosal tissue was hydrated by applying a constant flow of medium for 5 min. The dry particles (20.0 mg) were evenly distributed over the centre area of the mucosa (55 × 17 mm). After a contact time of 5 min, the flow channel was tilted to 45° and the flow was started. Ultra-pure water was used as flow medium for better sensitivity and precision of the calcium quantification by capillary electrophoresis.

The flow medium was collected in beakers, which were changed every 10 min and weighted to determine the sample volume. The duration of the experiment was 30 min. The remaining particles were scraped off the mucosa and washed out with flow medium into separate beakers. Samples were adjusted to pH 2.5 and analysed by capillary electrophoresis according to Section 2.3.2. For each formulation, the particle-retention assay was repeated three times.

The percentage of detached particles,  $FCC_{det}$ , was calculated for each collected fraction using Eq. (1):

$$FCC_{det} = \frac{FCC_{det}}{FCC_{app}} \quad (1)$$

where  $FCC_{det}$  is the mass of detached FCC determined by capillary electrophoresis, and  $FCC_{app}$  is the mass of FCC applied on the mucosa, i.e. the FCC content in 20 mg of tested formulations. The results of particle retention are the percentage of retained FCC,  $FCC_{ret}$ , which was calculated by Eq. (2):

$$FCC_{ret} = 1 - FCC_{det} \quad (2)$$

To measure the reliability of the experimental results, recovery of FCC was determined by Eq. (3):

$$Recovery = FCC_{det} + FCC_{muc} \quad (3)$$

where  $FCC_{muc}$  is the percentage of remaining particles which were scraped off the mucus after 30 min.

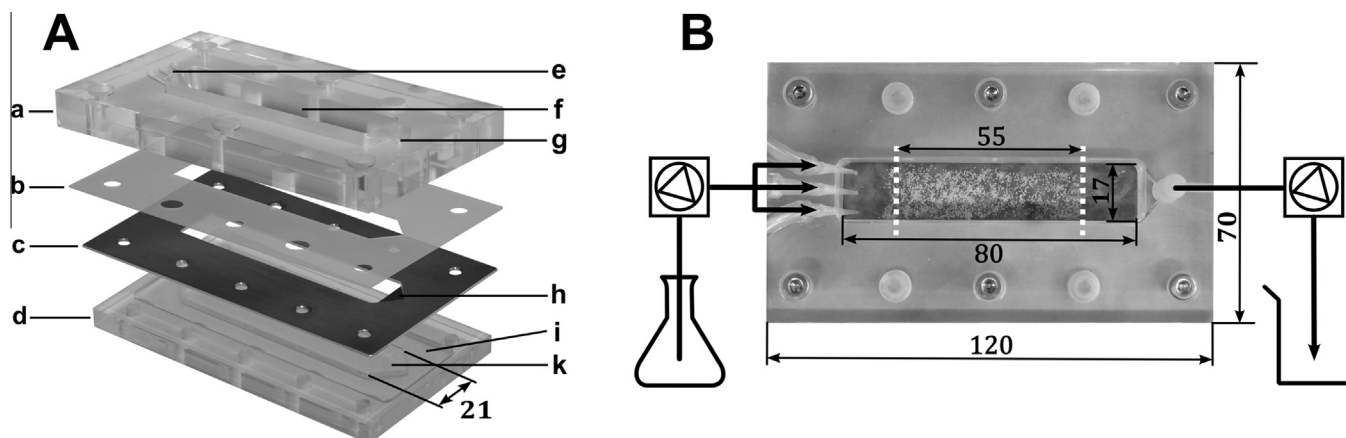


**Fig. 1.** Particle-retention assay for measuring mucoadhesivity under dynamic flow conditions. (A) The breakdown of the flow-channel assembly: (a) upper plate, (b) silicon seal, (c) fixation plate, (d) support plate, (e) nozzle plugs for inlet flow, (f) open channel, (g) vertical connection to collection region for outlet flow, (h) chamfered collection region, (i) excessive mucosa void space, and (k) mucosa holder. (B) The top view of the flow-channel assembly with schematic illustration of inlet and outlet flow using two peristaltic pumps. The area of particle application (55 × 17 mm) is indicated by dashed lines. The dimensions are in millimetres.

### 2.3.2. FCC quantification by capillary electrophoresis

For quantification of detached microparticles, marker-ion analysis was applied as described previously [26]. FCC content of collected samples from the particle-retention assay was determined by capillary electrophoresis using the Cation Analysis Kit (Beckman & Coulter, USA) for quantification of calcium ions [36]. FCC content in tested microparticles was also determined. The microparticles (50 mg) were decomposed to calcium ions and remaining components by adjusting the pH to pH 2.5 with HCl in a 50 ml volumetric flask. The samples were diluted (1 ml in 10 ml) with 3 mM HCl (pH 2.5), and filtered with 0.45 µm syringe filters. Samples were prepared in triplicate.

The area under the curves (AUCs) of calcium peaks was calculated using 32 Karat™ Software 8.0 (Beckman Coulter, Germany). The masses of FCC were calculated according to the calibration curve of FCC, which included 7 data points with FCC concentrations ranging from 1 to 80 µg/ml ( $R^2 > 0.990$ ). The calibration curve was re-measured every time before each test run, and each capillary electrophoresis measurement was carried out in duplicate.

### 2.3.3. Drug dissolution in USP IV and particle dispersibility

Drug-loaded, chitosan-coated, and silica-coated microparticles were filled in hard-shell gelatine capsules size 2 and tested in the USP IV dissolution apparatus (CE 6, Sotax, Switzerland) using a closed-loop system. The USP IV dissolution cells with 12 mm inner diameter were filled with 1 mm glass beads and covered with a sieve insert (90 µm mesh). Glass-microfiber filters (Whatman, GF/D, GE Healthcare Life Sciences, UK) with diameter of 25 mm and pore size of 2.7 µm were used to filter the dissolution medium prior to spectrophotometric measurement. The dissolution medium (1 l of phosphate buffer, pH 6.8, 37°C) was transported through the USP IV dissolution cells and back to the reservoir vessels with a piston pump (CY 7-50, Sotax, Switzerland) at a flow rate of 16 ml/min. The UV absorbance was measured online at 320 nm with a multi-cell UV-spectrophotometer (Amersham Bioscience, Ultro-spec 3100 pro).

The capsules were completely filled with the microparticles, and the sample size was weighted after closing of the capsule. Due to the different bulk densities, the sample size varied from 80 to 120 mg formulation per capsule, but sink conditions were provided in all experiments. Pure MBZ was filled in capsules size 3 with a sample size of 40 mg. For a qualitative comparison of particle dispersibility, the photographs of the dissolution cells were taken after opening of the capsule, and after 30 min of the experiment.

### 2.3.4. Particle drug content

To determine the drug content in prepared microparticles, a validated HPLC method was applied as described previously [37]. After extraction of MBZ with acetone, a first dilution (1 ml in 10 ml) with methanol, and second dilution (1 ml in 10 ml) with a mixture of ultra-pure water and methanol (90:10, v/v) were prepared. The resulting drug concentrations were in the validated range of the isocratic HPLC method. The samples were assayed with an HPLC-UV system (Agilent 1100 series) comprising an autosampler, binary pump, and variable wavelength detector. The C18 column (Nucleosil, Macherey-Nagel, Switzerland) with 120 mm length, 3 mm inner diameter, and 5 µm particle size was kept in a column oven (Perkin Elmer 200 series) set to 40°C. The mobile phase consisted of ammonium formate (10 mM, pH 4.5) and acetonitrile at a volumetric ratio of 50:50. Flow rate was 0.5 ml/min, and UV detection was performed at 320 nm.

### 2.3.5. Scanning electron microscopy (SEM)

The morphology of non-loaded, drug-loaded, chitosan-coated, silica-coated, and ethyl cellulose control microparticles was analysed with a scanning electron microscope (SEM; Nova Nano-SEM 230, FEI Company, USA). Samples were sputtered with a 20 nm gold layer by a high-vacuum sputter coater (EM ACE600, Leica, Germany).

### 2.3.6. Particle size

For measurement of particle size, a Camsizer XT (Retsch Technology, Germany) equipped with the X-Jet module for air pressure dispersion was used. A sample of 200 mg was applied via the vibrating feed chute and dispersed with a pressure of 300 kPa. The two-camera system and the included software for digital image processing allowed particle analysis in the range from 1 µm to 4.5 mm. In our study, results of particle size are presented as the longest Feret diameter, which is the longest possible distance between two parallel tangents of a projected particle. The amount of particles is presented as volume percentage (% v/v). For each formulation, five measurements were performed, and the mean volume percentage (% v/v) was calculated for each size fraction.

### 2.3.7. X-ray powder diffractometry (XRPD)

The crystalline state of the drug-loaded samples was investigated using a high-resolution XRPD system (SmartLab, Rigaku, Japan) equipped with Bragg-Brentano optics and a HyPix-3000 detector (Rigaku, Japan). A rotating anode X-ray source (45 kV



and 200 mA) was used for generation of the Cu K $\alpha$  radiation ( $\lambda = 1.5406 \text{ \AA}$ ). The samples were measured in 1D detection mode in an angular range of  $10\text{--}40^\circ$  ( $2\theta$ ) and with a step size of  $0.01^\circ$  ( $2\theta$ ).

For comparison purposes, co-evaporates of the drug and PVP K-25 in ratios of 50:50 and 10:90 (w/w) were prepared. The ratio of 50:50 was the same as in drug-loaded samples, and the ratio of 10:90 was for preparation of a solid dispersion. For preparation of both co-evaporates, a total mass of 1 g (MBZ and PVP) was dissolved in 20 ml of a mixture of acetone and ethanol (60:40, v/v). The solvents were removed using a rotary evaporator (R-114, Büchi, Switzerland) until a highly viscous solution was obtained which was filled into the depression of the sample holder, and dried in a vacuum oven set to  $40^\circ\text{C}$  and 250 mbar.

### 2.3.8. Differential scanning calorimetry (DSC)

Thermal analysis of the samples was carried out with a DSC 400 instrument (PerkinElmer, USA). A temperature scan from  $0^\circ\text{C}$  up to  $150^\circ\text{C}$  was performed in steps of  $10^\circ\text{C}/\text{min}$ . Samples size was between 4 and 9 mg.

For comparison purposes, the same co-evaporates of MBZ and PVP as described in Section 2.3.7 (drug-to-polymer ratio of 50:50 and 10:90, w/w) were analysed. One drop of the highly viscous solution was put in a DSC-analysis pan, and dried in a vacuum oven set to  $40^\circ\text{C}$  and 250 mbar.

### 2.3.9. Statistical analysis

For statistical analysis, we used the data analysis software (OriginPro 9.1.0, OriginLab, USA). All results were expressed as means  $\pm$  standard deviations (SD). A two-tailed *t*-test was performed to analyse the differences of mucoadhesivity between different mucoadhesive formulations. *P*-values  $< 0.05$  were considered as statistically significant.

## 3. Results

### 3.1. Particle-retention assay

The results of *in vitro* particle retention for mucoadhesive microparticles (without silica) are summarized in Fig. 2A. The data showed strongest particle retention for MMW-10 particles ( $74.79 \pm 4.79\%$ ) being significantly higher than for MMW-5 particles ( $p < 0.01$ ). It was possible to significantly improve the mucoadhesive performance by increasing the content of medium molecular weight chitosan coating from 5% to 10% (w/w). Interestingly, particles coated with LMW chitosan were significantly better retained than MMW-5 particles ( $p < 0.01$ ) with identical amount of

chitosan coating. For comparison purposes, non-mucoadhesive control particles (EC-5) comprising ethyl cellulose showed almost complete detachment after 30 min ( $6.67 \pm 8.38\%$ ). The average recoveries ranged from 87.91% to 111.78%, which was an indication for the good reliability of the experimental data.

Typical retention kinetics for different particles are plotted in Fig. 2B. LMW-5 particles showed an initial burst detachment within the first 10 min, followed by a reduced detachment rate for the rest of the experiment. Contrarily, most of the EC-5 particles were already washed off after 10 min.

In a next step, LMW-5 microparticles, coated with various concentrations of silica nanoparticles as potential dispersing agent, were also assayed for particle-retention on colonic mucosal tissue. The results are summarized in Fig. 2C. The average recoveries were between 75.79% and 113.72%. It should be noted that the addition of 2% and 5% (w/w) silica led to an insignificant decrease in mucoadhesivity compared to LMW-5 particles without silica ( $p > 0.1$ ), whereas 10% silica (w/w) reduced the particle retention significantly ( $p < 0.005$ ).

### 3.2. Drug dissolution in USP IV and particle dispersibility

Drug-dissolution profiles of pure drug, drug loaded particles, mucoadhesive, and non-mucoadhesive microparticles are shown in Fig. 3A. The drug-loaded batches PEG-MBZ-FCC and PVP-MBZ-FCC showed a much higher dissolution rate than pure MBZ powder. Contrarily, the drug-dissolution rate of chitosan-coated particles was lower than drug-loaded particles, which can be explained by the strong agglomeration effect of mucoadhesive microparticles. Fig. 4A shows a typical agglomerate of MMW-10 particles during dissolution studies, keeping the form of the capsule. The increased dissolution rate of LMW-5 compared to MMW-10 particles can be well explained by the better dispersibility of LMW-5 as shown in Fig. 4B.

Dissolution profiles of LMW-5 particles coated with silica are also shown in Fig. 3B. For the formulations containing 0%, 2%, and 5% silica, the average time until 60% of the drug had been released was  $>10$ , 3.6, and 2.9 h, respectively. Moreover, capsules filled with 10% silica could achieve a drug release of 80% after 4.6 h. This correlation of higher drug-dissolution rate with increasing silica concentrations can be explained by the capability of silica to disperse the particles and enlarge the surface area accessible by the dissolution medium. The improved particle dispersion was also found by visual observation as shown in Fig. 4D and F, showing LMW-5 particles coated with 5% and 10% silica, respectively, directly after disintegration of the capsule. Fig. 4E shows the LMW-5 particles

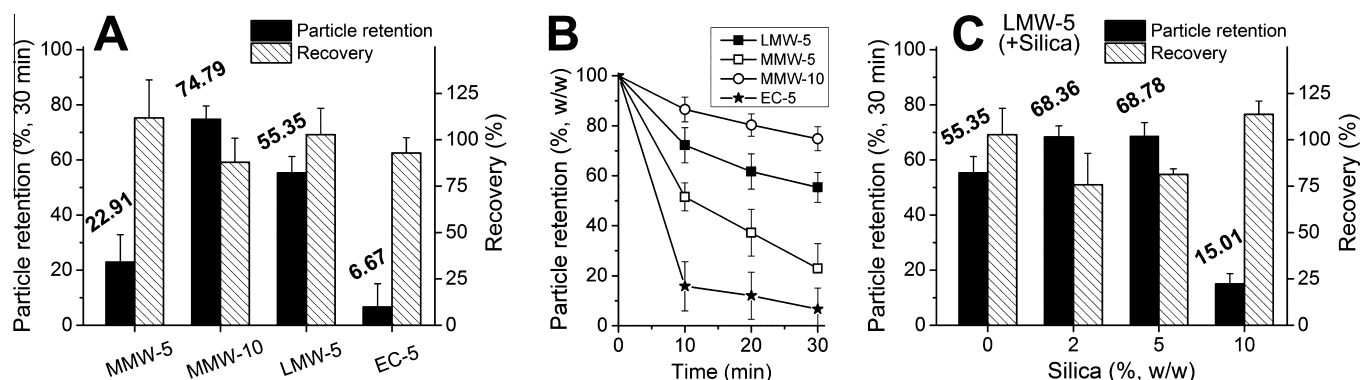


**Fig. 2.** Results of mucoadhesivity for chitosan-coated and silica-coated microparticles tested in the particle-retention assay. Panel A shows particle retention after 30 min for MMW-5, MMW-10, LMW-5, and EC-5 (non-mucoadhesive control). Panel B shows particle-retention kinetics for LMW-5, MMW-5, and EC-5. Panel C shows particle retention after 30 min for LMW-5 particles dry-coated with different amounts of silica. By increasing the silica concentration from 5% to 10% (w/w), the particle retention decreased significantly. The dashed bars in Panels A and C indicate the particle recovery (right y-axis). Error bars represent SD ( $n = 3$  for all, except  $n = 6$  for LMW-5).

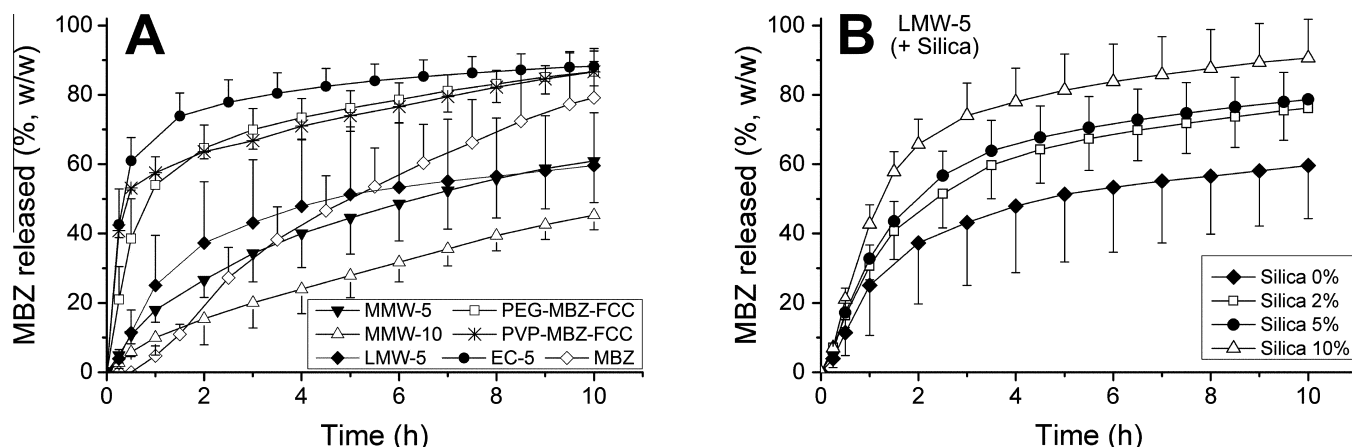


**Fig. 3.** USP IV drug-dissolution profiles of microparticles filled in capsules. Panel A shows results for drug-loaded, chitosan-coated, and non-mucoadhesive control particles. The slow drug release from MMW-5, MMW-10, and LMW-5 was associated with the formation of agglomerates. Panel B shows results for LMW-5 particles dry-coated with different concentrations of silica. The higher dissolution rate was an indication for improved dispersibility. Error bars represent SD ( $n = 3$  for all) and are shown only for one direction (+ or –) for better presentation of the results.

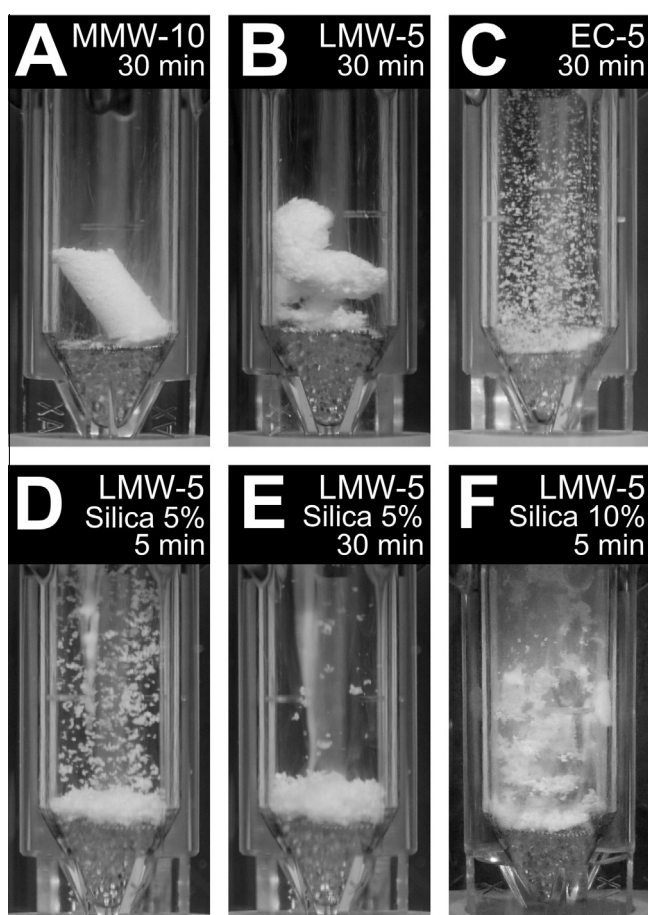


**Fig. 4.** Representative images of particle dispersion during USP IV dissolution studies after disintegration of the capsule shell. The photographs were taken 30 min after starting the flow, except (D) and (F) were taken after 5 min, i.e. after disintegration of the capsule. Contrary to MMW-5 and LMW-5 (A and B) showing dense agglomerates, EC-5 (C) was characterized by excellent dispersibility. The silica-coated (5%, w/w) LMW-5 particles showed good dispersion directly after capsule disintegration (D), but formation of loose agglomerates occurred after a certain period of time (E).

coated with 5% (w/w) silica after 30 min, indicating that, despite the good particle dispersion in the beginning of the dissolution run, agglomeration occurred after a certain time.

### 3.3. Scanning electron microscopy (SEM)

Typical SEM images of bulk FCC, drug-loaded PEG-MBZ-FCC, and drug-loaded PVP-MBZ-FCC particles are shown in Fig. 5A–C, respectively. Particles co-loaded with PEG still showed the characteristic pore structure of FCC, and they were mainly consisting of single FCC particles, whereas PVP-MBZ-FCC particles with higher drug and polymer content showed complete pore filling and bigger aggregates. In the example of PVP-MBZ-FCC, the drug can be identified as crystals embedded in the polymer layers.

Representative examples of chitosan-coated particles (MMW-5, MMW-10, and LMW-5) are shown in Fig. 5D–F, respectively, indicating a homogeneous layer of chitosan. The formation of granules was also observed, including EC-5 particles (Fig. 5G).

LMW-5 particles with different concentrations of silica nanoparticles were analysed by SEM to evaluate whether the dry-particle coating process was feasible. Fig. 5I shows a close-up view of a chitosan surface with 2% silica (w/w) revealing a homogeneous distribution of silica particles as a monolayer. However, due to the uneven surface morphology of the chitosan granules, there was a strong tendency of the silica nanoparticles to adsorb and accumulate between the gaps as shown in Fig. 5H. The same image shows that the major fraction of silica nanoparticles was present as agglomerates with sizes from 1 to 50  $\mu\text{m}$ .

### 3.4. Particle drug content

In Table 3, the theoretical and experimental drug loads of prepared microparticles are compared. Both drug-loading batches (PEG-MBZ-FCC and PVP-MBZ-FCC) deviated less than 1% (w/w) from expected MBZ contents (28.6% and 37.5%, respectively). For mucoadhesive and control particles, the discrepancies between theoretical and experimental drug loads were also within an acceptable range (1–2.5%, w/w).

### 3.5. Particle size

Median particle sizes (D50) of prepared microparticles are listed in Table 3, and plots of particle size distribution are shown in Fig. 6. PEG-MBZ-FCC particles were characterized by a very narrow size distribution (Fig. 6A), and median particle size was only slightly higher than for bulk FCC ( $10.10 \pm 0.07 \mu\text{m}$  vs.  $7.77 \pm 0.07 \mu\text{m}$ ). The PVP-MBZ-FCC particles, having increased drug and polymer



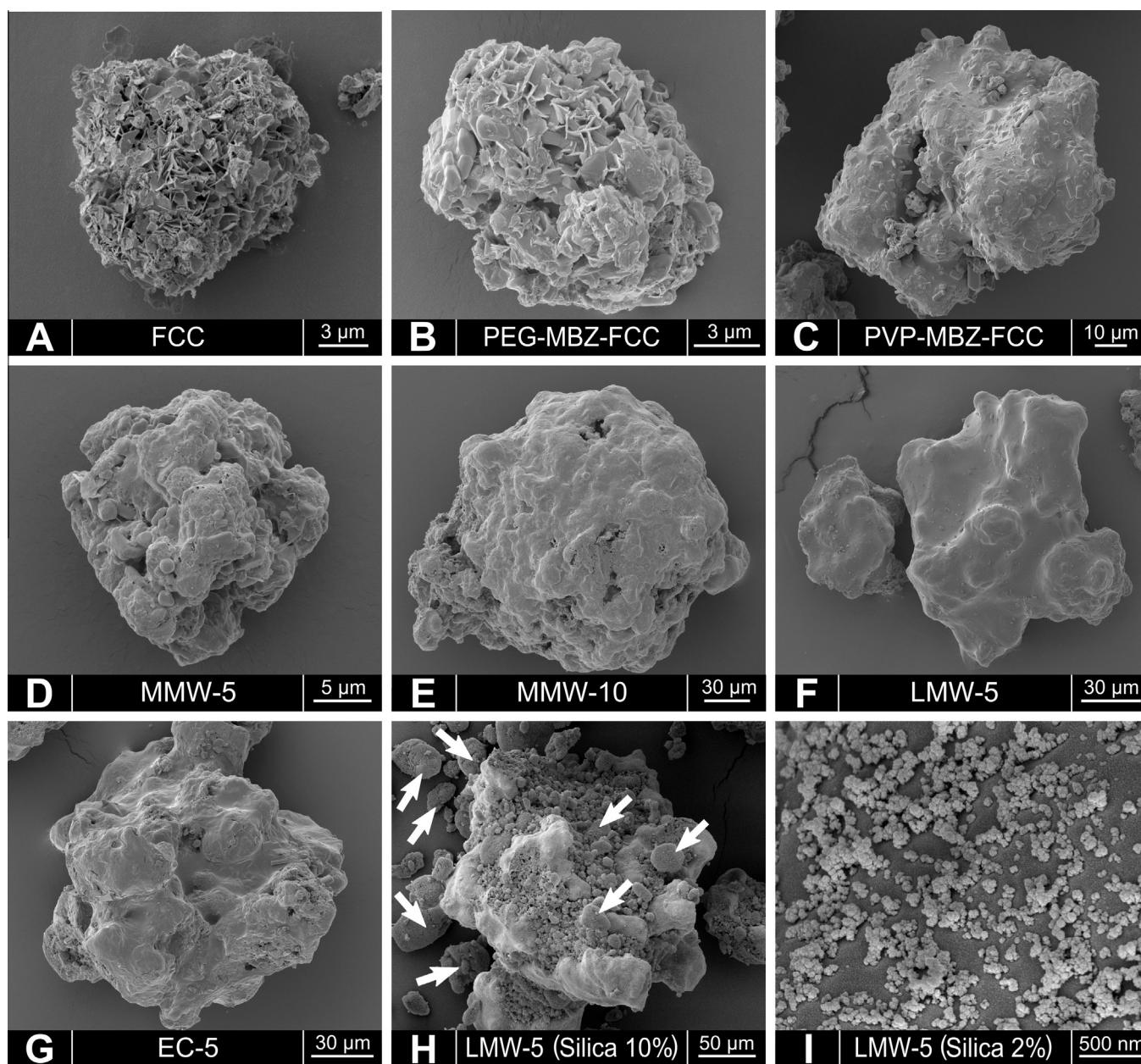


**Fig. 5.** Representative SEM images of bulk FCC (A), microparticles prepared in the fluidized bed (B,C), and LMW-5 particles dry-coated with fumed silica (H and I). (H) was dry-coated with 10% silica (w/w) and white arrows indicate silica agglomerates. (I) is a close-up view of a LMW-5 surface homogeneously coated with silica (2%, w/w).

content, showed a wider size distribution (Fig. 6B) and a higher median diameter ( $48.48 \pm 2.83 \mu\text{m}$ ) as expected.

Coating of the drug-loaded microparticles with chitosan led to a further increase in median particle size as shown in Table 3. By increasing the content of MMW chitosan from 5% to 10% (w/w), particles sizes increased approximately by a factor of 3 ( $54.40 \pm 2.01 \mu\text{m}$  vs.  $183.48 \pm 9.98 \mu\text{m}$ ). The median particle size of EC-5 particles was in between  $115.23 \pm 3.51 \mu\text{m}$ , which was important for the use as a control formulation.

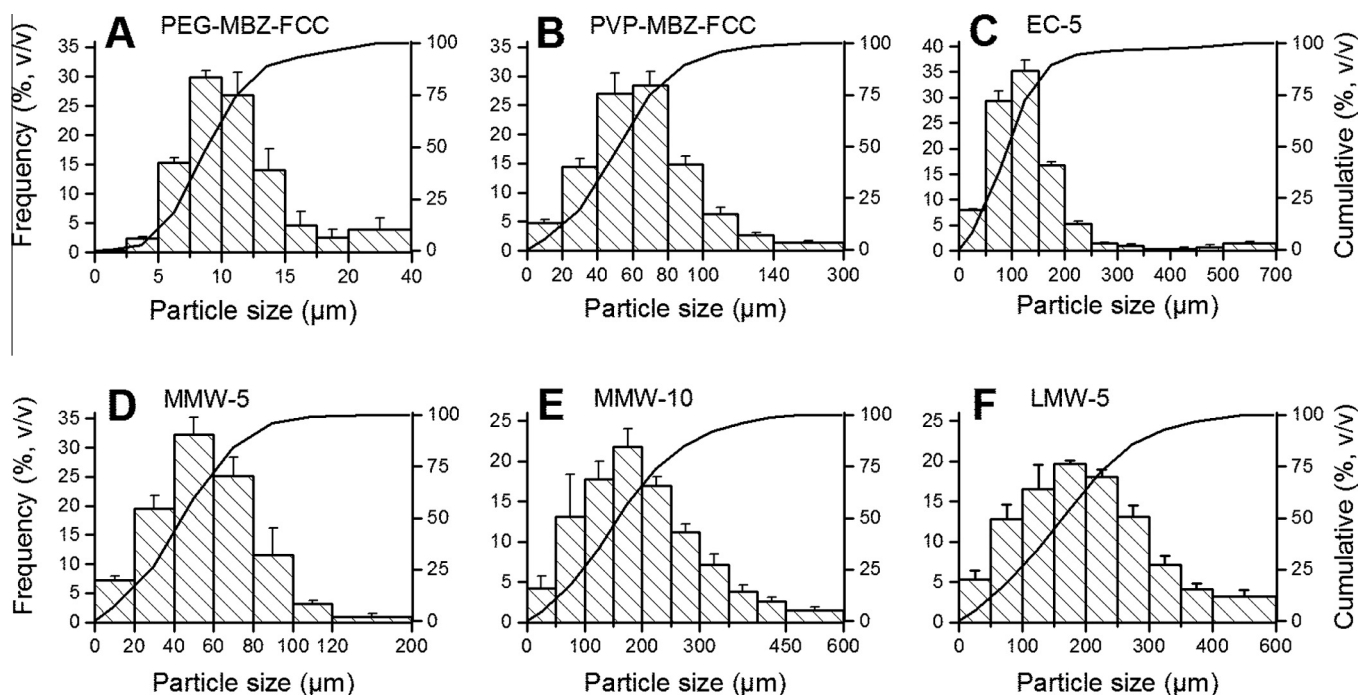
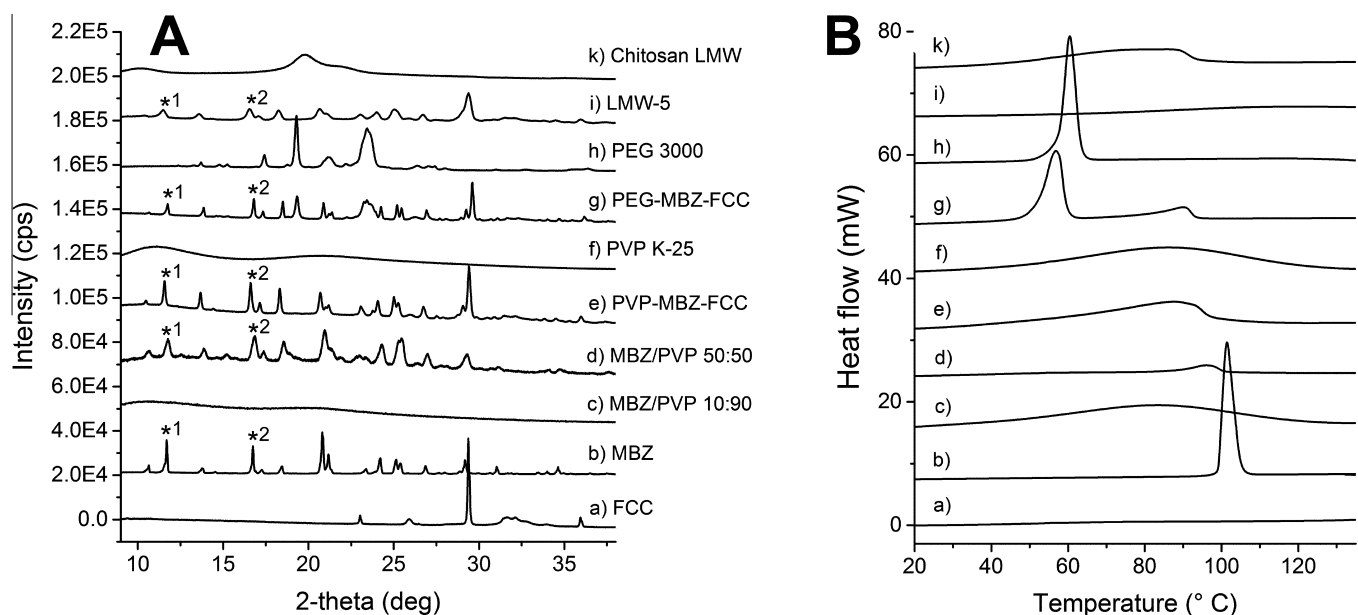
### 3.6. X-ray powder diffractometry XRPD

For the X-ray diffraction pattern of crystalline MBZ, we identified 2 characteristic peaks at  $12.11^\circ$  and  $17.27^\circ$  ( $2\theta$ ) which do not interfere with FCC and PEG. The characteristic peaks are labelled in Fig. 7B with \*1 and \*2, respectively, and were also detected in

samples of PEG-MBZ-FCC and PVP-MBZ-FCC. This clearly demonstrated that the major fraction of the drug was still in the crystalline state. As a reference for XRD sensitivity, mixtures of FCC and crystalline drug in low concentrations were prepared. Mixtures of 1% (w/w), 0.5% (w/w), and 0.1% (w/w) of MBZ in FCC were analysed (data not shown). It was possible to detect crystalline MBZ at the 1% concentration but no signal was detected at 0.5% concentration of drug. The characteristic peaks are labelled in Fig. 7B with \*1 and \*2, respectively, and were also detected in samples of PEG-MBZ-FCC and PVP-MBZ-FCC. In view of the high sensitivity and selectivity of the used method, we can assume that the major fraction of the drug was still in the crystalline state. The co-evaporate of MBZ and PVP in a ratio of 10:90 (w/w) led to stabilization of the amorphous form of MBZ as confirmed by the diffraction pattern without any peaks detected.

**Table 3**Experimental drug loads (% w/w,  $n = 3$ ), process yields (% w/w), and mean particle size (D50) of different batches prepared in the fluidized bed.

	Theoretical drug load (% w/w)	Experimental drug load (% w/w, $n = 3$ )	Process yield (% w/w)	Median particle size D50 ( $\mu\text{m}$ , $n = 5$ )
Bulk FCC	–	–	–	$7.77 \pm 0.06$
PEG-MBZ-FCC	28.57	$28.92 \pm 2.91$	98.4	$10.10 \pm 0.07$
PVP-MBZ-FCC	37.50	$38.19 \pm 0.24$	96.5	$48.48 \pm 2.83$
EC-5	32.39	$34.31 \pm 0.13$	97.5	$115.23 \pm 3.51$
MMW-5	27.14	$25.25 \pm 0.36$	98.2	$54.40 \pm 2.01$
MMW-10	25.71	$23.29 \pm 0.08$	102.0	$183.48 \pm 9.98$
LMW-5	35.63	$35.88 \pm 0.20$	101.1	$190.88 \pm 10.96$

**Fig. 6.** Particle size distributions (largest Feret diameter) of prepared particles measured by dynamic image analysis. The bar plots indicate the frequency by volume for the measured size ranges (% v/v, left y-axis), and the curve plots are the cumulative volume percentages (% v/v, right y-axis). Error bars represent SD ( $n = 5$ ).**Fig. 7.** Results of XRPD (A) and DSC analysis (B) of (a) FCC; (b) crystalline MBZ; (c) co-evaporate of MBZ and PVP (10:90, w/w) with all drugs in amorphous state; (d) co-evaporate of MBZ and PVP (50:50, w/w) with drug in crystalline state; (e) PVP-MBZ-FCC; (f) PVP K-25; (g) PEG-MBZ-FCC; and (h) PEG 3000. XRPD peaks labelled with \*1 and \*2 are characteristic for crystalline MBZ.

### 3.7. Differential scanning calorimetry (DSC)

Representative plots of DSC analysis are shown in Fig. 7A. For the crystalline MBZ, a sharp endothermic peak was observed at  $101.5 \pm 0.1$  °C with a melting enthalpy of  $93.0 \pm 0.9$  J/g. For the PEG-MBZ-FCC particles with a drug load of 28.57% (w/w), a first peak was detected close to 60 °C, which is in line with the endothermic peak from PEG alone. Therefore, the second peak at  $90.3 \pm 0.3$  with a melting enthalpy of  $13.10 \pm 0.8$  J/g corresponds to MBZ, even though the peak onset was shifted to lower temperatures. The melting enthalpy lower than the expected value for 28.57% of crystalline MBZ (26.6 J/g), and the peak onset shifted to lower temperatures were already observed previously in drug-loaded FCC samples [37]. It is also likely that MBZ has partially dissolved in liquid PEG resulting in an apparently reduced melting enthalpy. In case of PVP-MBZ-FCC particles, determination of melting enthalpy of MBZ was not possible due to the strongly interfering heat-flow curve of amorphous PVP.

## 4. Discussions

In this study, we present for the first time data on particle retention of chitosan-coated microparticles prepared in a fluidized-bed process. MMW-10 particles showed a 3-fold increase in particle retention compared to MMW-5 (see Fig. 2A). The LMW-5 particles also showed good *in vitro* particle retention ( $55.35\% \pm 5.94\%$ ) in comparison with non-mucoadhesive EC-5 particles. The use of LMW chitosan with lower concentration in the spray solution had a big advantage compared to MMW chitosan in terms of manufacturability, since the shorter chain length of chitosan and the lower concentration in the spray solution (1% vs. 1.5%) decreased the viscosity which was important to reduce the risk of nozzle blocking. Further optimizations of the LMW-5 formulation led to a higher drug load (see Table 1), i.e. higher dose, and a reduced process time due to increased spray rate of the chitosan coating solution (see Table 2).

Dissolution studies were performed using the USP IV apparatus since the resulting drug-release profiles were found to be similar to the results measured in the flow channel [26]. However, mucoadhesive microparticles tested in the USP IV apparatus have shown a strong agglomeration tendency, potentially affecting particle retention. To overcome this issue, we investigated the dispersibility-enhancing effect of dry-particle coating with nano-sized colloidal silica. A silica concentration in the range of 0.10.5% (w/w) is often used as a lubricant or glidant in tablets, and higher concentrations of 24% (w/w) were reported to act as a disintegrant [38]. In our study, we used relatively high silica concentrations (110%, w/w) to achieve the desired disintegration properties. From a toxicological point of view, it was reported that oral intake of colloidal silica up to 1500 mg/day is of no safety concern [39]. The simple blending and sieving process led to homogeneous silica monolayers adsorbed to the chitosan surfaces as shown in a typical example of an SEM image with high magnification (see Fig. 5I). However, the main fraction of silica was agglomerated and not adsorbed as shown by the arrows in Fig. 5H. These silica agglomerates were considered to be the main mechanism of improved dispersibility. Measuring drug dissolution in the USP IV apparatus presented a feasible method for indirect quantitative measurement of dispersibility. According to Noyes-Whitney and Nernst-Brunner equation (Eq. (4)), the surface area at the interface of the dissolution medium ( $A$ ), and the thickness of the diffusion layer to the interface of the dissolution medium ( $d$ ) are the two factors which influence the dissolution rate ( $dm/dt$ ) when agglomerates are formed.

$$\frac{dm}{dt} = A \frac{D}{d} (C_s - C_b) \quad (4)$$

where  $D$  is the diffusion coefficient,  $C_s$  is the drug solubility, and  $C_b$  is the drug concentration in the bulk medium [40]. Dispersibility enhancement means smaller agglomerates and more individual particles, i.e. a larger surface area and a shorter thickness of the diffusion layer, both of which increase the dissolution rate. This hypothesis was confirmed by the experimental data shown in Fig. 3B, where the dissolution rate and drug release after 10 h were increased with higher silica concentrations. All silica-coated mucoadhesive formulations showed a controlled release over several hours, which is desired for local treatment of colonic diseases directly at the site of action for prolonged period of time.

The mucoadhesion of LMW-5 particles coated with 2% and 5% (w/w) silica was marginally improved in comparison with non-coated LMW-5 particles, however, without significant difference ( $p > 0.1$ ). This is explained by the hydrophilic nature of the silica nanoparticles which allows them to diffuse into the hydrated chitosan coating and mucin meshwork, and interpenetration of the chitosan polymer chains into the mucin meshwork is not hindered. This assumption has to be further investigated with cryo-SEM or cryo-TEM imaging techniques to confirm an entanglement of the polymer and mucin chains. Contrarily, coating with 10% (w/w) silica decreased the mucoadhesivity significantly ( $p < 0.005$ ) as shown in Fig. 2C, probably due to an oversaturation with silica agglomerates, preventing a close contact of the chitosan polymer chains with the mucus. Thus, silica nanoparticles used as a dispersant aid may reduce drug-mucosa contact, thus affecting mucoadhesivity.

In addition to the chitosan coating, the fluidized-bed process was also shown to be feasible for drug loading of porous microcarriers with particle sizes from 5 to 12 µm and outer-pore sizes of approximately 0.1–1 µm. Qualitative SEM analysis confirmed that the outer pores were filled as shown in Fig. 5A–C. Since the fluidized-bed method is well suited for scale-up, it is preferable to the previously reported solvent-evaporation method [37]. Drug dissolution rates of PVP-MBZ-FCC and PEG-MBZ-FCC particles were much higher than those of pure MBZ powder as shown in Fig. 3. This increased dissolution rate was associated with the enlarged surface area of the inert microcarrier (FCC) as demonstrated recently [37], and probably also due to the solubility-enhancing effect given by the polymers. In both drug-loaded batches, MBZ was present in a crystalline state as demonstrated by XRPD and DSC analysis (see Fig. 7A and B), which could be an indicator for long shelf-life of the drug product [32]. It was not possible to distinguish between different crystal polymorphs based on registered diffraction patterns. However, a distinction between the amorphous and the crystalline state was possible. In case of PVP-MBZ-FCC particles, analysis of SEM images made it possible to identify drug crystals embedded in the polymer matrix. XRPD analysis of the co-evaporates with a drug-to-polymer ratio of 50:50 (w/w) showed that MBZ was not in an amorphous phase, hence, cannot contribute to increased dissolution rates. As a reference for solid dispersions, co-evaporation of PVP and MBZ in a high ratio of 90:10 (w/w) was performed, resulting in a glassy material. The absence of characteristic peaks in the X-ray diffraction pattern indicated that MBZ was present in amorphous form. This indicates a usability of the fluidized-bed process for preparation of mucoadhesive microparticles containing the drug as a solid dispersion. However, a higher drug-to-polymer ratio is required, which is decreasing the drug load, and potentially leading to drug stability issues [32].



## 5. Conclusions

The fluidized-bed process is a suitable method for preparation of mucoadhesive microparticles by applying a two-step method, i.e. drug loading and chitosan coating. The optimized LMW-5 particles showed good manufacturability, high drug load, and a good *in vitro* particle retention on porcine colonic mucosa. Dry coating of the chitosan-coated microparticles with hydrophilic fumed silica improved the dispersibility as indicated by visual observation and dissolution studies. Moreover, mucoadhesion was not negatively influenced by colloidal silica particles up to 5% (w/w) concentration. Since the formulation approach described here is applicable to other drugs, the results of this study present a basis for further development and optimization of mucoadhesive dosage forms for local treatment of gastrointestinal diseases.

## Acknowledgements

This project was financially supported by the Swiss Commission of Technology and Innovation (grant number: 13742.1 PFLR-LS) and Tillotts Pharma AG. The authors thank Dr. Markus Dürrenberger at the microscopy centre (University of Basel) for the assistance in using the SEM, Mrs. Evelyne Mühle from Centravo AG for providing fresh samples of porcine colonic tissue, Dr. Gabriela Québatte for her support with XRPD analysis, and Darryl Borland for editorial assistance.

## References

- [1] G.P. Andrews, T.P. Lavery, D.S. Jones, Mucoadhesive polymeric platforms for controlled drug delivery, *Eur. J. Pharm. Biopharm.* 71 (2009) 505–518, <http://dx.doi.org/10.1016/j.ejpb.2008.09.028>.
- [2] V. Hearnden, V. Sankar, K. Hull, D.V. Juras, M. Greenberg, A.R. Kerr, et al., New developments and opportunities in oral mucosal drug delivery for local and systemic disease, *Adv. Drug Deliv. Rev.* 64 (2012) 16–28, <http://dx.doi.org/10.1016/j.addr.2011.02.008>.
- [3] J.F. Pinto, Site-specific drug delivery systems within the gastro-intestinal tract: from the mouth to the colon, *Int. J. Pharm.* 395 (2010) 44–52, <http://dx.doi.org/10.1016/j.ijpharm.2010.05.003>.
- [4] G. Van den Mooter, Colon drug delivery, *Expert Opin. Drug Deliv.* 3 (2005) 111–125, <http://dx.doi.org/10.1517/17425247.3.1.111>.
- [5] A.K. Philip, B. Philip, Colon targeted drug delivery systems: a review on primary and novel approaches, *Oman Med. J.* 25 (2010) 79–87, <http://dx.doi.org/10.5001/omj.2010.24>.
- [6] E.F. Stange, S.P.L. Travis, The European consensus on ulcerative colitis: new horizons?, *Gut* 57 (2008) 1029–1031, <http://dx.doi.org/10.1136/gut.2007.146761>.
- [7] C. Schiller, C.-P. Fröhlich, T. Giessmann, W. Siegmund, H. Mönnikes, N. Hosten, et al., Intestinal fluid volumes and transit of dosage forms as assessed by magnetic resonance imaging, *Aliment. Pharmacol. Ther.* 22 (2005) 971–979, <http://dx.doi.org/10.1111/j.1365-2036.2005.02683.x>.
- [8] F.J.O. Varum, E.L. McConnell, J.J.S. Sousa, F. Veiga, A.W. Basit, Mucoadhesion and the gastrointestinal tract, *Crit. Rev. Ther. Drug Carrier Syst.* 25 (2008) 207–258.
- [9] M.E.A. McGirr, S.M. McAllister, E.E. Peters, A.W. Vickers, A.F. Parr, A.W. Basit, The use of the IntelliSite® Companion device to deliver mucoadhesive polymers to the dog colon, *Eur. J. Pharm. Sci.* 36 (2009) 386–391, <http://dx.doi.org/10.1016/j.ejps.2008.11.007>.
- [10] B. Abrahamsson, M. Alpstén, U.E. Jonsson, P.J. Lundberg, A. Sandberg, M. Sundgren, et al., Gastro-intestinal transit of a multiple-unit formulation (metoprolol CR/ZOK) and a non-disintegrating tablet with the emphasis on colon, *Int. J. Pharm.* 140 (1996) 229–235, [http://dx.doi.org/10.1016/0378-5173\(96\)04604-2](http://dx.doi.org/10.1016/0378-5173(96)04604-2).
- [11] F.J.O. Varum, H.A. Merchant, A.W. Basit, Oral modified-release formulations in motion: the relationship between gastrointestinal transit and drug absorption, *Int. J. Pharm.* 395 (2010) 26–36, <http://dx.doi.org/10.1016/j.ijpharm.2010.04.046>.
- [12] H. Takeuchi, H. Yamamoto, Y. Kawashima, Mucoadhesive nanoparticulate systems for peptide drug delivery, *Adv. Drug Deliv. Rev.* 47 (2001) 39–54, [http://dx.doi.org/10.1016/S0169-409X\(00\)00120-4](http://dx.doi.org/10.1016/S0169-409X(00)00120-4).
- [13] S. Sakuma, R. Sudo, N. Suzuki, H. Kikuchi, M. Akashi, Y. Ishida, et al., Behavior of mucoadhesive nanoparticles having hydrophilic polymeric chains in the intestine, *J. Control. Release* 81 (2002) 281–290, [http://dx.doi.org/10.1016/S0168-3659\(02\)00072-X](http://dx.doi.org/10.1016/S0168-3659(02)00072-X).
- [14] A. Sosnik, J. das Neves, B. Sarmento, Mucoadhesive polymers in the design of nano-drug delivery systems for administration by non-parenteral routes: a review, *Prog. Polym. Sci.* 39 (2014) 2030–2075, <http://dx.doi.org/10.1016/j.progpolymsci.2014.07.010>.
- [15] A. De Ascentiis, J.L. deGrazia, C.N. Bowman, P. Colombo, N.A. Peppas, Mucoadhesion of poly(2-hydroxyethyl methacrylate) is improved when linear poly(ethylene oxide) chains are added to the polymer network, *J. Control. Release* 33 (1995) 197–201, [http://dx.doi.org/10.1016/0168-3659\(94\)00087-B](http://dx.doi.org/10.1016/0168-3659(94)00087-B).
- [16] K.P.R. Chowdary, Y.S. Rao, Mucoadhesive microspheres for controlled drug delivery, *Biol. Pharm. Bull.* 27 (2004) 1717–1724.
- [17] J. Möschwitzer, R.H. Müller, Spray coated pellets as carrier system for mucoadhesive drug nanocrystals, *Eur. J. Pharm. Biopharm.* 62 (2006) 282–287, <http://dx.doi.org/10.1016/j.ejpb.2005.09.005>.
- [18] T. Pengpong, P. Sangvanich, K. Sirilertmukul, N. Muangsin, Design, synthesis and *in vitro* evaluation of mucoadhesive p-coumarate-thiolated-chitosan as a hydrophobic drug carriers, *Eur. J. Pharm. Biopharm.* 86 (2014) 487–497, <http://dx.doi.org/10.1016/j.ejpb.2013.11.009>.
- [19] F.J.O. Varum, F. Veiga, J.S. Sousa, A.W. Basit, Mucoadhesive platforms for targeted delivery to the colon, *Int. J. Pharm.* 420 (2011) 11–19, <http://dx.doi.org/10.1016/j.ijpharm.2011.08.006>.
- [20] Q.-R. Cao, Y. Liu, W.-J. Xu, B.-J. Lee, M. Yang, J.-H. Cui, Enhanced oral bioavailability of novel mucoadhesive pellets containing valsartan prepared by a dry powder-coating technique, *Int. J. Pharm.* 434 (2012) 325–333, <http://dx.doi.org/10.1016/j.ijpharm.2012.05.076>.
- [21] C. Schmidt, C. Lautenschlaeger, E.-M. Collnot, M. Schumann, C. Bojarski, J.-D. Schulzke, et al., Nano- and microscaled particles for drug targeting to inflamed intestinal mucosa—a first *in vivo* study in human patients, *J. Control. Release* 165 (2013) 139–145, <http://dx.doi.org/10.1016/j.jconrel.2012.10.019>.
- [22] P. He, S.S. Davis, L. Illum, *In vitro* evaluation of the mucoadhesive properties of chitosan microspheres, *Int. J. Pharm.* 166 (1998) 75–88, [http://dx.doi.org/10.1016/S0378-5173\(98\)00027-1](http://dx.doi.org/10.1016/S0378-5173(98)00027-1).
- [23] V.S. Belgamwar, S.J. Surana, Design and development of oral mucoadhesive multiparticulate system containing atenolol: *in vitro-in vivo* characterization, *Chem. Pharm. Bull. (Tokyo)* 58 (2010) 1168–1175.
- [24] Z. Liu, W. Lu, L. Qian, X. Zhang, P. Zeng, J. Pan, *In vitro* and *in vivo* studies on mucoadhesive microspheres of amoxicillin, *J. Control. Release* 102 (2005) 135–144, <http://dx.doi.org/10.1016/j.jconrel.2004.06.022>.
- [25] J.K. Patel, P.S. Patil, V.B. Sutariya, Formulation and characterization of mucoadhesive microparticles of cinnarizine hydrochloride using supercritical fluid technique, *Curr. Drug Deliv.* 10 (2013) 317–325.
- [26] D. Preisig, M. Weingartner, F.J.O. Varum, R. Bravo, R. Alles, J. Huwyler, et al., Marker-ion analysis for quantification of mucoadhesivity of microparticles in particle-retention assays, *Int. J. Pharm.* 487 (2015) 157–166, <http://dx.doi.org/10.1016/j.ijpharm.2015.04.020>.
- [27] D.B. Beten, K. Amighi, A.J. Moës, Preparation of controlled-release coevaporates of dipyrindamole by loading neutral pellets in a fluidized-bed coating system, *Pharm. Res.* 12 (1995) 1269–1272.
- [28] S. Muschert, F. Siepmann, B. Leclercq, B. Carlin, J. Siepmann, Drug release mechanisms from ethylcellulose: PVA-PEG graft copolymer-coated pellets, *Eur. J. Pharm. Biopharm.* 72 (2009) 130–137, <http://dx.doi.org/10.1016/j.ejpb.2008.12.007>.
- [29] T. Linnell, H.A. Santos, E. Mäkilä, T. Heikkilä, J. Salonen, D.Y. Murzin, et al., Drug delivery formulations of ordered and nonordered mesoporous silica: comparison of three drug loading methods, *J. Pharm. Sci.* 100 (2011) 3294–3306, <http://dx.doi.org/10.1002/jps.22577>.
- [30] H.-O. Ho, H.-L. Su, T. Tsai, M.-T. Sheu, The preparation and characterization of solid dispersions on pellets using a fluidized-bed system, *Int. J. Pharm.* 139 (1996) 223–229, [http://dx.doi.org/10.1016/0378-5173\(96\)04594-2](http://dx.doi.org/10.1016/0378-5173(96)04594-2).
- [31] N. Sun, X. Zhang, Y. Lu, W. Wu, *In vitro* evaluation and pharmacokinetics in dogs of solid dispersion pellets containing *Silybum marianum* extract prepared by fluid-bed coating, *Planta Med.* 74 (2008) 126–132, <http://dx.doi.org/10.1055/s-2008-1034294>.
- [32] C. Leuner, J. Dressman, Improving drug solubility for oral delivery using solid dispersions, *Eur. J. Pharm. Biopharm.* 50 (2000) 47–60, [http://dx.doi.org/10.1016/S0939-6411\(00\)00076-X](http://dx.doi.org/10.1016/S0939-6411(00)00076-X).
- [33] Sigma-Aldrich specification sheet of medium molecular weight chitosan, <[http://www.sigmaaldrich.com/Graphics/COFAInfo/SigmaSAPQM/SPEC/44/448877/448877-BULK\\_\\_\\_\\_ALDRICH\\_.pdf](http://www.sigmaaldrich.com/Graphics/COFAInfo/SigmaSAPQM/SPEC/44/448877/448877-BULK____ALDRICH_.pdf)>, 2015.
- [34] Sigma-Aldrich specification sheet of medium molecular weight chitosan, <[http://www.sigmaaldrich.com/Graphics/COFAInfo/SigmaSAPQM/SPEC/44/448877/448877-BULK\\_\\_\\_\\_ALDRICH\\_.pdf](http://www.sigmaaldrich.com/Graphics/COFAInfo/SigmaSAPQM/SPEC/44/448877/448877-BULK____ALDRICH_.pdf)>, 2015.
- [35] F.J.O. Varum, F. Veiga, J.S. Sousa, A.W. Basit, An investigation into the role of mucus thickness on mucoadhesion in the gastrointestinal tract of pig, *Eur. J. Pharm. Sci.* 40 (2010) 335–341, <http://dx.doi.org/10.1016/j.ejps.2010.04.007>.
- [36] Cation Analysis Kit <<http://www.absciex.com/Documents/Products/CationAnalysisUsersGuide.pdf>> 2013 (accessed November 1, 2014).
- [37] D. Preisig, D. Haid, F.J.O. Varum, R. Bravo, R. Alles, J. Huwyler, et al., Drug loading into porous calcium carbonate microparticles by solvent evaporation, *Eur. J. Pharm. Biopharm.* 87 (2014) 548–558, <http://dx.doi.org/10.1016/j.ejpb.2014.02.009>.
- [38] C. Hunnius, Hunnius Pharmazeutisches Wörterbuch, De Gruyter, 1998.
- [39] U. Charrondiere, D. Gott, Calcium silicate and silicon dioxide/silicic acid gel added for nutritional purposes to food supplements, *EFSA ANS* 1132 (2009) 1–24, <http://dx.doi.org/10.2903/j.efsa.2009.1132>.
- [40] P. Macheras, A. Iliadis, Modeling in Biopharmaceutics, Pharmacokinetics and Pharmacodynamics: Homogeneous and Heterogeneous Approaches, Springer Science & Business Media, 2006.

### **3.3 Loading of porous functionalized calcium carbonate microparticles: Distribution analysis with focused ion beam electron microscopy and mercury porosimetry**

Maryam Farzan <sup>1,†</sup>, Roger Roth <sup>1,†</sup>, Gabriela Québatte<sup>1</sup>, Joachim Schoelkopf<sup>2</sup>, Jörg Huwyler<sup>1</sup> and Maxim Puchkov <sup>1,\*</sup>

<sup>1</sup> Division of Pharmaceutical Technology, Department of Pharmaceutical Sciences, University of Basel, Switzerland

<sup>2</sup> Fundamental research, Omya International AG, Oftringen, Switzerland

**Pharmaceutics** 11(2019)32


#### **Personal contribution**

My contribution to this research article includes partial design of the study and the experimental setup. I prepared all BSA loadings and performed MIP analysis. I was involved in the imaging analysis, data processing and evaluation with the help of Maryam Farzan. I wrote the manuscript together with Maryam Farzan and the help of Gabriela Québatte, Joachim Schoelkopf, Jörg Huwyler and. Maxim Puchkov.



## Article

# Loading of Porous Functionalized Calcium Carbonate Microparticles: Distribution Analysis with Focused Ion Beam Electron Microscopy and Mercury Porosimetry

Maryam Farzan <sup>1,†</sup>, Roger Roth <sup>1,†</sup>, Gabriela Québatte <sup>1</sup>, Joachim Schoelkopf <sup>2</sup>,  
Jörg Huwyler <sup>1</sup> and Maxim Puchkov <sup>1,\*</sup>

<sup>1</sup> Division of Pharmaceutical Technology, Department of Pharmaceutical Sciences, University of Basel, Klingelbergstrasse 50, 4056 Basel, Switzerland; maryam.farzan@unibas.ch (M.F.); roger.roth@unibas.ch (R.R.); gabriela.quebatte@unibas.ch (G.Q.); joerg.huwyler@unibas.ch (J.H.)

<sup>2</sup> Fundamental research, Omya International AG, 4665 Oftringen, Switzerland; joachim.schoelkopf@omya.com

\* Correspondence: maxim.puchkov@unibas.ch; Tel.: +41-61-207-1619

† These authors contributed equally to this work.

Received: 30 October 2018; Accepted: 10 January 2019; Published: 15 January 2019



**Abstract:** Accurate analysis of intraparticle distribution of substances within porous drug carriers is important to optimize loading and subsequent processing. Mercury intrusion porosimetry, a common technique used for characterization of porous materials, assumes cylindrical pore geometry, which may lead to misinterpretation. Therefore, imaging techniques such as focused ion beam scanning electron microscopy (FIB-SEM) help to better interpret these results. The purpose of this study was to investigate the differences between mercury intrusion and scanning electron microscopy and to identify the limitations of each method. Porous microparticles, functionalized calcium carbonate, were loaded with bovine serum albumin and dipalmitoylphosphatidylcholine (DPPC) by solvent evaporation and results of the pore size distribution obtained by both methods were compared. The internal structure of the novel pharmaceutical excipient, functionalized calcium carbonate, was revealed for the first time. Our results demonstrated that image analysis provides a closer representation of the material distribution since it was possible to discriminate between blocked and filled pores. The physical nature of the loaded substances is critical for the deposition within the pores of functionalized calcium carbonate. We conclude, that a combination of mercury intrusion porosimetry and focused ion beam scanning electron microscopy allows for a reliable analysis of sub-micron porous structures of particulate drug carriers.

**Keywords:** porous drug carrier; functionalized calcium carbonate; drug loading; focused ion beam scanning electron microscopy; mercury intrusion porosimetry; dipalmitoylphosphatidylcholine; bovine serum albumin

## 1. Introduction

Porous microparticles are promising carriers for the delivery of a wide variety of substances. In particular, loading drugs into the porous structure of microparticles may increase the dissolution rate and the solubility of poorly soluble active pharmaceutical ingredients (API). This is achieved on one hand by enlarging the surface area, which is exposed to a dissolution medium, and on the other hand by increasing the internal energy of an API due to amorphization, because initial crystallization is inhibited by the restricted space inside the pore [1]. Microparticles can be used to deliver drugs to the site of action, for either systemic uptake or local treatment. Close contact between the microparticle and the

site of action can be achieved by mucoadhesion and additionally, drug release can be modulated [2–4]. In contrast to nanoparticles, microparticles can be used for the production of solid dosage forms [5,6]. Orally administered microparticles are not absorbed into systemic circulation due to their size. Enteral administration of chemically inert and biodegradable drug carriers (such as, for example, calcium carbonate) is therefore considered to be safe [7,8].

A variety of different inorganic carriers have been explored for use in drug delivery. One of the most extensively used material in this field is calcium phosphate [9]. Other materials include titanium dioxide [10], alumina silicate [11], calcium carbonate [12], and silicon dioxide [13]. Porous calcium phosphate carriers in the form of scaffolds have been explored for local delivery of drugs and biologics to different tissues, e.g., bone tissue [14,15]. Porosity of such carriers directly influences the maximal achievable drug load (DL) [14,16].

Methods to load porous carriers with drugs include adsorption (e.g., fluidized bed processing), soaking, and solvent evaporation methods [2,17,18]. However, these methods often lead to deposition of substances on the surface of the carrier. This may lead to subsequent challenges in the manufacturing process due to modified surface properties. This includes altered flowability, compactability, and changes in the properties of the final product like delayed or retarded disintegration [19]. It would therefore be beneficial to load internal porous structures instead of surface deposition of drugs. This approach has additional advantages. Pore loading leads to taste masking and enhanced protection of sensitive substances against mechanical and oxidative stress. For example, shear stress was reported to induce loss of activity in enzymes and other protein-based drugs [20,21]. After loading, microparticles can be coated to provide an additional protection for sensitive cargo against enzymatic or microbial degradation and the harsh conditions within the gastrointestinal tract.

Drugs can be integrated into a particle during its synthesis, which has the advantage of a single step operation, but also brings a lot of variability into the final structure [22]. However, a more convenient strategy is to load substances into prefabricated inert carrier particles, which can be manufactured under controlled conditions and later can be combined with a variety of substances. However, due to the limited drug loading capacity of these structures, complete pore filling is important. In any case, sensitive analytical methods are needed to optimize loading protocols and to exploit the full capacity of porous structures. One of the problems for quantification of drug load is to distinguish between the fraction of intraparticle and extraparticle drug deposition. There are combinations of methods suggested, including thermal analysis, atomic force microscopy (AFM), sorption methods (i.e., BET), helium pycnometry, flow imaging microscopy,  $\mu$ CT etc. The BET sorption method is commonly used for characterization of porous structure and drug load. However, if the drug deposition on the surface leads to a blockage of pores, sorption methods will give an overestimation of drug load. In addition, if the deposited drug forms fractal surfaces on pore walls, overstated high specific surface areas will be registered [1]. Helium pycnometry could give more realistic results but has its own drawbacks such as helium entrapment inside pores [23]. Differential scanning calorimetry (DSC) has been used with the assumption that the drug in the pores does not melt or melts at lower temperature than the fraction of drug on the surface, due to smaller crystal size [24].

During the last few years, our group has investigated the properties of so-called functionalized calcium carbonate (FCC), which was recently introduced as a pharmaceutical excipient. It is a co-precipitate from calcium carbonate and calcium phosphate which are, depending on the type, mixed at different ratios ranging from 13 to 85% (*w/w*) calcium phosphate content and a porosity of approximately 60% (*v/v*) [25]. Exploring this new excipient led to several innovative drug delivery devices such as orally disintegrating or floating tablets [26–28], mucoadhesive delivery systems for colon targeting [2], delivery of proteins, and loading of various small molecule drugs [17,18]. For the mentioned applications [2,17,18,26–29], we have identified a major problem with drug loading into deep porous regions of investigated microparticles as well as the understanding of the internal structure. Markl et al. used a combination of terahertz pulse imaging,  $\mu$ CT, MIP and pycnometry together with an experimental setting for water sorption of FCC compacts. They interpreted the results



as anisotropic pores that are perpendicular to the compaction direction of a tablet [30,31]. However, so far, no convincing data has been available which reveals the internal structure of single FCC particles.

Therefore, this particular research aims to propose a method for most effective characterization of drug loading efficiency into porous materials composed of coprecipitated inorganic salts of calcium such as hydroxyapatite and calcium carbonate. The present study combines two analytical methods (i.e., mercury intrusion porosimetry (MIP) and focused ion beam scanning electron microscopy (FIB-SEM) to study the material distribution within the porous structure of FCC. Bovine serum albumin was used as a hydrophilic, high molecular weight compound. Dipalmitoylphosphatidylcholine (DPPC) was its small molecular weight and lipophilic counterpart. Compounds were loaded by solvent evaporation [17]. Although MIP (Figure 1b) is the most common technique for porosity analysis, there are some limitations, which should be considered when interpreting its results [32]. First, assuming a cylindrical pore shape leads to a wrong interpretation, since this technique measures only the largest pore opening (throat) and not the actual inner diameter of a cavity (body). Therefore, it is not possible to discriminate whether a volume attributed to a certain diameter corresponds to several small pores or one large pore with the same throat diameter. Second, MIP cannot measure inaccessible pores: a particle with blocked periphery pores shows the same internal volume and pore size distribution as a completely filled particle. Thus, MIP measures pore size distribution and skeleton density, but is not capable to distinguish between filled and blocked pores. MIP was therefore combined with FIB-SEM (Figure 1a) to visualize the true inner structure of FCC particles. In our experimental setup, a focused gallium ion beam was used to dissect FCC particles. The exposed inner surfaces were then visualized by SEM. It was thus possible to distinguish between blocked and filled porous structures. The results from FIB-SEM and MIP were combined to discuss the limitations and necessities of each method with respect to their capability to characterize drug loaded porous materials. Finally, previously unexplored porous structure of FCC was revealed and physical properties of the loading solutions, which affect the penetration into the porous particle were identified.

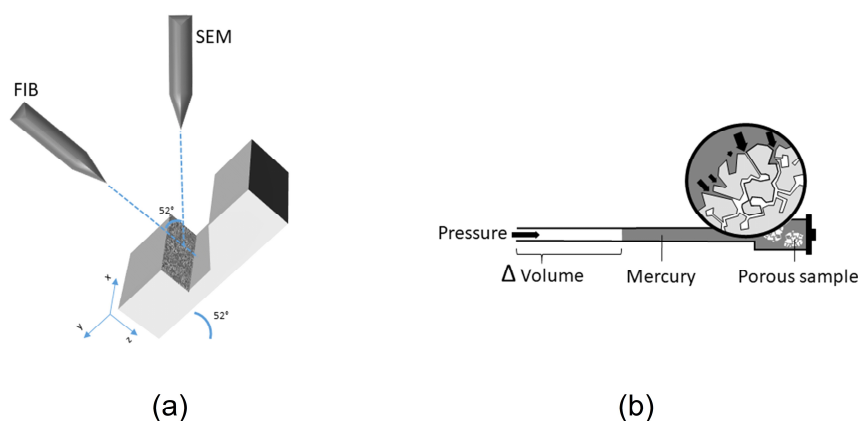


**Figure 1.** A schematic representation of focused ion beam scanning electron microscopy (FIB-SEM) and mercury intrusion porosimetry (MIP). (a) For FIB-SEM, a sample is tilted to be perpendicular to the ion (gallium) beam. The ion beam then mills a trench in the z direction of the sample, revealing a cross section, which is then imaged by the electron beam. (b) In an MIP setting, the pressure applied to the penetrometer pushes a non-wetting liquid (mercury) inside the pores of the sample. Pore size is calculated based on the pressure needed to force mercury into pores.

## 2. Materials and Methods

Omyapharm FCC (OG-500) was supplied by Omya International AG (Oftringen, Switzerland). Dipalmitoylphosphatidylcholine (DPPC) that has a phase transition temperature of 42 °C was kindly provided by Lipoid AG (Ludwigshafen, Germany). Bovine serum albumin (BSA) is commonly used as a standard reference protein in lab experiments. Heat shock fractionated BSA and Ph. Eur. grade methanol were purchased from Sigma Aldrich (St. Louis, MA, USA). Ultrapure water (<18.2 M $\Omega$ ·cm

resistivity) was obtained using a Milli-Q filtration station (Millipore, Billerica, MA, USA), calcium carbonate for density measurement was obtained from Lehmann and Voss and Co. (Hamburg, Germany). All substances were used as received without any further purification.

To calculate the intraparticle porosity  $P_I$  of the FCC, the particles were consolidated into a round, flat tablet with a diameter of 13 mm applying a pressure of 37 MPa. At this pressure, the interparticle voids were not present anymore. The density of the tablet  $\rho_T$  (kg/m<sup>3</sup>) was calculated using Equation (1):

$$\rho_T = \frac{m_T}{V_T}, \quad (1)$$

where  $m_T$  is the mass and  $V_T$  is the volume of the tablet.  $P_I$  can then be calculated using Equation (2):

$$P_I = 1 - \frac{\rho_T}{\rho_S}, \quad (2)$$

where  $\rho_S$  is the averaged (assuming 51:49 mass ratio [25]) skeletal density (2.95 kg/m<sup>3</sup>) of the two components hydroxyapatite and calcium carbonate, which are 3.16 [33], and 2.73 kg/m<sup>3</sup>, respectively [measured on a helium pycnometer (Accupyc 1330, Micromeritics, Norcross, GA, USA)].

The total intraparticle pore volume  $V_P$  (cm<sup>3</sup>) can be calculated using Equation (3):

$$V_P = V_T - V_S, \quad (3)$$

where  $V_S$  is the volume of the skeleton structure. The volume of the skeleton structure is defined by Equation (4):

$$V_S = \frac{m_T}{\rho_S}, \quad (4)$$

### 2.1. Loading

FCC particles were loaded with DPPC and BSA at different drug loads ( $DL$ ). The  $DL$  is described as the ratio between the loaded material and the total mass of the sample and was calculated by Equation (5):

$$DL = \frac{m_M}{m_M + m_{FCC}}, \quad (5)$$

where  $m_M$  is the mass of the loaded material (g) and  $m_{FCC}$  is the mass of FCC (g).

Low, medium and high loading formulations corresponding to 5% and 6.25%, 20% and 25%, and 30% and 37.5% ( $w/w$ ) theoretical  $DL$ s for BSA and DPPC, respectively, were prepared by a solvent evaporation method as follows: Required amounts (Equation (5)) of DPPC and BSA were dissolved in 20 mL of methanol and ultrapure water, respectively. Afterwards defined amounts of FCC was added and dispersed in a 250 mL round bottom flask to achieve the theoretical  $DL$  (Equation (5)). Solvents were evaporated in a rotary evaporator (Rotavap R-114, Büchi, Flawil, Switzerland) at 60 rpm. The temperature of the preheated water bath was 50 °C (product temperature was 39 °C) and 40 °C (product temperature was 36 °C) and initial pressure was 300 mbar and 100 mbar for DPPC and BSA, respectively. Pressures were gradually reduced to 20 mbar and held at this pressure for 1 h and 2 h for DPPC and BSA, respectively to completely remove residual solvents. The dry product was gently ground in a mortar and sieved through a 355 µm sieve. All formulations were produced in triplicate.

### 2.2. Content Measurement by Thermogravimetry

The content of BSA and DPPC in FCC was measured with a thermogravimetric method. Samples were heated from 35 to 950 °C in a thermogravimetric analyzer (TGA7SDTA 851e, Mettler Toledo, OH, USA). The rate of heating was 10 °C/min. Pure DPPC, BSA, and unloaded FCC were used as references. Mass loss curves of separate components were recorded against temperature. Contents were calculated using the mass losses between 150 and 600 °C and the results were corrected for FCC mass loss in this temperature range.

The drug loads were calculated by Equation (6):

$$DL = \frac{m_M}{m_{Tot}}, \quad (6)$$

where  $DL$  is drug load (%),  $m_M$  is mass of loaded material in the sample (mg) and  $m_{Tot}$  is total initial mass of the sample (mg).

$m_M$  was calculated from the system of Equation (7):

$$\begin{cases} m_M = m_{Tot} - m_{FCC} \\ \Delta m_{Tot} = m_M \times f_M + m_{FCC} \times f_{FCC} \end{cases}, \quad (7)$$

which yields:

$$m_{FCC} = \frac{\Delta m_{Tot} - f_M \times m_{Tot}}{f_{FCC} - f_M}, \quad (8)$$

where  $\Delta m_{Tot}$  is the total mass loss during the measurement (mg),  $f_{ref}$  is the fraction of mass loss (%) that was measured for both, the loaded materials (pure BSA or DPPC) and FCC, respectively.  $f_{ref}$  is defined in Equation (9):

$$f_{ref} = \frac{\Delta m_{ref}}{m_{ref}}, \quad (9)$$

where  $\Delta m_{ref}$  is mass loss during TGA (thermogravimetric analysis) in a temperature range of 150–600 °C, and  $m_{ref}$  is the initial mass of the reference material (pure DPPC, BSA, or FCC).

### 2.3. Mercury Porosimetry

To exclude interparticulate voids from the measurement, 200 mg of loaded FCC was consolidated to a 13 mm flat tablet applying 37 MPa using a manual hydraulic press (4350 L, Carver Ink., IN, USA). Pore size distribution of the samples was measured on a mercury intrusion porosimeter (Autopore IV, Micromeritics, Norcross, GA, USA). A 3 cm<sup>3</sup> penetrometer with an intrusion volume of 0.387 mL and a stem volume of 0.412 mL was used. Pressures ranged from 3.59 to 206.64 kPa for low pressure intrusion and from 206.64 kPa to 206.78 MPa for the high pressure intrusion. The equilibration time was 10 s for both, the high and low pressure intrusion [29]. The pressure  $P$  that is required to push mercury into a capillary with a given diameter can be described by the Young–Laplace equation (Equation (10)) [34]:

$$P = \frac{-4 \times \gamma \times \cos\theta}{d}, \quad (10)$$

where  $\gamma$  is the surface tension (mN/m) of the penetrating liquid,  $\theta$  is the contact angle (deg) of the liquid to the porous material, and  $d$  is the diameter [m] of the capillary. Figure 1b shows the principle behind mercury intrusion porosimetry. Using this experimental setup, pores ranging from 5 nm (min) up to 360 µm (max) could be measured. Additionally, information about the total pore volume or porosity, skeletal density, and the specific surface area of a sample was obtained (AutoPore Software v1.09, Micromeritics). All calculations were done based on raw data. For visual representation only (Figure 2), a moving average function with a period of 5 was applied to smoothen intrusion curves. The moving average function was not applied to regions showing extrema.

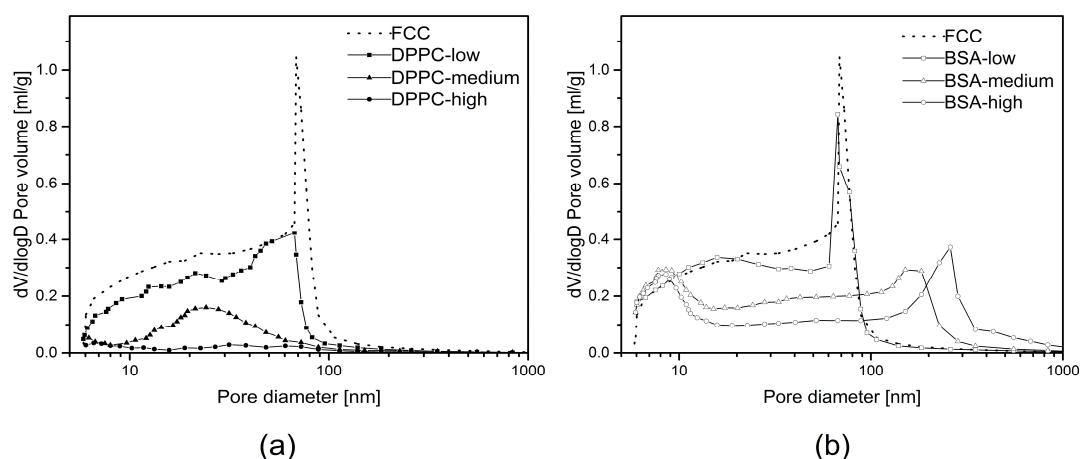


**Figure 2.** Pore size distribution obtained from mercury intrusion porosimetry. (a) Dipalmitoylphosphatidylcholine (DPPC) and (b) bovine serum albumin (BSA) loaded functionalized calcium carbonate (FCC) particles. Drug loads are defined in Table 1. Reference material was unloaded FCC. Samples were consolidated to exclude interparticulate pores. Smoothed curves represent means of  $n = 3$  measurements.

#### 2.4. FIB-SEM

Samples were mounted on carbon adhesives, fixed with silver paste, and sputtered with 20 nm gold (EM ACE600, Leica, Wetzlar, Germany). The FIB-SEM (Helios NanoLab 650, FEI, OR, USA) consisted of an electron emission gun and a focused gallium ion beam column. The two sources were placed at an angle of  $52^\circ$  relative to each other. To protect the surface of the samples from damage by the ion beam, we first applied a 200 nm thick platinum band at the location of the cut. The stage was then tilted in the microscope to  $52^\circ$  so that it was perpendicular to the ion beam. Trenches with a final size of 20  $\mu\text{m}$  width, 12  $\mu\text{m}$  length, 10  $\mu\text{m}$  depth were milled, using a 21 nA ion beam current to reveal cross sections of the sample. Milling time required for these settings was approx. 20 min. From each formulation, one batch was selected and three cross sections at least 20  $\mu\text{m}$  apart were visualized. Cross sections were subsequently polished with a 100 pA ion beam. To reduce artifacts and charging effect on the images, the cross sections were sputtered with 3 nm platinum prior to imaging. Additionally, it is important to keep the samples fixed on the stubs during the milling process. The ion beam current had to be set to the lowest possible values for processing material to avoid sample ablation. Images were acquired from three different detectors: In Chamber Electron Detector (ICE), Everhart Thornley Detector (ETD) and Through Lens Detector (TLD). All images were taken by collecting secondary electrons (SE mode). Acquired images were corrected for tilt ( $-38^\circ$ ). Figure 1a shows a schematic representation of the FIB-SEM.

#### 2.5. Image Analysis

For image analysis, FIJI distribution of ImageJ software was used [35]. From each cross section, the largest possible region of interest (ROI) without physical presence of foreign objects (e.g., external walls or ion depositions) was selected. A stripes filter with Daubechies wavelets (DB15) and a damping coefficient of 4.00 was used to remove curtaining effect [36]. To remove brightness gradients in the images, an FFT bandpass filter was applied. For segmentation of the images, a Python (v. 3.6.1, Continuum Analytics, Inc. Austin, TX, USA) code for SLIC based Superpixel Segmentation was used [37]. From these binary images, visually detected outliers were excluded, assuring that each cross section has at least one image included for calculations. The 2D porosity and average pore area were calculated using the particle analyzer function of ImageJ. To calculate pore volumes, pores were assumed to be spherical for the purpose of calculation. Therefore, absolute values of the pores cross sectional area that was obtained by image analysis, was used as area of a disc. The radius of this disc

was then used to calculate the volume of a sphere. Bin sizes for pore size distribution were chosen in the same range as for MIP. The specific pore volume  $V_{SP}$  [mL/kg] was calculated from image analysis using Equation (11):

$$V_{SP} = \frac{V_{PI}}{W_I \times H_I \times D_{AV} \times \rho_T}, \quad (11)$$

where  $V_{PI}$  is the total pore volume (mL) that is created by the pores of the image,  $W_I$  (m) is the width and  $H_I$  (m) is the height of the image, and  $D_{AV}$  (m) is the average pore diameter from the same image. The density of the tablet  $\rho_T$  (kg/m<sup>3</sup>) was used to calculate the weight (g) of the sample.

## 2.6. Contact Angle Measurement

All measurements required to calculate the contact angle between the loading solutions and the surface of FCC were performed under atmospheric pressure at a temperature of 39 °C and 36 °C for DPPC-methanol and BSA-water, respectively. Densities of the loading solutions were measured using 3 mL glass pycnometers. Viscosity of the two solutions was measured with an Ubbelohde viscosimeter (Size 0, Paragon scientific Ltd., Wirral, UK).

Surface tension and sorption measurements were performed on a tensiometer (T100, Krüss, Hamburg, Germany). Surface tension was measured using the Wilhelmy plate method. For the sorption measurements, a sample holder with an inner diameter of 9 mm was filled with 900 mg of FCC and subsequently tapped until the powder bed was consolidated to a final height of 45 mm. N-hexane was used to determine the capillary constant. Liquid uptake was plotted as squared mass [g] against time [s] and the contact angle [deg] was calculated using Equation (12):

$$\cos\theta = \frac{m^2 \times \eta}{c \times \rho^2 \times \sigma \times t}, \quad (12)$$

where  $m$  is the mass of the absorbed liquid (g),  $t$  is time (s),  $\eta$  is the viscosity (MPa·s),  $\rho$  is the density (g/mL),  $\sigma$  is the surface tension (mN/m) of the solutions, and  $c$  is the capillary constant of FCC. All measurements were done in triplicate.

## 2.7. Solubility

The solubility of BSA in water was determined by agitation of a saturated solution for 4 h at 36 °C in a 1.5 mL Eppendorf tube, ensuring presence of undissolved BSA particles. Subsequently, the samples were centrifuged for 30 min at 14,000 rpm (5415 C, Eppendorf, Hamburg, Germany), the supernatant was diluted, and the concentration was measured in a spectrophotometer (Spectramax M2, Molecular Devices, San Jose, CA, USA) at 280 nm in a 10 mm cuvette. A calibration line with a linear regression of  $R^2 > 0.999$  was used to determine concentrations.

To determine the solubility of DPPC, the material was added in approximately 100 mg portions into glass vials containing 3 mL of methanol. The vials were kept at 39 °C in a water bath. Due to high viscosity, the experiment was stopped after adding 3.3 g of DPPC. Experiments were as well carried out at 50 °C, which is the temperature at the final stage of the evaporation process, when cooling due to evaporation becomes insignificant.

## 3. Results

### 3.1. Initial Loading Solution Properties

Table 1 summarizes physical properties of loading solutions at the start of the evaporation process. Solubility of DPPC in methanol was >1.1 g/mL at 39 °C. However, at 50 °C, only 300 µL of methanol was necessary to turn 1 g of solid DPPC into a clear, highly viscous mass. Pure DPPC does not melt at 50 °C. The solubility of BSA in water at 36 °C was 0.392 g/mL.

**Table 1.** Physical properties of loading solutions. For density, viscosity, and surface tension, values are means  $\pm$  SD ( $n = 3$ ). Contact angle was calculated based on values from the table and the averaged results from the sorption measurements ( $n = 3$ ).

Loading Solution	Density (kg/m <sup>3</sup> )	Viscosity (MPa·s)	Surface Tension (mN/m)	Contact Angle (deg)
Methanol (DPPC-high)	789.0 $\pm$ 0.4	0.59 $\pm$ 0.01	22.0 $\pm$ 0.1	45.3
Methanol (DPPC-medium)	790.9 $\pm$ 1.9	0.57 $\pm$ 0.01	21.9 $\pm$ 0.1	24.2
Methanol (DPPC-low)	785.6 $\pm$ 0.2	0.54 $\pm$ 0.01	21.8 $\pm$ 0.1	34.9
Water (BSA-high)	1001.7 $\pm$ 1.1	0.82 $\pm$ 0.01	47.5 $\pm$ 0.3	53.4
Water (BSA-medium)	1002.0 $\pm$ 0.9	0.75 $\pm$ 0.01	48.7 $\pm$ 0.4	39.8
Water (BSA-low)	999.1 $\pm$ 0.1	0.69 $\pm$ 0.01	50.8 $\pm$ 0.5	66.3

### 3.2. Loading

FCC was loaded by solvent evaporation with low, medium and high amounts of DPPC (using methanol as a solvent) and BSA (using water) as model substances. The content of the loaded substances in the samples was measured by thermogravimetry. The results were  $5.2 \pm 0.1\%$  (Low),  $21.3 \pm 0.8\%$  (Medium), and  $29.5 \pm 3.6\%$  (High) ( $w/w$ ) for BSA samples and  $5.8 \pm 0.2\%$  (Low),  $25.0 \pm 0.9\%$  (Medium), and  $38.6 \pm 0.8\%$  (High) ( $w/w$ ) for DPPC samples. Total yield was  $>90\%$  ( $w/w$ ) for all formulations. After milling and sieving, all formulations appeared as fine white powder. Results of TGA are available in supplementary data, Figure S1.

### 3.3. Mercury Intrusion Porosimetry

Figure 2 shows MIP plots for BSA and DPPC loaded FCC. Both plots show a decrease in total pore volume at increasing loads. At the highest loading, the total pore volume is reduced to approximately 11% and 61% ( $v/v$ ) of the pure FCC for DPPC and BSA, respectively. MIP showed different evolution of the pore size distribution while increasing the amount of loaded substances. While the pore volume below 10 nm is reduced significantly for the DPPC samples, BSA loaded FCC does not show any change at this range. At medium and high loadings, BSA samples show a shift of pore size distribution towards larger pores, indicating the formation of additional pores between 100 and 1000 nm. In contrast, the volume decreases for the entire population of pore sizes in DPPC samples but there is no sign for the formation of new pores. This is also visible when looking at the main peak between 60 and 100 nm, which disappears in case of DPPC but remains nearly unchanged for BSA at low loads. At the highest loading of DPPC, MIP shows almost no residual pore volume anymore.

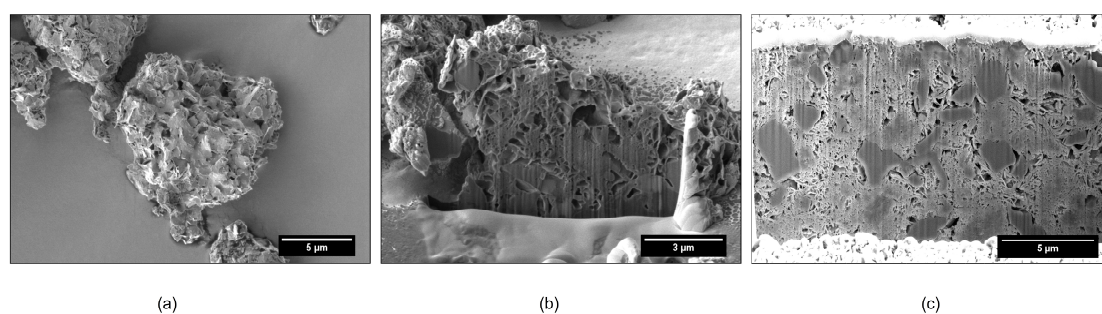
### 3.4. FIB-SEM and Image Analysis

Figures 3 and 4 show SEM and FIB-SEM images of unloaded FCC, or FCC loaded with BSA, or FCC loaded with DPPC. Apart from the porous structure, solid non-porous cores of calcium carbonate are visible in the images.

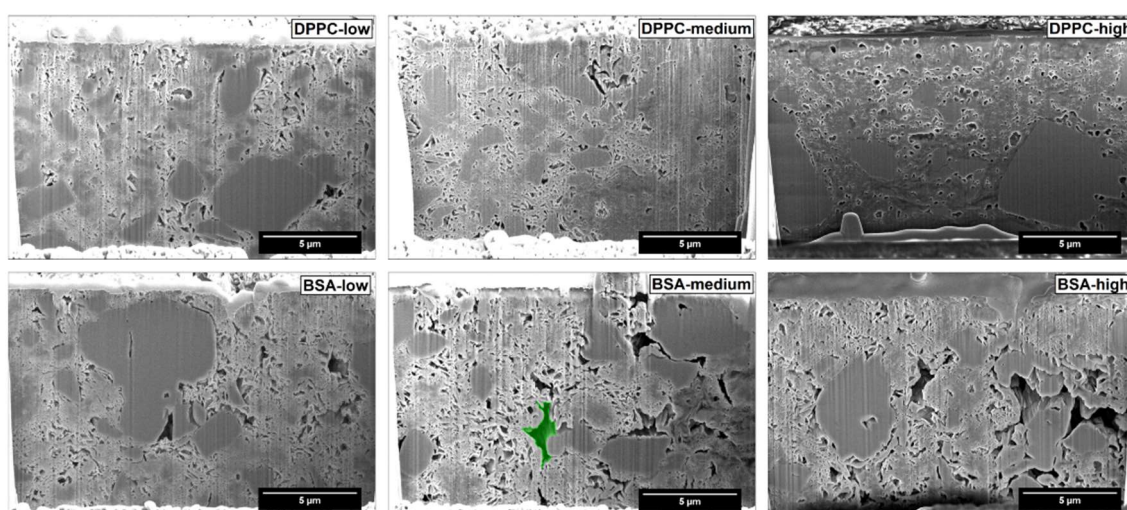
The SEM images showed reduction in pore size in DPPC formulations at higher loading. The pores were smaller, isolated, and had a different morphology than in unloaded FCC (Figure 3), with the FCC lamellae almost not distinguishable anymore. Figure 4 shows that the change in pore size or morphology is almost not detectable at lower loadings. Images show clearly the occurrence of interparticulate voids for FCC loaded with BSA, which are not present in case of DPPC.

Figure 5 shows the quantitative assessment of results from FIB-SEM image analysis. Porosity of FCC was reduced with increasing loading of DPPC, while BSA loaded samples had no obvious trend of change in total porosity. The average pore diameter for both materials was almost unchanged at low loadings. At medium and high loadings, DPPC loaded FCC showed reduced pore size ( $p < 0.001$ ) and BSA loaded FCC showed increase in pore diameter ( $p < 0.0001$ ).

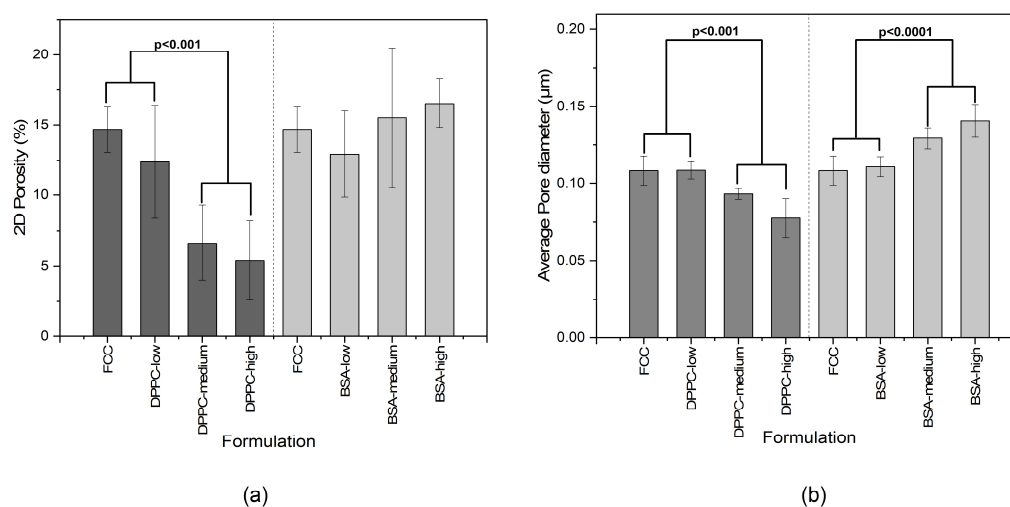




**Figure 3.** Visualization of unloaded FCC; (a) SEM analysis of an individual FCC particle; (b) focused ion beam scanning electron microscopy (FIB-SEM) based visualization of a cross section of an individual particle; (c) unloaded FCC after consolidation at 37 MPa.



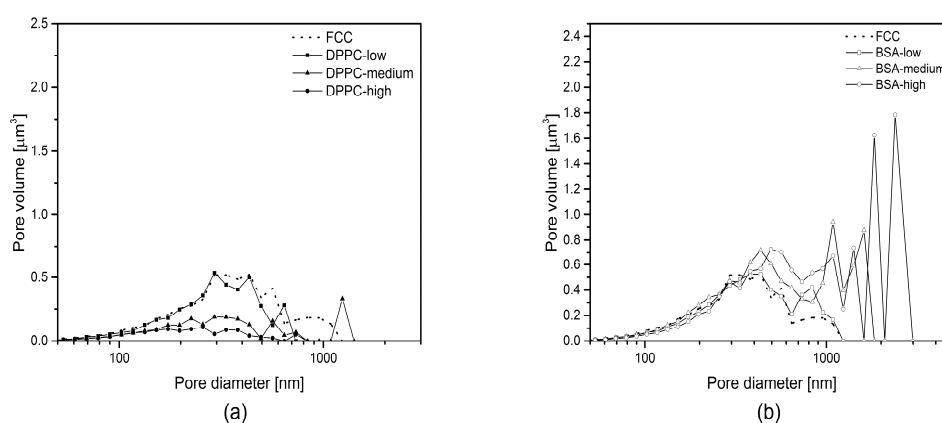
**Figure 4.** Analysis of consolidated FCC particles loaded with DPPC or BSA. Particles loaded with DPPC (top row) or BSA (bottom row) were analyzed by FIB-SEM. Mercury intrusion porosimetry results for the same material are shown in Figure 2. An example showing an interparticulate void is highlighted in green.



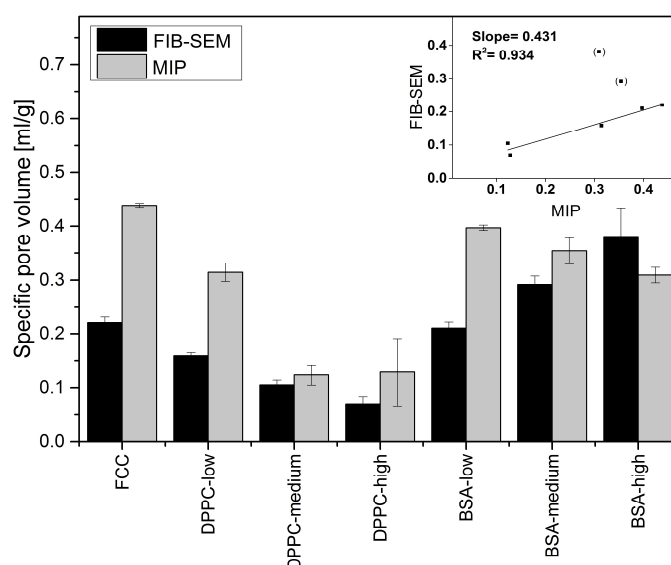
**Figure 5.** Quantitative assessment of porosity and pore diameter of FCC formulations. Results of (a) calculated 2D porosity and (b) average pore diameter from analysis of FIB-SEM images from different formulations of DPPC and BSA loaded into FCC. P-Values were calculated from one way ANOVA and Bonferroni post hoc test. Values are means  $\pm$  SD, ( $n \geq 3$ ).

Figure 6 shows calculated pore size distributions based on image analysis. The difference in pore diameter obtained from MIP (Figure 2) and SEM (Figure 6) is due to different pore shape assumptions in the two methods (cylindrical in MIP and spherical in image analysis). Average pore size (Figure 5) and pore size distribution from image analysis (Figure 6) were in accordance with MIP, showing larger sized pores at higher BSA loading. A trend of pore reduction in all sizes in the DPPC samples was observed. However, for the highest loading of DPPC, mercury intrusion results indicated complete pore filling, while the FIB-SEM images of this formulation showed presence of smaller, inaccessible pores.

Figure 7 shows the specific pore volumes (mL/g) obtained by the two different methods. Data from MIP suggests, that the specific pore volumes decrease with increasing *DL* from 0.438 (unloaded FCC) to 0.128 and 0.309 mL/g for DPPC-high and BSA-high, respectively. Image analysis shows a reduction of the specific pore volume from 0.22 (unloaded FCC) to 0.069 mL/g for DPPC-high, but an increase up to 0.381 mL/g for BSA-high. The correlation coefficient of the two methods is  $R^2 = 0.934$  and the slope of the trend line is 0.431 (Figure 7, top right corner). The two data point in brackets (BSA-high and BSA-medium) are excluded from the linear fit due to observed external crystallization.



**Figure 6.** Pore size distribution based on FIB-SEM image analysis. Calculations were done assuming spherical pore shapes; (a) DPPC low, medium, and high loadings were compared to unloaded FCC; (b) BSA low, medium and high loadings were compared to unloaded FCC. Large voids (pore diameter > 1000 nm) in higher loadings of BSA are indicative of external crystallisation of BSA. Values are means of  $n \geq 3$ .



**Figure 7.** Specific pore volumes of FCC formulations. Pore volumes were calculated based on FIB-SEM image analysis (black) or by MIP (grey). Insert: correlation plot for both methods. Values are means  $\pm$  SD, ( $n \geq 3$ ).



#### 4. Discussion

Porous microparticles such as FCC can be used as carriers for drugs and other materials. In the present study, FCC particles were loaded by an established solvent evaporation method [17] using two model compounds: a hydrophilic macromolecule (BSA with a molecular weight of 66 kDa) and a small and lipophilic compound, i.e., DPPC. Loading efficiency was over 90% for both compounds and a drug load of 30% and 38% was measured for BSA and DPPC, respectively. Despite these similarities with respect to loading efficiency and loading capacity, the actual mechanism of drug loading is clearly different. The loading solution for DPPC shows a lower surface tension than the one for BSA as well as a lower viscosity. Due to the resulting lower contact angle, DPPC penetrates and solidifies within the pores. This notion is supported by the following observations: First, MIP as well as image analysis show gradual pore volume reduction. This applies to pores smaller than 500 nm. Second, DPPC does not lead to formation of additional interparticulate pores due to major penetration/deposition into the porous meshwork. In contrast, BSA is deposited solely on the surface of particles. This is supported by the observation that no filling of pores <500 nm can be detected by image analysis. In addition, upon loading, voids with a size of over 500 nm are created in between particles representing external crystallization. The occurrence of external crystallization can be explained by the solubility of the model substances. DPPC is highly soluble in methanol. In contrast, during the evaporation process, BSA reaches its solubility limit, when the volume of the remaining water is approx. 2.3 mL. At this point, only approx. 40% (v/v) of the BSA-solution is inside the pores of the FCC particles leading to external deposition of precipitated BSA.

Our results clearly indicate, that the methods used (i.e., FIB-SEM and MIP) have to be combined to give a realistic picture of the inner structure and porosity of the studied particles. FIB-SEM provides a detailed insight into the inner structure of FCC. The structure of the lamella and the solid starter cores is consistent with the process of FCC production explained by Levy et al. [38]. Pores of various sizes and shapes can be easily distinguished. Upon loading, filling of intraparticle pores and the formation of surface deposits can be documented.

Surprisingly, the obtained results did not necessarily correlate with results from mercury intrusion porosimetry. For example, average pore sizes obtained by both methods were very different. The average pore diameters of pure FCC determined by image analysis and MIP are 108 and 23 nm, respectively. This considerable difference can be explained by the ink bottle effect during MIP measurement. MIP assumes a cylindrical pore shape, while image analysis reveals the actual size of the pores, which in fact can consist of a small opening being connected to a much larger inner body. Thus, image analysis is giving information about the diameter of such pores bodies, while MIP is reporting the largest opening (throat) towards a pore. The ratio (4.7) between the average pore diameters obtained by the two different methods might therefore reflect the geometrical ratio of the body diameter of a pore to its throat. With respect to the specific pore volume, FIB-SEM and MIP show a good correlation ( $R^2 = 0.934$ ). This does not apply to BSA formulations with a  $DL > 5\%$  (w/w) due to the aforementioned external crystallization leading to the formation of interparticle pores. However, 2D imaging can only visualize a cross-section of a particle. The negative correlation plot (Figure 7) indicates that the pore volumes obtained by image analysis might be underestimated by a factor of 2. This can be attributed to the assumption of a spherical pore geometry when calculating pore volumes from 2D images. Selecting the right pore geometry is therefore crucial for reliable measurements based on image analysis. Based on images of the internal structure of FCC (Figure 3b) it seems obvious, that other pore geometries such as frustum, bipyramid or other polyhedra might describe the pore geometry much closer. It remains, however, to be determined if such a detailed structural analysis would be an added value.

MIP is a fast, precise, and accurate method for the analysis of materials that contain accessible and interconnected pores, but becomes less accurate when pores are isolated, e.g., due to clogging. MIP requires rather large sample sizes (0.1–1 g) and interpretation must respect the incapability of the machine to register isolated pores. MIP should therefore be combined with other methods such as flow

imaging microscopy, thermoporometry, and terahertz time domain spectroscopy [30,39,40]. In contrast to these alternative methods, however, FIB-SEM is able to directly visualize the internal structure of a porous material with a resolution of several nanometers. Results are not influenced by pore accessibility or connectivity or type of loading [41]. Another advantage of FIB-SEM is its possibility to be coupled with an EDX detector, which allows to differentiate between structural components of a multiple component carrier system, deposits within pores and the surrounding structural material.

Compared to MIP, the range of materials that can be studied with FIB-SEM is wider. Considering the high pressures (up to 400 MPa) acting on the samples during a MIP analysis, one cannot exclude damages to the sample, e.g., deformation or fracture. However, image analysis has limitations since it is applicable only for a small area of the sample. For geometrically complex structures such as FCC, not all pores are reliably recognized by the algorithm. This requires extensive manual work for image processing. More repetitions are therefore needed to get statistically relevant data. Here, MIP has a clear advantage over image analysis, since the sample size (number of pores) is much larger (approx. factor  $10^4$ ). However, investigation of the geometrical properties of the porous structure, which is essential to study liquid flow in porous media especially in clogged pore conditions, is impossible without micro tomographic sectioning using FIB-SEM.

## 5. Conclusions

As both FIB-SEM image analysis and MIP each have their limitations, we propose that both methods should be combined to allow for accurate interpretation of substance distribution within porous microcarriers. Using such a combined approach, we could for the first time visualize the internal structure of FCC and clearly discriminate between open, blocked, and drug loaded pores.

**Supplementary Materials:** The following are available online at <http://www.mdpi.com/1999-4923/11/1/32/s1>, Figure S1: Thermogravimetric results of pure FCC, BSA, DPPC, and the final formulations.

**Author Contributions:** Conceptualization, methodology, formal analysis, investigation, writing—original draft preparation, visualization, M.F. and R.R.; resources J.S.; writing—review and editing, G.Q., J.H. and M.P.; supervision, G.Q. and M.P.; project administration, M.P.; funding acquisition, M.P., G.Q. and J.H.

**Funding:** This research was funded by grants from the Phospholipid Research Center and Omya International AG.

**Acknowledgments:** We would like to thank Daniel Mathys from the Nano Imaging Lab of the Swiss Nanoscience Institute for help with FIB-SEM, and Darryl Borland for manuscript proofreading and editorial assistance.

**Conflicts of Interest:** The authors declare no conflict of interest. All experiments were carried out at the University of Basel. J.S. declares that Omya AG had no role in the design of the study or interpretation of data.

## References

- Salonen, J.; Kaukonen, A.M.; Hirvonen, J.; Lehto, V.-P. Mesoporous silicon in drug delivery applications. *J. Pharm. Sci.* **2008**, *97*, 632–653. [CrossRef] [PubMed]
- Preisig, D.; Roth, R.; Tognola, S.; Varum, F.J.O.; Bravo, R.; Cetinkaya, Y.; Huwyler, J.; Puchkov, M. Mucoadhesive microparticles for local treatment of gastrointestinal diseases. *Eur. J. Pharm. Biopharm.* **2016**, *105*, 156–165. [CrossRef] [PubMed]
- Vallet-Regí, M.; Doadrio, J.C.; Doadrio, A.L.; Izquierdo-Barba, I.; Pérez-Pariente, J. Hexagonal ordered mesoporous material as a matrix for the controlled release of amoxicillin. *Solid State Ionics* **2004**, *172*, 435–439. [CrossRef]
- Doadrio, A.L.; Sousa, E.M.B.; Doadrio, J.C.; Pérez Pariente, J.; Izquierdo-Barba, I.; Vallet-Regí, M. Mesoporous SBA-15 HPLC evaluation for controlled gentamicin drug delivery. *J. Control. Release* **2004**, *97*, 125–132. [CrossRef] [PubMed]
- Pace, C.N.; Treviño, S.; Prabhakaran, E.; Scholtz, J.M. Protein structure, stability and solubility in water and other solvents. *Philos. Trans. R. Soc. Lond. B Biol. Sci.* **2004**, *359*, 1225–1235. [CrossRef] [PubMed]
- Anderson, J.M.; Shive, M.S. Biodegradation and biocompatibility of PLA and PLGA microspheres. *Adv. Drug Deliv. Rev.* **2012**, *64*, 72–82. [CrossRef]

7. Karlsson, H.L.; Gustafsson, J.; Cronholm, P.; Möller, L. Size-dependent toxicity of metal oxide particles—A comparison between nano- and micrometer size. *Toxicol. Lett.* **2009**, *188*, 112–118. [\[CrossRef\]](#)
8. Kim, H.W.; Ahn, E.-K.; Jee, B.K.; Yoon, H.-K.; Lee, K.H.; Lim, Y. Nanoparticulate-induced toxicity and related mechanism in vitro and in vivo. *J. Nanopart. Res.* **2009**, *11*, 55–65. [\[CrossRef\]](#)
9. Mizushima, Y.; Ikoma, T.; Tanaka, J.; Hoshi, K.; Ishihara, T.; Ogawa, Y.; Ueno, A. Injectable porous hydroxyapatite microparticles as a new carrier for protein and lipophilic drugs. *J. Control. Release* **2006**, *110*, 260–265. [\[CrossRef\]](#)
10. Wu, L.; Wu, S.; Xu, Z.; Qiu, Y.; Li, S.; Xu, H. Modified nanoporous titanium dioxide as a novel carrier for enzyme immobilization. *Biosens. Bioelectron.* **2016**, *80*, 59–66. [\[CrossRef\]](#)
11. Byrne, R.S.; Deasy, P.B. Use of porous aluminosilicate pellets for drug delivery. *J. Microencapsul.* **2005**, *22*, 423–437. [\[CrossRef\]](#) [\[PubMed\]](#)
12. Sukhorukov, G.B.; Volodkin, D.V.; Günther, A.M.; Petrov, A.I.; Shenoy, D.B.; Möhwald, H. Porous calcium carbonate microparticles as templates for encapsulation of bioactive compounds. *J. Mater. Chem.* **2004**, *14*, 2073–2081. [\[CrossRef\]](#)
13. Kumeria, T.; McInnes, S.J.P.; Maher, S.; Santos, A. Porous silicon for drug delivery applications and theranostics: Recent advances, critical review and perspectives. *Expert Opin. Drug Deliv.* **2017**, *14*, 1407–1422. [\[CrossRef\]](#)
14. Parent, M.; Baradari, H.; Champion, E.; Damia, C.; Viana-Trecant, M. Design of calcium phosphate ceramics for drug delivery applications in bone diseases: A review of the parameters affecting the loading and release of the therapeutic substance. *J. Control. Release* **2017**, *252*, 1–17. [\[CrossRef\]](#) [\[PubMed\]](#)
15. Dutta, S.R.; Passi, D.; Singh, P.; Bhuihar, A. Ceramic and non-ceramic hydroxyapatite as a bone graft material: A brief review. *Irish J. Med. Sci.* **2015**, *184*, 101–106. [\[CrossRef\]](#) [\[PubMed\]](#)
16. Mouriño, V.; Boccaccini, A.R. Bone tissue engineering therapeutics: Controlled drug delivery in three-dimensional scaffolds. *J. R. Soc. Interface* **2010**, *7*, 209–227. [\[CrossRef\]](#) [\[PubMed\]](#)
17. Preisig, D.; Haid, D.; Varum, F.J.O.; Bravo, R.; Alles, R.; Huwyler, J.; Puchkov, M. Drug loading into porous calcium carbonate microparticles by solvent evaporation. *Eur. J. Pharm. Biopharm.* **2014**, *87*, 548–558. [\[CrossRef\]](#)
18. Roth, R.; Schoelkopf, J.; Huwyler, J.; Puchkov, M. Functionalized calcium carbonate microparticles for the delivery of proteins. *Eur. J. Pharm. Biopharm.* **2018**, *122*, 96–103. [\[CrossRef\]](#)
19. Qu, L.; Zhou, Q.; Denman, J.A.; Stewart, P.J.; Hapgood, K.P.; Morton, D.A.V. Influence of coating material on the flowability and dissolution of dry-coated fine ibuprofen powders. *Eur. J. Pharm. Sci.* **2015**, *78*, 264–272. [\[CrossRef\]](#)
20. Charm, S.E.; Wong, B.L. Shear effects on enzymes. *Enzyme Microb. Technol.* **1981**, *3*, 111–118. [\[CrossRef\]](#)
21. Stasio, E.D.; Cristofaro, R.D. The effect of shear stress on protein conformation. Physical forces operating on biochemical systems: The case of von willebrand factor. *Biophys. Chem.* **2010**, *153*, 1–8. [\[PubMed\]](#)
22. Dorozhkin, S.V.; Dorozhkina, E.I. The influence of bovine serum albumin on the crystallization of calcium phosphates from a revised simulated body fluid. *Colloids Surf. A Physicochem. Eng. Asp.* **2003**, *215*, 191–199. [\[CrossRef\]](#)
23. Finkelstein, Y.; Saig, A.; Danon, A.; Koresh, J.E. Study of Type-A Zeolites. Part 1: Mechanism of He and Ne Encapsulation. *J. Phys. Chem. B* **2003**, *107*, 9170–9174. [\[CrossRef\]](#)
24. Salonen, J.; Paski, J.; Vähä-Heikkilä, K.; Heikkilä, T.; Björkqvist, M.; Lehto, V.-P. Determination of drug load in porous silicon microparticles by calorimetry. *Phys. Status Solidi A* **2005**, *202*, 1629–1633. [\[CrossRef\]](#)
25. Levy, C.L.; Matthews, G.P.; Laudone, G.M.; Gribble, C.M.; Turner, A.; Ridgway, C.J.; Gerard, D.E.; Schoelkopf, J.; Gane, P.A.C. Diffusion and Tortuosity in Porous Functionalized Calcium Carbonate. *Ind. Eng. Chem. Res.* **2015**, *54*, 9938–9947. [\[CrossRef\]](#)
26. Eberle, V.A.; Schoelkopf, J.; Gane, P.A.C.; Alles, R.; Huwyler, J.; Puchkov, M. Floating gastroretentive drug delivery systems: Comparison of experimental and simulated dissolution profiles and floatation behavior. *Eur. J. Pharm. Sci.* **2014**, *58*, 34–43. [\[CrossRef\]](#) [\[PubMed\]](#)
27. Wagner-Hattler, L.; Wyss, K.; Schoelkopf, J.; Huwyler, J.; Puchkov, M. In vitro characterization and mouthfeel study of functionalized calcium carbonate in orally disintegrating tablets. *Int. J. Pharm.* **2017**, *534*, 50–59. [\[CrossRef\]](#)

28. Stirnimann, T.; Maiuta, N.D.; Gerard, D.E.; Alles, R.; Huwyler, J.; Puchkov, M. Functionalized calcium carbonate as a novel pharmaceutical excipient for the preparation of orally dispersible tablets. *Pharm. Res.* **2013**, *30*, 1915–1925. [\[CrossRef\]](#)
29. Stirnimann, T.; Atria, S.; Schoelkopf, J.; Gane, P.A.C.; Alles, R.; Huwyler, J.; Puchkov, M. Compaction of functionalized calcium carbonate, a porous and crystalline microparticulate material with a lamellar surface. *Int. J. Pharm.* **2014**, *466*, 266–275. [\[CrossRef\]](#)
30. Markl, D.; Wang, P.; Ridgway, C.; Karttunen, A.-P.; Chakraborty, M.; Bawuah, P.; Pääkkönen, P.; Gane, P.; Ketolainen, J.; Peiponen, K.-E.; et al. Characterization of the Pore Structure of Functionalized Calcium Carbonate Tablets by Terahertz Time-Domain Spectroscopy and X-Ray Computed Microtomography. *J. Pharm. Sci.* **2017**, *106*, 1586–1595. [\[CrossRef\]](#)
31. Markl, D.; Wang, P.; Ridgway, C.; Karttunen, A.-P.; Bawuah, P.; Ketolainen, J.; Gane, P.; Peiponen, K.-E.; Zeitler, J.A. Resolving the rapid water absorption of porous functionalised calcium carbonate powder compacts by terahertz pulsed imaging. *Chem. Eng. Res. Des.* **2018**, *132*, 1082–1090. [\[CrossRef\]](#)
32. Giesche, H. Mercury Porosimetry: A General (Practical) Overview. *Part. Part. Syst. Charact.* **2006**, *23*, 9–19. [\[CrossRef\]](#)
33. Anthony, J.W.; Bideaux, R.A.; Bladh, K.W.; Nichols, M.C. *Handbook of Mineralogy: Arsenates, Phosphates, Vanadates*; Mineral Data Publishing: Tucson, AZ, USA, 2000; ISBN 978-0-9622097-3-4.
34. Washburn, E.W. The Dynamics of Capillary Flow. *Phys. Rev.* **1921**, *17*, 273–283. [\[CrossRef\]](#)
35. Schindelin, J.; Arganda-Carreras, I.; Frise, E.; Kaynig, V.; Longair, M.; Pietzsch, T.; Preibisch, S.; Rueden, C.; Saalfeld, S.; Schmid, B.; et al. Fiji: An open-source platform for biological-image analysis. *Nat. Methods* **2012**, *9*, 676–682. [\[CrossRef\]](#) [\[PubMed\]](#)
36. Münch, B.; Trtik, P.; Marone, F.; Stampanoni, M. Stripe and ring artifact removal with combined wavelet—Fourier filtering. *Opt. Express* **2009**, *17*, 8567–8591. [\[CrossRef\]](#)
37. Achanta, R.; Shaji, A.; Smith, K.; Lucchi, A.; Fua, P.; Süsstrunk, S. *SLIC Superpixels*; Image and Visual Representation Lab (IVRL): Lausanne, Switzerland, 2010.
38. Levy, C.L.; Matthews, G.P.; Laudone, G.M.; Beckett, S.; Turner, A.; Schoelkopf, J.; Gane, P.A.C. Mechanism of adsorption of actives onto microporous functionalised calcium carbonate (FCC). *Adsorption* **2017**, *23*, 603–612. [\[CrossRef\]](#)
39. Sediq, A.S.; Waasdorp, S.K.D.; Nejadnik, M.R.; van Beers, M.M.C.; Meulenaar, J.; Verrijck, R.; Jiskoot, W. A Flow Imaging Microscopy–Based Method Using Mass-to-Volume Ratio to Derive the Porosity of PLGA Microparticles. *J. Pharm. Sci.* **2017**, *106*, 3378–3384. [\[CrossRef\]](#)
40. Majda, D.; Ikonen, T.; Krupa, A.; Lehto, V.-P.; Makowski, W. Application of thermoporometry for characterization of mesoporous silicon: In search for probe liquid aimed at large pores. *Microporous Mesoporous Mater.* **2018**, *264*, 1–7. [\[CrossRef\]](#)
41. Liu, Y.; King, H.E.; van Huis, M.A.; Drury, M.R.; Plümper, O. Nano-Tomography of Porous Geological Materials Using Focused Ion Beam-Scanning Electron Microscopy. *Minerals* **2016**, *6*, 104. [\[CrossRef\]](#)



© 2019 by the authors. Licensee MDPI, Basel, Switzerland. This article is an open access article distributed under the terms and conditions of the Creative Commons Attribution (CC BY) license (<http://creativecommons.org/licenses/by/4.0/>).

### 3.4 Coating of PLA-nanoparticles with cyclic, arginine-rich cell penetrating peptides

#### enables oral delivery of liraglutide

P. Uhl<sup>1</sup>; C. Grundmann<sup>1</sup>; M. Sauter<sup>1,2</sup>; P. Storck<sup>1</sup>; A. Tursch<sup>3</sup>; S. Özbek<sup>3</sup>; K. Leotta<sup>1</sup>; R. Roth<sup>4</sup>; D. Witzigmann<sup>4,5</sup>; J. Kulkarni<sup>5</sup>; PR. Cullis<sup>5</sup>; G. Fricker<sup>6</sup>; W. Mier<sup>1\*</sup>

<sup>1</sup> Department of Nuclear Medicine, Heidelberg University Hospital, Heidelberg, Germany

<sup>2</sup> Department of Clinical Pharmacology and Pharmacoepidemiology, Heidelberg University Hospital, Heidelberg, Germany

<sup>3</sup> University of Heidelberg, Centre for Organismal Studies, Department of Molecular Evolution and Genomics, Heidelberg, Germany

<sup>4</sup> Division of Pharmaceutical Technology, Department of Pharmaceutical Sciences, University of Basel, Basel, Switzerland

<sup>5</sup> Department of Biochemistry and Molecular Biology, University of British Columbia, Health Sciences Mall, Vancouver, British Columbia, Canada

<sup>6</sup> Institute of Pharmacy and Molecular Biotechnology, Department of Pharmaceutical Technology and Biopharmacy, Ruprecht-Karls University, Heidelberg, Germany

Manuscript submitted to the journal **Biomaterials**

#### Personal contribution

My contribution to this research article includes the performance of the particle retention assay including sample collection.



## **Coating of PLA-nanoparticles with cyclic, arginine-rich cell penetrating peptides enables oral delivery of liraglutide**

P. Uhl<sup>1</sup>; C. Grundmann<sup>1</sup>; M. Sauter<sup>1,2</sup>; P. Storck<sup>1</sup>; A. Tursch<sup>3</sup>; S. Özbek<sup>3</sup>; K. Leotta<sup>1</sup>; R. Roth<sup>4</sup>; D. Witzigmann<sup>4,5</sup>; J. Kulkarni<sup>5</sup>; PR. Cullis<sup>5</sup>; G. Fricker<sup>6</sup>; W. Mier<sup>1\*</sup>

1: Department of Nuclear Medicine, Heidelberg University Hospital, Heidelberg, Germany

2: Department of Clinical Pharmacology and Pharmacoepidemiology, Heidelberg University Hospital, Heidelberg, Germany

3: University of Heidelberg, Centre for Organismal Studies, Department of Molecular Evolution and Genomics, Heidelberg, Germany

4: Division of Pharmaceutical Technology, Department of Pharmaceutical Sciences, University of Basel, Basel, Switzerland

5: Department of Biochemistry and Molecular Biology, University of British Columbia, Health Sciences Mall, Vancouver, British Columbia, Canada

6: Institute of Pharmacy and Molecular Biotechnology, Department of Pharmaceutical Technology and Biopharmacy, Ruprecht-Karls University, Heidelberg, Germany

\* Corresponding author at:

Department of Nuclear Medicine, Heidelberg University Hospital, Im Neuenheimer Feld 400, D-69120 Heidelberg, Germany

Phone: +49-6221-567720

E-mail: walter.mier@med.uni-heidelberg.de

**Abstract:**

Until today, the oral delivery of peptide drugs is limited due to their instability in the gastrointestinal tract and low mucosa penetration. In order to overcome these hurdles, PLA (polylactide acid)-nanoparticles coated with a cyclic, polyarginine-rich, cell penetrating peptide (CPP) were examined.

For this purpose, a cyclic R9-CPP was synthesized by solid-phase synthesis and an additional cysteine was incorporated for coupling of the CPP to maleimide-functionalized PLA via the thiol group of the cysteine residue.

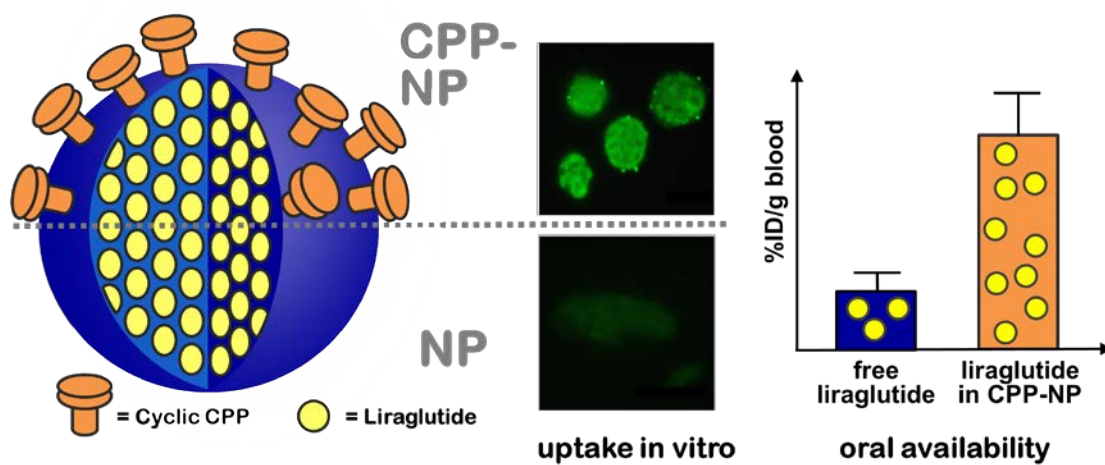
These surface-modified nanoparticles using 0.5% (v/v) Tween® 85 as surfactant showed a size ( $184.30 \pm 1.15$  nm) and polydispersity index ( $0.148 \pm 0.010$ ) comparable to standard PLA-nanoparticles, while the zeta potential showed a significant increase indicating the successful coupling of the CPP to the surface of the nanoparticles. Furthermore, a high encapsulation efficiency of the model lipopeptide drug liraglutide as detected by HPLC-measurements could be observed. Cryo-EM micrographs verified the size and morphology of the modified and unmodified nanoparticles. Cytotoxicity tests using Caco-2 cells showed no significant cytotoxicity for all nanoparticle concentrations indicating the good tolerability of this novel formulation. Furthermore, a strongly enhanced mucosa binding and penetration could be achieved by this nanoparticle modification as demonstrated by the Caco-2 binding and uptake assay.

In a proof of concept study using female Wistar rats, a substantial, 4.5-fold increase in the oral availability of the iodine-125 radiolabeled peptide drug liraglutide could be observed for the nanoparticles modified with the cyclic R9 CPP. This highlights the importance of this novel nanoparticle formulation for the oral delivery of peptide drugs.

**Keywords:**

Nanoparticles; Polylactide acid; Cell penetrating peptides; Oral delivery; Peptide drugs; Liraglutide





## 1. Introduction:

The oral administration of macromolecular drugs (i.e. peptides, proteins, and antibodies) proves to be a current challenge in the field of drug discovery and development [1]. Both, the drugs' instability in the acidic milieu of the stomach as well as the low absorption across the intestinal barrier hamper the oral bioavailability of these therapeutics [2]. For this reason, only parenteral delivery routes (such as subcutaneous or intravenous injection) are possible which are expensive, time-consuming and result in low patient compliance [3, 4]. To overcome these hurdles and to facilitate the oral delivery, several approaches have been studied in recent years, including nano- or micro-emulsions [5], polymeric micelles [6], hydrogel micro-particles [7], tetraether-lipid liposomes [2, 8] or surface-modified liposomes [9-11] - but with limited success.

For this reason, improved formulation technologies should be investigated. An alternative approach is the use of nanoparticles (NP) consisting of biodegradable materials such as polylactide acid (PLA) and poly lactic-co-glycolic acid (PLGA). Despite several attempts to enable oral drug delivery [12-15], none of the previous PLA or PLGA iterations achieved a breakthrough [13, 16-19]. Reasons for this phenomenon are primarily the poor mucosal penetration in the intestine and also the rapid removal by the mucus [4]. A novel strategy to enhance the mucosa uptake of these nanoparticles is the surface-modification with cell penetrating peptides (CPPs) [20]. CPPs are short peptides of less than 30 amino acids (mostly positively charged [21]) that are able to penetrate cell membranes and translocate different cargoes into cells [22]. The potential

cargoes can range from small molecules to proteins [23]. Arginine rich CPPs are currently exhaustively investigated [24, 25]. Recently, Herce et al. [26] reported the successful development of functional cell-permeable nanobodies by the use of cyclic arginine-rich CPPs. Other studies showed enhanced absorption rates of insulin after oral co-administration with CPPs [27-29].

In the present study, the surface of PLA nanoparticles was coated with a cyclic R9-CPP derivative to facilitate the intestinal retention and mucosa penetration of peptide therapeutics. Currently, CPPs are the most promising modification for oral peptide delivery. As one developmental step of this study, a cyclic CPP was used because it is less susceptible to hydrolysis by peptidases. In addition, cyclic peptides have been shown to be enzymatically more stable [30]. Therefore, the peptide liraglutide (LRT), a widely used antidiabetic drug, was studied as a model drug for animal studies [31]. LRT can be also used as drug against obesity [32, 33], though requiring long term administration, where patient compliance is demonstrably reduced [34]. Until now, the application of LRT is hampered due to its limitation to subcutaneous administration.

Based on this urgent need, an oral formulation of LRT using a novel class of CPP-coated PLA nanoparticles was investigated. Maleimide coupling of the CPPs to PLA was chosen due to the high stability of the covalent binding as previously shown by Youngblood et al. [35]. PLA nanoparticles were systematically prepared with surfactants covering the entire hydrophilic-lipophilic balance (HLB) chart in order to determine the most suitable for preparation of the CPP-nanoparticles. Nanoparticle characterization by dynamic light scattering demonstrated that Tween® 85 resulted in smallest nanoparticles, which is advantageous for mucosa penetration. By the use of this technology, a high encapsulation efficiency of the model drug LRT was achieved. The successful coating of the CPP on the nanoparticle surface was verified by the increase in zeta potential of the particles. Interestingly, these nanoparticles could be successfully freeze-dried for long term storage providing an additional benefit [36]. In a Caco-2 binding assay the strongly enhanced mucosa adhesion of the modified nanoparticles was clearly demonstrated. Animal trials using Wistar rats were performed and showed a strongly improved uptake of LRT after oral administration as compared to the free peptide.

## **2. Material and Methods**

### **2.1 Materials**

Maleimide-modified polylactide acid (MW = 5000 g/mol) was obtained from Sigma Aldrich (Steinheim, Germany) and Amicon® Ultra-4 centrifugal filters from Merck Millipore (Tullagreen, Ireland) while Filtropur S 0.2 sterile filters were purchased from Sarstedt (Nümbrecht, Germany). Dulbecco's phosphate buffered saline was applied from Gibco® by life technologies™ (Paisley, UK); Tween® 85 from Sigma Aldrich (Steinheim, Germany), Atto dyes from Atto-tec GmbH (Siegen, Germany), NAP™-5 columns were obtained from GE Healthcare (Buckinghamshire, UK) and radioiodine I-125 was purchased from Hartmann Analytic GmbH® (Braunschweig, Germany), while Triton™ X-100, cholesterol, chloroform, methanol and all other solvents were obtained from Sigma Aldrich (Taufkirchen, Germany). Liraglutide was isolated of Victoza®-pens by preparative HPLC and the cyclic R9-CPP was synthesized by solid phase synthesis in our laboratory. For the cell binding assay, DMEM medium (high glucose), Fetal Bovine Serum and Trypsin-EDTA was purchased from Thermo Fisher (Waltham, Massachusetts, USA) while glass coverslips were obtained from Greiner-Bio one (Frickenhausen, Germany). The dye DAPI was obtained from Sigma Aldrich (Steinheim, Germany), Mowiol 4-88 from Roth (Karlsruhe, Germany) and Alamar Blue® from Bio-Rad antibodies (Puchheim, Germany).

### **2.2 Nanoparticles**

#### **2.2.1 Preparation of nanoparticles**

Nanoparticles were prepared by a modified double emulsion technique according to Zambaux et al. [37] and Li et al. [38]. First, the required amount of the peptide drug LRT and 6 mg of the polymer PLA and 4 mg of a maleimide-modified PLA were dissolved in 1 ml acetone followed by sonication for 5 min. Afterwards, the resulting mixture was added drop wise into 2 ml of a Tween® 85 aqueous solution (0.5% v/v) under constant and fast stirring. The required amount of the CPP (0.5 mg) was dissolved in another 2 ml of an aqueous solution of Tween® 85 and finally added to the obtained mixture (coupling principle see **figure 1**). The coupling of the CPP could be performed by the reaction of the thiol group of its cysteine to the maleimide-modified PLA. Prior to characterization, the nanoparticles were stirred overnight in order to evaporate the organic solvent. In order to remove free LRT and free CPP, the nanoparticles were purified by Sephadex G-25 gel filtration chromatography (NAP™-5 columns). As elution buffer, 0.5% (v/v) Tween® 85 in water was used.

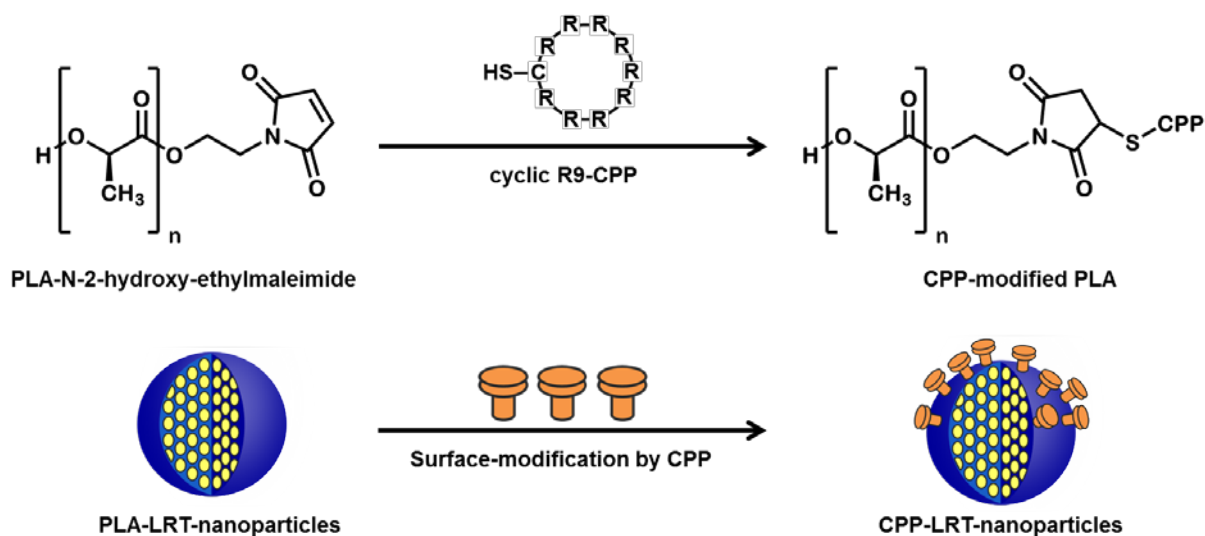


**Figure 1** Illustration of the nanoparticle surface modification with the cyclic R9-CPP. For this coupling strategy, the cyclic R9-CPP contained an additional cysteine. Covalent binding was achieved by the reaction of the free thiol group of the cysteine with the maleimide group of the modified PLA.

### 2.2.2 Characterization of nanoparticles

The particle size, PDI and zeta potential of the nanoparticles were determined at room temperature using the automatic mode of a Zetasizer Nano ZS from Malvern™ (Malvern Instruments Ltd., Worcestershire, United Kingdom). Size and PDI were measured after dilution to a PLA concentration of 0.10 mg/ml with a 10 mM phosphate buffer pH 7.4, while the zeta potential was determined after dilution to a PLA concentration of 0.20 mg/ml by a 50 mM phosphate buffer pH 7.4 (default settings of the automatic mode of the Zetasizer Nano ZS see supplementary data).

### 2.2.3 Nanoparticle characteristics using various surfactants

Various surfactants for the preparation of PLA-nanoparticles have been intensively examined, above all polyvinyl alcohol (PVA) in several concentrations [32, 34-36], but nevertheless, until now, no comprehensive data covering the whole range of the HLB-value regarding size and PDI of PLA-nanoparticles exist. For this reason, several surfactants covering the whole HLB-range were examined. The surfactants used for this study are listed in the supplementary data **table S1**. All nanoparticles were prepared by the modified double emulsion method and the size and PDI were determined as described previously.

### 2.2.4 Encapsulation efficiency of LRT

The encapsulation efficiency of LRT was determined by reversed phase HPLC (Agilent 1100 Series) using a C18 column (Chromolith® Performance RP-18e, 100-3 mm) applying a linear gradient of 0.1% TFA in water (eluent A) to 0.1% TFA in acetonitrile (eluent B) within 5 minutes according to Uhl et al. [2]. After preparation, the nanoparticles were divided into two samples (1 ml each). The first sample was used to calculate the 100%-value after dissolving the nanoparticles by acetonitrile (1:1 v/v), while the other sample was purified from not entrapped LRT by NAP™-5 size exclusion gel chromatography according to Uhl et al. [2]. After following dissolution by acetonitrile (1:10 v/v), the sample was injected in the HPLC in order to calculate the X-% value of entrapped LRT by the following equation under consideration of different sample volumes:

$$E(\%) = \frac{[AUC]_{LRT \text{ part 2}}}{[AUC]_{LRT \text{ part 1}}}$$

Whereby [AUC] LRT part 2 is the concentration of LRT in the nanoparticles after purification and [AUC] LRT part 1 is the concentration of LRT in the unpurified nanoparticle suspension.

### 2.2.5 Release of LRT

The release of LRT out of the CPP nanoparticles was determined over a period of 28 d. Therefore, the nanoparticles were prepared as described above and the free LRT was removed by size exclusion chromatography (SEC). The amount of LRT after the purification step (day 0) was determined by HPLC and considered as 100% value. Afterwards the nanoparticles were stored at 2-8 °C and samples were taken at 7, 14 and 28 d. These samples were purified again and the remaining amount of LRT was compared with the amount of day 0.

## 2.3 Cryo-EM micrographs

Cryo-TEM was performed as previously described by Kulkarni et al. [39]. Concentrated particles were applied to glow-discharged copper grids and plunge-frozen using a FEI Mark IV Vitrobot (FEI, Hillsboro, OR). Grids were stored in liquid nitrogen until imaged. Grids were moved into a Gatan 70° cryo-tilt transfer system and inserted into the microscope. An FEI LaB6 G2 TEM (FEI, Hillsboro, OR) operating at 200 kV under low-dose conditions was used to image all samples. A bottom-mount FEI Eagle 4K CCD camera was used to capture all images. All samples were imaged at a 55,000 x magnification with a nominal under-focus of 1-3 μm to enhance contrast. Sample preparation and imaging was performed at the UBC Bioimaging Facility (Vancouver, BC).

## 2.4 Peptide synthesis and radiolabeling

### 2.4.1 Synthesis of cyclic R9-CPP by solid phase synthesis

The cyclic cell penetrating peptide Cys-(Arg)<sub>9</sub> (cyc R9-CPP) was synthesized via solid phase peptide synthesis (SPPS) on a chlorotrityl resin (2-CTC) employing the Fmoc/tBu strategy. 117 mg (0.2 mmol) Fmoc-Cys(Trt)-OH dissolved in dichloromethane (DCM) with 5 eq. diisopropylethylamine (DIPEA) were loaded onto 250 mg of 2-CTC for 90 min at RT in order to yield a loading of 0.8 mmol/g. The resin was pre-swelled in DCM. After the coupling of Fmoc-Cys(Trt)-OH to the resin, the uncoupled part of the amino acid was removed by washing with DCM for three times. Subsequently, free reactive sites on the resin were blocked by the addition of DCM/methanol/DIPEA (17/2/1 v/v) for 30 min. Then, the resin was washed with DCM and DMF followed by nine consecutive steps of coupling Fmoc-Arg(Pbf)-OH in DMF, using an excess of 5 eq. amino acid, 4.75 equivalents HBTU and 4 equivalents DIPEA. Fmoc-groups were removed after each coupling by treatment with 20% piperidine in DMF. In between steps, the resin was washed rigorously with DMF. The resulting peptide was then cleaved from the resin with 10% acetic acid and 20% trifluoroethanol in DCM. The procedure was repeated two times for 3 h. The cleavage solution was subsequently evaporated with an excess of toluene for three times for quantitative removal of acetic acid.

The side chain protected peptide was dissolved in DMF in a peptide concentration of 3 mg/ml. Afterwards, the cyclization was performed with 4 equivalents of PyAOP and DIPEA at RT overnight. After stopping the reaction with water, the solution was concentrated to a fiftieth of the starting volume and the side chain protected cyclic peptide precipitated by pouring into cold tButyl-methylether. The precipitated protected cyclic peptide was dried and subsequently deprotected with a mixture of 5% dithioethanol in TFA. Finally, the peptide was precipitated in diethyl ether and centrifuged two times for 5 min at 3000 g. The pellet was dried under vacuum and the peptide was purified via preparative HPLC (Reposil Pur 120 C18-AQ, 5 µm (250 x 25mm), 0 – 30% acetonitrile + 0.1% TFA in 25 min) and the purity of the peptide was confirmed by high resolution mass spectrometry (see supplementary data **figure S1**).

### 2.4.2 Purification of LRT

LRT was isolated out of Victoza®-pens by preparative HPLC (Reposil Pur 120 C18-AQ, 5 µm (250 x 25 mm), 50 – 80% acetonitrile + 0.1% TFA in 25 min) and the purity of LRT was confirmed by high resolution mass spectrometry (see supplementary data **figure S2**)

### 2.4.3 Radiolabeling of LRT

To 25 µl of LRT (1 mM stock solution in 0.25 M phosphate buffer pH 7.5) the required amount of radioactive iodine-125 (<sup>125</sup>I) was added. The radiolabeling was performed using the chloramine T method according to Crim et al. [40]. The reaction mixture was purified by semi preparative HPLC as described by Schieck et al. [41]. Afterwards, the purity of the radiolabeling was determined by radio-HPLC (Agilent 1100 series) using a Chromolith® Performance RP-18e 100-3 mm column applying a linear gradient of 0.1% TFA in water (eluent A) to 0.1% TFA in acetonitrile (eluent B) within 5 minutes; flow rate 2 ml/min; UV absorbance  $\lambda = 214$  nm;  $\gamma$ -detection. The radio-HPLC analysis of the unpurified and the purified <sup>125</sup>I-LRT is shown in the supplementary data, figure S3.

### 2.5 Lyophilisation to obtain long term storage stability

To avoid LRT-release out of the CPP nanoparticles and in order to enable long term storage, the CPP nanoparticles were freeze dried with a main drying carried out at -20 °C for 2 days followed by a secondary drying at 0 °C for at least 6 hours in a Delta 1-20 KD from Martin Christ (Osterode, Germany). Sucrose and trehalose in concentrations of 100 - 700 mM were used as lyoprotector as described previously [42]. Briefly, the nanoparticles were prepared as described above and the required amount of sucrose respectively trehalose was added to the aliquots (50 µl each). Afterwards, the aliquots were shock frozen in liquid nitrogen and freeze dried. In order to assess the quality of the freeze-dried products, the nanoparticles were rehydrated with 50 µl 0.5% (v/v) Tween® 85 in water and the size and PDI were determined by Zetasizer measurements as described above.

### 2.6 Cell binding assays of nanoparticles

#### 2.6.1 Labelling of CPP-modified nanoparticles and LRT with fluorescent dyes

For this cell binding assay, the model substance LRT was labelled with a fluorescent dye (NHS-Atto495, green color). Furthermore, another dye (NHS-Atto610, red color) was coupled to an amine-modified PLA. Both reactions took place in a mixture of PBS (pH 8.3) and DMF (4:1 v/v). After coupling under constant shaking overnight, the mixture of LRT and NHS-Atto495 was lyophilized and dissolved again in a mixture of water and acetonitrile (50:50 v/v). This mixture was purified by preparative HPLC (Reposil Pur 120 C18-AQ, 5 µm (250 x 25mm), 35 – 70%

acetonitrile + 0.1% TFA, 25 min). The success of the purification step was verified by HPLC/MS-analysis. In case of the mixture of amine-modified PLA and NHS-Atto610, the purification was performed by solvent extraction using various volumes of water/chloroform (1:1 v/v).

### **2.6.2 Caco-2 cell binding assay**

Caco-2 cells were kept in culture medium comprising DMEM medium (high glucose) supplied with 20% Fetal Bovine Serum at 37 °C. When cells reached a confluency of 50%, they were washed in pre-warmed DPBS for 10 minutes. Dissociation of the cells was performed using Trypsin-EDTA (0.25%) at 37 °C. The cell suspension was counted using a Neubauer counting chamber. 100.000 cells were seeded into each well of a 48-well plate already containing glass coverslips. On the next day, cells were washed in DPBS and kept in 50% culture medium/50% (v/v) DPBS during the experiment. Cells were incubated with a nanoparticle suspension diluted 1:40 for the time periods indicated. Afterwards, Caco-2 cells were washed four times in DPBS for 5 minutes each and subsequently fixed in 4% formaldehyde/DPBS for 10 minutes on ice. Fixative was removed by washing four times in DPBS at room temperature (RT). Cell nuclei were stained using DAPI diluted 1:1000 in DPBS for 10 minutes at RT. Cells were mounted in Mowiol 4-88 and analyzed using a Nikon Eclipse Ti microscope.

### **2.6.3 Particle retention assay using porcine intestine**

In order to evaluate the mucoadhesion of the CPP nanoparticles in comparison to unmodified particles, a particle retention assay according to Preisig et al. [43, 44] was performed. In brief, the nanoparticle suspension (equal amounts of nanoparticle-lyophilisates were suspended in 250 µl of water) was applied on the pig intestine and incubated for 10 min at 37 °C without any flow. For the incubation time, the flow channel was kept in horizontal position, during the experiment, the assembly was tilted to 45° and the flow was started. The flow (5 ml/min water; total volume = 25 ml; recirculating system) was initiated and samples (200 µl each) were withdrawn at 5, 15, 30, 60 and 120 min. This mucoadhesion assay was performed for each formulation in triplicates. Analysis of the samples (in triplicates) took place by Zetasizer measurements. For these measurements, 50 µl of each sample were diluted with 950 µl of a 10 mM PBS. By means of the derived count rate, the part of the detached nanoparticles could be determined. For the analysis of this assay, the amount of measured particles for each time point was compared with the previous time point (% increase in free particles).



## **2.7 Cytotoxicity assay**

### **2.7.1 Cell cultivation**

The Caco-2 cells were cultivated in DMEM supplemented with 20% Fetal Bovine Serum, 1 mM sodium pyruvate, GlutaMAX® (4 mM L-Alanyl-Glutamine) and 1% non-essential amino acids. The cells were cultured at 37 °C in an atmosphere of 95% air and 5% CO<sub>2</sub>. Subcultures were taken when cells reached 80% confluence.

### **2.7.2 Cytotoxicity assay**

Caco-2 cells were seeded into 96 well plates and grown for 14 days after the formation of a monolayer. Medium was changed every 2 days. Nanoparticles were added in appropriate concentrations and incubated for 3 hours. Subsequently the medium was replaced by growth medium supplemented with 10% Alamar Blue® and the cells were incubated for 3 h. Fluorescence was measured on an Infinite® Tecan Plate reader at a wavelength of 590 nm with an excitation wavelength of 560 nm. The cell viability was normalized to values of wells containing untreated cells and wells without cells as blank.

## **2.8 Proof of concept study: animal trials**

The procedures of this study were approved by the Animal Care and Use Committee at Regierungspräsidium Karlsruhe (Karlsruhe, Germany). For this study, female Wistar rats with a body weight of about 150 - 200 g were used. The model substance LRT was labelled with <sup>125</sup>I and incorporated into the nanoparticles as described previously. 0 - 24 h post oral administration, the LRT uptake was measured by direct counting of the radioactivity in the blood samples. Briefly, three groups (n = 3) of female Wistar rats were formed. Prior to 12 h of the experiment, the rats were kept without food, but with free access to water. Oral application of the nanoparticles and the free peptide took place by gavage. Each rat of group 1 obtained a dose corresponding to 0.5 megabecquerel (MBq) of the labeled free peptide (negative control), while each rat of group 2 obtained a dose corresponding to 0.5 MBq of the unmodified nanoparticles. The rats of group 3 obtained a dose corresponding to 0.5 MBq of the nanoparticles coated with the cyclic R9-CPP. The rats were sacrificed 24 h post oral administration and the radioactivity of all blood samples was measured using a Cobra Auto  $\gamma$ -Counter (Packard Bioscience, USA) in comparison with standards. The radioactivity of the blood samples was related to the total injected dose (ID) and expressed as a percentage of the total injected dose per gram of tissue (%ID/g) as described previously [2, 41].

## 2.9 Statistical analyses

The statistical data were processed using the Prism® software (GraphPad Software, San Diego, CA, USA) and presented as mean  $\pm$  standard deviation of the mean (S.D.). The different groups of the animal trial were compared by unpaired t-test using the Prism® software and considered significant at \* $p < 0.05$ , \*\* $p < 0.01$  and \*\*\* $p < 0.001$ .

## 3. Results and discussion

### 3.1 Nanoparticle characterization

Various surfactants covering the entire HLB-range (1.8 - 29) for the preparation of the surface-modified PLA-nanoparticles were examined (see supplement **table S1**). Tween® 85 and Cremophor® EL (HLB-values = 11 - 12) provided favorable particle size and PDI (data see supplement **figure S4**). Interestingly, the combination of PLA and PVA, a popular combination for nanoparticle preparation [37, 45-47], did not provide comparable results. The average size of the unmodified nanoparticles (prepared using Tween® 85) was in a range of 120 - 220 nm depending on the amount of the model drug LRT incorporated (**figure 2A**). In general, as the LRT concentrations increased, so did the size of the nanoparticles. The size of the CPP-PLA particles was slightly higher than the unmodified PLA particles and showed as well an increase in size with increasing amounts of encapsulated LRT. The same effect was observed on the PDI of the nanoparticles. Compared with the work of Zambaux et al. [37] and Lamprecht et al. [45], where PVA was used as a surfactant, unmodified particles (without drug) had a size of 200 - 250 nm. In contrast, the utilization of Tween® 85 as surfactant could provide nanoparticles with a significant smaller size (approximately 120 nm). This demonstrates the significant influence of the surfactant for the nanoparticle characteristics (see supplement **figure S4**).

The zeta-potential of the CPP-modified nanoparticles showed a strong increase compared with the unmodified nanoparticles due to the positively charged amino acid arginine ( $pK_a$  arginine = 2.17) of the cyclic R9-CPP (**figure 2B**) confirming the successful coupling of the CPP on the surface of the particles [48, 49].

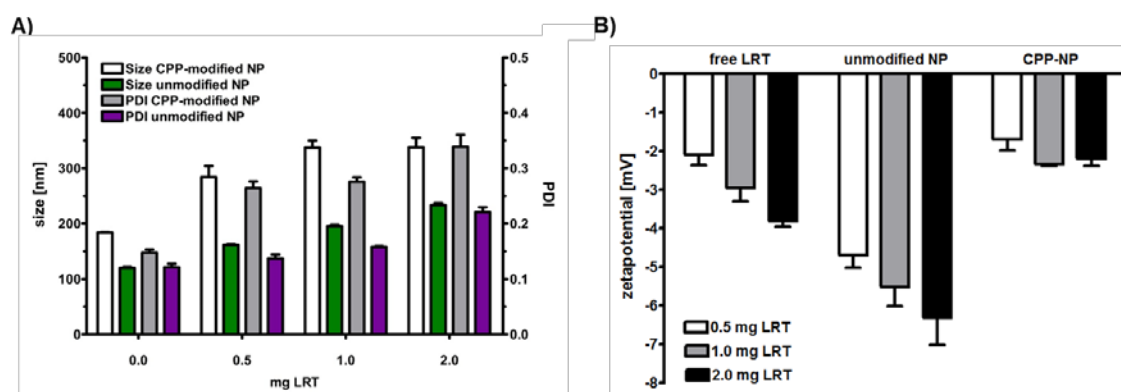


**Figure 2: A)** Size and PDI of unmodified and CPP-modified NP ( $n = 5$ ) without LRT and also with different LRT concentrations (0.5, 1.0 and 2.0 mg of LRT). It could be shown, that both the surface modification of the NP and the incorporation of LRT led to an moderate increase in the size of the NP. In general, CPP-modified NP showed higher size than the unmodified NP. **B)** Zetapotential of different concentrations of LRT (induced by micelle effect) in solution (0.5% Tween® 85 in water) in comparison with the same amounts of LRT incorporated into unmodified NP and CPP-modified NP ( $n = 3$ ). The significant increase of the zetapotential for the CPP-modified NP can be traced to the highly positive charge of the cyclic R9-CPP and therefore demonstrates the successful surface modification of the NP.

### 3.2 Encapsulation efficiency of LRT

The CPP-modified nanoparticles showed an encapsulation efficiency of 70 - 77% depending on the amount of LRT (**figure 3A**). Notably, the amount of LRT in the range of 0.5 - 2 mg had no significant influence on the encapsulation efficiency. In comparison with encapsulation efficiencies obtained for other drugs such as doxorubicin (40 - 70% [50]) and insulin (40% [51] – 70% [18]), the CPP-modified nanoparticles for LRT provided comparable values.

### 3.3 Release of LRT

The release of LRT at various time points is shown in **figure 3B**. A time-depending release of LRT out of nanoparticles could be clearly demonstrated. For this reason, the nanoparticles were freeze-dried to obtain a dosage form with increased storage and particle stability.

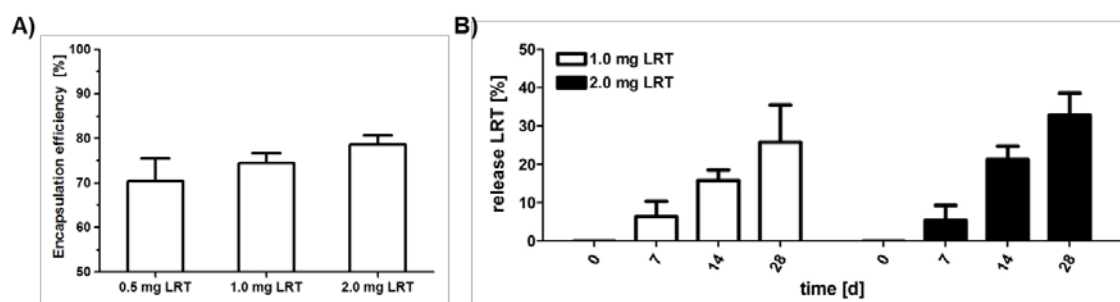


**Figure 3:** A) Encapsulation efficiency of various amounts of LRT in the CPP-modified NP (n = 5). No significant difference between the different LRT concentrations could be observed, demonstrating that the encapsulation efficiency of the CPP-modified NP does not significantly depend on the amount of LRT used in this study. B) Release of LRT out of the nanoparticles at different time points (n = 3). It is clearly shown, that LRT leaks out of the NP by storage at 2 – 8 °C independent of the LRT concentration. Therefore, in following studies, the nanoparticles were freeze-dried in order to obtain a solid dosage form for long term storage.

### 3.4 Cryo-TEM

The Cryo-TEM images of unmodified and CPP-modified nanoparticles verified the size of the particles obtained by dynamic light scattering measurements (**figure 4**). Furthermore, these images showed the high homogeneity of the particle size and surface characteristics. Besides, the samples of both modified and unmodified nanoparticles showed additionally the occurrence of filaments, which can probably be caused by the used polymer PLA. Nevertheless, these additional filaments do not hamper the use of the nanoparticles as oral drug delivery system.

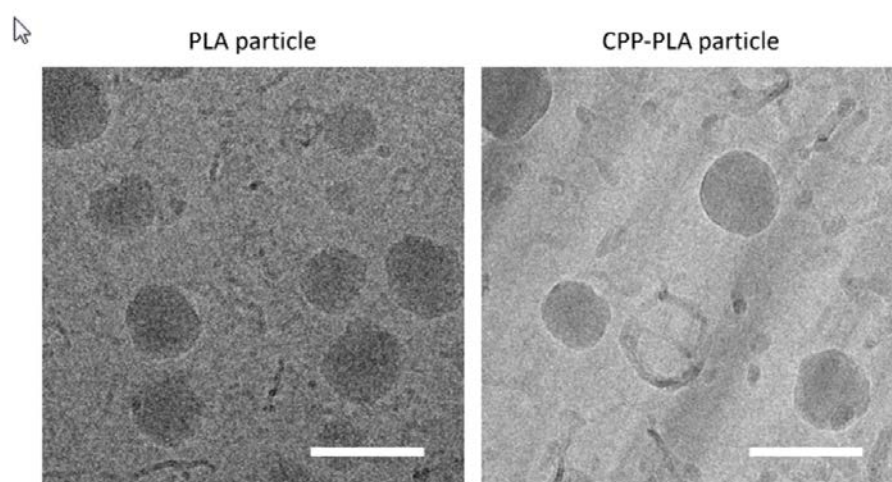


**Figure 4:** Cryo-TEM micrographs of unmodified (left, A) and CPP-modified NP (right, B). The micrographs show no noticeable difference in surface characteristics and size between modified and unmodified NP. But for both formulations the high homogeneity of the particles is obvious.

### 3.5 Freeze-drying

Previous findings [36, 52, 53] also showed, that saccharides as lyoprotectors can provide encouraging results for freeze-drying of nanoparticles. The freeze-drying of CPP-modified nanoparticles suspended in sucrose and trehalose as cryo protective agents was compared at different molar concentrations (100 - 700 mM). At  $\geq 500$  mM sucrose, particle sizes and PDI remained similar to pre-lyophilisation (**figure 5A**). In case of trehalose, the highest concentration of the lyoprotector (700 mM) suggested some protection from an increase in particle size (120 nm prior to lyophilisation and  $\sim 180$  nm after), but sucrose afforded much better preservation of size and PDI. Nevertheless, a further increase in the concentration of the lyoprotector (700 mM sucrose) did not result in vast improvements in protection of the size and PDI.

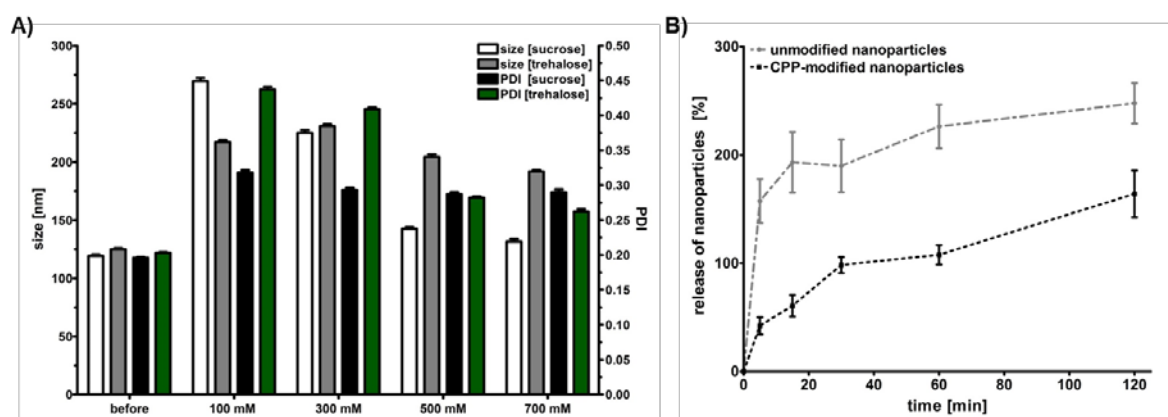


**Figure 5:** A) Size and PDI of the CPP-modified NP before and after freeze drying with two different lyoprotectors (sucrose and trehalose) at various molar ratios ( $n = 3$ ). It is clearly shown that in general, both lyoprotectors show promising results at  $\geq 500$  mM concentration. Higher concentrations of the lyoprotector did not provide better results for NP characteristics. B) Particle retention assay of CPP-modified and unmodified NP using porcine intestine ( $n = 3$ ). A prolonged retention time of the CPP-modified nanoparticles in comparison to unmodified NP is clearly shown.

### 3.6 Particle retention, cytotoxicity and cell-binding assays

The particle retention assay using pig intestine could clearly confirm the prolonged adhesion to pig intestine of the CPP-modified nanoparticles compared to the unmodified particles (**figure 5B**). Regarding the cytotoxicity studies, both, modified and unmodified PLA-nanoparticles showed no significant toxicity in all tested, calculated target concentrations in the Alamar blue® assay (**figure 6A**). Altogether, it could be claimed that the surface-modified nanoparticles are non-toxic in the concentrations tested as previously shown for PLA-nanoparticles in general [54].

The cell binding studies using fluorescent-labeled LRT (green fluorescence, Atto495) and PLA (red fluorescence, Atto610) showed a strongly enhanced binding to Caco-2 cells for the CPP-modified nanoparticles over a period of 60 min (**figure 6B**) compared with the unmodified nanoparticles. Furthermore, the uptake of the fluorescent-labeled LRT was also strongly enhanced for the CPP-modified nanoparticles. Importantly, this enhanced binding of the nanoparticles mediated by the CPP enables a prolonged retention time on the mucus in the intestine probably leading to increased uptake values.

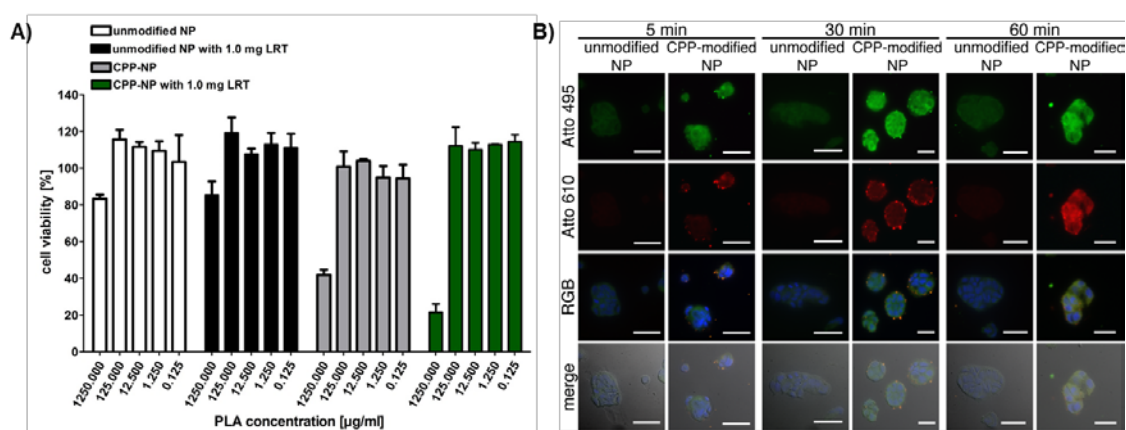


**Figure 6:** A) Cytotoxicity studies of nanoparticles with and without LRT (n = 3). It is clearly shown that both LRT and the surface modification of the nanoparticles with the cyclic R9-CPP do not influence the cytotoxicity of the NP. In general, the nanoparticles show no cytotoxicity in all calculated therapeutic concentrations. B) Caco-2 cell binding assay of nanoparticles containing 0.5 mol-% of an Atto610 dye (red) on their surface. Incorporated into the nanoparticles was LRT coupled to an Atto495 dye (green). Cell binding and uptake of the modified LRT into the Caco-2 cells was determined at various time points (5 min, 30 min and 60 min; scale bar indicates 50 µm). It is clearly shown, that the accumulation of LRT in the Caco-2 cells is dramatically increased (green signal) by the use of the CPP-modified NP in comparison with the control NP.

### 3.7 Proof of concept animal trials

The animal studies demonstrated a significant increase in the blood levels of I-125 labeled LRT for the nanoparticles modified with the cyclic R9 CPP (after oral administration) when compared with free I-125 labeled LRT (**figure 7**). The blood levels of LRT were significantly higher ( $p = 0.0039$ ), which was also observed for the area under the curves (AUCs). The AUC of LRT using CPP-modified nanoparticles (12.70) was 4.5-fold higher than the AUC of free LRT (2.798). Interestingly, unmodified nanoparticles (AUC = 2.818) resulted in nearly the same oral bioavailability as the free peptide drug LRT demonstrating the need of the CPP surface-modification for enhancing oral delivery of peptide drugs. These results strongly highlight the

benefit in the oral availability of LRT by the use of the nanoparticles surface-modified by the cyclic R9 CPP.

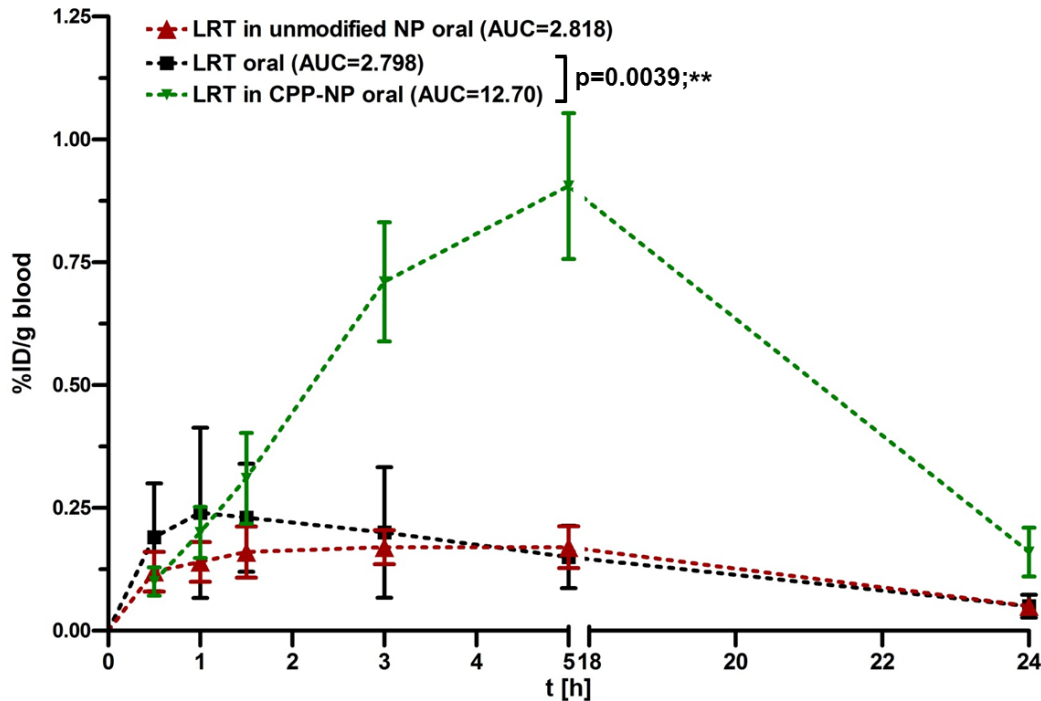


**Figure 7:** Blood levels of I-125 radiolabeled LRT 0-24 h post oral administration (n = 3). LRT encapsulated into the CPP-modified NP showed significantly higher blood levels of LRT than free LRT after oral administration (p=0.0039). Unmodified NP did not enhance the LRT bioavailability.

Thus far, only few examples for oral peptide delivery with CPPs exist. Nielsen et al. [27] and Morishita/Kamei et al. [28, 29] investigated a co-administration strategy of insulin and CPPs and showed a significant benefit for the co-administration strategy. In these studies, linear CPPs were used. In order to improve this, we used a cyclic, arginine-rich cell penetrating peptide with improved enzymatic stability, which was covalently linked to the surface of the nanoparticles. Other studies tried to enhance the peptide stability in the intestine by the incorporation of D-form amino acids [55], which is a less cost-effective strategy when compared to cyclized peptides. By the method used in this study, a strongly enhanced mucosal binding and penetration could be achieved as demonstrated by the Caco-2 binding and uptake assay (**figure 6B**) leading to strongly increased oral availability of LRT (**figure 7**). For a linear R8 peptide, Kamei et al. [56] performed mechanistic studies for the uptake across Caco-2 monolayers and postulated an intestinal epithelial transport via energy-independent pathways. It can be assumed that related pathways also play a role in the penetration of CPP-modified nanoparticles. A particle retention assay using

pig intestine demonstrated the prolonged retention time on the mucus (**figure 5B**), which might influence nanoparticle uptake and therefore the oral bioavailability of the incorporated peptide drug LRT.

Therefore, it could be claimed that the addition of CPPs for oral peptide delivery may enhance the mucosa penetration and could therefore be a promising tool for oral delivery of poorly resorbed drugs [29, 57]. Our studies showed no relevant cytotoxicity for the concentrations of the model R9-CPP tested in our Caco-2 assays (**figure 6A**). These encouraging results strongly recommend the further evaluation of cyclic CPPs as so-called resorption enhancers for peptide delivery.

But with respect to oral peptide delivery and to obtain a bioavailability sufficient for clinical use, further improvements such as prolonged mucosa adhesion obtained possibly by PEGylation as shown by Yang et al. [58] and Wang et al. [59] should be implemented. In addition, further studies need to focus on up-scaling and testing of these nanoparticles in mammals.

## **4. Conclusion**

In this study, a promising oral delivery system for peptide drugs such as the model substance LRT was developed by the surface-modification of common PLA nanoparticles with a cyclic, arginine-rich CPP. A significant benefit of this novel formulation is the absence of toxicity in the tested concentrations on Caco-2 cell assays. Furthermore, a strong dependence of the surfactant's HLB-value for nanoparticle characteristics (size, PDI) was demonstrated. This method also enabled the fast and reproducible preparation of the nanoparticles. The main benefit of this nanoformulation was highlighted by animal trials using female Wistar rats, which showed a significant, 4.5-fold increase of the oral bioavailability of LRT using the surface-modified cyclic-R9 nanoparticles when compared to the free peptide or unmodified nanoparticles.

## **5. Acknowledgement:**

DW is supported by an Early Postdoc Mobility Fellowship from the Swiss National Science Foundation (SNF grant No. 174975). The authors gratefully thank the "Innovationsfond Frontier" (ZUK 49/2 5.2.160) for financial support.



## References

- [1] H. Malhaire, J.-C. Gimel, E. Roger, J.-P. Benoît, F. Lagarce, How to design the surface of peptide-loaded nanoparticles for efficient oral bioavailability?, *Advanced Drug Delivery Reviews*, (2016).
- [2] P. Uhl, F. Helm, G. Hofhaus, S. Brings, C. Kaufman, K. Leotta, S. Urban, U. Haberkorn, W. Mier, G. Fricker, A liposomal formulation for the oral application of the investigational hepatitis B drug Myrcludex B, *European Journal of Pharmaceutics and Biopharmaceutics*, (2016).
- [3] M. Goldberg, I. Gomez-Orellana, Challenges for the oral delivery of macromolecules, *Nature Reviews Drug Discovery*, 2 (2003) 289-295.
- [4] L.M. Ensign, R. Cone, J. Hanes, Oral drug delivery with polymeric nanoparticles: the gastrointestinal mucus barriers, *Advanced Drug Delivery Reviews*, 64 (2012) 557-570.
- [5] G. Fricker, T. Kromp, A. Wendel, A. Blume, J. Zirkel, H. Rebmann, C. Setzer, R.-O. Quinkert, F. Martin, C. Müller-Goymann, Phospholipids and lipid-based formulations in oral drug delivery, *Pharmaceutical Research*, 27 (2010) 1469-1486.
- [6] G. Gaucher, P. Satturwar, M.-C. Jones, A. Furtos, J.-C. Leroux, Polymeric micelles for oral drug delivery, *European Journal of Pharmaceutics and Biopharmaceutics*, 76 (2010) 147-158.
- [7] S. Sajeesh, K. Bouchemal, V. Marsaud, C. Vauthier, C.P. Sharma, Cyclodextrin complexed insulin encapsulated hydrogel microparticles: An oral delivery system for insulin, *Journal of Controlled Release*, 147 (2010) 377-384.
- [8] J. Parmentier, B. Thewes, F. Gropp, G. Fricker, Oral peptide delivery by tetraether lipid liposomes, *International Journal of Pharmaceutics*, 415 (2011) 150-157.
- [9] K. Gradauer, S. Dünnhaupt, C. Vonach, H. Szöllösi, I. Pali-Schöll, H. Mangge, E. Jensen-Jarolim, A. Bernkop-Schnürch, R. Prassl, Thiomers-coated liposomes harbor permeation enhancing and efflux pump inhibitory properties, *Journal of Controlled Release*, 165 (2013) 207-215.
- [10] K. Gradauer, J. Barthelmes, C. Vonach, G. Almer, H. Mangge, B. Teubl, E. Roblegg, S. Dünnhaupt, E. Fröhlich, A. Bernkop-Schnürch, Liposomes coated with thiolated chitosan enhance oral peptide delivery to rats, *Journal of Controlled Release*, 172 (2013) 872-878.
- [11] M. Werle, H. Takeuchi, Chitosan-aprotinin coated liposomes for oral peptide delivery: development, characterisation and in vivo evaluation, *International Journal of Pharmaceutics*, 370 (2009) 26-32.
- [12] K.Y. Win, S.-S. Feng, Effects of particle size and surface coating on cellular uptake of polymeric nanoparticles for oral delivery of anticancer drugs, *Biomaterials*, 26 (2005) 2713-2722.
- [13] F. Cui, K. Shi, L. Zhang, A. Tao, Y. Kawashima, Biodegradable nanoparticles loaded with insulin-phospholipid complex for oral delivery: preparation, in vitro characterization and in vivo evaluation, *Journal of Controlled Release*, 114 (2006) 242-250.
- [14] C. Damgé, P. Maincent, N. Ubrich, Oral delivery of insulin associated to polymeric nanoparticles in diabetic rats, *Journal of Controlled Release*, 117 (2007) 163-170.
- [15] S.-S. Feng, L. Mei, P. Anitha, C.W. Gan, W. Zhou, Poly (lactide)-vitamin E derivative/montmorillonite nanoparticle formulations for the oral delivery of Docetaxel, *Biomaterials*, 30 (2009) 3297-3306.
- [16] X. Zhang, M. Sun, A. Zheng, D. Cao, Y. Bi, J. Sun, Preparation and characterization of insulin-loaded bioadhesive PLGA nanoparticles for oral administration, *European Journal of Pharmaceutical Sciences*, 45 (2012) 632-638.
- [17] A.j. Tao, D.m. Cun, L.q. Zhang, K. Shi, Preparation of insulin loaded PLGA-Hp55 nanoparticles for oral delivery, *Journal of Pharmaceutical Sciences*, 96 (2007) 421-427.
- [18] B. Sarmiento, A. Ribeiro, F. Veiga, P. Sampaio, R. Neufeld, D. Ferreira, Alginate/chitosan nanoparticles are effective for oral insulin delivery, *Pharmaceutical Research*, 24 (2007) 2198-2206.
- [19] J. Sheng, L. Han, J. Qin, G. Ru, R. Li, L. Wu, D. Cui, P. Yang, Y. He, J. Wang, N-trimethyl chitosan chloride-coated PLGA nanoparticles overcoming multiple barriers to oral insulin

- absorption, *ACS applied Materials & Interfaces*, 7 (2015) 15430-15441.
- [20] C. Foged, H.M. Nielsen, Cell-penetrating peptides for drug delivery across membrane barriers, *Expert Opinion on Drug Delivery*, 5 (2008) 105-117.
- [21] E. Koren, V.P. Torchilin, Cell-penetrating peptides: breaking through to the other side, *Trends in Molecular Medicine*, 18 (2012) 385-393.
- [22] M. Zorko, Ü. Langel, Cell-penetrating peptides: mechanism and kinetics of cargo delivery, *Advanced Drug Delivery Reviews*, 57 (2005) 529-545.
- [23] M. Lindgren, M. Hällbrink, A. Prochiantz, Ü. Langel, Cell-penetrating peptides, *Trends in pharmacological sciences*, 21 (2000) 99-103.
- [24] N. Schmidt, A. Mishra, G.H. Lai, G.C. Wong, Arginine-rich cell-penetrating peptides, *FEBS letters*, 584 (2010) 1806-1813.
- [25] H.D. Herce, D. Schumacher, A.F. Schneider, A.K. Ludwig, F.A. Mann, M. Fillies, M.-A. Kasper, S. Reinke, E. Krause, H. Leonhardt, Cell-permeable nanobodies for targeted immunolabelling and antigen manipulation in living cells, *Nature Chemistry*, (2017).
- [26] H.D. Herce, D. Schumacher, A.F. Schneider, A.K. Ludwig, F.A. Mann, M. Fillies, M.-A. Kasper, S. Reinke, E. Krause, H. Leonhardt, Cell-permeable nanobodies for targeted immunolabelling and antigen manipulation in living cells, *Nature Chemistry*, 9 (2017) 762.
- [27] E.J.B. Nielsen, S. Yoshida, N. Kamei, R. Iwamae, E.-S. Khafagy, J. Olsen, U.L. Rahbek, B.L. Pedersen, K. Takayama, M. Takeda-Morishita, In vivo proof of concept of oral insulin delivery based on a co-administration strategy with the cell-penetrating peptide penetratin, *Journal of Controlled Release*, 189 (2014) 19-24.
- [28] M. Morishita, N. Kamei, J. Ehara, K. Isowa, K. Takayama, A novel approach using functional peptides for efficient intestinal absorption of insulin, *Journal of Controlled Release*, 118 (2007) 177-184.
- [29] N. Kamei, M. Morishita, Y. Eda, N. Ida, R. Nishio, K. Takayama, Usefulness of cell-penetrating peptides to improve intestinal insulin absorption, *Journal of Controlled Release*, 132 (2008) 21-25.
- [30] D. Mandal, A. Nasrolahi Shirazi, K. Parang, Cell-Penetrating Homochiral Cyclic Peptides as Nuclear-Targeting Molecular Transporters, *Angewandte Chemie International Edition*, 50 (2011) 9633-9637.
- [31] A.L. McDonell, U. Kiiskinen, D.C. Zammit, R.W. Kotchie, P.-O. Thuresson, C. Nicolay, T. Haslam, M. Bruinsma, A.-J. Janszen-Van Oosterhout, T. Otto, Estimating the real world daily usage and cost for exenatide twice daily and liraglutide in Germany, the Netherlands, and the UK based on volumes dispensed by pharmacies, *ClinicoEconomics and outcomes research: CEOR*, 7 (2015) 95.
- [32] A. Astrup, S. Rössner, L. Van Gaal, A. Rissanen, L. Niskanen, M. Al Hakim, J. Madsen, M.F. Rasmussen, M.E. Lean, N.-S. Group, Effects of liraglutide in the treatment of obesity: a randomised, double-blind, placebo-controlled study, *The Lancet*, 374 (2009) 1606-1616.
- [33] K. Raun, P. von Voss, C.F. Gotfredsen, V. Golozoubova, B. Rolin, L.B. Knudsen, Liraglutide, a long-acting glucagon-like peptide-1 analog, reduces body weight and food intake in obese candy-fed rats, whereas a dipeptidyl peptidase-IV inhibitor, vildagliptin, does not, *Diabetes*, 56 (2007) 8-15.
- [34] J. Jin, G.E. Sklar, V.M.S. Oh, S.C. Li, Factors affecting therapeutic compliance: A review from the patient's perspective, *Therapeutics and Clinical Risk Management*, 4 (2008) 269.
- [35] D.S. Youngblood, S.A. Hatlevig, J.N. Hassinger, P.L. Iversen, H.M. Moulton, Stability of cell-penetrating peptide-morpholino oligomer conjugates in human serum and in cells, *Bioconjugate Chemistry*, 18 (2007) 50-60.
- [36] W. Abdelwahed, G. Degobert, S. Stainmesse, H. Fessi, Freeze-drying of nanoparticles: formulation, process and storage considerations, *Advanced Drug Delivery Reviews*, 58 (2006) 1688-1713.
- [37] M. Zambaux, F. Bonneaux, R. Gref, P. Maincent, E. Dellacherie, M. Alonso, P. Labrude, C.

- Vigneron, Influence of experimental parameters on the characteristics of poly (lactic acid) nanoparticles prepared by a double emulsion method, *Journal of Controlled Release*, 50 (1998) 31-40.
- [38] Y.-P. Li, Y.-Y. Pei, X.-Y. Zhang, Z.-H. Gu, Z.-H. Zhou, W.-F. Yuan, J.-J. Zhou, J.-H. Zhu, X.-J. Gao, PEGylated PLGA nanoparticles as protein carriers: synthesis, preparation and biodistribution in rats, *Journal of Controlled Release*, 71 (2001) 203-211.
- [39] J.A. Kulkarni, M.M. Darjuan, J.E. Mercer, S. Chen, R. van der Meel, J.L. Thewalt, Y.Y.C. Tam, P.R. Cullis, On the Formation and Morphology of Lipid Nanoparticles Containing Ionizable Cationic Lipids and siRNA, *ACS Nano*, 12 (2018) 4787-4795.
- [40] J.W. Crim, S.F. Garczynski, M.R. Brown, Approaches to radioiodination of insect neuropeptides, *Peptides*, 23 (2002) 2045-2051.
- [41] A. Schieck, A. Schulze, C. Gähler, T. Müller, U. Haberkorn, A. Alexandrov, S. Urban, W. Mier, Hepatitis B virus hepatotropism is mediated by specific receptor recognition in the liver and not restricted to susceptible hosts, *Hepatology*, 58 (2013) 43-53.
- [42] M. Ausborn, H. Schreier, G. Brezesinski, H. Fabian, H.W. Meyer, P. Nuhn, The protective effect of free and membrane-bound cryoprotectants during freezing and freeze-drying of liposomes, *Journal of Controlled Release*, 30 (1994) 105-116.
- [43] D. Preisig, M. Weingartner, F.J. Varum, R. Bravo, R. Alles, J. Huwyler, M. Puchkov, Marker-ion analysis for quantification of mucoadhesivity of microparticles in particle-retention assays, *International Journal of Pharmaceutics*, 487 (2015) 157-166.
- [44] D. Preisig, R. Roth, S. Tognola, F.J. Varum, R. Bravo, Y. Cetinkaya, J. Huwyler, M. Puchkov, Mucoadhesive microparticles for local treatment of gastrointestinal diseases, *European Journal of Pharmaceutics and Biopharmaceutics*, 105 (2016) 156-165.
- [45] A. Lamprecht, N. Ubrich, M.H. Perez, C.-M. Lehr, M. Hoffman, P. Maincent, Influences of process parameters on nanoparticle preparation performed by a double emulsion pressure homogenization technique, *International Journal of Pharmaceutics*, 196 (2000) 177-182.
- [46] M. Zambaux, F. Bonneaux, R. Gref, E. Dellacherie, C. Vigneron, Preparation and characterization of protein C-loaded PLA nanoparticles, *Journal of Controlled Release*, 60 (1999) 179-188.
- [47] R.A. Petros, J.M. DeSimone, Strategies in the design of nanoparticles for therapeutic applications, *Nature Reviews Drug Discovery*, 9 (2010) 615-627.
- [48] E.L. Snyder, S.F. Dowdy, Cell penetrating peptides in drug delivery, *Pharmaceutical research*, 21 (2004) 389-393.
- [49] S. Deshayes, M. Morris, G. Divita, F. Heitz, Cell-penetrating peptides: tools for intracellular delivery of therapeutics, *Cellular and Molecular Life Sciences CMLS*, 62 (2005) 1839-1849.
- [50] H. Wang, Y. Zhao, Y. Wu, Y.-l. Hu, K. Nan, G. Nie, H. Chen, Enhanced anti-tumor efficacy by co-delivery of doxorubicin and paclitaxel with amphiphilic methoxy PEG-PLGA copolymer nanoparticles, *Biomaterials*, 32 (2011) 8281-8290.
- [51] J.M. Barichello, M. Morishita, K. Takayama, T. Nagai, Encapsulation of hydrophilic and lipophilic drugs in PLGA nanoparticles by the nanoprecipitation method, *Drug Development and Industrial Pharmacy*, 25 (1999) 471-476.
- [52] Y.N. Konan, R. Gurny, E. Allémann, Preparation and characterization of sterile and freeze-dried sub-200 nm nanoparticles, *International Journal of Pharmaceutics*, 233 (2002) 239-252.
- [53] D. Quintanar-Guerrero, A. Ganem-Quintanar, E. Allémann, H. Fessi, E. Doelker, Influence of the stabilizer coating layer on the purification and freeze-drying of poly (D, L-lactic acid) nanoparticles prepared by an emulsion-diffusion technique, *Journal of Microencapsulation*, 15 (1998) 107-119.
- [54] K. Hu, J. Li, Y. Shen, W. Lu, X. Gao, Q. Zhang, X. Jiang, Lactoferrin-conjugated PEG-PLA nanoparticles with improved brain delivery: in vitro and in vivo evaluations, *Journal of Controlled Release*, 134 (2009) 55-61.
- [55] N. Kamei, M. Morishita, Y. Kanayama, K. Hasegawa, M. Nishimura, E. Hayashinaka, Y.

Wada, Y. Watanabe, K. Takayama, Molecular imaging analysis of intestinal insulin absorption boosted by cell-penetrating peptides by using positron emission tomography, *Journal of Controlled Release*, 146 (2010) 16-22.

[56] N. Kamei, Y. Onuki, K. Takayama, M. Takeda-Morishita, Mechanistic study of the uptake/permeation of cell-penetrating peptides across a caco-2 monolayer and their stimulatory effect on epithelial insulin transport, *Journal of Pharmaceutical Sciences*, 102 (2013) 3998-4008.

[57] N. Kamei, M. Morishita, K. Takayama, Importance of intermolecular interaction on the improvement of intestinal therapeutic peptide/protein absorption using cell-penetrating peptides, *Journal of Controlled Release*, 136 (2009) 179-186.

[58] M. Yang, S.K. Lai, Y.Y. Wang, W. Zhong, C. Happe, M. Zhang, J. Fu, J. Hanes, Biodegradable nanoparticles composed entirely of safe materials that rapidly penetrate human mucus, *Angewandte Chemie International Edition*, 50 (2011) 2597-2600.

[59] Y.Y. Wang, S.K. Lai, J.S. Suk, A. Pace, R. Cone, J. Hanes, Addressing the PEG mucoadhesivity paradox to engineer nanoparticles that “slip” through the human mucus barrier, *Angewandte Chemie International Edition*, 47 (2008) 9726-9729.

## 4. Discussion

### 4.1 FCC for the delivery of peptide drugs – Validity of the model system

To prove the applicability of FCC for the delivery of PD, the stability of these peptides is of highest priority. Like for small molecules, compatibility of the ingredients of a formulation must be guaranteed. Besides microbiological examination, the stability test for formulations containing small molecule drugs, includes the confirmation of content and the absence of degradation products. Since PD can undergo structural rearrangement without changing their molecular weight, one has to demonstrate, that the activity is maintained. For this purpose, lysozyme and BSA were used as model substances [119]. Lysozyme is a well-studied enzyme, that has been used as a model throughout the literature [87,120–123]. It is therapeutically used in marketed products, where it acts against gram positive bacteria. However, the question arises, whether it represents a good model to demonstrate the compatibility of an excipient, e.g. FCC. First, every enzyme or protein behaves different under various conditions, e.g. isoelectrical precipitation. Therefore, it is not possible to generalize findings, which were obtained using one model enzyme. Second, lysozyme is described in literature as a hard protein with spherical shape [124–127]. As mentioned previously, hard proteins have a high structural stability and can withstand relatively harsh conditions. Therefore, lysozyme might not be sensitive/fragile enough to reflect degrading effects caused by the surface of FCC. Nevertheless, lysozyme is interesting since it has a high PI of 10.7 leading to a positive charge at a physiological pH. Same characteristic is valid for cationic peptide antibiotics which represent an interesting class of API for local delivery. It is also a counterpart to BSA, which has an PI of 4.7 [128]. Similar to lysozyme, BSA has also been used extensively as a model protein in pharmaceutical and other applications [89,129,130]. The molecule is well known and several studies have investigated the influence of various parameters on its structure [131–133]. In contrast to lysozyme it is categorized as a soft protein with a flexible structure and it is known to adsorb to a variety of surfaces [86,134,135]. This makes it an ideal model to study adsorption related phenomena. Within the scope of this work BSA did not show structural changes after being released from FCC. It was also shown, that BSA adsorbs strongly to the surface of FCC, which was confirmed by sorption experiments (data not shown). Drawback of the study was the fact, that only the structure of released BSA and lysozyme could be measured with circular dichroism (CD) spectroscopy, but not the structure of BSA and lysozyme that was immobilized on the surface of FCC. Therefore, BSA that was immobilized on the surface of the particles was in fact not included in the measurement. In order to accomplish a complete separation of BSA from FCC, it would have been necessary to dissolve the particle by lowering the pH, which would have introduced additional parameters making it impossible to attribute

structural changes to either surface interaction or changed external factors such as pH or ionic strength. To study the structure of proteins that are adsorbed on a surface, CD was already used [136]. However, a prerequisite for such measurement is that the size of the particles should be in the nano range for two reasons. First, the background becomes the dominating signal in case of large particles. Secondly, large particles sediment too fast for the measurement to be carried out. Eventually, the experiments could only confirm, that the released fraction of both models (lysozyme and BSA) did not undergo structural changes.

## **4.2 Incomplete release of BSA**

Experiments have demonstrated, that BSA shows incomplete release from FCC [119]. At the lowest DLs 2% w/w, the fraction that was released was only  $26.9 \pm 9.7$  % after 160 min. Sorption experiment have confirmed strong association of BSA molecules with FCC (data not shown). In the study it was speculated, that the adsorption of BSA might be caused by the opposite charges of the molecule and the surface. However, sorption experiment at different pH could not confirm this assumption (data not shown).

If the incomplete release is caused by irreversible adsorption of BSA to the surface of FCC, the adsorbed amount has to be considered as a loss, which reduces the efficiency of the delivery device. Assuming irreversible adsorption to the carrier in form of a monolayer, the volume that is occupied by this monolayer can be roughly estimated: Monolayers created by BSA molecules have been reported to have a thickness of approx.  $0.87 \pm 0.03$  to  $1.74 \pm 0.39$  nm and is estimated to be in the same range for other proteins [137–139].

FCC OG-500 has a specific surface area of  $55.4 \text{ m}^2/\text{g}$ . Assuming a peptide layer thickness of 1 nm across the entire surface, the amount of peptides [% w/w] that will be adsorbed to FCC is approximately 7.2%. For highly potent PD, this amount is not acceptable. For example, the weight of one international unit (IU) of human insulin is 0.035mg. It seems obvious, that for PD, surface enlargement for increased dissolution rate is not required, but can decrease the efficiency of a formulation by retaining large amounts of actives. Therefore, it is suggested to use carriers with smaller surface area and larger pores for the delivery of substances with a tendency of irreversible surface binding. Additionally, larger pores might lead to improved drug loading, since the filling of small pores was less pronounced as shown by FIB/SEM analysis [140].

As described in the introduction, the adsorption and desorption of peptides is dependent on several factors such as temperature, ionic strength, and pH. Therefore, co-loading of substances which promote desorption could increase the efficiency of a delivery system. It was demonstrated, that substances like glycerol and

trehalose, as well as increased salinity, reduce the adsorption to hydrophilic and hydrophobic surfaces [141,142]. Another approach to overcome the problems associated with surface binding is modification of the surface. Polyethyleneglycols (PEG) and polyglycerol coatings are known to effectively reduce the protein adsorption to solid surfaces like glass vials or medical devices [143–146]. Garapaty and Champion demonstrated, that phosphorylcholines can effectively reduce protein adsorption to micro and nanoparticles [147].

### 4.3 Modified release

The release of large and small molecules from FCC was measured [63,119]. Experiments using lysozyme as model substance showed relatively fast release from FCC [119]. Since it is the goal, to keep a mucoadhesive delivery device on the site of interest for a prolonged period of time, strategies that allow for extended/slow release are indispensable [63]. Release studies with metronidazole benzoate have shown, that loading into FCC leads to increased dissolution rates when compared to unprocessed drug if mucoadhesive chitosan coating was not added. This was mainly attributed to increased surface area as well as amorphisation of the drug. Even though, release was found to be influenced by chitosan coatings, the reduced dissolution rate was mainly a result of particle agglomeration and resulting reduced surface area [63]. This was shown visually in USP IV dissolution apparatus and supported by release experiments. The comparison between low and medium molecular weight chitosans showed no significant differences with respect to release kinetics, while higher amounts led to intensified agglomeration resulting in reduced surface area and hence reduced dissolution rates. Although chitosan was described in literature as a matrix material and has been used successfully to reduce dissolution rates of drugs, the mentioned delivery systems were large, compared to an FCC particle [148–150]. Therefore, the ability to reduce the dissolution rate from an individual microparticle when chitosan is used as a coating with a thickness of a few micrometers remains questionable. More efficient in prolonging the dissolution is the use of polymers, which are only soluble in organic solvents. This would allow for much thinner coatings, and thus maintain the particles size. So far, the downside is a general limitation to small molecules, since organic solvents have great potential to degrade PD [124]. An elegant strategy to overcome the issue of PD degradation is a controlled deposition of the sensitive material in deeper regions of the particle and subsequent encapsulation.

Besides coating, the release from porous microparticles is also controlled by the porous meshwork. The elongated diffusion pathway reduces the rate of mass exchange with the surrounding medium. However,

a prerequisite for such an approach is a precise and controlled spatial deposition of a drug within a certain region of the FCC microparticle.

#### 4.4 Penetration of liquids into pores

Penetration of liquids (solutions) into the porous structure of FCC is a critical step during the loading process, as well as for later release because it might control mass transport of substances within the particle. To estimate the potential of a solvent to penetrate into FCC particles, a simple method was used (figure 12A): The weight of an object, which is submersed in water can be calculated when the volume and the density of the displaced liquid is known. The skeletal volume of FCC can be measured with helium pycnometry. A tensiometer registers the weight of a sample, which is submerged in the liquid of interest. Using equation 5 gives information about the pore volume  $V_A$ , which is accessible by the liquid of interest:

$$V_A = \frac{W_I}{W_S - (V_S \cdot \rho_L)} \quad (5)$$

where  $W_I$  is the experimentally registered weight of the immersed sample,  $W_S$  is the sample weight,  $V_S$  is the skeleton volume of the sample, and  $\rho_L$  is the density of the liquid of interest.

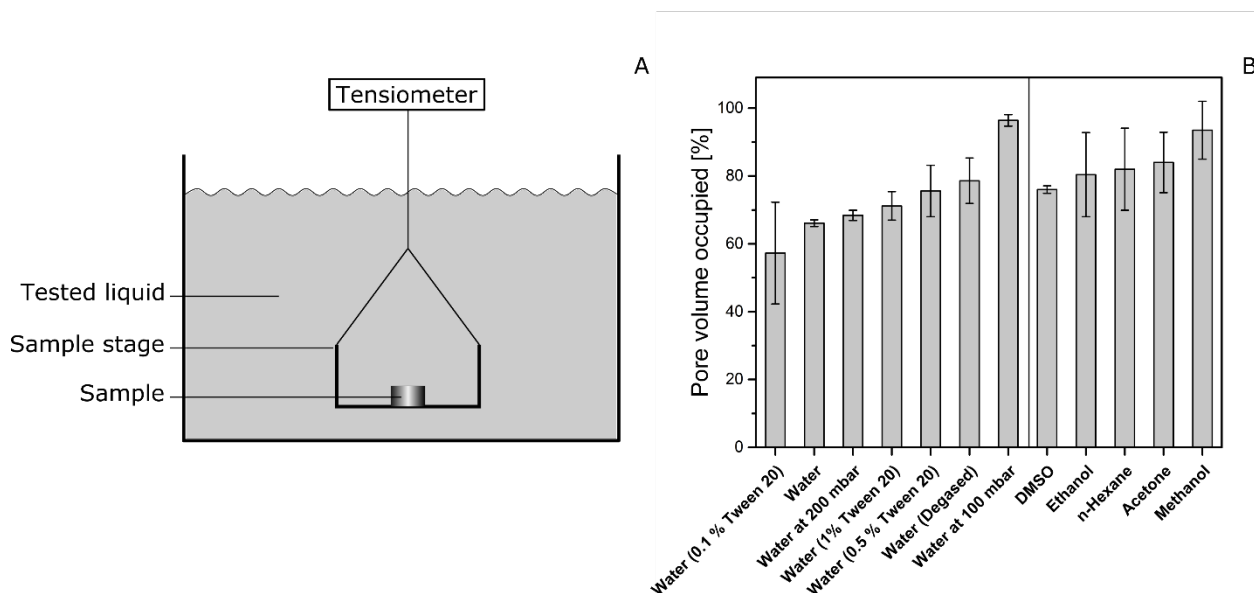


Figure 12: Liquid penetration into FCC. A) Schematic representation of the experimental setup to study liquid penetration into FCC. B) The graph represents the fraction of the total pore volume, which is accessible for a solvent within 10 min.



Observations from pore filling experiments indicate facilitated penetration of liquids with lower surface tension and viscosity. Under atmospheric pressure, only methanol showed superior pore filling abilities compared to water, even when higher concentrations of surfactants (1% v/v) were used (figure 12B). This is in agreement with the results from image analysis, where deeper deposition of DPPC was attributed to facilitated penetration of the methanol based solution [140]. Controversially, penetration experiments have shown, that water penetrates very efficiently into FCC when a vacuum is applied, which applied for BSA loading in the rotary evaporator. Therefore, the final deposition of the loaded material is not only dependent on penetration into pores, but likely also on mass migration towards the periphery during the drying process. Confirming almost complete penetration of water into FCC when vacuum is applied is a valuable information, since water is the preferred solvent for production and the most appropriate solvent when working with PD.

Besides loading, liquid penetration also plays a fundamental role during the release of a substance: Where the dissolution medium has no access, dissolution will not take place. This might cause insufficient release, e.g. in case of mucoadhesive formulations where the particle is not supposed to be dissolved in the acidic environment of the stomach. It was shown by researchers, that under certain conditions, liquid penetration into small cavities is a very slow process, that can take several hours to days even though relatively large cavities were chosen in the experiments (60  $\mu\text{m}$ ) [151]. It was shown, that drug release can be controlled by displacement of air [152]. Figure 13 shows the mechanism of air displacement during pore filling. Initially, air is entrapped in the pore due to surface tension and resulting contact angle. Liquid evaporates into the pore and initiates capillary condensation in corners and narrow areas. At the same time, entrapped air starts to dissolve into the liquid phase. When liquids are degassed prior to penetration, entrapped air will dissolve at a higher rate into the liquid phase, hence the volume of entrapped air will be reduced quicker. Both mass transfer processes continuously reduce the volume of the entrapped air until eventually growing condensates and an advancing liquid front fuse and the entrapped air bubble will be released.

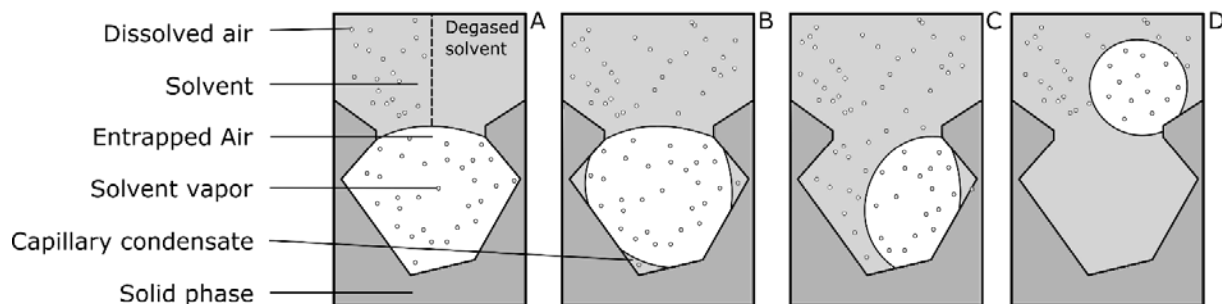


Figure 13: Mechanism of air displacement. A) Air is entrapped as a result of surface tension and counteracting pressure, air starts dissolving into liquid phase (process is faster in degassed solvents). B) Evaporation of liquid phase into pore, followed by capillary condensation in space restricted areas. C) Condensates grow until fusing with outer liquid phase. D) Entrapped air is displaced.

Obviously, the situation changes, when pores are loaded with drugs or other materials. The mechanisms involved in pore penetration might change due to modification of the surface of the pores, e.g. hydrophobic compounds, which lead to increased contact angle and therefore prolonged time for penetration. In contrast to a hydrophobic compound, a hydrophilic, soluble material might accelerate penetration due to an erosion controlled contribution to the process. Assuming a layer of a water soluble compound inside the pores, one can imagine a water front advancing along the soluble material layer, accelerating the connection of the liquid phase at the opening and the condensate in the pore. Additionally, hygroscopic substances would accelerate the condensation in the pores.

#### 4.5 Strategies to maximize drug load

To facilitate the administration of a dosage form, size reduction is an important factor [153–155]. Therefore, maximizing drug load is a key strategy, when using porous drug carriers. Drug loading of FCC led to predominant material deposition on the surface of the particles. Based on previously discussed observations from FIB-SEM [140] and liquid penetration (figure 12B), it is assumed, that material deposition on the surface of FCC is at least partially caused by mass migration towards the periphery of the particle during the drying process. Therefore, strategies to reduce this mass flow are discussed in the next section.

A promising strategy to counteract peripheral mass flow is freeze drying. Once the pores of FCC are filled, freeze drying would immobilize drug solution. The solvents could then be removed by sublimation, which causes less mass migration compared to evaporation from a liquid phase [156].

Another approach is the loading with solid solutions where solvents are replaced by polymers. Drugs could therefore be dissolved in molten polymers and loaded into FCC, where the solution solidifies. Alternatively, *in situ* polymerization might be beneficial for thermolabile materials such as PD. The particle shown in figure 14 supports this hypothesis: It shows an FCC particle that was loaded with cyanoacrylate under vacuum and analyzed with FIB-SEM. However, the two mentioned strategies (freeze drying and solid solution) are based on solvents or polymer, which transport drugs into pores. Drawback of these approaches is the limited solubility of most drugs. For example: ibuprofen is highly soluble in acetone (607 mg/ml [102]). Taking into account its density (1.03 g/cm<sup>3</sup>), the volume occupied by the drug accounts for 59% v/v. This means, that 41 % of the available pore volume is occupied by the solvent. Assuming no mass migration during solvent removal, this leads to incomplete filling of pores. Multiple cycle loadings could help to reduce the remaining volume to a minimum, but is less attractive in terms of cost effectiveness, especially when considering less soluble materials, where the volume fraction of the solvent is considerably higher.

As an alternative, solvent free methods should be considered. Therefore, using melts of pure drugs would be an efficient method to fill pores completely, since no volume fraction is occupied by solvents. Unfortunately, this method is not suitable for PD, since they rather denature, than melt at elevated temperature. The following table 3, gives an overview on drugs, which might be suitable to be loaded into FCC as melts.

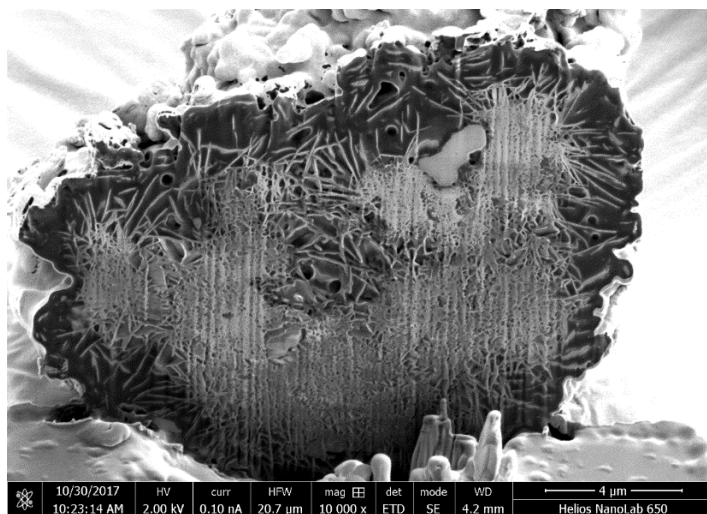


Figure 14: FIB-SEM of resin filled FCC after loading (vacuum assisted). Mass migration towards the periphery might be reduced when resins cure inside the pores.

Table 3: Common drugs and their melting temperature

Drug	Indication	Dose	Melting Point [°C]	Solubility/Solvent [mg/ml]	Stable for process
Acetaminophen	Pain	500 mg	159-169	14 in water, ethanol	Yes [157]
Alprazolam	Anxiety	6 mg/d	228	ethanol	-
Amitryptine	Depression	100 mg/d	196	10 in water	-
Nifedipine	High blood pressure	50 mg	135-173	0.056 mg in water	Yes [158]
Amoxicillin	Bacterial infection	200-1000 mg	194	water	Yes [159]
Lorazepam	Anxiety	1-4 mg	168	0.08 in water	-
Atorvastatin	High cholesterol	10-80 mg	159-197	0.012 in water	Yes [160]
Azithromycin	Bacterial infection	200-500 mg	113	Insoluble in water	-
Ciprofloxacin	Bacterial infection	500 mg	320	-	Degradation [159]
Citalopram	Depression	10-40 mg	182	slightly in water ethanol	Yes [162]
Clonazepam	Anticonvulsant	0.5 mg	238	-	-
Codeine	Cough	50 mg	156	9 in Water	-
Gabapentin	Seizure	3600 mg/d	167	-	-
Ibuprofen	Pain	200-800 mg	76	0.021 in water	-
Lisinopril	High blood pressure	2.5-20 mg/d	148	97 water 14 in methanol	-
Loratadin	Allergies	10 mg	136	slightly in acetone and methanol	-
Lorazepam	Anxiety	1-2.5 mg	168	0.08 in water	-

<b>Losartan</b>	Blood high pressure	50 mg	184	-	-
<b>Pregabalin</b>	Seizure	100-600 mg/d	188	freely soluble in water	-
<b>Meloxicam</b>	NSAID		254	0.007 in water	-
<b>Metformin</b>	Diabetes	500-1000 mg	220	-	-
<b>Metoprolol</b>	High blood pressure	25-200 mg	124	-	-
<b>Naproxen</b>	Pain, inflammation	250-500 mg	152	slightly in water	-
			246		
<b>Omeprazol</b>	Reflux, ulcers	20-40 mg	156	0.08 in water	-
				Methanol, ethanol, dichlormethan	
<b>Oxycodone</b>	Pain	5-80 mg	219	Ethanol, chloroform	-
<b>Pantoprazole</b>	Reflux, ulcers	20-40 mg	140	water	-
				slightly in ethanol	
<b>Tramadol</b>	Pain	50 mg	181	water	-
<b>Trazodone</b>	Depression, sleep-dissorders	50-100 mg	87	0.03 in water	-
<b>Sildenafil</b>	Erectile dysfunction	25-100 mg	189	4 in water	-
<b>Bupropion</b>	Depression	150-300 mg	234 (Hydrochlorid)	320 in water	-
<b>Alprazolam</b>	Anxiety, Panic	4 mg/d	228	ethanol	-
<b>Norfloxazin</b>	Bacterial infeciton		228	slightly in water, ethanol and aceton	Yes [163]

#### 4.6 Mucoadhesion

The mucoadhesive properties of chitosan coated FCC [63] as well as PLA [manuscript submitted] nanoparticles were evaluated, using the particle retention assay developed by Preisig et al. The aim of this section is to point out the advantages and disadvantages of the two experimental setups and not to compare the mucoadhesive properties of the formulations. Table 4 provides a comparison of the experimental setup which are important for the assessment of mucoadhesion when using a flow cell.

Table 4: Comparison of the experimental parameters of the different particle retention assays.

Formulation:	Chitosan coated FCC	PLA nanoparticles
Mucosa origin:	Porcine colon	Porcine small intestine
Mucoadhesive polymer:	Chitosan	PLA
Particle application:	Dry, manual distribution	Suspended in 250 µl of water
Incubation time [s]:	5	10
Flow rate [ml/min]:	20	5
Quantification:	Capillary electrophoresis	Dynamic light scattering (Zetasizer)

The tissues were chosen according to the intended site of application to ensure physiological conditions as close as possible. The small intestine had a smoother surface and a more consistent thickness compared to the colon, which was decorated with large folds. The smooth surface of the small intestine allowed for a continuous film to flow over the surface at lower flow rates. In contrast, when flow rates less than 20ml/min were used, complete immersion of the colonic tissue could not be insured, causing high variability of the experiments. The use of tissue from animal origin might be closer to the conditions *in vivo*, but brings a lot of variability, such as surface irregularities as well as differences within the mucus layer due to inconsistent preparation procedure like sectioning and washing. Additionally, acquisition of fresh animal tissue can be challenging. Therefore, artificial substrates that provide the conditions similar to those found on mucus membranes would lead to standardized surface properties ensuring reproducible flow.

FCC particles were distributed manually as a dry powder. Due to the large size of the particles, relatively homogenous distribution on the mucosa could be confirmed visually. Nevertheless, small inconsistencies could not be avoided, e.g. particles on top of each other or attracted by electrostatic forces to the acrylic flow cell. The PLA nanoparticles were applied as a suspension which was fast and precise, meaning that no material was misplaced. In contrast to the FCC particles, PLA nanoparticles are not detectable, therefore no visual control of the retained particles is possible. The visual detection was possible for FCC particles, which was very useful to detect outliers and problems with inconsistent flow pattern. It is well known, that prehydrated polymers have decreased mucoadhesive properties when compared to particles, which are hydrated by the mucus layer, promoting interpenetration of the polymer chains. Prehydrated application might closer represent *in vivo* conditions but the effect of mucoadhesion might not be detected due to insufficient sensitivity.

Incubation time for the particles was 5 and 10 minutes for FCC and PLA particles, respectively. Contact time between particle and mucosa affects the mucoadhesive strength and is considered to be an important factor. When particles are applied as dry powder, the contact time can be exactly determined. When particles are applied as a dispersion, measurement of the contact time is not as precise, since the particles require a certain time to sediment to the mucosa, especially for particles in the nanometer range [164].

Detached FCC particles were quantified by measuring calcium ion concentration using capillary electrophoresis. Unfortunately, calcium ions appear in most tissues and can influence the results of the measurement. This requires blank runs of the mucosa that is used. The nanoparticles were quantified by DLS in a Zetasizer, where it was not possible to distinguish between nanoparticles and particles originating from the mucosa, e.g. detached cell compartments and residual fecal mass. Blank runs had to be performed, still leading to detachment of more than 100 % of the applied particles. Therefore, only relative but no absolute information can be obtained from the experiment.

In both tissues, either through small fissures or by diffusion, the washing medium accumulated between the tissue and the acrylic support, leading to the formation of a bulge, which in some cases altered the flow pattern of the washing media. To avoid forming a bulge, a perforated support would probably solve the problem.

The dispersibility of the mucoadhesive FCC formulation was improved *in vitro* by the addition of colloidal silica. It was concluded, that a dry coating with silica particles prevents the mucoadhesive FCC particles from agglomerating. Dispersibility was studied in a USP 4 flow through dissolution system. Compared to the situation found *in vivo*, the viscosity of the medium is in orders of magnitude lower, which might lead

to wrong interpretation of the results. Mixing of high viscosity fluids such as intestinal contents is characterized by increased shear forces on one hand, but decreased turbulences and diffusion on the other hand. Increased shear forces have a deagglomerating effect, which would naturally increase the dispersibility of the delivery system within the GIT. Unfortunately, a homogeneous distribution of particles in a high viscosity fluid requires much more time, due to missing eddy currents, and reduced mobility of the particles [164].

A variety of polymeric delivery systems with promising mucoadhesive potential as well as multiple methods for mucoadhesive evaluation are described in the literature. All described methods are isolated and artificial systems that mainly focus on interactions between mucin and a polymer, but no method takes into account on how formulations reach the targeted mucosa when considering *in vivo* conditions. Formulations, intended to adhere to intestinal tissues, are exposed to peristalsis as well as to the shearing contents of the digestive system. The consistency of the chyme changes dramatically along the digestive system from almost liquid in the oral cavity to solid in the colon, indicating that a streaming film of water does not reflect realistic conditions of the small intestine and colon. Therefore, the experimental setups chosen in the scope of this work might be more suited for the evaluation of delivery systems for the oral cavity.

More realistic methods to evaluate the effectiveness of a mucoadhesive system for drug delivery should take into account the fact, that initial contact between particles and mucosa cannot be controlled (homogenous distribution of particles on the mucosa and incubation time). Additionally, this includes the viscosity of relevant fluids and closer imitation of forces involved at a specific site of application (e.g. peristalsis vs. tongue movement). Most test methods for particulate systems take particle retention as a measure for mucoadhesion. In a more realistic approach, particles would be suspended in the medium, while passing along a mucosal substrate. Decrease in particle concentration in the medium would deliver more valuable information on a systems effectiveness.



#### 4.7 Colloidal electrospray for drug loading and coating of microparticles

Preliminary results of the experiments are presented and discussed in this section.

The aim of this pilot test was to estimate the potential of the colloidal electrospinning/ spraying process when applied to FCC in order to eventually improve the loading of substances into the particle as well as using the technique to coat individual particles. Two different setups were tested: Setup (A) was a classical assembly, with a plate collector intended for the collection of fibers containing large particles such as FCC. For setup (B), the spray was accelerated through a ring collector and subsequently dried and collected in a cyclone. Figure 13 shows a scheme of the two different setups.

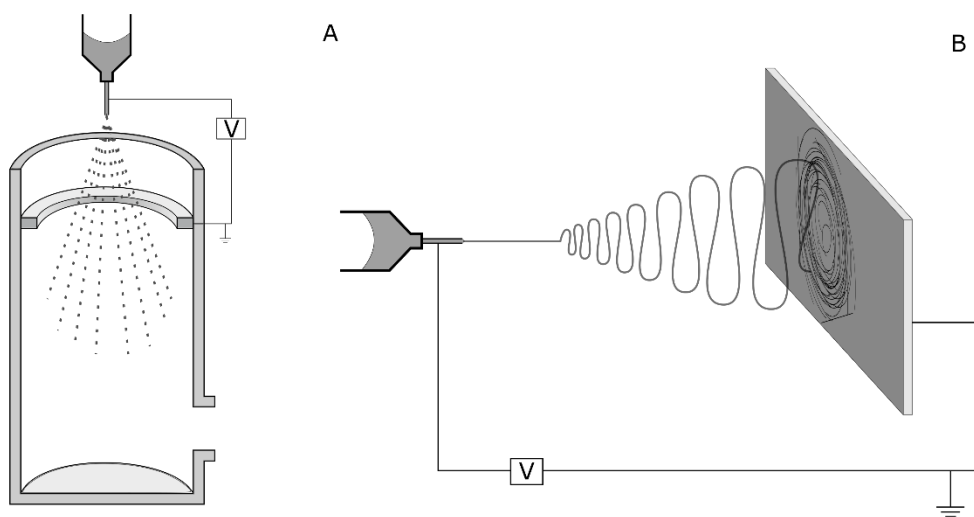


Figure 15: Setups for colloidal electrospraying and electrospinning. A) Colloidal electrospray is accelerated through a grounded ring collector. Subsequently, the electrosprayed particles dry during the time of flight towards the collector cyclone (not shown in figure). B) Classical electrospinning setup: Spinneret is connected to high voltage supply. Fibers are collected on a grounded collector plate.

**Methods:** Different compositions for the spray dispersion have been tried ranging from 10-15% (w/v) PCL in chloroform-methanol mixtures and 0.5-2% w/v chitosan in the ethanol-water-acetic acid mix. The voltage was varied between 5 and 20 kV, distance to the collector ranged from 50 -300 mm, and the feed rate was chosen between 10 and 100  $\mu\text{l}/\text{min}$ . All experiments were performed only once, environmental conditions such as relative humidity and temperature were not considered or documented.

Composition of the used dispersions:

(A) 10 g of polycaprolactone (PCL) was dissolved in a chloroform-methanol mix (75:25 v/v. then 20 g of FCC was added and mixed using a magnetic stirrer.

(B) 0.5 g of high molecular weight chitosan was dissolved in 100 ml of a mix of ethanol, water and acetic acid (25:73:2 v/v/v) and vacuum filtered through 10  $\mu\text{m}$  filter paper. Subsequently, 10% w/v of BSA was added to the solution and finally 10% w/v of FCC was suspended.

Table 5 lists the settings of the two different setups A and B.

*Table 5: Parameters and settings of the two different electrospray/ spin setups.*

Process:	A) Electrospinning	B) Electro spraying
Collector Type:	Plate	Ring +Cyclone
Voltage [kV]:	10	10-15
Distance to collector [mm]:	150	70
Feedrate [ $\mu\text{l}/\text{min}$ ]:	10-20	10-20

**Results and discussion:** Preparation of the dispersion for electrospinning was straightforward. PCL dissolved well in the solvent mix and filtration was not required. Electrospinning of purely organic solutions produced a stable spray/fiber that was collected on a cover glass mounted on a brass plate. Figure 16A shows a light microscopy of the spun fibers with a polarizing filter. The bright spots are FCC particles, which are integrated into PCL fibers. The fibers had a diameter of approx. 1  $\mu\text{m}$ .

Electrospraying of the aqueous dispersion was not as straightforward as the electrospinning of the organic dispersion. Maintaining a stable spray was difficult and the sprays behavior changed during the process. Large fractions of the product accumulated on the collector ring and the interior wall of the drying tube and cyclone as a crust. The particles that were collected in the cyclone are shown in figure 16B, C, and D. The particles were spherical, had a smooth surface and were in the same size range as the raw FCC particles. Figure 16B shows the appearance of agglomerates, as well as particles, that are smaller than regular FCC.

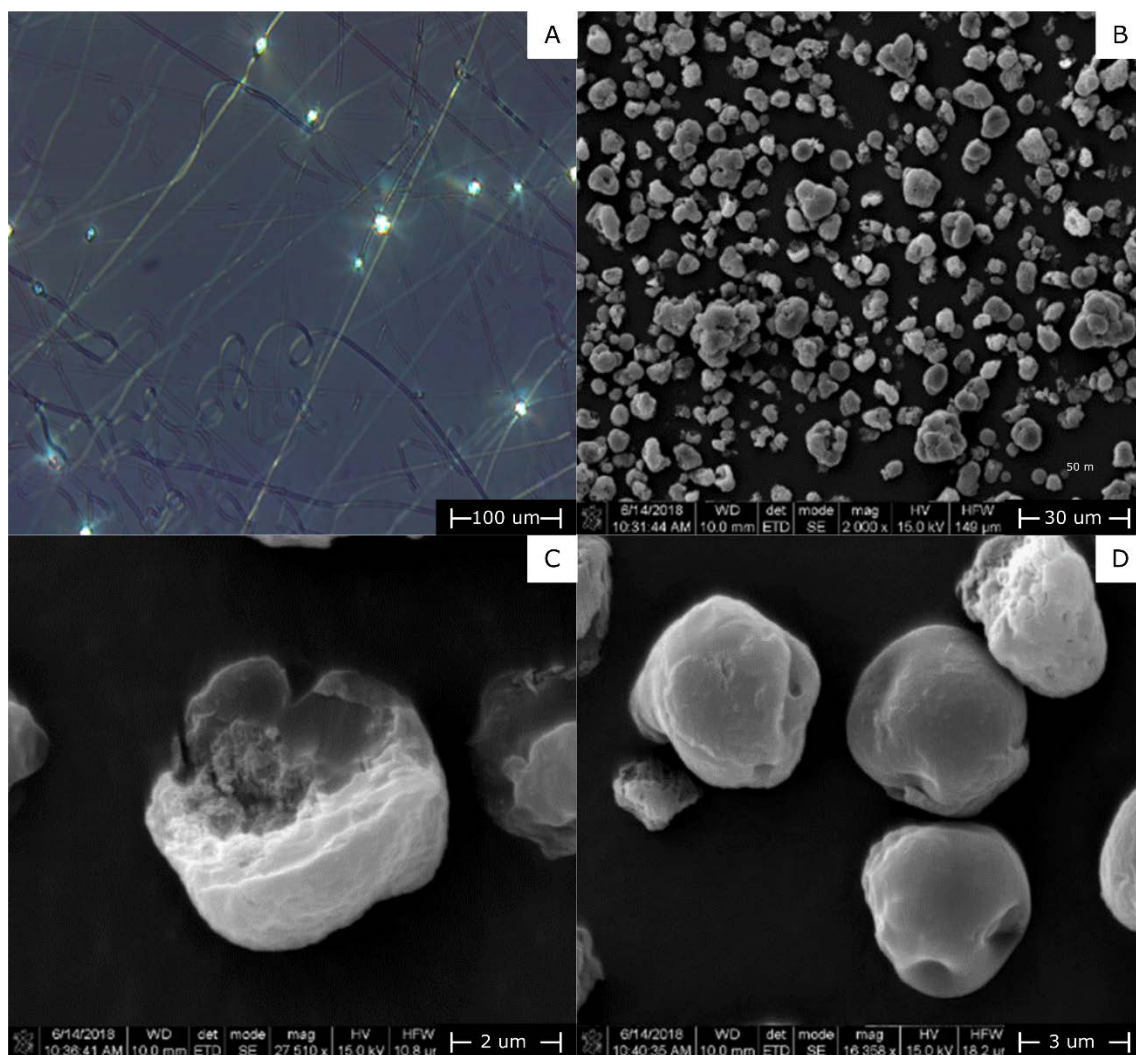


Figure 16: SEM pictures of electrospayed/electrospun particles and fibers. A) Images of electrospun FCC integrated into PCL fibers. B) Electrospayed FCC coated with chitosan/BSA. Bigger agglomerates as well as small probably spray dried polymer particles. C) A broken particle clearly shows an integrated individual FCC particle. D) Smooth surface of the spherical particles.

The following section discusses the observations from the electrospray experiment, and highlights the benefits when it is used in combination with other industrial processes, which have been applied to FCC.

Morphology of the particles was spherical with a relatively smooth surface. The samples also showed large amounts of agglomerated particles as well as smaller particles which might not contain FCC. This clearly shows the need for further improvement of the technique.

One of the main problems when preparing the chitosan solutions was the fact that acetic acid, which is necessary to dissolve chitosan, also causes FCC to dissolve. Therefore, the concentration of acetic acid

needed to be kept as low as possible, which limits the solubility of the polymer. Secondly, the high viscosity of chitosan solutions even at low concentrations (0.5% w/w) made the vacuum filtration through filters < 10  $\mu\text{m}$  difficult. Filtration of chitosan solutions is necessary, since the used chitosan contained large amounts of impurities. For the spraying process, it was noted, that the addition of ethanol was beneficial to stabilize the spray, disadvantage was the poor miscibility of the aqueous chitosan solution with the ethanol, which was a limiting factor for the amount of ethanol that could be used. Whether the use of ethanol has a denaturizing effect on BSA was not investigated. Organic solvents are known to have both, stabilizing and destabilizing effects on proteins, e.g. it was shown, that 2.5% v/v of ethanol inhibits denaturation in hemoglobin, while 0.25 % v/v of toluene increases the proteins denaturation by factor 4 and both effects were concentration dependent [165].

The above mentioned strategies of drug loading by using a solvent free approach or replacing solvents by polymers might lead to optimized deposition of drug within pores. A previous study on FCC has demonstrated the feasibility of hot melt extrusion (HME) for the production of FCC-PCL composite material. The produced extrudates were cryomilled for further processing. Although, the intention was not to load PCL into FCC, this work points out, that the process leads to the formation of a continuous polymer matrix containing embedded FCC particles, with PCL filling interparticulate pores. It was shown, that the production of water impermeable composite material is achievable with this method. However, from SEM pictures it is visible, that the final particles after cryomilling are rough and have a size of approx. 10-100 fold larger than the original FCC particles [166]. Additionally, the occurrence of polymers that are not associated with FCC particles cannot be avoided (see figure 17).

Spray drying is a commonly used method to produce particles in the micrometer range, by removing solvents from individual polymer solution droplets. Colloidal spray drying of polymer solutions that contain FCC particles has been tried in the course of this work (data not shown). The formed particles were agglomerates, similar to those produced by fluidized bed coating [63]. The main reason for the formation of agglomerates was assumed to be the size of the droplets which is likely to exceed the size of an FCC particle. This leads to the occurrence of multiple particles per droplet, and finally to the formation of agglomerates. To reduce the droplet size, higher atomization pressures are required, resulting in elevated shear stress. The limiting factor in a classical spray dryer is therefore the nozzle, which is not able to produce droplets small enough to enclose a single particle.

Hot melt extrusion has demonstrated its capability of producing water impermeable composite material, while spray drying enables the production of smooth and completely coated agglomerates. Drawbacks of

these processes were additional milling steps (particle destruction) for HME and particle agglomeration for spray drying.

A potential solution to overcome the drawbacks of an additional milling step as well as limitations of a classical spray nozzle is the use of an electrospray. In contrast to classical one- or two-fluid nozzles whose principles rely on pressurized liquids or the interaction of liquids and gases at high speed, the electrospray uses high electric potentials to disperse a liquid into a fine aerosol. This results in smaller individual particles with a smooth continuous coating. In addition, loading of materials into deeper pores of the FCC particle could be more pronounced, due to high pressures involved in the HME process [167]. However, this assumption still needs to be confirmed by FIB-SEM. As mentioned before, high temperatures in molten polymers might be not suitable to process PD. Therefore, solvent based approaches have to be considered. Even though, the principle of solvent evaporation is not as attractive as *in situ* solidification of polymers, colloidal electrospraying might still improve the loading and coating process of FCC.

The drying process during electrospraying differs from conventional methods such as solvent evaporation from bulk. The particles are isolated from each other and interparticulate pores are not present. This leads to a more homogenous material distribution in the final bulk as well as improved association with the particles. For bulk drying, the interparticulate voids account for additional pore volume, in which material will be deposited preferentially as it was observed by image analysis [140]. This leads to increased deposition on the particles surface. The material in the interparticulate voids will form solid bridges, leading to agglomerates of different size and shape.

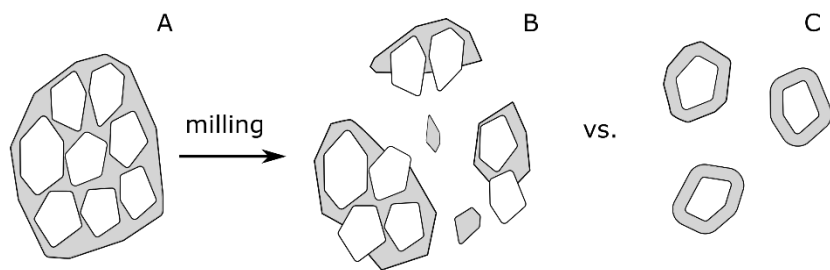


Figure 17: Milling vs, colloidal electrospray. A) Particles produced with fluidized bed, solvent evaporation or HME are agglomerates, that have to be milled to reduce the particle size, which leads to the occurrence of irregular shapes, fractures and defective surface coverage. C) Individual particles produced by colloidal electrospray.

Whether material deposition within deeper regions of the particles is favored by an electrospray process is not clear but following consideration should be taken into account affecting material distribution within the porous particles. First, the pressure within a droplet which surrounds a particle increases with decreasing diameter. The pressure difference or Laplace pressure  $\Delta P$  [Pa] can be estimated by equation 6:

$$\Delta P = \frac{2\gamma}{r}, \quad (6)$$

where  $\gamma$  is the surface tension [N/m], and  $r$  is the radius of the drop [m]. For a water droplet ( $\gamma=72$  mN/m) with a diameter of 10  $\mu\text{m}$  (size range of FCC),  $\Delta P = 0.288$  bar, which might be insignificant. However, for smaller droplets  $\Delta P$  becomes very large, e.g. 28.8 bar for a 100 nm diameter droplet. These increased pressures might be beneficial for loading processes, due to additional forces acting on a penetrating liquid. Second, the drying process is much shorter: While drying from bulk might take several hours, electrosprayed particles dry within the time of flight to the cyclone. This is reported to have an effect on mass exchange with the exterior or material flow within the particle. Third, the formation of a skin or shell on the droplets surface has been reported to have an influence on the redistribution of substances as well [168].

## 5. Conclusion and Outlook

The aim of this work was to explore the possibilities and limitations of FCC for the delivery of PD with emphasis on mucoadhesive formulations, as well as to improve the loading of substances in and onto the particle. The following chapter summarizes the findings of the study and suggests further investigation to optimize the systems performance.

This work has demonstrated the feasibility of FCC as a carrier for local delivery of PD. The used model substances lysozyme and BSA were loaded into the porous particles. Dissolution experiments in a closed channel flow cell pointed out the individual release behavior of the models. While lysozyme was released completely from all formulations, large fractions of BSA were bound to the particles indicating strong adsorption. The substances were mainly loaded on the particles surface and no difference could be evaluated between the spatial deposition of the different model peptides. Circular dichroism and Michaelis-Menten experiments demonstrated structural stability and enzymatic activity, respectively. Two model substances were used in order to demonstrate compatibility of FCC with PD. However, compatibility of FCC with PD cannot be generalized. Therefore, compatibility studies have to be carried out for other cases individually. Further investigation should also focus on the phenomenon of peptide adsorption to the carrier in order to improve the efficacy of the delivery system especially for highly potent (low dose) drugs. Another open question which should be addressed is the potential of FCC to protect sensitive cargo from forces that occur during tableting or other industrial processes.

A scalable process to manufacture mucoadhesive particles using fluidized bed equipment was developed and the mucoadhesive potential of the produced formulations was evaluated in a customized flow cell via particle retention assay. The produced particles were agglomerates in the size range of approx. 100  $\mu\text{m}$  and showed good *in vitro* particle retention on porcine mucosa. Dispersibility of the formulation was improved by the addition of fumed silica particles. Dissolution rate was slightly reduced for larger particles mainly due to reduced surface area to volume ratio. Future research in this area should focus on more realistic test methods for the evaluation of mucoadhesive systems.

A concept for the investigation of material distribution within porous microparticles was developed. Therefore, results from MIP were compared with results from image analysis in order to spot the limitations of each method. It was concluded, that MIP is not able to provide accurate information on spatial material distribution, since it does not allow to differentiate between filled and clogged pores. Image analysis demonstrated, that material distribution is dependent on physical characteristics of the loaded material.

Findings suggest, that loading of melts or *in situ* curing polymers would improve material deposition in deeper regions of FCC. The internal structure of FCC was revealed for the first time and earlier assumptions could be disproved. The use of a focused ion beam to study material distribution has great potential for the optimization of drug loading. Therefore, future research should focus on techniques to control the spatial material deposition within the porous structure of microparticles.

Within the scope of this work, several techniques to improve loading and coating of FCC have been evaluated. Colloidal electrospray was the only technique which showed convincing results with respect to coating of individual FCC particles. This application has great industrial potential, since it enables the production of coated particles with a size of approx. 10 micrometers or less. This is attractive for pharmaceutical applications, e.g. for the development of solid, multiparticulate formulations such as mucoadhesive systems. Besides coating, the technique provides unique conditions for drug loading, since individual particles can dry in absence of interparticulate pores. The presented results show clearly, that intensive improvement of the technique is necessary. Development of a flexible lab-scale prototype to further explore the possibilities and limitations of the system would be the next logical step and might result in the discovery of new applications for FCC.



## 6. References

- [1] M.J. John, V. Jaison, K. Jain, N. Kakkar, J.J. Jacob, Erythropoietin use and abuse, *Indian J. Endocrinol. Metab.* 16 (2012) 220–227. doi:10.4103/2230-8210.93739.
- [2] R.E.W. Hancock, R. Lehrer, Cationic peptides: a new source of antibiotics, *Trends Biotechnol.* (1998) 82–88.
- [3] S. Frokjaer, D.E. Otzen, Protein drug stability: a formulation challenge, *Nat. Rev. Drug Discov.* 4 (2005) 298–306. doi:10.1038/nrd1695.
- [4] A.A. Kaspar, J.M. Reichert, Future directions for peptide therapeutics development, *Drug Discov. Today*. 18 (2013) 807–817. doi:10.1016/j.drudis.2013.05.011.
- [5] D.J. Craik, D.P. Fairlie, S. Liras, D. Price, The Future of Peptide-based Drugs, *Chem. Biol. Drug Des.* 81 (2013) 136–147. doi:10.1111/cbdd.12055.
- [6] J. Oleck, S. Kassam, J.D. Goldman, Commentary: Why Was Inhaled Insulin a Failure in the Market?, *Diabetes Spectr. Publ. Am. Diabetes Assoc.* 29 (2016) 180–184. doi:10.2337/diaspect.29.3.180.
- [7] R.C. Fellner, S.T. Terryah, R. Tarran, Inhaled protein/peptide-based therapies for respiratory disease, *Mol. Cell. Pediatr.* 3 (2016). doi:10.1186/s40348-016-0044-8.
- [8] T.K. Ghosh, W.R. Pfister, *Drug Delivery to the Oral Cavity; Molecules to Market*, CRC Press, 2005.
- [9] K.Y. Lum, S.T. Tay, C.F. Le, V.S. Lee, N.H. Sabri, R.D. Velayuthan, H. Hassan, S.D. Sekaran, Activity of Novel Synthetic Peptides against *Candida albicans*, *Sci. Rep.* 5 (2015). doi:10.1038/srep09657.
- [10] P.-W. Tsai, C.-Y. Yang, H.-T. Chang, C.-Y. Lan, Human antimicrobial peptide LL-37 inhibits adhesion of *Candida albicans* by interacting with yeast cell-wall carbohydrates, *PloS One*. 6 (2011) e17755. doi:10.1371/journal.pone.0017755.
- [11] S. Paulone, A. Ardizzoni, A. Tavanti, S. Piccinelli, C. Rizzato, A. Lupetti, B. Colombari, E. Pericolini, L. Polonelli, W. Magliani, S. Conti, B. Posteraro, C. Cermelli, E. Blasi, S. Peppoloni, The synthetic killer peptide KP impairs *Candida albicans* biofilm in vitro, *PLoS ONE*. 12 (2017). doi:10.1371/journal.pone.0181278.
- [12] L. Zhang, W.K.K. Wu, R.L. Gallo, E.F. Fang, W. Hu, T.K.W. Ling, J. Shen, R.L.Y. Chan, L. Lu, X.M. Luo, M.X. Li, K.M. Chan, J. Yu, V.W.S. Wong, S.C. Ng, S.H. Wong, F.K.L. Chan, J.J.Y. Sung, M.T.V. Chan, C.H. Cho, Critical Role of Antimicrobial Peptide Cathelicidin for Controlling *Helicobacter pylori* Survival and Infection, *J. Immunol.* 196 (2016) 1799–1809. doi:10.4049/jimmunol.1500021.
- [13] P. Su, Y. Li, H. Li, J. Zhang, L. Lin, Q. Wang, F. Guo, Z. Ji, J. Mao, W. Tang, Z. Shi, W. Shao, J. Mao, X. Zhu, X. Zhang, Y. Tong, H. Tu, M. Jiang, Z. Wang, F. Jin, N. Yang, J. Zhang, Antibiotic Resistance of *Helicobacter Pylori* Isolated in the Southeast Coastal Region of China, *Helicobacter*. 18 (2013) 274–279. doi:10.1111/hel.12046.
- [14] M.M. Gerrits, A.H. van Vliet, E.J. Kuipers, J.G. Kusters, *Helicobacter pylori* and antimicrobial resistance: molecular mechanisms and clinical implications, *Lancet Infect. Dis.* 6 (2006) 699–709. doi:10.1016/S1473-3099(06)70627-2.
- [15] K.D. Fine, L.R. Schiller, AGA Technical Review on the Evaluation and Management of Chronic Diarrhea, *Gastroenterology*. 116 (1999) 1464–1486. doi:10.1016/S0016-5085(99)70513-5.

- [16] G.R. Corazza, M.G. Menozzi, A. Strocchi, L. Rasciti, D. Vaira, R. Lecchini, P. Avanzini, C. Chezzi, G. Gasbarrini, The diagnosis of small bowel bacterial overgrowth: Reliability of jejunal culture and inadequacy of breath hydrogen testing, *Gastroenterology*. 98 (1990) 302–309. doi:10.1016/0016-5085(90)90818-L.
- [17] A.C. Dukowicz, B.E. Lacy, G.M. Levine, Small Intestinal Bacterial Overgrowth, *Gastroenterol. Hepatol*. 3 (2007) 112–122.
- [18] P. Singh, A. Arora, T.A. Strand, D.A. Leffler, C. Catassi, P.H. Green, C.P. Kelly, V. Ahuja, G.K. Makharia, Global Prevalence of Celiac Disease: Systematic Review and Meta-analysis, *Clin. Gastroenterol. Hepatol*. 16 (2018) 823–836.e2. doi:10.1016/j.cgh.2017.06.037.
- [19] J. Gass, M.T. Bethune, M. Siegel, A. Spencer, C. Khosla, Combination Enzyme Therapy for Gastric Digestion of Dietary Gluten in Patients With Celiac Sprue, *Gastroenterology*. 133 (2007) 472–480. doi:10.1053/j.gastro.2007.05.028.
- [20] J. Ehren, S. Govindarajan, B. Morón, J. Minshull, C. Khosla, Protein engineering of improved prolyl endopeptidases for celiac sprue therapy, *Protein Eng. Des. Sel*. 21 (2008) 699–707. doi:10.1093/protein/gzn050.
- [21] T. Marti, Ø. Molberg, Q. Li, G.M. Gray, C. Khosla, L.M. Sollid, Prolyl Endopeptidase-Mediated Destruction of T Cell Epitopes in Whole Gluten: Chemical and Immunological Characterization, *J. Pharmacol. Exp. Ther*. 312 (2005) 19–26. doi:10.1124/jpet.104.073312.
- [22] M. Hamosh, R.O. Scow, Lingual Lipase and Its Role in the Digestion of Dietary Lipid, *J. Clin. Invest*. 52 (1973) 88–95.
- [23] S.C.G. Tseng, M.J. Jarvinen, W.G. Nelson, J.-W. Huang, J. Woodcock-Mitchell, T.-T. Sun, Correlation of specific keratins with different types of epithelial differentiation: Monoclonal antibody studies, *Cell*. 30 (1982) 361–372. doi:10.1016/0092-8674(82)90234-3.
- [24] A. Davies, G. Munding, J. Vriens, K. Webber, A. Buchanan, M. Waghorn, The Influence of Low Salivary Flow Rates on the Absorption of a Sublingual Fentanyl Citrate Formulation for Breakthrough Cancer Pain, *J. Pain Symptom Manage*. 51 (2016) 538–545. doi:10.1016/j.jpainsymman.2015.11.018.
- [25] S.P. Humphrey, R.T. Williamson, A review of saliva: Normal composition, flow, and function, *J. Prosthet. Dent*. 85 (2001) 162–169. doi:10.1067/mpr.2001.113778.
- [26] Schauf, Moffet, Moffet, *Medizinische Physiologie*, 1993.
- [27] L. Ovesen, F. Bendtsen, U. Tage-Jensen, N.T. Pedersen, B.R. Gram, S.J. Rune, Intraluminal pH in the stomach, duodenum, and proximal jejunum in normal subjects and patients with exocrine pancreatic insufficiency, *Gastroenterology*. 90 (1986) 958–962. doi:10.1016/0016-5085(86)90873-5.
- [28] G. Hounnou, C. Destrieux, J. Desmé, P. Bertrand, S. Velut, Anatomical study of the length of the human intestine, *Surg. Radiol. Anat*. 24 (2002) 290–294. doi:10.1007/s00276-002-0057-y.
- [29] Peptide therapeutics: current status and future directions, (n.d.). <http://www.sciencedirect.com/science/article/pii/S1359644614003997> (accessed October 10, 2016).
- [30] C.A. Squier, The permeability of keratinized and nonkeratinized oral epithelium to horseradish peroxidase, *J. Ultrastruct. Res*. 43 (1973) 160–177. doi:10.1016/S0022-5320(73)90076-2.
- [31] C.A. Squier, B.K. Hall, The permeability of mammalian nonkeratinized oral epithelia to horseradish peroxidase applied in vivo and in vitro, *Arch. Oral Biol*. 29 (1984) 45–50.

- [32] C.A. Squier, B.K. Hall, The Permeability of Skin and Oral Mucosa to Water and Horseradish Peroxidase as Related to the Thickness of the Permeability Barrier, *J. Invest. Dermatol.* 84 (1985) 176–179. doi:10.1111/1523-1747.ep12264711.
- [33] M. Derrien, M.W. van Passel, J.H. van de Bovenkamp, R.G. Schipper, W.M. de Vos, J. Dekker, Mucin-bacterial interactions in the human oral cavity and digestive tract, *Gut Microbes.* 1 (2010) 254–268. doi:10.4161/gmic.1.4.12778.
- [34] C. Triantos, N. Koukias, G. Karamanolis, K. Thomopoulos, Changes in the esophageal mucosa of patients with non erosive reflux disease: How far have we gone?, *World J. Gastroenterol. WJG.* 21 (2015) 5762–5767. doi:10.3748/wjg.v21.i19.5762.
- [35] C.H. Huh, M.S. Bhutani, E.B. Farfán, W.E. Bolch, Individual variations in mucosa and total wall thickness in the stomach and rectum assessed via endoscopic ultrasound, *Physiol. Meas.* 24 (2003) N15–22.
- [36] R. Bansil, B.S. Turner, The biology of mucus: Composition, synthesis and organization, *Adv. Drug Deliv. Rev.* 124 (2018) 3–15. doi:10.1016/j.addr.2017.09.023.
- [37] A.G. Beule, Physiology and pathophysiology of respiratory mucosa of the nose and the paranasal sinuses, *GMS Curr. Top. Otorhinolaryngol. Head Neck Surg.* 9 (2011). doi:10.3205/cto000071.
- [38] A.M. Lowman, M. Morishita, M. Kajita, T. Nagai, N.A. Peppas, Oral delivery of insulin using pH-responsive complexation gels, *J. Pharm. Sci.* 88 (1999) 933–937. doi:10.1021/js980337n.
- [39] F. Cui, K. Shi, L. Zhang, A. Tao, Y. Kawashima, Biodegradable nanoparticles loaded with insulin-phospholipid complex for oral delivery: Preparation, in vitro characterization and in vivo evaluation, *J. Controlled Release.* 114 (2006) 242–250. doi:10.1016/j.jconrel.2006.05.013.
- [40] M. Morishita, T. Goto, K. Nakamura, A.M. Lowman, K. Takayama, N.A. Peppas, Novel oral insulin delivery systems based on complexation polymer hydrogels: Single and multiple administration studies in type 1 and 2 diabetic rats, *J. Control. Release Off. J. Control. Release Soc.* 110 (2006) 587–594. doi:10.1016/j.jconrel.2005.10.029.
- [41] V.A. Eberle, J. Schoelkopf, P.A.C. Gane, R. Alles, J. Huwyler, M. Puchkov, Floating gastroretentive drug delivery systems: Comparison of experimental and simulated dissolution profiles and floatation behavior, *Eur. J. Pharm. Sci.* (2014) 34–43.
- [42] R. Gröning, M. Berntgen, M. Georgarakis, Acyclovir serum concentrations following peroral administration of magnetic depot tablets and the influence of extracorporeal magnets to control gastrointestinal transit, *Eur. J. Pharm. Biopharm.* 46 (1998) 285–291. doi:10.1016/S0939-6411(98)00052-6.
- [43] H. Park, K. Park, D. Kim, Preparation and swelling behavior of chitosan-based superporous hydrogels for gastric retention application, *J. Biomed. Mater. Res. A.* 76A (2006) 144–150. doi:10.1002/jbm.a.30533.
- [44] J.D. Smart, The basics and underlying mechanisms of mucoadhesion, *Adv. Drug Deliv. Rev.* 57 (2005) 1556–1568. doi:10.1016/j.addr.2005.07.001.
- [45] E. Mathiowitz, D.E.C. III, C.-M. Lehr, *Bioadhesive Drug Delivery Systems: Fundamentals, Novel Approaches, and Development*, CRC Press, 1999.
- [46] G.P. Andrews, T.P. Laverty, D.S. Jones, Mucoadhesive polymeric platforms for controlled drug delivery, *Eur. J. Pharm. Biopharm.* 71 (2009) 505–518. doi:10.1016/j.ejpb.2008.09.028.

- [47] European Pharmacopoeia, 8th ed., European directorate for the quality of medicine and healthcare, n.d.
- [48] K. Takayama, M. Hirata, Y. Machida, T. Masada, T. Sannan, T. Nagai, Effect of Interpolymer Complex Formation on Bioadhesive Property and Drug Release Phenomenon of Compressed Tablet Consisting of Chitosan and Sodium Hyaluronate, *Chem. Pharm. Bull. (Tokyo)*. 38 (1990) 1993–1997. doi:10.1248/cpb.38.1993.
- [49] H. Blanco-Fuente, B. Vila-Dorrio, S. Anguiano-Igea, F.J. Otero-Espinar, J. Blanco-Méndez, Tanned leather: A good model for determining hydrogels bioadhesion, *Int. J. Pharm.* 138 (1996) 103–112. doi:10.1016/0378-5173(96)04542-5.
- [50] S. Keely, A. Rullay, C. Wilson, A. Carmichael, S. Carrington, A. Corfield, D.M. Haddleton, D.J. Brayden, In Vitro and ex Vivo Intestinal Tissue Models to Measure Mucoadhesion of Poly (Methacrylate) and N-Trimethylated Chitosan Polymers, *Pharm. Res.* 22 (2005) 38–49. doi:10.1007/s11095-004-9007-1.
- [51] D. J. Hall, O. V. Khutoryanskaya, V. V. Khutoryanskiy, Developing synthetic mucosa-mimetic hydrogels to replace animal experimentation in characterisation of mucoadhesive drug delivery systems, *Soft Matter*. 7 (2011) 9620–9623. doi:10.1039/C1SM05929G.
- [52] M.T. Cook, S.L. Smith, V.V. Khutoryanskiy, Novel glycopolymer hydrogels as mucosa-mimetic materials to reduce animal testing, *Chem. Commun.* 51 (2015) 14447–14450. doi:10.1039/C5CC02428E.
- [53] J.B. da Silva, V.V. Khutoryanskiy, M.L. Bruschi, M.T. Cook, A mucosa-mimetic material for the mucoadhesion testing of thermogelling semi-solids, *Int. J. Pharm.* 528 (2017) 586–594. doi:10.1016/j.ijpharm.2017.06.025.
- [54] M.T. Cook, V.V. Khutoryanskiy, Mucoadhesion and mucosa-mimetic materials—A mini-review, *Int. J. Pharm.* 495 (2015) 991–998. doi:10.1016/j.ijpharm.2015.09.064.
- [55] In vitro/ex vivo methods for the evaluation of bioadhesive polymers. A preliminary study | Request PDF, ResearchGate. (n.d.). [https://www.researchgate.net/publication/291848599\\_In\\_vitroex\\_vivo\\_methods\\_for\\_the\\_evaluation\\_of\\_bioadhesive\\_polymers\\_A\\_preliminary\\_study](https://www.researchgate.net/publication/291848599_In_vitroex_vivo_methods_for_the_evaluation_of_bioadhesive_polymers_A_preliminary_study) (accessed October 15, 2018).
- [56] S.A. Mortazavi, J.D. Smart, An investigation of some factors influencing the in vitro assessment of mucoadhesion, *Int. J. Pharm.* 116 (1995) 223–230. doi:10.1016/0378-5173(94)00299-K.
- [57] M. Davidovich-Pinhas, H. Bianco-Peled, Mucoadhesion: a review of characterization techniques, *Expert Opin. Drug Deliv.* 7 (2010) 259–271. doi:10.1517/17425240903473134.
- [58] M.E. de Vries, H.E. Boddé, H.J. Busscher, H.E. Junginger, Hydrogels for buccal drug delivery: properties relevant for muco-adhesion, *J. Biomed. Mater. Res.* 22 (1988) 1023–1032. doi:10.1002/jbm.820221106.
- [59] F.J.O. Varum, F. Veiga, J.S. Sousa, A.W. Basit, An investigation into the role of mucus thickness on mucoadhesion in the gastrointestinal tract of pig, *Eur. J. Pharm. Sci. Off. J. Eur. Fed. Pharm. Sci.* 40 (2010) 335–341. doi:10.1016/j.ejps.2010.04.007.
- [60] A. Bernkop-Schnürch, S. Steininger, Synthesis and characterisation of mucoadhesive thiolated polymers, *Int. J. Pharm.* 194 (2000) 239–247. doi:10.1016/S0378-5173(99)00387-7.

- [61] A.M.L. Ray, P. Iooss, A. Gouyette, V. Vonarx, T. Patrice, C. Merle, Development of a “Continuous-Flow Adhesion Cell” for the Assessment of Hydrogel Adhesion, *Drug Dev. Ind. Pharm.* 25 (1999) 897–904. doi:10.1081/DDC-100102250.
- [62] K.V.R. Rao, P. Buri, A novel in situ method to test polymers and coated microparticles for bioadhesion, *Int. J. Pharm.* 52 (1989) 265–270. doi:10.1016/0378-5173(89)90229-9.
- [63] D. Preisig, R. Roth, S. Tognola, F. Varum, R. Bravo, Y. Cetinkaya, J. Huwyler, M. Puchkov, Mucoadhesive microparticles for local treatment of gastrointestinal diseases. - PubMed - NCBI, *Eur. J. Pharm. Sci.* (2016) 156–165.
- [64] W.A. Ducker, T.J. Senden, R.M. Pashley, Measurement of forces in liquids using a force microscope, *Langmuir*. 8 (1992) 1831–1836. doi:10.1021/la00043a024.
- [65] J. Cleary, L. Bromberg, E. Magner, Adhesion of Polyether-Modified Poly(acrylic acid) to Mucin, *Langmuir*. 20 (2004) 9755–9762. doi:10.1021/la048993s.
- [66] L. Joergensen, B. Klösgen, A.C. Simonsen, J. Borch, E. Hagesaether, New insights into the mucoadhesion of pectins by AFM roughness parameters in combination with SPR, *Int. J. Pharm.* 411 (2011) 162–168. doi:10.1016/j.ijpharm.2011.04.001.
- [67] I. Henriksen, Bioadhesion of hydrated chitosans: An in vitro and in vivo study, *Int. J. Pharm.* 145 (1996) 231–240. doi:10.1016/S0378-5173(96)04776-X.
- [68] K. Albrecht, M. Greindl, C. Kremser, C. Wolf, P. Debbage, A. Bernkop-Schnürch, Comparative in vivo mucoadhesion studies of thiomers formulations using magnetic resonance imaging and fluorescence detection, *J. Controlled Release*. 115 (2006) 78–84. doi:10.1016/j.jconrel.2006.06.023.
- [69] E.E. Hassan, J.M. Gallo, A Simple Rheological Method for the in Vitro Assessment of Mucin-Polymer Bioadhesive Bond Strength, *Pharm. Res.* 7 (1990) 491–495. doi:10.1023/A:1015812615635.
- [70] H. Hägerström, K. Edsman, Limitations of the rheological mucoadhesion method: The effect of the choice of conditions and the rheological synergism parameter, *Eur. J. Pharm. Sci.* 18 (2003) 349–357. doi:10.1016/S0928-0987(03)00037-X.
- [71] Mucoadhesion of pectin as evidence by wettability and chain interpenetration - Dimensions, (n.d.). <https://app.dimensions.ai/details/publication/pub.1017856275> (accessed October 16, 2018).
- [72] C.-M. Lehr, J.A. Bouwstra, H.E. Boddé, H.E. Junginger, A Surface Energy Analysis of Mucoadhesion: Contact Angle Measurements on Polycarbophil and Pig Intestinal Mucosa in Physiologically Relevant Fluids, *Pharm. Res.* 9 (1992) 70–75. doi:10.1023/A:1018931811189.
- [73] H. Takeuchi, J. Thongborisute, Y. Matsui, H. Sugihara, H. Yamamoto, Y. Kawashima, Novel mucoadhesion tests for polymers and polymer-coated particles to design optimal mucoadhesive drug delivery systems, *Adv. Drug Deliv. Rev.* 57 (2005) 1583–1594. doi:10.1016/j.addr.2005.07.008.
- [74] L. Jason-Moller, M. Murphy, J. Bruno, Overview of Biacore systems and their applications, *Curr. Protoc. Protein Sci.* Chapter 19 (2006) Unit 19.13. doi:10.1002/0471140864.ps1913s45.
- [75] D.L. Nelson, *Lehninger Principles of Biochemistry*, 3rd ed., n.d.
- [76] H.L. Casal, U. Köhler, H.H. Mantsch, Structural and conformational changes of  $\beta$ -lactoglobulin B: an infrared spectroscopic study of the effect of pH and temperature, *Biochim. Biophys. Acta BBA - Protein Struct. Mol. Enzymol.* 957 (1988) 11–20. doi:10.1016/0167-4838(88)90152-5.

- [77] M.E. Bohlin, L.G. Blomberg, N.H.H. Heegaard, Effects of ionic strength, temperature and conformation on affinity interactions of  $\beta$ 2-glycoprotein I monitored by capillary electrophoresis, *ELECTROPHORESIS*. 32 (2011) 728–737. doi:10.1002/elps.201000538.
- [78] E. Cao, Y. Chen, Z. Cui, P.R. Foster, Effect of freezing and thawing rates on denaturation of proteins in aqueous solutions, *Biotechnol. Bioeng.* 82 (2003) 684–690. doi:10.1002/bit.10612.
- [79] P. Sen, S. Yamaguchi, T. Tahara, New Insight into the Surface Denaturation of Proteins: Electronic Sum Frequency Generation Study of Cytochrome c at Water Interfaces, *J. Phys. Chem. B*. 112 (2008) 13473–13475. doi:10.1021/jp8061288.
- [80] E. Di Stasio, R. De Cristofaro, The effect of shear stress on protein conformation: Physical forces operating on biochemical systems: The case of von Willebrand factor. - PubMed - NCBI, *Biophys. Chem.* (2010) 1–8.
- [81] S.E. Charm, B.L. Wong, Shear effects on enzymes, *Enzyme Microb. Technol.* 3 (1981) 111–118. doi:10.1016/0141-0229(81)90068-5.
- [82] V.V. Mozhaev, K. Heremans, J. Frank, P. Masson, C. Balny, High pressure effects on protein structure and function, *Proteins Struct. Funct. Bioinforma.* 24 (1996) 81–91. doi:10.1002/(SICI)1097-0134(199601)24:1<81::AID-PROT6>3.0.CO;2-R.
- [83] M. Klukkert, M. van de Weert, M. Fanø, T. Rades, C.S. Leopold, Influence of Tableting on the Conformation and Thermal Stability of Trypsin as a Model Protein, *J. Pharm. Sci.* 104 (2015) 4314–4321. doi:10.1002/jps.24672.
- [84] M. Rabe, D. Verdes, S. Seeger, Understanding protein adsorption phenomena at solid surfaces, *Adv. Colloid Interface Sci.* 162 (2011) 87–106. doi:10.1016/j.cis.2010.12.007.
- [85] T. Arnebrant, K. Barton, T. Nylander, Adsorption of  $\alpha$ -lactalbumin and  $\beta$ -lactoglobulin on metal surfaces versus temperature, *J. Colloid Interface Sci.* 119 (1987) 383–390. doi:10.1016/0021-9797(87)90284-0.
- [86] É. Kiss, Temperature dependence of bovine serum albumin adsorption onto a poly(ethylene oxide)-grafted surface, *Colloids Surf. Physicochem. Eng. Asp.* 76 (1993) 135–140. doi:10.1016/0927-7757(93)80071-L.
- [87] G. Jackler, R. Steitz, C. Czeslik, Effect of Temperature on the Adsorption of Lysozyme at the Silica/Water Interface Studied by Optical and Neutron Reflectometry, *Langmuir*. 18 (2002) 6565–6570. doi:10.1021/la025605i.
- [88] S. Demanèche, J.-P. Chapel, L.J. Monrozier, H. Quiquampoix, Dissimilar pH-dependent adsorption features of bovine serum albumin and  $\alpha$ -chymotrypsin on mica probed by AFM, *Colloids Surf. B Biointerfaces*. 70 (2009) 226–231. doi:10.1016/j.colsurfb.2008.12.036.
- [89] H.T.M. Phan, S. Bartelt-Hunt, K.B. Rodenhausen, M. Schubert, J.C. Bartz, Investigation of Bovine Serum Albumin (BSA) Attachment onto Self-Assembled Monolayers (SAMs) Using Combinatorial Quartz Crystal Microbalance with Dissipation (QCM-D) and Spectroscopic Ellipsometry (SE), *PLoS ONE*. 10 (2015). doi:10.1371/journal.pone.0141282.
- [90] A.M. Hyde, S.L. Zultanski, J.H. Waldman, Y.-L. Zhong, M. Shevlin, F. Peng, General Principles and Strategies for Salting-Out Informed by the Hofmeister Series, *Org. Process Res. Dev.* 21 (2017) 1355–1370. doi:10.1021/acs.oprd.7b00197.

- [91] T.E. Benavidez, D. Torrente, M. Marucho, C.D. Garcia, Adsorption of Soft and Hard Proteins onto OTCEs under the influence of an External Electric Field, *Langmuir ACS J. Surf. Colloids.* 31 (2015) 2455–2462. doi:10.1021/la504890v.
- [92] Driving forces for protein adsorption at solid surfaces - Norde - 1996 - *Macromolecular Symposia* - Wiley Online Library, (n.d.). <http://onlinelibrary.wiley.com/doi/10.1002/masy.19961030104/full> (accessed May 29, 2017).
- [93] Z.S. Olempska-Beer, R.I. Merker, M.D. Ditto, M.J. DiNovi, Food-processing enzymes from recombinant microorganisms—a review, *Regul. Toxicol. Pharmacol.* 45 (2006) 144–158. doi:10.1016/j.yrtph.2006.05.001.
- [94] A. Khusainova, Enhanced Oil Recovery with Application of Enzymes, (n.d.) 130.
- [95] N. Durán, E. Esposito, Potential applications of oxidative enzymes and phenoloxidase-like compounds in wastewater and soil treatment: a review, *Appl. Catal. B Environ.* 28 (2000) 83–99. doi:10.1016/S0926-3373(00)00168-5.
- [96] V.P. Torchilin, *Immobilized Enzymes in Medicine*, Springer Science & Business Media, 2012.
- [97] C.L. Levy, G.P. Matthews, G.M. Laudone, C.M. Gribble, A. Turner, C.J. Ridgway, D.E. Gerard, J. Schoelkopf, P.A.C. Gane, Diffusion and Tortuosity in Porous Functionalized Calcium Carbonate, *Ind. Eng. Chem. Res.* 54 (2015) 9938–9947. doi:10.1021/acs.iecr.5b02362.
- [98] C.L. Levy, G.P. Matthews, G.M. Laudone, S. Beckett, A. Turner, J. Schoelkopf, P.A.C. Gane, Mechanism of adsorption of actives onto microporous functionalised calcium carbonate (FCC), *Adsorption.* 23 (2017) 603–612. doi:10.1007/s10450-017-9880-7.
- [99] T. Stirnimann, N.D. Maiuta, D.E. Gerard, R. Alles, J. Huwyler, M. Puchkov, Functionalized Calcium Carbonate as a Novel Pharmaceutical Excipient for the Preparation of Orally Dispersible Tablets, *Pharm. Res.* (2013) 1915–1925.
- [100] T. Stirnimann, S. Atria, J. Schoelkopf, P.A.C. Gane, R. Alles, J. Huwyler, M. Puchkov, Compaction of functionalized calcium carbonate, a porous and crystalline microparticulate material with a lamellar surface, *Int. J. Pharm.* (2014) 266–275.
- [101] V.A. Eberle, A. Häring, J. Schoelkopf, P.A.C. Gane, J. Huwyler, M. Puchkov, In silico and in vitro methods to optimize the performance of experimental gastroretentive floating mini-tablets, *Drug Dev. Ind. Pharm.* 42 (2016) 808–817. doi:10.3109/03639045.2015.1078350.
- [102] D. Preisig, D. Haid, F.J.O. Varum, R. Bravo, R. Alles, J. Huwyler, M. Puchkov, Drug loading into porous calcium carbonate microparticles by solvent evaporation, *Eur. J. Pharm. Biopharm.* (2014) 548–558.
- [103] L.A. Giannuzzi, F.A. Stevie, A review of focused ion beam milling techniques for TEM specimen preparation, *Micron.* 30 (1999) 197–204. doi:10.1016/S0968-4328(99)00005-0.
- [104] Z. Dong, S.J. Kennedy, Y. Wu, Electrospinning materials for energy-related applications and devices, *J. Power Sources.* 196 (2011) 4886–4904. doi:10.1016/j.jpowsour.2011.01.090.
- [105] M. Zhu, J. Han, F. Wang, W. Shao, R. Xiong, Q. Zhang, H. Pan, Y. Yang, S.K. Samal, F. Zhang, C. Huang, Electrospun Nanofibers Membranes for Effective Air Filtration, *Macromol. Mater. Eng.* 302 (2016) 1600353. doi:10.1002/mame.201600353.

- [106] D. Aussawasathien, C. Teerawattananon, A. Vongachariya, Separation of micron to sub-micron particles from water: Electrospun nylon-6 nanofibrous membranes as pre-filters, *J. Membr. Sci.* 315 (2008) 11–19. doi:10.1016/j.memsci.2008.01.049.
- [107] M. Faccini, G. Borja, M. Boerrigter, D. Morillo Martín, S. Martínez Crespiera, S. Vázquez-Campos, L. Aubouy, D. Amantia, Electrospun Carbon Nanofiber Membranes for Filtration of Nanoparticles from Water, *J. Nanomater.* (2015). doi:10.1155/2015/247471.
- [108] T. Kowalczyk, A. Nowicka, D. Elbaum, T.A. Kowalewski, Electrospinning of Bovine Serum Albumin. Optimization and the Use for Production of Biosensors., *Biomacromolecules.* 9 (2008) 2087–2090. doi:10.1021/bm800421s.
- [109] S. Lee, S.K. Obendorf, Developing protective textile materials as barriers to liquid penetration using melt-electrospinning, *J. Appl. Polym. Sci.* 102 (2006) 3430–3437. doi:10.1002/app.24258.
- [110] P. Zahedi, I. Rezaeian, S.-O. Ranaei-Siadat, S.-H. Jafari, P. Supaphol, A review on wound dressings with an emphasis on electrospun nanofibrous polymeric bandages, *Polym. Adv. Technol.* 21 (2010) 77–95. doi:10.1002/pat.1625.
- [111] T.J. Sill, H.A. von Recum, Electrospinning: Applications in drug delivery and tissue engineering, *Biomaterials.* 29 (2008) 1989–2006. doi:10.1016/j.biomaterials.2008.01.011.
- [112] X. Hu, S. Liu, G. Zhou, Y. Huang, Z. Xie, X. Jing, Electrospinning of polymeric nanofibers for drug delivery applications, *J. Controlled Release.* 185 (2014) 12–21. doi:10.1016/j.jconrel.2014.04.018.
- [113] R. Rangkupan, D.H. Reneker, Electrospinning Process of Molten Polypropylene in Vacuum, (n.d.) 7.
- [114] Z.-M. Huang, Y.-Z. Zhang, M. Kotaki, S. Ramakrishna, A review on polymer nanofibers by electrospinning and their applications in nanocomposites, *Compos. Sci. Technol.* 63 (2003) 2223–2253. doi:10.1016/S0266-3538(03)00178-7.
- [115] A. Jaworek, Micro- and nanoparticle production by electrospraying, *Powder Technol.* 176 (2007) 18–35. doi:10.1016/j.powtec.2007.01.035.
- [116] D. Crespy, K. Friedemann, A.-M. Popa, Colloid-Electrospinning: Fabrication of Multicompartment Nanofibers by the Electrospinning of Organic or/and Inorganic Dispersions and Emulsions, *Macromol. Rapid Commun.* 33 (2012) 1978–1995. doi:10.1002/marc.201200549.
- [117] E. Klimov, V. Raman, R. Venkatesh, W. Heckmann, R. Stark, Designing Nanofibers via Electrospinning from Aqueous Colloidal Dispersions: Effect of Cross-Linking and Template Polymer, *Macromolecules.* 43 (2010) 6152–6155. doi:10.1021/ma100750e.
- [118] I.W. Lenggoro, B. Xia, K. Okuyama, J.F. de la Mora, Sizing of Colloidal Nanoparticles by Electrospray and Differential Mobility Analyzer Methods, *Langmuir.* 18 (2002) 4584–4591. doi:10.1021/la015667t.
- [119] R. Roth, J. Schoelkopf, J. Huwyler, M. Puchkov, Functionalized calcium carbonate microparticles for the delivery of proteins, *Eur. J. Pharm. Biopharm.* 122 (2018) 96–103. doi:10.1016/j.ejpb.2017.10.012.
- [120] C. Calderon, E. Abuin, E. Lissi, R. Montecinos, Effect of Human Serum Albumin on the Kinetics of 4-Methylumbelliferyl- b -D- N-N 0 - N 00 Triacetylchitotrioside Hydrolysis Catalyzed by Hen Egg White Lysozyme, *Protein J.* (2011) 367–373.



- [121] S.M. Daly, T.M. Przybycien, R.D. Tilton, Aggregation of lysozyme and of poly(ethylene glycol)-modified lysozyme after adsorption to silica, *Colloids Surf. B Biointerfaces*. 57 (2007) 81–88. doi:10.1016/j.colsurfb.2007.01.007.
- [122] A.A. Vertegel, R.W. Siegel, J.S. Dordick, Silica Nanoparticle Size Influences the Structure and Enzymatic Activity of Adsorbed Lysozyme., *Langmuir*. (2004) 6800–6807.
- [123] Prevention of thermal inactivation and aggregation of lysozyme by polyamines - Kudou - 2003 - The FEBS Journal - Wiley Online Library, (n.d.). <http://onlinelibrary.wiley.com/doi/10.1046/j.1432-1033.2003.03850.x/full> (accessed January 24, 2017).
- [124] M. van de Weert, J. Hoehstetter, W.E. Hennink, D.J.A. Crommelin, The effect of a water/organic solvent interface on the structural stability of lysozyme, *J. Controlled Release*. 68 (2000) 351–359. doi:10.1016/S0168-3659(00)00277-7.
- [125] J. P. Mann, A. McCluskey, R. Atkin, Activity and thermal stability of lysozyme in alkylammonium formate ionic liquids —influence of cation modification, *Green Chem*. 11 (2009) 785–792. doi:10.1039/B900021F.
- [126] S. Venkataramani, J. Truntzer, D.R. Coleman, Thermal stability of high concentration lysozyme across varying pH: A Fourier Transform Infrared study, *J. Pharm. Bioallied Sci*. 5 (2013) 148–153. doi:10.4103/0975-7406.111821.
- [127] V. Lechevalier, T. Croguennec, S. Pezenec, C. Guérin-Dubiard, M. Pasco, F. Nau, Ovalbumin, Ovotransferrin, Lysozyme: Three Model Proteins for Structural Modifications at the Air–Water Interface, *J. Agric. Food Chem*. 51 (2003) 6354–6361. doi:10.1021/jf034184n.
- [128] S. Ge, K. Kojio, A. Takahara, T. Kajiyama, Bovine serum albumin adsorption onto immobilized organotrichlorosilane surface: influence of the phase separation on protein adsorption patterns., *J. Biomater. Sci. Polym. Ed.* (1998) 131–151.
- [129] T. Estey, J. Kang, S.P. Schwendeman, J.F. Carpenter, BSA degradation under acidic conditions: a model for protein instability during release from PLGA delivery systems, *J. Pharm. Sci*. 95 (2006) 1626–1639. doi:10.1002/jps.20625.
- [130] R. Li, Z. Wu, Y. Wangb, L. Ding, Y. Wang, Role of pH-induced structural change in protein aggregation in foam fractionation of bovine serum albumin, *Biotechnol. Rep*. 9 (2016) 46–52. doi:10.1016/j.btre.2016.01.002.
- [131] B. Beykal, M. Herzberg, Y. Oren, M.S. Mauter, Influence of surface charge on the rate, extent, and structure of adsorbed Bovine Serum Albumin to gold electrodes, *J. Colloid Interface Sci*. 460 (2015) 321–328. doi:10.1016/j.jcis.2015.08.055.
- [132] V. Bloomfield, The Structure of Bovine Serum Albumin at Low pH \*, *Biochemistry*. 5 (1966) 684–689. doi:10.1021/bi00866a039.
- [133] H. Larsericsdotter, S. Oscarsson, J. Buijs, Structure, stability, and orientation of BSA adsorbed to silica, *J. Colloid Interface Sci*. 289 (2005) 26–35. doi:10.1016/j.jcis.2005.03.064.
- [134] Y.L. Jeyachandran, E. Mielczarski, B. Rai, J.A. Mielczarski, Quantitative and Qualitative Evaluation of Adsorption/Desorption of Bovine Serum Albumin on Hydrophilic and Hydrophobic Surfaces, *Langmuir*. 25 (2009) 11614–11620. doi:10.1021/la901453a.
- [135] S. Fukuzaki, H. Urano, K. Nagata, Adsorption of protein onto stainless-steel surfaces, *J. Ferment. Bioeng*. 80 (1995) 6–11. doi:10.1016/0922-338X(95)98168-K.

- [136] P. Billsten, M. Wahlgren, T. Arnebrant, J. McGuire, H. Elwing, Structural Changes of T4 Lysozyme upon Adsorption to Silica Nanoparticles Measured by Circular Dichroism, *J. Colloid Interface Sci.* 175 (1995) 77–82. doi:10.1006/jcis.1995.1431.
- [137] I. Langmuir, V.J. Schaefer, Properties and Structure of Protein Monolayers., *Chem. Rev.* 24 (1939) 181–202. doi:10.1021/cr60078a002.
- [138] N. Aggarwal, K. Lawson, M. Kershaw, R. Horvath, J. Ramsden, Protein adsorption on heterogeneous surfaces, *Appl. Phys. Lett.* 94 (2009) 083110. doi:10.1063/1.3078397.
- [139] R. Seitz, R. Brings, R. Geiger, Protein adsorption on solid–liquid interfaces monitored by laser-ellipsometry, *Appl. Surf. Sci.* 252 (2005) 154–157. doi:10.1016/j.apsusc.2005.02.012.
- [140] M. Farzan, R. Roth, G. Québatte, J. Schoelkopf, J. Huwyler, M. Puchkov, Loading of Porous Functionalized Calcium Carbonate Microparticles: Distribution Analysis with Focused Ion Beam Electron Microscopy and Mercury Porosimetry, *Pharmaceutics*. 11 (2019) 32. doi:10.3390/pharmaceutics11010032.
- [141] F. Evers, R. Steitz, M. Tolan, C. Czeslik, Reduced Protein Adsorption by Osmolytes, *Langmuir*. 27 (2011) 6995–7001. doi:10.1021/la2010908.
- [142] L. Han, B. Yan, L. Zhang, M. Wu, J. Wang, J. Huang, Y. Deng, H. Zeng, Tuning protein adsorption on charged polyelectrolyte brushes via salinity adjustment, *Colloids Surf. Physicochem. Eng. Asp.* 539 (2018) 37–45. doi:10.1016/j.colsurfa.2017.12.004.
- [143] K. Bergström, K. Holmberg, A. Safran, A.S. Hoffman, M.J. Edgell, A. Kozłowski, B.A. Hovanes, J.M. Harris, Reduction of fibrinogen adsorption on PEG-coated polystyrene surfaces, *J. Biomed. Mater. Res.* 26 (1992) 779–790. doi:10.1002/jbm.820260607.
- [144] R. Michel, S. Pasche, M. Textor, D.G. Castner, The Influence of PEG Architecture on Protein Adsorption and Conformation, *Langmuir ACS J. Surf. Colloids*. 21 (2005) 12327–12332. doi:10.1021/la051726h.
- [145] K. Höger, T. Becherer, W. Qiang, R. Haag, W. Friess, S. Küchler, Polyglycerol coatings of glass vials for protein resistance, *Eur. J. Pharm. Biopharm. Off. J. Arbeitsgemeinschaft Pharm. Verfahrenstechnik EV.* 85 (2013) 756–764. doi:10.1016/j.ejpb.2013.04.005.
- [146] M. Malmsten, K. Emoto, J.M. Van Alstine, Effect of Chain Density on Inhibition of Protein Adsorption by Poly(ethylene glycol) Based Coatings, *J. Colloid Interface Sci.* 202 (1998) 507–517. doi:10.1006/jcis.1998.5513.
- [147] A. Garapaty, J.A. Champion, Non-covalent phosphorylcholine coating reduces protein adsorption and phagocytic uptake of microparticles, *Chem. Commun.* 51 (2015) 13814–13817. doi:10.1039/C5CC03459K.
- [148] T. Chandy, C.P. Sharma, Chitosan beads and granules for oral sustained delivery of nifedipine: in vitro studies, *Biomaterials*. 13 (1992) 949–952. doi:10.1016/0142-9612(92)90119-9.
- [149] T. Chandy, C.P. Sharma, Chitosan matrix for oral sustained delivery of ampicillin, *Biomaterials*. 14 (1993) 939–944. doi:10.1016/0142-9612(93)90136-P.
- [150] K. Oungbho, B.W. Müller, Chitosan sponges as sustained release drug carriers, *Int. J. Pharm.* (1997) 229–237.

- [151] D. Seo, A.M. Schrader, S.-Y. Chen, Y. Kaufman, T.R. Cristiani, S.H. Page, P.H. Koenig, Y. Gizaw, D.W. Lee, J.N. Israelachvili, Rates of cavity filling by liquids, *Proc. Natl. Acad. Sci.* 115 (2018) 8070–8075. doi:10.1073/pnas.1804437115.
- [152] S.T. Yohe, Y.L. Colson, M.W. Grinstaff, Superhydrophobic Materials for Tunable Drug Release: Using Displacement of Air To Control Delivery Rates, *J. Am. Chem. Soc.* 134 (2012) 2016–2019. doi:10.1021/ja211148a.
- [153] J. Fields, J.T. Go, K.S. Schulze, Pill Properties that Cause Dysphagia and Treatment Failure, *Curr. Ther. Res.* 77 (2015) 79–82. doi:10.1016/j.curtheres.2015.08.002.
- [154] H. Miura, M. Kariyasu, [Effect of size of tablets on easiness of swallowing and handling among the frail elderly], *Nihon Ronen Igakkai Zasshi Jpn. J. Geriatr.* 44 (2007) 627–633.
- [155] K. Kasashi, K. Tei, Y. Totsuka, T. Yamada, K. Iseki, The influence of size, specific gravity, and head position on the swallowing of solid preparations, *Oral Sci. Int.* 8 (2011) 55–59. doi:10.1016/S1348-8643(11)00028-0.
- [156] F. Kiekens, R. Zelkó, J.P. Remon, A Comparison of the Inter- and Intragranular Drug Migration in Tray- and Freeze-Dried Granules and Compacts, *Pharm. Dev. Technol.* 4 (1999) 415–420. doi:10.1081/PDT-100101377.
- [157] R.K. Gilpin, W. Zhou, Studies of the Thermal Degradation of Acetaminophen Using a Conventional HPLC Approach and Electrospray Ionization-Mass Spectrometry, *J. Chromatogr. Sci.* 42 (2004) 15–20. doi:10.1093/chromsci/42.1.15.
- [158] R. Da Silva Leite, R. De Oliveira Macedo, S.M. Torres, C.C.N. Batista, L. De Oliveira Baltazar, S.A.L. Neto, F.S. De Souza, Evaluation of thermal stability and parameters of dissolution of nifedipine crystals, *J. Therm. Anal. Calorim.* 111 (2013) 2117–2123. doi:10.1007/s10973-012-2605-y.
- [159] O. Svahn, E. Björklund, Thermal stability assessment of antibiotics in moderate temperature and subcritical water using a pressurized dynamic flow-through system, 11 (2015) 9.
- [160] E.P. da Silva, M.A.V. Pereira, I.P. de Barros Lima, N.G.P.B. Lima, E.G. Barbosa, C.F.S. Aragão, A.P.B. Gomes, Compatibility study between atorvastatin and excipients using DSC and FTIR, *J. Therm. Anal. Calorim.* 123 (2016) 933–939. doi:10.1007/s10973-015-5077-z.
- [161] A.A. Silva-Júnior, M.V. Scarpa, K.C. Pestana, L.P. Mercuri, J.R. de Matos, A.G. de Oliveira, Thermal analysis of biodegradable microparticles containing ciprofloxacin hydrochloride obtained by spray drying technique, *Thermochim. Acta.* 467 (2008) 91–98. doi:10.1016/j.tca.2007.10.018.
- [162] B.V. Pinto, A.P.G. Ferreira, E.T.G. Cavalheiro, Thermal degradation mechanism for citalopram and escitalopram, *J. Therm. Anal. Calorim.* 133 (2018) 1509–1518. doi:10.1007/s10973-018-7226-7.
- [163] P.R. Oliveira, L.S. Bernardi, F.S. Murakami, C. Mendes, M.A.S. Silva, Thermal characterization and compatibility studies of norfloxacin for development of extended release tablets, *J. Therm. Anal. Calorim.* 97 (2009) 741. doi:10.1007/s10973-009-0347-2.
- [164] H. Paul C., R. Raj, *Principles of Colloid and Surface Chemistry*, 3rd ed., 1997.
- [165] T. Asakura, K. Adachi, E. Schwartz, Stabilizing effect of various organic solvents on protein, *J. Biol. Chem.* 253 (1978) 6423–6425.
- [166] L. Wagner-Hattler, J. Schoelkopf, J. Huwyler, M. Puchkov, Characterization of new functionalized calcium carbonate-polycaprolactone composite material for application in geometry-constrained drug

release formulation development, *Drug Dev. Ind. Pharm.* 43 (2017) 1669–1676. doi:10.1080/03639045.2017.1328435.

- [167] A. Schittny, H. Ogawa, J. Huwyler, M. Puchkov, A combined mathematical model linking the formation of amorphous solid dispersions with hot-melt-extrusion process parameters, *Eur. J. Pharm. Biopharm.* 132 (2018) 127–145. doi:10.1016/j.ejpb.2018.09.011.
- [168] D. Huang, MODELING OF PARTICLE FORMATION DURING SPRAY DRYING, (n.d.) 3.

## 7. Curriculum Vitae

**Roger Roth**

Gellertpark 3

4052 Basel

Switzerland

Rogerdotroth@gmail.com

Mobile +41 79 821 08 00

17.06.1984

Switzerland

PhD Student in Pharmaceutical  
Technology



---

**Education**

2015-2019	PhD Thesis in Pharmaceutical Technology	Basel, Switzerland
2014	Master thesis in Pharmaceutical Technology	Basel, Switzerland
2006-2014	Master degree in Pharmaceutical sciences	Basel, Switzerland
1998-2005	High School (Gymnasium Kirschgarten)	Basel, Switzerland

---

---

**Skills**

Language	German (native), English (fluent), French (basic knowledge)
Software	Microsoft Office, Origin Pro, Adobe Illustrator, GIMP, Solid Works
Teaching	Practical course: Pharmaceutical Technology; Solid dosage formulation for bachelor students Supervision of master students
Technical	Mercury Porosimetry, Dissolution, HPLC, Isothermal Titration Calorimetry (ITC), Fluidized Bed Processing, Tableting, Drum Coating,

---

---

## Private Activities and Interests

Snowboarding and hiking

Handcrafting

Exploring

---

---

## Publications

P. Uhl, C. Grundmann, M. Sauter, P. Storck, A. Tursch, S. Özbek, **R. Roth**, D. Witzigmann, J. Kulkarni, G. Fricker, W. Mier, (2018), Coating of PLA-nanoparticles with a cyclic, arginine-rich cell penetrating peptide highly improves oral delivery of liraglutide, submitted to *Biomaterials* .

**R. Roth**, M. Farzan, G. Québatte, J. Schoelkopf, J. Huwyler, M. Puchkov, (2018), Loading of porous functionalized calcium carbonate microparticles: Distribution analysis with focused ion beam electron microscopy and mercury porosimetry, *Pharmaceutics*, **2019**, 11, 32.

**R. Roth**, J. Schoelkopf, J. Huwyler, M. Puchkov, (2018), Functionalized calcium carbonate microparticles for the delivery of proteins, *European Journal of Pharmaceutics and Biopharmaceutics*, 122 (2018) 96–103. doi:10.1016/j.ejpb.2017.10.012.

D. Preisig, **R. Roth**, S. Tognola, F.J.O. Varum, R. Bravo, Y. Cetinkaya, J. Huwyler, M. Puchkov, (2016), Mucoadhesive microparticles for local treatment of gastrointestinal diseases, *European Journal of Pharmaceutics and Biopharmaceutics*, 105 (2016) 156–165. doi:10.1016/j.ejpb.2016.06.009.

---

---

## Posters and Talks

Poster presentation at the Swiss Pharma Science Day in Bern, Switzerland (2016, 2018)

Poster presentation at the Controlled Release Society Meeting in Seattle, USA (2016)

Talk at the Pharmaceutical Technology Meeting in Geneva, Switzerland (2016)

Poster presentation at the Annual Research Meeting in Basel, Switzerland (2015)

---